Design and build of novel electric machines for transport electrification (Alternative Format Thesis)

Yin, Boyuan

Award date:
2022

Awarding institution:
University of Bath

UNIVERSITY OF BATH

Design and build of novel electric machines for transport electrification

By

Boyuan Yin

BEng

The thesis submitted for the degree of

Doctor of Philosophy

in

The Department of
Electronic and Electrical Engineering
University of Bath

November 2022

Signature:…… Date:……

Contents

Abstract

Decarbonisation has been a worldwide target to achieve global emissions reduction. The electrification of transportation has been proposed not only for sustainable and net-zero targets but also to provide a more energy-efficient solution. Electric propulsion has been widely considered in ship systems and aviation. An integrated full electric propulsion (IFEP) system removes the direct mechanical coupling between a prime mover and a propeller, which is replaced by an all-electric onboard network to supply both the ship services such as the domestic/hotel loads (navigation, lighting, air-conditioning, etc) and also the propulsion systems, which can subsequently reduce fuel consumption, increase system reliability and reduce maintenance costs. To help achieve these goals during this PhD research project a magnetically decoupled dual wound generator and a novel fast-operation moving coil actuator were designed, built and experimentally tested.

A dual wound generator, designed as the power supply for an IFEP system, provides power simultaneously for the ship services and propulsion systems. The main challenge of the design of a dual wound generator for an IFEP system is the decoupling of the two outputs. A fully magnetically decoupled dual wound generator with 2-pole and 6-pole windings for ships power requirements is developed in this thesis. The harmonics calculation using an algebraic method is described in detail for the winding design. A 2D finite element model is built and simulated in COMSOL, to investigate the magnetic field distributions and machine dynamical performance. A prototype dual wound generator is manufactured and tested to further validate the decoupling of the two outputs. Different load conditions are tested considering the practical operations. The experimental results demonstrate that the two outputs including the end-windings are fully decoupled under complex load conditions.

Hydrogen-powered all-electric aircraft, developed for the requirements of sustainability and decarbonisation, have higher energy efficiency, less fuel consumption and potential

weight reductions. One of the key limitations to improving the reliability of onboard DC networks is the design of fast operating DC circuit breakers to isolate high and fast-rise DC fault currents. A novel design of a moving coil actuator with compensation coils topology for hybrid DC circuit breakers is also presented in this thesis. The actuator topology is designed and simulated by 2D finite element modelling in COMSOL. A prototype moving coil actuator is built and experimentally tested with a vacuum interrupter. Mechanical latching springs and other supporting structures are also included in the prototype to eliminate the effect of bouncing, rebounding and welding. The experimental results demonstrate that the compensation coils can eliminate the saturation, reducing the coil equivalent inductance and improving the operating speed.

Publications

[1] **B. Yin**, X. Pei, J. F. Eastham, H. Wang, C. Hodge, O. Simmonds, C. Vagg and X. Zeng, “Magnetic Decoupling of Winding Design in Dual Wound Generators,” in IEEE Transactions on Energy Conversion, 2022, doi: 10.1109/TEC.2022.3191952.

[2] **B. Yin**, X. Zeng, J. F. Eastham, D. Vilchis-Rodriguez and X. Pei, “Novel fast operating moving coil actuator with compensation coil for HVDC circuit breakers,” in CSEE Journal of Power and Energy Systems, vol. 7, no. 5, pp. 1041-1050, Sep. 2021, doi: 10.17775/CSEEJPES.2020.06910.

[3] H. Wang, X. Pei, **B. Yin**, J. F. Eastham, C. Vagg and X. Zeng, “A novel double-sided offset stator axial-flux permanent magnet motor for electric vehicles,” in World Electric Vehicle Journal (WEVJ), vol. 13, no. 3, pp. 1-13, Mar. 2022, doi: 10.3390/wevj13030052

[4] **B. Yin**, X. Pei, J. F. Eastham, X. Zeng, “Analysis of stator end-winding in a dual wound machine using Biot-Savart law,” PEMD 2022: The 11th International Conference on Power Electronics, Machines and Drives.

[5] **B. Yin**, X. Pei, X. Zeng, F. Eastham, C. Hodge and O. Simmonds, “Design and analysis of dual wound machine for electric ships,” 2020 International Conference on Electrical Machines (ICEM), 2020, pp. 104-110, doi: 10.1109/ICEM49940.2020.9270913.

[6] **B. Yin**, X. Pei, X. Zeng and F. Eastham, “A comparison between moving magnet and moving coil actuators for vacuum interrupters,” IECON 2019 - 45th Annual Conference of the IEEE Industrial Electronics Society, 2019, pp. 5651-5656, doi: 10.1109/IECON.2019.8927691.

[7] C. Hodge, **B. Yin**, X. Pei, J. F. Eastham, X. Zeng and O. Simmonds, “The implementation of a dual wound machine using a fractional slot winding,” INEC 2020: The 15th International Naval Engineering Conference and Exhibition.

[8] **B. Yin**, X. Pei, J. F. Eastham, H. Wang, X. Zeng, “Experimental testing of the dynamic performance of a magnetic decoupled dual wound generator,” (submitted).

[9] **B. Yin**, X. Pei, J. F. Eastham, Emelie Nilsson, Jean-francois Rouquette, Jean Rivenc, Ludovic Ybanez, X. Zeng, “A fast operating moving coil actuator with compensation coils for vacuum interrupters,” (submitted).

Acknowledgement

I would like to express my deepest gratitude to my supervisor, Dr Xiaoze Pei, for her invaluable supervision, patient guidance and encouragement throughout the course of my PhD degree. I have been extremely lucky to have a supervisor who cared so much about my work and always responded to my questions and queries so promptly.

I would also like to express my heartfelt gratitude to Prof. John Fred Eastham. I appreciate for his insightful comments and suggestions to my research. His immense knowledge inspires me to the right path.

Great thanks to Dr Xianwu Zeng for his guidance to my prototype designs, Michael Linham for his great helps on fabricating excellent mechanical works, David Chapman who provides me a lot help on design technologies, Ann Linfield for her great support for my life at the University. I would like to thank Dr Damian Vilchis-Rodriguez from the University of Manchester, Christ Hodge and Oliver Simmonds from BMT Ltd, and Chris Vagg for their guidance during my study.

I would like to express my gratefulness to Dr Chenghong Gu, Dr Kang Ma for constructive suggestions and advice. I would also like to express my thanks to my fellow friends and colleagues, Dr Qixing Sun, Dr Dong Xing, Dr Jiawen Xi for their support at the beginning of my study, Dr Wenjuan Song, Dr Hammond, Dr Zhongying Wang, Dr Roberto Henrique De Oliveira, Mr Moanis Khedr, Mr Han Wang, Miss Xue Bai, Mr Peilin Liu, Mr Constantinos Liagas, Mr Xin Gao, Mr Yuanbin Zhu, Mr Junlong Li, Mr Jiahang Li, and Mr Yuchun Lin for their wonderful collaboration.

Special thanks to my friends, Mr Renjie Wei, Mr Xuyang Wang, Miss Tian Gan, Mr Qiliang Xu and Mr Pengkun Yuan, for their accompany out of my research life.

Finally, I would like to take this opportunity to express my greatest thanks to my family,

especially to my parents and my grandparents who support me in every step of my study period. Thanks to their endless encouragement and support, I was able to touch on world-leading studies.

List of Figures

List of Tables

List of Abbreviations

Abbreviation	Meaning
AC	Alternating current
DC	Direct current
ETO	Emitter turn-off thyristor
FCPS	Fuel cells propulsion system
FEA	Finite element analysis
GaN	Gallium nitride
GTO	Gate turn-off thyristor
HCB	Hybrid circuit breaker
HVDC	High voltage direct current
IFEP	Integrated full electric propulsion
IGBT	Insulated-gate bipolar transistor
IGCT	Integrated gate-commutated thyristor
IPM	Interior permanent magnet
JFET	Junction-gate field-effect transistors
LCS	Load commutation switch
LN_2	Liquid nitrogen
MCA	Moving coil actuator
MCB	Mechanical circuit breaker
MMA	Moving magnet actuator
MOSFET	Metal–oxide–semiconductor field-effect transistor

MOV	Metal oxide varistor
MVDC	Medium voltage direct current
NPS	Negative phase sequence
PDE	Partial differential equation
PMA	Permanent magnet actuator
PPS	Positive phase sequence
SCR	Silicon-controlled rectifier
SF_6	Sulfur hexafluoride
SiC	Silicon carbide
SSCB	Solid-state circuit breaker
TCA	Thomson coil actuator
TEPS	Turbo electric propulsion system
VSC	Voltage-source converters
ZnO	Zinc oxide
ZPS	Zero phase sequence

List of Symbols

Symbol	Definition	S.I. Unit
α	Coil short-pitched angle	°
B	Magnetic flux	Wb
B_g	Airgap flux density	T
E	Electrical field	V/m
E_k	Kinetic energy	J
E_c	Energy in the capacitor	J
F_{mag}	Electromagnetic force	N
I	Current through the coil	A
J	Charge density in coils	$C \cdot m^3$
l	Coil length	m
L_{DC}	Equivalent circuit inductance	H
L_w	Compensation coil inductance	H
m	Number of coils per phase band	
N_s	Number of conductors in slot in the general s^{th} slot	
N_p	Conductor distribution for the p^{th} harmonic	
N_{pR}	Conductor distribution for the p^{th} harmonic for phase 'R'	
N_{pRT}	Conductor distribution for the p^{th} harmonic for phase 'R' at top layer	
p	Harmonic number	
ρ	Charge density	$C \cdot m^3$
R_c	Coil resistance	Ω

R_w	Compensation coil resistance	H
r	Coil radius	m
U	Voltage across the capacitor	V
v	Velocity	m/s
θ_s	Slot angle	°
2δ	Slot opening	m

Chapter 1.

Introduction

Chapter contents:

This chapter overviews the background, motivation, objectives, challenges and contributions. It also presents the structure of this thesis.

1.1. Background and motivation

1.1.1. Integrated full electric propulsion (IFEP) ship system

A ship system contains both a propulsion system and ship services such as the domestic/hotel loads (navigation, lighting, air-conditioning, etc.). Conventional large ships or naval warships use diesel propulsion engines to directly drive propellers via shafts. The ship services are supplied by a set of diesel generators, as shown in Fig. 1-1(a) [1]. This direct-drive diesel system can occupy a large onboard space with low power efficiency [2]. Alternatively, an electric propulsion system, as shown in Fig. 1-1(b), is proposed to use electric motors to drive the propellers [3]-[5]. Thus, separate generators are used to provide power for the whole system. An integrated full electric propulsion (IFEP) system integrates both the propulsion and ship services requirements into an all-electric network, making the propulsion motors become loads of the generator sets. Since all the generators are providing power for the electric network, the total number of engines can be reduced to save onboard space and system weight, as well as vibration and noise [4]. An IFEP system removes the direct mechanical coupling between a propeller and a prime mover, achieving more flexible control and ship arrangement. For example, a generator set can be placed away from the propeller/drive motor units to balance the weight distribution, which results in a flexible solution for commercial applications and therefore reduces the maintenance and capital costs. Compared with diesel ship systems, the publications to date suggest an IFEP system has great potential to reduce fuel consumption, enhance dynamic performance and increase system reliability [6].

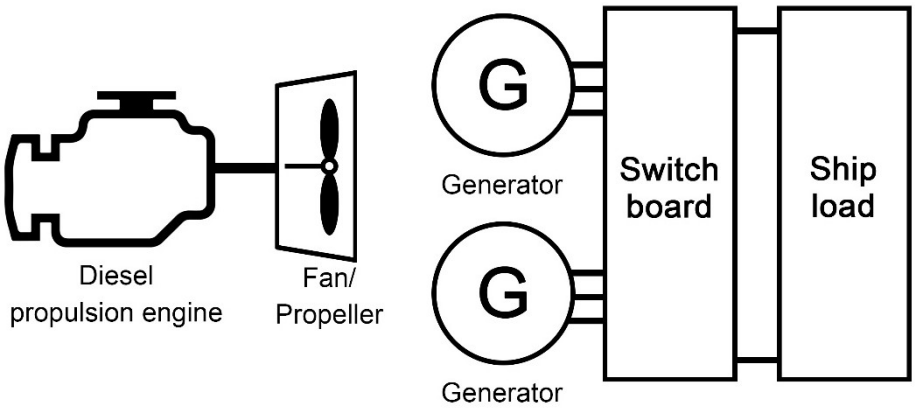

(a) Conventional direct-drive diesel ship system

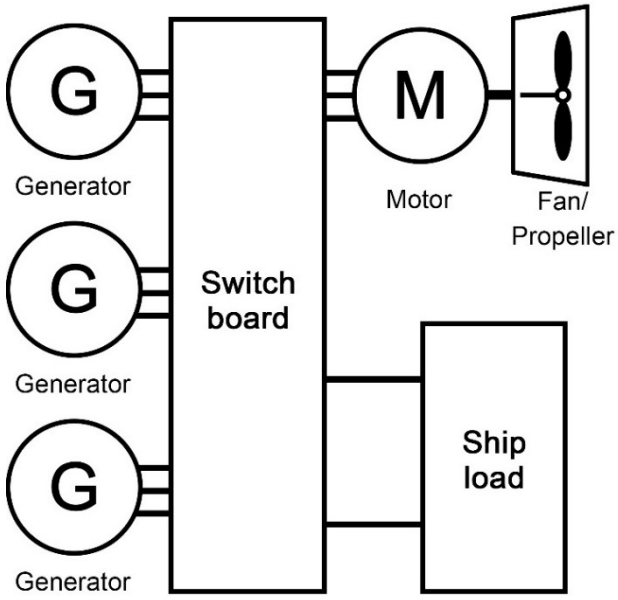

(b) Electric propulsion ship system

Fig. 1-1 Conventional ship system vs electric propulsion ship system

Most of the electric propulsion ship systems use alternating current (AC) power networks [7]. However, direct current (DC) onboard networks have become more attractive in recent years with the development of semiconductor devices, converters and DC circuit breakers. The advantages of DC distribution networks are investigated in terms of economic and environmental considerations in [7], which can increase system efficiency,

reduce carbon dioxide emissions and also improve fuel consumption.

In this Thesis a dual wound generator is proposed to supply different subsystems from a single compact machine, which can also provide a redundant system, to reduce the number of generators required to save onboard space and weight [8]. A dual wound generator can generate two outputs from connection to only one prime mover. The output voltage, power and frequency can be adjusted by the design of the winding distributions. Thus, one dual wound generator can supply both the propulsion system and the onboard ship service loads simultaneously [9], which achieves a more compact power system due to the reduction of the number of diesel engines, generators and transformers required.

1.1.2. Medium voltage direct current (MVDC) systems

DC transmission has been proven to have great advantages over long-distances and high-power electric distribution networks compared to traditional three-phase AC systems as there are almost no inductive and capacitive losses. DC systems may benefit from higher efficiency, better flexibility and lower costs in specific applications such as offshore wind farm collector systems and aviation on-board electric networks [10]-[13]. MVDC systems are being widely studied and have become more suitable for transmission and distribution for renewable energy systems, which has come about because of the development of high-voltage voltage-source converters (VSC) [14]-[16]. MVDC distribution grids are expected to have a great contribution to future electric energy systems, including the collection grid of renewable energy power plants, electrified railway systems, large ship distribution networks and aviation on-board cryogenic electric systems.

In 2014, Network Equilibrium successfully developed a back-to-back 33 kV / 20 MVA MVDC-Link to connect two separate networks in the South West of England [17]. In 2015,

Scottish Enterprise conducted a detailed study on MVDC technology about Market Opportunities and Economic Impacts [18]. In 2016, SP Energy Networks started the "Angle DC" project, which aimed to build a MVDC link to increase the volumes of renewable generation [19]. In 2017, Siemens started the "MVDC plus" project to investigate MVDC utility technology at the product level [20]. The US Navy proposed a MVDC distribution architecture for the next-generation all-electric ship [21]. This project also investigated the MVDC technology for a surface combatant design, which indicated that MVDC power distribution systems are important to future naval warships equipped with electric weapons and high-power sensors.

Decarbonisation has been one of the most urgent global challenges to help mitigate the effects of Climate Change [22]-[28]. Most countries are planning to achieve full decarbonisation and net zero targets by 2050 [29]. Decarbonisation is significant in many areas including transportation, industrial applications, residential applications and commercial activities. As reported in [30], transportation is the main contributor of greenhouse gas emissions, which contributes more than the total emissions from electricity generation, industry, commercial, residential, and the agricultural sectors. The aviation industry is especially concerned to eliminate CO_2 emissions [30]-[33]. The development of electric aircraft is significant to meet the requirements of sustainability and decarbonisation targets. A battery-based electric aircraft has zero emissions during flight. However, this topology is presently not scalable to large planes with long flight ranges due to the low energy density, short lifetimes and long charging times of the present battery technology [32]. Hydrogen, as an ultra lightweight natural energy vector, provides a highly efficient, feasible, safe and clean alternative solution for commercial vehicles [32]. Therefore, a hydrogen propulsion system shows a potential competitive solution to medium and long ranged airplane flights. The all-electric hydrogen-powered aircraft is being developed and has a great potential to contribute to decarbonisation and net-zero targets [31].

AIRBUS UpNext launched an advanced superconducting and cryogenic experimental powertrain demonstrator (ASCEND) project in 2021, to develop a superconducting full-electric aircraft propulsion system [34]. This project is investigating the application of liquid hydrogen as source for the internal combustion engines or fuel cell in the net-zero project (ZEROe). Cryogenic and superconducting technologies are also considered to support ultra-efficient electric propulsion systems for future aircraft. The Center for High-Efficiency Electrical Technologies for Aircraft (CHEETA) is also developing an electric-hydrogen powered aircraft, which uses cryogenic liquid hydrogen as an energy storage method [35].

An electric propulsion system on aircraft transmits and distributes energy from power sources (e.g. fuel cells or generators) to motors driving propellers. A DC distribution network is proposed in the transmission system including the converters, inverters, circuit breakers and other power electronics devices, which have higher energy efficiency, better power quality, lower environmental impact and save onboard space. The fuel cells propulsion system (FCPS), as one of the main hydrogen electric solutions, is shown in Fig. 1-2 [30]. The FCPS achieves 100% electric propulsion, which consists of electric motors driving propellers.

A number of fuel cells are linked together in a system to provide electric power to the DC distribution network. The inverters on the motor side are used to control the operation of the propulsion motors. Some batteries are used to ensure fast load following.

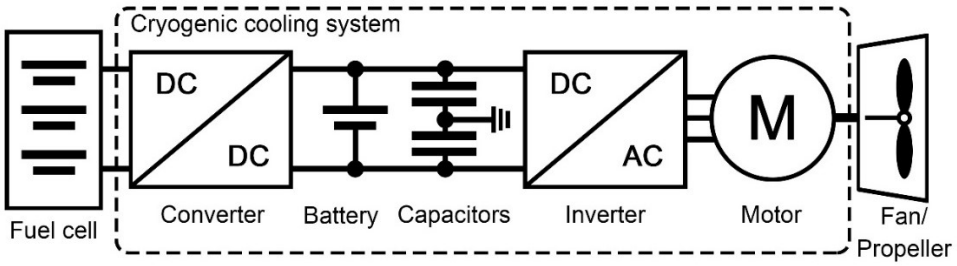

Fig. 1-2 Fuel cell propulsion system topology [36]

The hydrogen turbo electric propulsion system (HTEPS) is another electric propulsion system that directly burns hydrogen. It allows turbo electric distributed propulsion but also has slightly lower energy conversion efficiency. Fig. 1-3 shows an example of a TEPS with series-connected propulsors [36], which is proposed to achieve high voltage transmission and thus, save overall weight. Another HTEPS with parallel connected propulsors, alternatively, provides high current transmission.

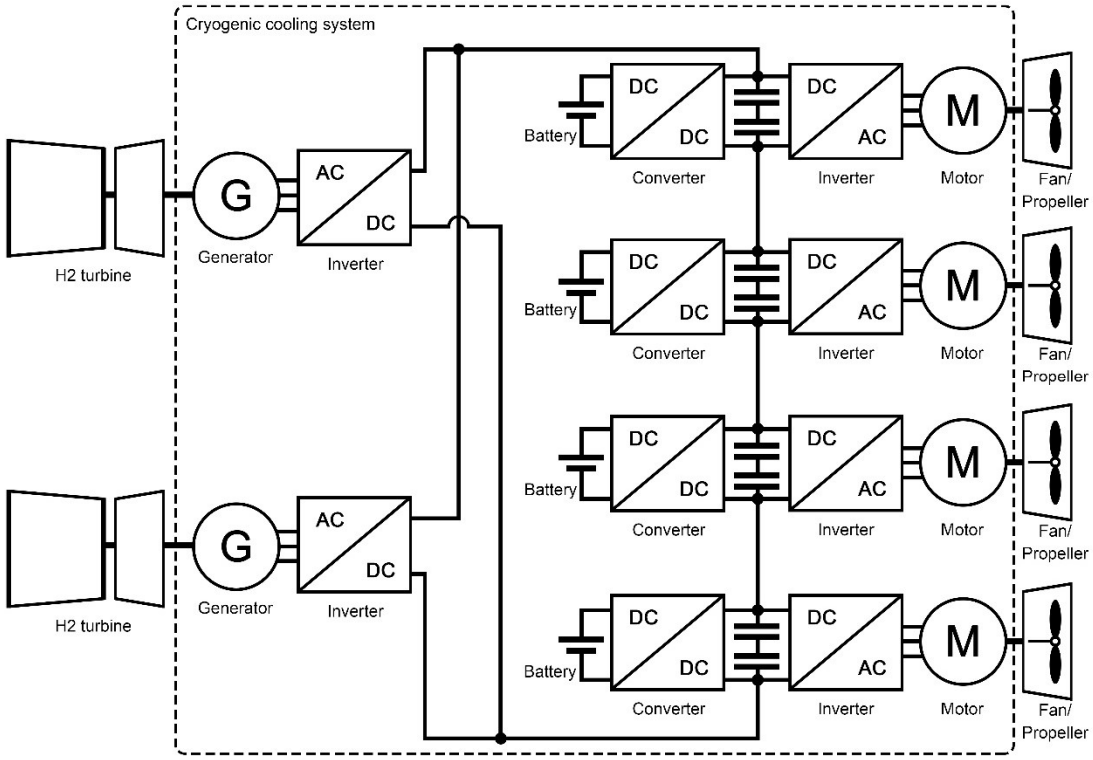

Fig. 1-3 Hydrogen turbo electric propulsion system topology [36]

Both the FCPS and HTEPS are proposed with DC networks. The onboard electric system could suffer from a high and fast-rising DC fault current due to the large energy storage in the capacitors and batteries. Thus, fault protection becomes especially important to clear a fault and protect the system's devices. The design and development of onboard DC circuit breakers and fault current limiters, therefore, shows great significance. A strong and reliable circuit breaker is urgently needed to interrupt the large DC fault currents with a considerable fast operating speed. This Thesis proposes a novel

moving coil actuator topology that provides improvements to the operating speed for hybrid DC circuit breakers.

1.2. Aims and objectives

As essential parts of an electric propulsion system, this research project aims to develop a fully-decoupled dual wound generator, as the system power supply, and a moving coil actuator for a vacuum interrupter, contributing to the fault protection circuit of the generator electrical system. Prototypes are proposed to be built and experimentally tested to investigate their behaviours and validate numerical modelling.

The objectives of this research project are:

- Design and build a dual wound generator that can generate two independent power supplies of different frequencies for an IFEP ship system. The two groups of windings will share the same stator slots in one machine frame. The main design challenge is to ensure full magnetic decoupling between the two outputs. When the proposed dual wound generator is integrated into an electric ship system, the power supply for the propulsion system should be independent of the power supply for the ship services system.
- Build and experimentally test the prototype dual wound generator. The full independence of the two outputs will be investigated considering more complex practical operating conditions. The generator behaviour under different loads conditions will be investigated such as the resistive load, inductive load and rectified DC load. Both static tests with unchanged loads and dynamic tests with changing loads performance will be tested to ensure that a change in one of the outputs does not have an impact on the other output.
- Design a fast operating MCA for a vacuum interrupter circuit breaker. A novel actuator topology with compensation coils is considered to improve the actuating

performance. The compensation coils can generate opposite-direction magnetic field against the magnetic field generated by the moving coils, thus reduce the core saturation and compensate the equivalent system inductance. The improvement of the proposed actuator topology design should be considered in terms of operating speed, efficiency and reliability. The design should be based on the onboard DC system fault protection requirements.

- Build and experimentally test a prototype of the designed MCA with compensation coils for a vacuum interrupter. Evidence that the compensation coils provide additional benefits compared with the original MCA will be investigated. Different connections for the moving coils and compensation coils will be considered and individually tested. Both the electrical and mechanical performance will also be investigated.

1.3. Thesis layout

This Thesis is composed of seven chapters, which is organised as follows:

Chapter 1 introduces the background of this research project. The development of IFEP ship systems and full-electric aircraft systems are presented to indicate the benefits of proposing a dual wound generator and fast-operation circuit breaker. The aims and objectives are also presented.

Chapter 2 reviews the existing literature on dual wound electric machines, along with DC circuit breakers and actuators for MCBs. The advantages and challenges of designing a dual wound generator for an IFEP system are described. The operating principles of three main kinds of DC circuit breaker topologies are also introduced. A comparison of the performance of each circuit breaker topology is investigated. Finally, different actuator topologies for MCBs are presented and compared.

Chapter 3 presents the magnetic decoupling winding design for a 2-pole and 6-pole dual wound generator for IFEP ship systems. Harmonics analysis is calculated using an algebraic method. A 2D finite element model is built in COMSOL to analyse the magnetic field distributions and the machine's dynamic performance. A prototype dual wound generator is built to further investigate the full decoupling between the two outputs.

Chapter 4 presents the experimental testing of the prototype dual wound generator that was proposed in Chapter 3, to investigate the full decoupling between the two outputs. Furthermore, the dynamical operation of the prototype generator under more complex load conditions is also investigated including with resistive loads, inductive loads and rectifier DC loads.

Chapter 5 introduces a novel design of a moving coil actuator topology with compensation coils for a vacuum interrupter. The compensation coils eliminate the saturation in the magnetic core and increase the rate of rise of the excitation current, thus increasing the operating speed. A 2D finite element model is built to investigate the optimal design of the system, and a prototype design is proposed.

Chapter 6 explains the build and experimental testing of the prototype moving coil actuator with compensation coils that was proposed in Chapter 5. This actuator is experimentally tested with a vacuum interrupter. Mechanical latching, springs and other supporting structures are included to eliminate the effects of bouncing, rebounding and welding. The experimental test results demonstrate the dynamical performance of the actuator with four possible connections. The comparison of each connections of the designed moving coil actuator is presented.

Chapter 7 summarises the conclusions of this research project, including the main findings and contributions of this Thesis. The potential of future continued works is also presented.

1.4. References

[1] Anish, “Electrical propulsion system in ships,” Marine electrical, May. 2019.

[2] R. T. Meyer, R. A. DeCarlo, S. Pekarek, and C. J. Doktorcik, “Gas turbine engine behavioral modeling,” Journal of Engineering for Gas Turbines and Power, Dec. 2015.

[3] S. Castellan, R. Menis, M. Pigani, G. Sulligoi and A. Tessarolo, “Modeling and Simulation of Electric Propulsion Systems for All-Electric Cruise Liners,” 2007 IEEE Electric Ship Technologies Symposium, 2007, pp. 60-64.

[4] J. F. Hansen and F. Wendt, “History and state of the art in commercial electric ship propulsion, integrated power systems, and future trends,” in Proceedings of the IEEE, vol. 103, no. 12, pp. 2229-2242, Dec. 2015.

[5] T. J. McCoy and J. V. Amy, “The state-of-the-art of integrated electric power and propulsion systems and technologies on ships,” 2009 IEEE Electric Ship Technologies Symposium, 2009, pp. 340-344.

[6] I. M. Elders, P. J. Norman, J. D. Schuddebeurs, C. D. Booth, G. M. Burt, J. R. McDonald, J. Apsley, M. Barnes, A. Smith, S. Williamson, S. Loddick and I. Myers, “Modelling and analysis of electro-mechanical interactions between prime-mover and load in a marine IFEP system,” 2007 IEEE Electric Ship Technologies Symposium, Arlington, VA, 2007, pp. 77-84.

[7] S. Kim and H. Jeon, “Comparative analysis on AC and DC distribution systems for electric propulsion ship,” Journal of Marine Science and Engineering, vol. 10, no. 5, p. 559, Apr. 2022.

[8] L. Rashkin, R. Matthews, J. Neely and N. Doerry, “Dynamic response comparison of dual-wound and single-wound machines in multi-bus power system architectures,” 2020 IEEE Transportation Electrification Conference & Expo (ITEC), 2020, pp. 784-788.

[9] Y. Li, Z. Zhu, X. Wu, A. S. Thomas and Z. Wu, “Comparative study of modular

dual 3-phase permanent magnet machines with overlapping/non-overlapping windings," IEEE Transactions on Industry Applications, vol. 55, no. 4, pp. 3566-3576, Jul. 2019.

[10] S. C. Raval, R. Botta and H. N. Raval, "Comparison of energy production cost for MVAC and MVDC offshore wind farm distribution system," 2017 Asian Conference on Energy, Power and Transportation Electrification (ACEPT), 2017, pp. 1-6.

[11] G. Abeynayake, G. Li, J. Liang and N. A. Cutululis, "A Review on MVdc Collection Systems for High-Power Offshore Wind Farms," 2019 14th Conference on Industrial and Information Systems (ICIIS), 2019, pp. 407-412.

[12] M. Ghassemi, A. Barzkar and M. Saghafi, "All-Electric NASA N3-X Aircraft Electric Power Systems," in IEEE Transactions on Transportation Electrification.

[13] A. Barzkar and M. Ghassemi, "Components of Electrical Power Systems in More and All-Electric Aircraft: A Review," in IEEE Transactions on Transportation Electrification.

[14] F. Mura and R. W. De Doncker, "Design aspects of a medium-voltage direct current (MVDC) grid for a university campus," in 8th International Conference on Power Electronics-ECCE Asia, pp. 2359-2366, 2011.

[15] W. Li et al., "State of the art of researches and applications of MVDC distribution systems in power grid," in IECON 2019-45th Annual Conference of the IEEE Industrial Electronics Society, vol. 1, pp. 5680-5685, 2019.

[16] L. Qu et al., "Planning and analysis of the demonstration project of the MVDC distribution network in Zhuhai," Frontiers in Energy, vol. 13, no. 1, pp. 120-130, 2019.

[17] Western Power Distribution - Network equilibrium, "Balancing generation and demand," 2014. Available: https://www.westernpower.co.uk/downloads-view-reciteme/2677 Access: 23/08/2022.

[18] Scottish Eenterprise, tnei enterprise with energy, "MVDC Technology Study –

Market Opportunities and Economic Impact," Available: https://www.evaluationsonline.org.uk/evaluations/Browse.do?ui=browse&action=show&id=562&taxonomy=BUI, Access: 23/08/2022.

[19] SP ENERGY NETWORKS, "Angle-DC: operation AC to DC," Available: https://www.spenergynetworks.co.uk/userfiles/file/Angle-DC_Fact_Card_Visual_Version.pdf Access: 23/08/2022.

[20] Siemens Energy, "MVDC PLUS – the grid connector," Available: https://www.siemens-energy.com/global/en/offerings/power-transmission/portfolio/medium-voltage-direct-current.html, Access: 23/08/2022.

[21] N. H. Doerry, "Next generation integrated power systems for the future fleet," Corbin A McNeill SymposiumAt: USNA, Annapolis MD, Mar. 2019.

[22] J. E. M. Mora, "Decarbonization of the power generation system in Central America," 2019 IEEE 39th Central America and Panama Convention (CONCAPAN XXXIX), 2019, pp. 1-4, doi: 10.1109/CONCAPANXXXIX47272.2019.8976940.

[23] J. D. d. Magalhães and J. Villar, "Ramp analysis of the Portuguese net load under different decarbonization scenario," 2019 IEEE Milan PowerTech, 2019, pp. 1-6, doi: 10.1109/PTC.2019.8810718.

[24] J. Teremranova and A. Sauhats, "Electrification and decarbonization potential assessment of Latvian Dwellings," 2020 IEEE 61th International Scientific Conference on Power and Electrical Engineering of Riga Technical University (RTUCON), 2020, pp. 1-7.

[25] B. L. Smith, M. Woodhouse, D. Feldman and R. Margolis, "Towards decarbonization: stablishing a sustainable, equitable, diverse workforce in the U.S. photovoltaic industry," 2021 IEEE 48th Photovoltaic Specialists Conference (PVSC), 2021, pp. 2632-2636.

[26] C. McGarry, S. Galloway and G. Burt, "Decarbonisation of rural networks within mainland Scotland: in support of intentional islanding," The 9th Renewable Power

Generation Conference (RPG Dublin Online 2021), 2021, pp. 283-288.

[27] M. O. Ibne Bashir, “Application internet of things (IoT) to calibrate with IMO 2050 decarbonization charters and phase out greenhouse gases from the shipping industry of Bangladesh,” OCEANS 2022 - Chennai, 2022, pp. 1-5.

[28] F. Lanati and M. Gaeta, “How to achieve a complete decarbonization of the Italian energy system by 2050?,” 2020 17th International Conference on the European Energy Market (EEM), 2020, pp. 1-5.

[29] S. Simoes, W. Nijs, P. Ruiz, A. Sgobbi and C. Thiel, “Decarbonised pathways for a low carbon EU28 power sector until 2050,” 11th International Conference on the European Energy Market (EEM14), 2014, pp. 1-5.

[30] P. J. Ansell, “Hydrogen-electric aircraft technologies and integration: enabling an environmentally sustainable aviation future,” in IEEE Electrification Magazine, vol. 10, no. 2, pp. 6-16, June 2022.

[31] J. Huete, D. Nalianda, B. Zaghari and P. Pilidis, “A strategy to decarbonize civil aviation: a phased innovation approach to hydrogen technologies,” in IEEE Electrification Magazine, vol. 10, no. 2, pp. 27-33, June 2022.

[32] Y. Gao, C. Jausseme, Z. Huang and T. Yang, “Hydrogen-powered aircraft: hydrogen–electric hybrid propulsion for aviation,” in IEEE Electrification Magazine, vol. 10, no. 2, pp. 17-26, June 2022.

[33] V. Sethi et al., “Enabling cryogenic hydrogen-based CO2-free air transport: meeting the demands of zero carbon aviation,” in IEEE Electrification Magazine, vol. 10, no. 2, pp. 69-81, June 2022.

[34] “Cryogenics and superconductivity for aircraft, explained | Airbus,” www.airbus.com, Sep. 01, 2021. https://www.airbus.com/en/newsroom/stories/2021-03-cryogenics-and-superconductivity-for-aircraft-explained

[35] Steven Schneider, “Some NASA perspectives on H2,” NASA Glenn Research Center, Nov. 2020.

[36] J. K. Nøland, “Hydrogen electric airplanes: A disruptive technological path to clean up the aviation sector,” in IEEE Electrification Magazine, vol. 9, no. 1, pp. 92-102, March 2021.

Chapter 2.

Literature review

Chapter contents:

This chapter reviews the literature of dual wound machines, DC circuit breakers, and different types of actuators.

2.1. Dual wound machines

A dual wound machine is an electric machine with two groups of windings that share the same stator slots in one frame. Generally, a dual wound machine can either operate as an electric motor or as a generator. Dual three-phase motors are proven to have the potential to improve the torque density and torque quality, with even higher efficiency. Furthermore, dual wound generators are proposed to generate two power supplies simultaneously with only one attached prime mover, which achieves a compact design.

2.1.1. Multiphase dual wound machines

With dual three-phase windings, a dual wound machine can also be considered as the implementation of a range of multiphase machines. Multiphase machines are commonly implemented on-board electric ships and rail vehicle applications, which benefit from their fault-tolerance capability and torque quality [1]. Compared with a conventional three-phase machine, a multiphase machine can have the advantages of:

- As the three-phase voltages are reformed into multi phases, the voltage on each phase can be effectively reduced. Thus, high-power variable-speed drives of multiphase machines can be achieved using lower powered devices and cable connections. This is suitable for on-board propulsion systems with a limited supply voltage [1].

- Multiphase machines can have great fault-tolerance capability. When one of the stator phases is open-circuited, for example, the other phases can still operate but at a derated working point [1].

- The number of independent phases of a machine is directly related to the number of control degrees in a drive system. A multiphase machine could have more

degrees of freedom compared with conventional three-phase machines, which provides more potential to the drive system design, thus enhancing the drive performance [1].

- The torque ripple can be reduced in a multiphase machine. As the torque ripple is caused by the spatial harmonics of magneto-motive force (mmf), which is excited by the fundamental current in the stator phases, the increasing of the phase number can increase the harmonic orders. Therefore, the torque ripple can be reduced and the efficiency can be improved [1]-[2].

2.1.2.Winding design of dual wound machines

Research of dual wound machines has been popular due to their higher torque densities, enhanced efficiency and fault-tolerant capabilities. Two groups of windings provide more possibilities to the machine winding arrangements and distributions, which can affect the machine performance, including the phase resistance, harmonics and torque quality.

A six-phase dual wound permanent magnet synchronous machine was proposed in [2], where two identical dual three-phase asymmetrical winding sets were separately distributed in the two halves of the stator frame at 180 mechanical degrees. This winding distribution may achieve a lower phase resistance and thus, copper losses. The torque quality were improved as well. A dual three-phase machine with an interior permanent-magnet (IPM) rotor was investigated in [3], where the stator windings were arranged with distributed windings. The machine's performance was compared with a commercial automotive traction machine, the Nissan Leaf IPM machine. The dual three-phase machine was shown to have improved torque density and torque quality without compromising efficiency. Another permanent-magnet dual wound machine was designed and discussed in [4], where the windings of the stator were of the concentrated windings arrangement to achieve electrical and magnetic isolation. The designed dual wound

machine could either work in motor or generator operation mode. This paper also discussed the performance between distributed windings and concentrated winding topologies. Both the simulation and experimental results showed that the location of the coils in the stator periphery had a great effect on minimum coupling. A dual wound generator designed for the Navy's next generation all-electric warships was designed and built in [5], which was able to provide power supplies for both the port and starboard power distribution busses. This approach offered redundancy and reduced the effects of prime mover light loading. However, the coupling between the two outputs of the dual wound generator was not fully independent. A fault or load changes on one output could impact the other output due to the dual wound coupling effect.

A 20 MW dual wound gas turbine generator system was proposed through finite element modelling, and a reduced scale 10 kW prototype of the dual wound machine was manufactured and validated through hardware experiments demonstrating the electromagnetic coupling between the two phase sets [6]. The electrical test schematic of the dual wound generator is shown in Fig. 2-1. The results indicated that a disturbance of the load on one output of the generator could have a significant effect on the other output, which showed the possibility of load faults on one bus creating disturbances on the other. Thus, coupling between the two outputs must be eliminated for this type of power system architecture. Furthermore, a solution of using active control of the field excitation to maintain constant airgap flux in the machine, thus reducing the coupling effect was also proposed. However, this method can only mitigate not eliminate the coupling effects between the two windings.

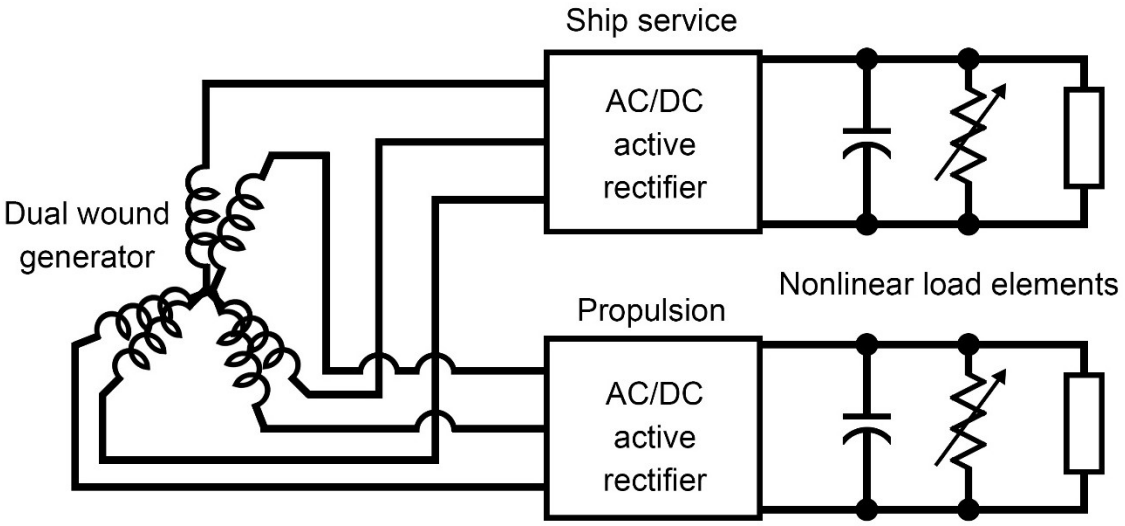

Fig. 2-1 Electrical schematic of dual wound generator test platform

The research in [7] investigated the offset between two sets of windings, which could reinforce the fundamental mmf waveform and suppress the oppositional harmonic mmf waveform, effectively eliminating the harmonics coupling between the two windings sets. The calculation was based on a modular planar windings model. Further harmonics analysis of machine excitations and phase windings was proposed in [8]-[9], which provided a theoretical method to cancel the coupling between the two outputs of a dual wound generator.

This Thesis aims to propose a dual wound generator design with fully magnetically decoupled windings sets for electric ship systems. The two outputs of the dual wound generator should be fully independent to ensure that the change of the operating condition of one output will not impact the other output, and therefore, the propulsion system and ship services can work independently even though they are powered from one prime mover.

2.2. DC circuit breakers

With the development of DC distribution and transmission systems, DC fault protection technology is facing a great challenge to propose reliable DC fault current limiters and DC circuit breakers for a range of present and future industrial applications. The design of DC circuit breakers is generally more difficult than AC circuit breakers due to the fact that DC current does not have any natural zero-crossing point and also a high rate of rise in a fault current condition. The series inductance and shunt capacitance of DC cables can release a large amount of energy during fault conditions. A circuit breaker, therefore, must clear a fault with a very fast operating speed, which is defined as less than 3 ms in this research, and dissipate the energy left in the inductance and capacitance of the system. Furthermore, a DC circuit breaker should also operate with a low conductive loss during normal no-fault conditions. The key requirements of the design of a DC circuit breaker are as follows:

- Fast fault current interruption speed
- Low losses during normal no-fault operating conditions
- Dissipate the energy stored in the system inductance
- Reclose after the clearance of a fault
- Withstand and limit the high overvoltage
- Overcurrent capability
- High efficiency
- High reliability and long lifetime

There are three main topologies of DC circuit breakers listed below, which will be explained in more detail in the following section.

- Mechanical DC circuit breaker
- Solid-state DC circuit breaker
- Hybrid DC circuit breaker

2.2.1.Mechanical circuit breakers

A mechanical circuit breaker (MCB) is the most conventional DC circuit breaker. Its structure is basically a mechanical switch. During normal operation, the two contacts of the switch are closed to support the DC current flow, with low operating losses. The on-state resistance of a mechanical DC circuit breaker can be as low as 10 μΩ. Once a fault occurs, the two contacts will separate and an electric arc will form between the two contacts, which needs to be extinguished rapidly. The arc can be extinguished either by mechanically lengthening and cooling or by electrically creating an artificial zero-crossing. Once the arc is extinguished, the electric isolation between the two contacts will be recovered to ensure no re-striking occurs. The dielectric strength should also be strong enough to withstand system overvoltages. The arc quenching method and the isolation gas method can distinguish these type of MCBs. Air, vacuum and sulfur hexafluoride (SF_6) are commonly used as the medium in MCBs for electric isolation due to their great dielectric strength.

2.2.1.1 Air circuit breakers

An air circuit breaker is a mature and cost-efficient DC fault interruption technology. One of the air circuit breaker topologies is the air chute circuit breaker, which has an air chute for the arc quenching process. Once an electric arc is formed between the contacts, it will be driven into the air chute due to both thermal and electromagnetic effects. The arc in the chute will become cooled, lengthened and split. Lengthening and cooling the arc efficiently increases the arc voltage. Once the arc voltage becomes larger than the system voltage, it will be quenched. Air chute circuit breakers have been widely investigated for decades for fault protection applications [10]-[11]. Recent research using arc chute topology with liquid nitrogen as an arc extinguishing medium is presented in [12].

Another air circuit breaker topology is the air blast circuit breaker, which uses compressed air to lengthen, cool and finally blow out an arc. They have a relatively fast arc quenching speed but require a sufficiently high capacity air compressor for frequent operations [13]. Air circuit breakers are conventional technologies that have been used in low-voltage fault protection applications for decades [14]. In the early 1940s, for example, a 5 kV “magnetic-blast” air circuit breaker was developed using the principles of magnetic action and thermal reaction [15]-[16].

2.2.1.2 Vacuum circuit breakers

Vacuum circuit breakers use vacuum as the arc extinction medium, which can provide high insulating strength and superior arc quenching properties. The two contacts are enclosed in a permanently sealed vacuum interrupter. Thus, arc quenching will occur in a vacuum chamber. Fig. 2-2 shows a typical vacuum interrupter. A moving contact and a fixed contact are located at the ends of a ceramic high vacuum arcing chamber. This is supported by ceramic insulators, one of which encloses bellows to support the movement of the contact. Once a fault occurs, the two contacts separate, and an arc is formed between the two contacts in the vacuum chamber. A fault current will be interrupted at the first current zero. The dielectric strength can recover rapidly after an arc is extinguished. Due to the excellent recovery of a vacuum circuit breaker, they are commonly used in the design of ultra-fast circuit breakers for industrial applications.

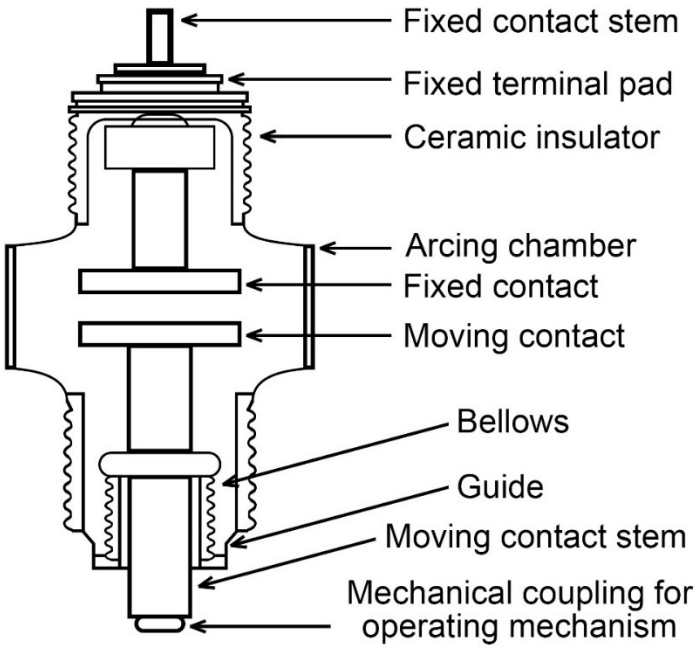

Fig. 2-2 Vacuum interrupter topology [17]

The advantages of a vacuum circuit breaker can be listed as follows:

- The vacuum has a high dielectric strength, which can support high voltage applications
- The vacuum has a rapid recovery of high dielectric strength after a fault current interruption
- Vacuum is relatively environmental friendly
- A vacuum interrupter is compact and self-contained, and can typically be installed in any required orientation
- A vacuum circuit breaker has the least requirements for maintenance and therefore, is high reliability. Furthermore, a vacuum circuit breaker does not need periodic refilling and is not flammable compared to filling of oil or gas of other types of circuit breakers.

The technology of the vacuum circuit breakers in medium voltage applications has been dominating primary switchgear from 5 kV to 40.5 kV. However, the weakness still be considered, for example, a vacuum circuit breaker normally requires extra force to

prevent welding due to its contacts working environment.

2.2.1.3 SF_6 circuit breakers

SF_6 circuit breakers use compressed SF_6 gas in an enclosed vessel as the quench medium. The same as vacuum, SF_6 can help to extinguish an electric arc, but with even stronger dielectric strength. Thus, SF_6 circuit breakers are commonly used in high voltage AC grid applications. However, SF_6 is a potent greenhouse gas with a high global warming potential [18]. Furthermore, SF_6 decomposes under electrical stress, forming toxic by-products that can be a health threat for personnel in the event of exposure [18]. Therefore, SF_6 circuit breakers are not environmentally friendly and are also not suitable for onboard systems such as electric ships and aircraft.

The air, vacuum, and SF_6 circuit breakers are designed for AC systems. Since there is no zero-crossing in DC systems, a passive resonance circuit or an active resonance circuit is therefore introduced to generate a zero-crossing point for DC circuit breaker applications.

2.2.1.4 Passive resonance DC circuit breaker

A passive resonance DC circuit breaker uses the self-oscillation of an inductor and capacitor to create a zero-crossing point for a mechanical interrupter. Fig. 2-3 shows a typical topology of a passive resonance circuit [19], which includes the main interruption branch, a commutation branch and an energy absorption branch. The main breaker can be an air, vacuum or SF_6 AC circuit breaker. The commutation branch consists of an inductor and a capacitor in a series connection, composed of a resonant circuit, to generate the zero-crossing point. The energy absorption branch is a varistor, to dissipate the energy left in the system inductance, which represents a nonlinear resistor where the resistance changes with the voltage. Metal oxide varistors (MOVs) such as Zinc Oxide (ZnO) varistors, are widely used in voltage clamping applications. There is a large

inductor connected with the branches to suppress the rate of rise of a fault circuit in most cases.

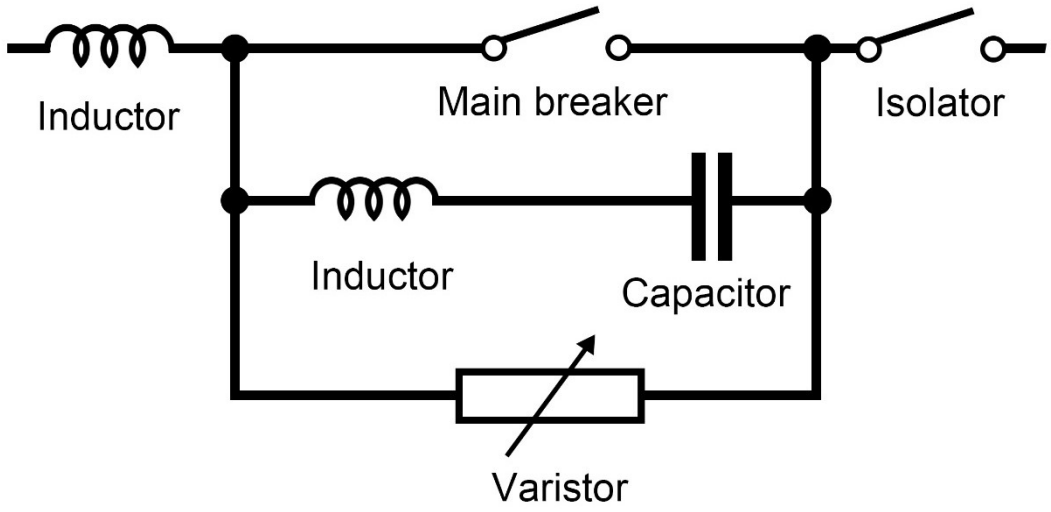

Fig. 2-3 Passive resonance DC circuit breaker topology

During normal operation, the current will flow through the main breaker with a negligible power loss due to its low conductive resistance. Therefore, the voltage drop across the breaker and the capacitor is almost zero. Once a fault occurs, the two contacts of the breaker separate with an electric arc produced. A fault current will be commuted from the breaker branch into the inductor and capacitor branch. The inductor and capacitor then generate exponentially increasing current oscillations. Once this oscillating current fully opposes the arc current in the breaker branch, the arc will be extinguished. The fault current then flows into the commutation branch and charges the capacitor until it reaches the system voltage. The dielectric strength of the breaker has to be able to withstand the system voltage. Once the amplitude of the capacitor voltage exceeds the varistor's knee point, where significant current flows through the lowered varistor resistance, the varistor begins to conduct and dissipate the energy left in the system inductance. Finally, the current in the main circuit reduces to zero and a fault is fully isolated.

The passive resonance circuit breaker has a relatively simple design with fewer requirements for the control system. However, the fault interrupting time is slow, up to tens of milliseconds, and the circuit breaker itself is large in size. A 500 kV passive electro-mechanical DC circuit breaker was proposed in [20], which can break a 5 kA fault current in 60-100 ms as an example.

2.2.1.5 Active resonance DC circuit breaker

An active resonance DC circuit breaker has a similar artificial zero-crossing generating principle to the passive resonance circuit, which uses a capacitor and inductor oscillation to generate opposite currents against the arc current. However, the capacitor is pre-charged and an injection switch is applied to excite the resonant circuit, as shown in Fig. 2-4 [19]. The injection switch generally employs a thyristor or semiconductor switch for a fast operation. In this case, the current oscillation with the pre-charged capacitor can increase rapidly to create a zero-crossing point for the electric arc in the mechanical breaker when a fault is detected. Once the arc is extinguished, the current will be commutated into the varistor and dissipate the energy left in the system inductance until the current decays to zero.

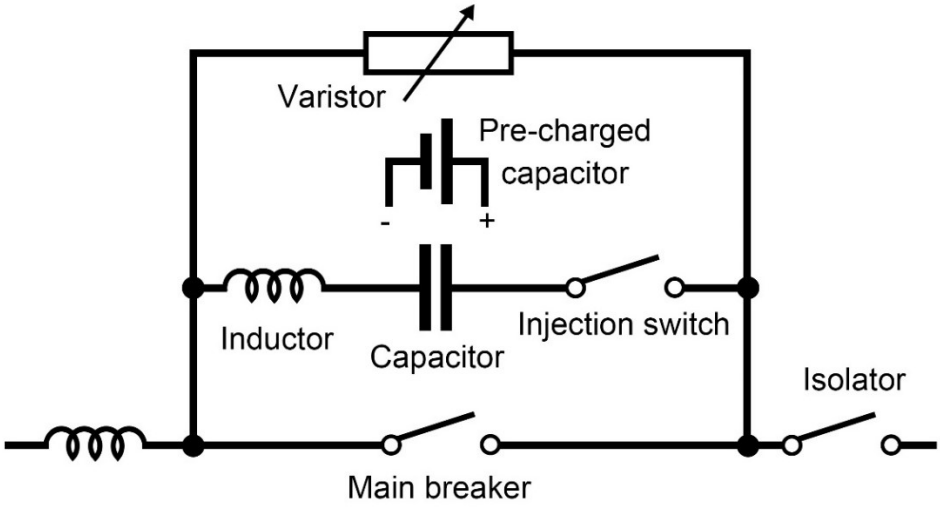

Fig. 2-4 Active resonance DC circuit breaker topology

An active resonance DC circuit breaker can generate current oscillations rapidly, which means it can operate much faster compared to passive resonance circuit breakers. An MCB with an active resonance circuit proposed in [21] successfully cleared a fault current of 10.5 kA in less than 5 ms. However, the design topology of the active resonance circuit breaker is more complex and requires high reliability for the injection switch. A thyristor with their reliable and fast operation, however, need a large amount to be connected together in series to withstand the DC voltage during the off state, which results in issues including higher costs and difficulty in trigger consistency. An external control circuit for the injection switch and the charge of the capacitor is also needed adding further costs and complexity.

2.2.1.6 DC mechanical circuit breaker commercial products

Fuji Electric developed a DC high-speed vacuum circuit breaker with an active resonance circuit, as shown in Fig. 2-5 [22]. The Fuji electric DC MCB VDC series has voltage ranges from 750 V – 1,500 V and current ranges from 2 – 4 kA. Due to the arc-less circuit interruption, a long lifetime of this type of circuit breaker can be expected. Thus, maintenance costs are dramatically reduced. Space-saving designs are also proposed to reduce construction costs and make renewals easy. This circuit breaker uses dry capacitors, which are incombustible and eco-friendly. The detailed introduction of Fuji electric DC MCB are summarised in Table 2-1.

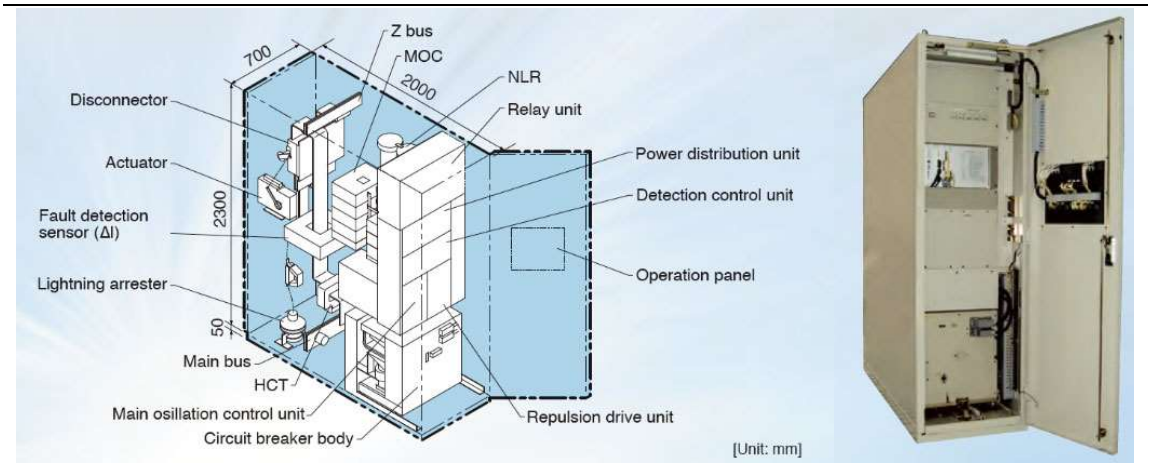

Fig. 2-5 Fuji electric vacuum DC circuit breaker [22]

Gerapid developed a single pole, high-speed, air circuit breaker for traction applications [23]. The rated current ranges from 2.6 kA to 8 kA, with voltage ranges up to 3.6 kV. Gerapid employed a 2-stage contact system (main and arcing contacts) for prolonged contact life and simple contact replacement. Tripping is via a spring energy trip mechanism with a mechanical latch. A powerful solenoid with an integrated control unit provides the closing energy. Fig. 2-6 shows the Gerapid circuit breaker topology. Table 2-2 summarises the detailed parameters of the Gerapid circuit breaker.

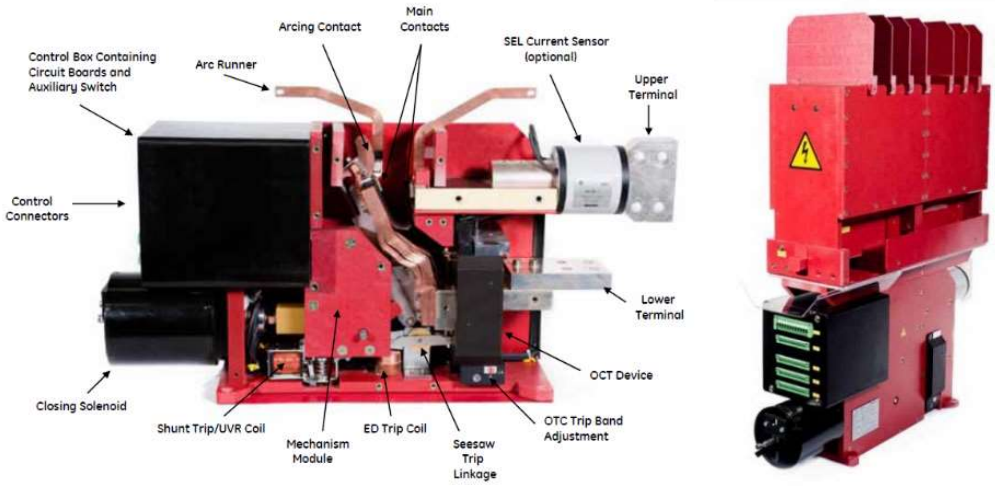

Fig. 2-6 Gerapid vacuum DC circuit breaker [23]

Xi'an Jiaotong University proposed a novel design of a liquid nitrogen MCB, which is a

kind of mechanical switch using liquid nitrogen (LN_2) as an arc extinguishing medium [12]. The LN_2 switch is characterised by extremely low contact resistance and can reduce the conduction loss significantly. The topology of a liquid nitrogen MCB is shown in Fig. 2-7, which has a similar chute structure to air chute circuit breakers. The experimental results showed that the LN_2 switch could interrupt a 1 kV / 2 kA fault current within 20 ms. Potential applications of LN_2 circuit breakers can be cryogenic electric aircraft or DC superconducting systems.

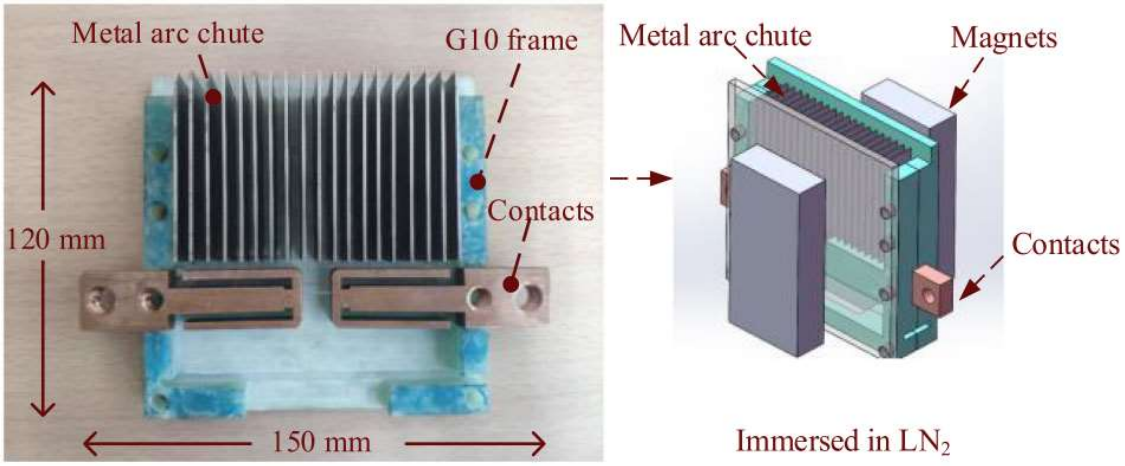

Fig. 2-7 Liquid nitrogen mechanical circuit breaker [12]

TABLE 2-1

FUJI ELECTRIC DC MCB SPECIFICATION [22]

Mechanical circuit breaker	VDC215-P	VDC208-P	VDC215-T	VDC208-T
Type (active/passive resonance)	Active	Active	Active	Active
Rated current	2000A/3000A/4000A	2000A/3000A/4000A	2000A/3000A/4000A	2000A/3000A/4000A
Breaking capacity	50 kA	50 kA	100 kA	100 kA
Maximum operating voltage	DC 1500 V	DC 750 V	DC 1500 V	DC 750 V
Chamber (Air/Vacuum)	Vacuum	Vacuum	Vacuum	Vacuum
Breaking speed	6 ms	6 ms	6 ms	6 ms
Making speed	2 s (electric-spring)	2 s (electric-spring)	2 s (electric-spring)	2 s (electric-spring)
Volume	2000 x 700 x 2300 mm	2000 x 700 x 2300 mm	2000 x 700 x 2300 mm	2000 x 700 x 2300 mm
Lifetime	10000 times (mechanical) 100 times (short-circuit current interruption)	10000 times (mechanical) 100 times (short-circuit current interruption)	10000 times (mechanical) 100 times (short-circuit current interruption)	10000 times (mechanical) 100 times (short-circuit current interruption)

TABLE 2-2

GERAPID DC MCB SPECIFICATION [23]

Mechanical circuit breaker	Gerapid 2607	Gerapid 4207	Gerapid 6007	Gerapid 8007
Type	Arc chute*	Arc chute*	Arc chute*	Arc chute*
Rated current	2600 A	4150 A	6000 A	6000 A
Breaking capacity	30 – 70 kA	30 - 70 kA	35 - 56 kA	50 kA
Maximum operating voltage	2000 – 4000 V	2000 – 4000 V	1000 – 4000 V	1000 – 2000 V
Chamber (Air/Vacuum)	Air	Air	Air	Air
Breaking speed	150 ms	150 ms	150 ms	150 ms
Operating temperature min	-5 °C	-5 °C	-5 °C	-5 °C
Operating temperature max	35/55 °C	35/55 °C	35/55 °C	35/55 °C
Mass (kg)	120 – 160	120 – 160	150 – 165	190 - 210
Volume	400 x 1200 x 1000 mm	400 x 1200 x 1000 mm	400 x 1200 x 1000 mm	400 x 1200 x 1000 mm
Lifetime	10000	10000	10000	10000

2.2.2.Solid-state DC circuit breakers

Solid-state circuit breakers (SSCBs) are semiconductor-based protection devices. Unlike mechanical DC circuit breakers, SSCBs use semiconductor components, thus achieving an ultra-fast fault clearance speed, which can interrupt DC current within less than 100 μs [24]-[26]. In addition, because no electric arc exists during the interruption process, SSCBs are expected to have better reliability and a long lifetime.

The semiconductor components used for SSCBs can be divided into different categories by their predominant materials, for example, silicon (Si), silicon carbide (SiC) and gallium nitride (GaN). The silicon-controlled rectifier (SCR), insulated-gate bipolar transistor (IGBT), integrated gate-commutated thyristor (IGCT), gate turn-off thyristor (GTO) and the emitter turn-off thyristor (ETO) are commonly used in solid-state DC circuit breaker applications. These semiconductor devices can interrupt voltages up to 6.5 - 8.5 kV with rated currents up to 3 - 6 kA [27].

Although SSCB can achieve a high operating speed, semiconductor devices typically have higher conduction losses. Due to their high on-state resistance, the temperature rising effect is significant in SSCBs. An additional cooling system is usually employed to ensure the normal operation of SSCBs, which makes the system bulky.

To reduce the on-state losses, some promising semiconductor devices have been proposed such as SiC junction-gate field-effect transistors (JFETs), which achieve lower conduction resistance and no control signal is needed to maintain their ‘on’ state. Research in [28] successfully used SiC JEFTs to interrupt a 200 A fault current with a system voltage up to 400 V. A SiC unipolar device with only 2.5 mΩ cm^2 conduction resistance that blocks the voltage of 1.2 kV was proposed in [29].

SiC metal–oxide–semiconductor field-effect transistors (MOSFETs) have also

considered for solid-state DC circuit breakers use due to their low on-state losses and high temperature working performance. SiC MOSFETs-based circuit breakers have been investigated in [30]-[31] under voltages of 270 V, 380 V and 850 V with fault currents up to 450 A.

GaN devices have better performance of low on-state resistance and fast operation speed. A prototype SSCB was demonstrated in [32] to clear a fault current of 45 A under 300 V voltage within 0.8 μs.

IGBT devices are popular in the applications of SSCBs. A prototype bi-directional SSCB using two IGBTs in parallel, which successfully interrupted a 100 A fault current was developed and discussed in [33]. A SSCB for VS-HVDC systems was developed in [34], which utilised ten IGBTs connected in series. This SSCB successfully interrupted a 5.1 kA fault current under 10 kV, which indicated the feasibility of SSCB with series-connected IGBTs. An IGBT-based SSCB for onboard MVDC systems was developed in [35], which interrupted a 400 A DC fault current in less than 300 μs [36] compared to IGCTs and IGBTs for circuit breakers in ship electrical systems. This result confirmed that IGBTs are more appropriate for downstream relative low-current rated SSCBs with fast operating speed, and IGCTs are more suitable for upstream relative medium-current SSCBs. MOSFETs, IGBTs, and MCTs performance for SSCBs was compared in [37], where determined that the limiting factor in power delivery for semiconductor devices is junction temperature.

The voltage and current levels of SSCBs are determined by the applied semiconductor devices. An individual device has limited voltage and current ratings, which means a large number of semiconductor devices need to be series and/or parallel connected to increase the voltage and/or current capability. The typical voltage and current levels of semiconductor device technologies is shown in Fig. 2-8 [27].

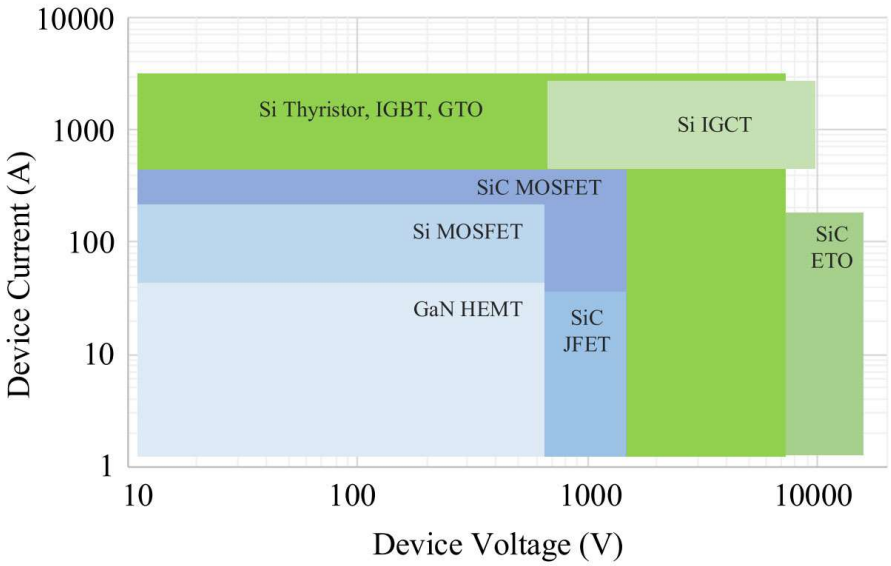

Fig. 2-8 Voltage and current levels of different semiconductor devices [27]

There are three main types of SSCBs: SSCBs with parallel varistors, SSCBs with a freewheeling diode and Z-source SSCBs.

SSCBs with parallel varistors are a basic topology, as shown in Fig. 2-9 [38]-[39]. The semiconductor device (T) is the key component to break the fault current. L_{dc} is the equivalent system inductance. During normal operation, T turns on and supports the current flow. Once a fault occurs, T turns off and blocks the fault current. The paralleled varistor limits the voltage across T and dissipates the energy left in the system inductance.

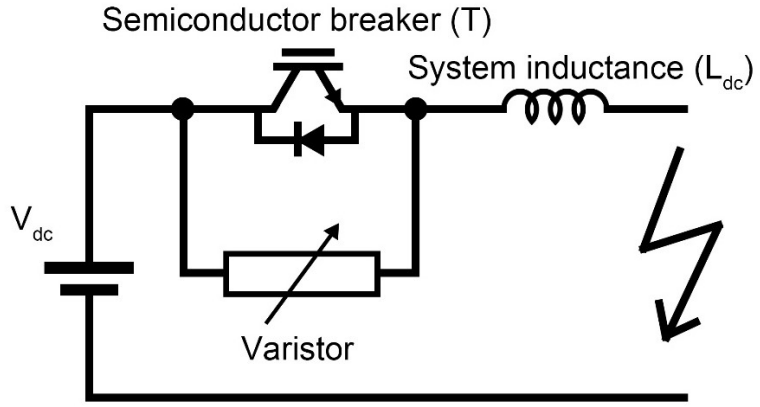

Fig. 2-9 Solid-state circuit breaker with parallel varistor

The circuit topology of an SSCB with a freewheeling diode is shown in Fig. 2-10 [38]. The freewheeling diode (D) is series connected with the varistor. During normal operation, T turns on and delivers system current. Once a fault is detected, T turns off. The fault current then flows through D and the varistor. Thus, there is no current through the DC source and the semiconductor device. The varistor then dissipates the energy left in the system inductance. Once the current drops to zero, the fault is isolated.

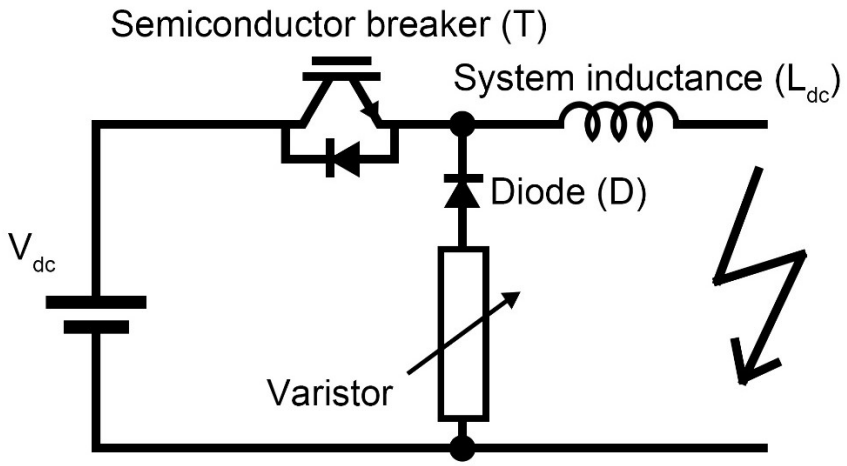

Fig. 2-10 SSCB with a freewheeling diode

Instead of semiconductor devices with turn-off capability in the above two SSCB topologies, a thyristor SCR is used in the Z-source SSCB to isolate a fault current, as shown in Fig. 2-11(a) [40]. This topology includes an SCR, two capacitors (C) and two inductors (L) that are paralleled with a diode-resistor branch. During normal operation, the SCR turns on. The current flows through the SCR, two inductors and the system load R_L. Since the voltage across the inductors is zero, the two capacitors can be regarded as parallel connected. Once a fault occurs, though the current in the main circuit is rapidly increased, the current through the inductors maintains the same. Thus, the current through the capacitors is shown in Fig. 2-11(b). The two capacitors, therefore, are regarded as series connected. Once the current through the capacitors rises and reaches the inductor current, the current through the SCR will be decreased to zero,

which automatically turns off. When the voltage across the inductors drops to negative, the diodes will be turned on. The current through the capacitors is commuted into the diode-resistor branch. The resistors then dissipate the energy left in the system inductance.

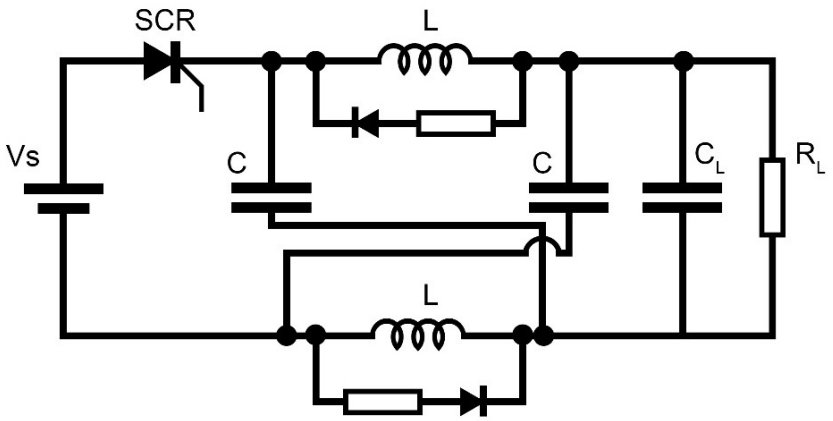

(a) Z-source SSCB circuit topology

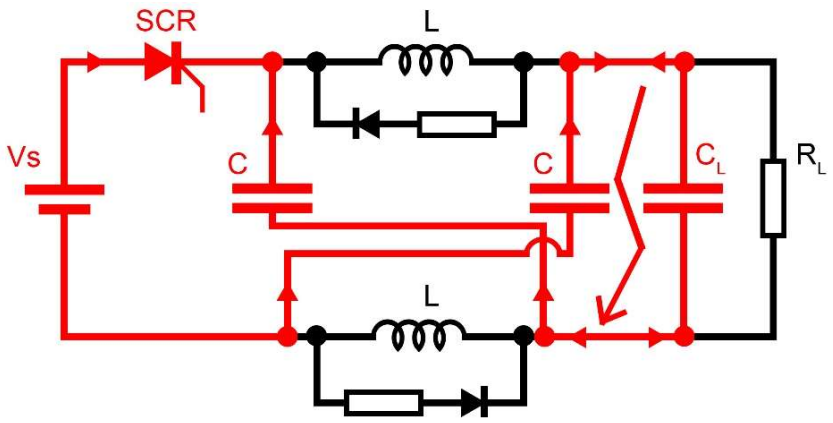

(b) Current flow once fault happens

Fig. 2-11 Z-source solid-state circuit breaker

Z-source SSCBs do not need a fault detection circuit and are more cost-efficient compared with the other types of SSCBs. However, they only respond to fault currents with a high dynamical rising rate [40].

2.2.3.Hybrid DC circuit breakers

To combine the advantages of low conductive losses of MCBs and the fast operating speed of SSCBs, a hybrid circuit breaker (HCB) for DC systems has been proposed. Fig. 2-12 shows a conventional hybrid DC circuit breaker with natural current commutation, which includes a mechanical branch, a semiconductor branch and an energy absorption varistor branch [19]. During normal operation, current flows through a mechanical switch with low conduction losses. Once a fault is detected, a MCB turns off and the main breaker turns on. The electric arc then generates between the contacts of the mechanical switch, which leads to the fault current being commutated from the mechanical branch to the semiconductor branch. During this commutation process, the arc voltage across the mechanical switch must be greater than the turn-on saturation voltage drop on the main breaker. Otherwise, the current commutation fails and the main breaker cannot be conducted. When a fault current is fully commutated from the mechanical switch into the main breaker, the mechanical switch is able to block the full system voltage. The main breaker then turns off and the varistor starts to conduct, clamping the voltage across the HCB and dissipating the rest of the energy left in the system inductance. After the current decreases to zero, the fault is fully cleared.

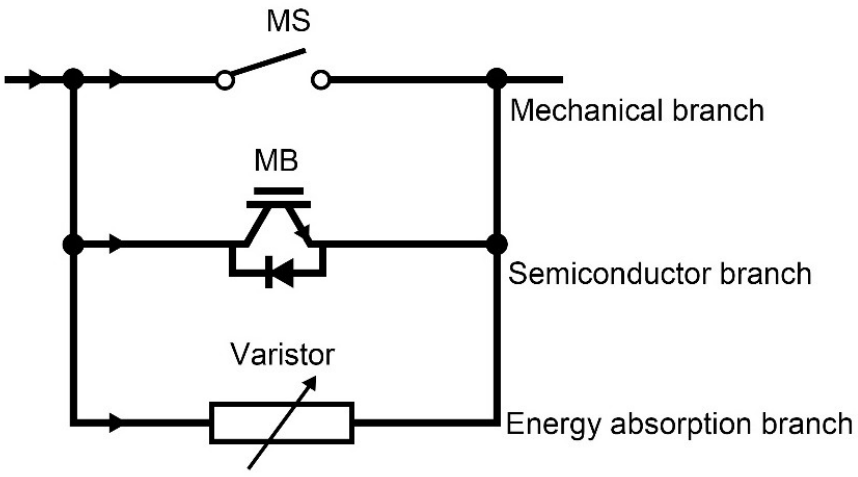

Fig. 2-12 Conventional hybrid DC circuit breaker

The conventional natural current commutation HCB achieves low conduction losses during normal operation. The operating speed of this conventional HCB topology highly depends on the mechanical switch and the passive commutation process. Thus, a proactive HCB is proposed to effectively reduce the commutating time. Fig. 2-13 shows a typical proactive hybrid DC circuit breaker topology, which was firstly developed by ABB in 2012 [41]. The circuit topology contains a mechanical switch branch with a series connected load commutation switch (LCS), solid-state devices as the main breaking branch and a varistor energy absorption branch.

During normal operation, the current flows through a mechanical switch and a load commutation switch. The load commutation switch contains only a few semiconductor devices, and therefore there are relatively low conductive losses. The main breaker can either be in an on or off state. Once a fault is detected, the load commutation switch turns off, while the main breaker turns on to commutate the fault current to the main breaker branch. Once the current through the load commutation switch decreases to zero, the mechanical switch can turn off without any electric arc. When the mechanical switch is fully opened, it can hold the system voltage. Thus, the semiconductor main breaker can turn off to break the fault current, at which time, a transient recovery voltage will be generated across the HCB. Once this voltage exceeds the knee point of the energy absorption, the varistor begins to conduct and dissipate the energy left in the system inductance.

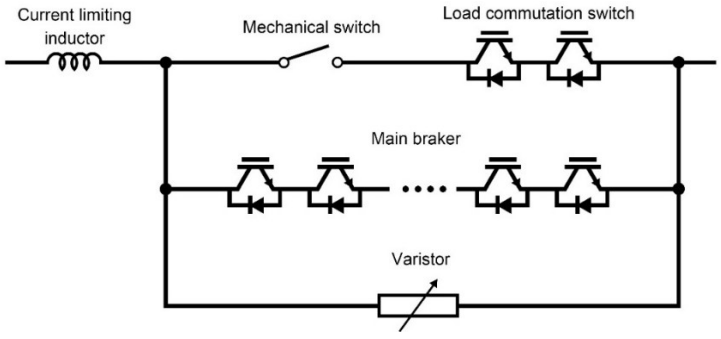

Fig. 2-13 Proactive hybrid DC circuit breaker

The proactive hybrid DC circuit breaker employs a load commutation switch to reduce the current commutation delay time and also allows the mechanical switch to open without any arcing effect, thus extending the mechanical switch's lifetime. A load commutation switch is a small group of semiconductor devices, producing on-state losses that are significantly lower than the main SSCB.

Some detailed modelling of proactive hybrid DC circuit breakers are given in [42]-[45]. The details of proactive HCBs in high voltage direct current (HVDC) system applications were introduced in [46]. A 15 kV proactive hybrid DC circuit breaker for MVDC systems was investigated in [47], which can conduct 45 A normal current and interrupt a maximum of more than 100 A fault current in less than 4 ms. A hybrid HVDC circuit breaker prototype developed in [48] was proposed to interrupt a 7 kA fault current at 120 kV. SGRI launched the world's first 200 kV DC circuit breaker that could interrupt a 15 kA fault current in 3 ms, in 2015 [49]. In [50], a topology based on a thyristor-controlled resistor and current limiting inductor of a hybrid DC circuit breaker used for VSC-HVDC systems was developed to minimise the amount of absorbed energy. Researches in [51]-[56] investigated different load commutation switch schemes, which are called forced commutation circuits, using thyristors, inductors, pre-charged capacitors and diodes, to reduce the on-state losses. However, the main drawbacks are the relatively long operation time and the complex control process in the case of bi-directional current flow.

2.2.4. Comparison of different types of DC circuit breakers

MCBs have the lowest losses and the simplest design but also are the slowest DC circuit breaker and make mechanical noise during operation. The arcing effect limits a MCB's lifetime. SSCBs have no arcing effect during operation and thus have an extended lifetime because of the semiconductor devices used, but the on-state losses are large and their volume can be as large as the cooling system required. SSCBs have the fastest

operating speed and can interrupt extremely high fault currents as long as enough semiconductor devices are used in the circuit, however, this results in a higher device cost and more complex system design. HCBs combine the advantages of MCBs and SSCBs with low on-state losses and relatively high operating speeds. The proactive commutation makes HCBs fully controllable. However, the operating speed is highly determined by the MCBs and the interrupting capability depends on the SSCBs. Table. 2-3 lists a summary of the advantages and disadvantages of the different types of DC circuit breakers.

TABLE 2-3

COMPARISON OF DIFFERENT DC CIRCUIT BREAKERS

Circuit breaker type	Advantages	Disadvantages	References
MCBs	●Low on-state losses ●Low cost ●Simple topology ●No complex circuit design	●Slow interruption speed ●Limited lifetime by contact erosion ●Large noise at operation	●[10]- [23]
SSCBs	●No arc ●Ultra-fast interruption ●Long lifetime ●No noise	●High on-state losses ●High costs ●Cooling system required ●Large volume	●[24]- [40]
HCBs	●Fast interruption ●Relatively low losses ●No arc ●Highly controllable	●Cooling system required ●High costs ●Large volume ●Complex control system	●[41]- [56]

2.3. Actuators for mechanical circuit breakers

An actuator is a mechanical component to switch the on and off status of a circuit breaker. A spring mechanism actuator is a conventional technology that stores energy in a compressed spring that is latched in place. When the latch is removed, the energy quickly releases and the actuator can perform a directional motion. The spring actuator generally allows manual operation but is always used in applications without high-speed operating requirements. Electromagnetic actuators, which convert electrical energy to mechanical energy, are widely used in relay applications, electric locks, valves and MCBs. The actuators explained in this section are all electromagnetic actuators, as they can achieve higher operating speed with better performance in MCB applications.

2.3.1. Permanent magnet actuators

A permanent magnet actuator (PMA) is a conventional technology that is widely used in linear motors and generators such as compressors, pumps, electromagnetic valve actuators, active shock absorbers and vibrators [57]. This electromagnetic-based actuator was proposed to replace the conventional spring-operated mechanisms in [58].

Fig. 2-14 shows a typical PMA topology constructed with a vacuum interrupter that was developed by ABB [59], which consists of a fixed iron core, permanent magnets, a steel moving plunger and two coils for the opening and closing process.

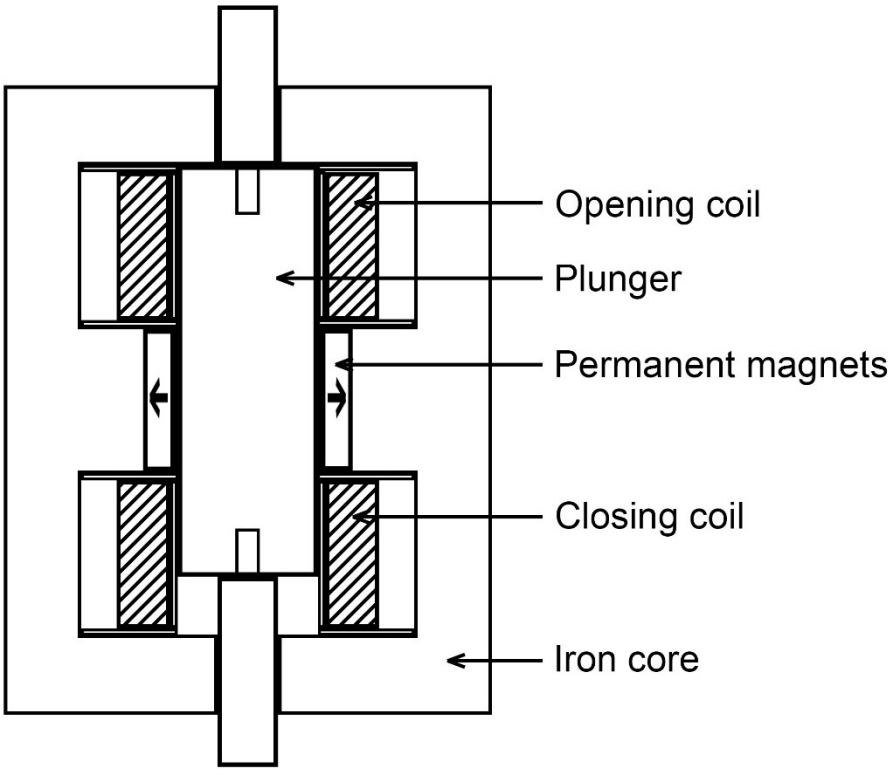

Fig. 2-14 Permanent magnet actuator topology [59]

The concept of a PMA is to use the moving plunger and the iron core to form a low magnetic resistance path to latch the moving plunger at a certain position. The actuating process is triggered by an energised coil generating an additional magnetic field to compensate for the original magnetic field from the permanent magnet and direct the plunger to move to the other end. Fig. 2-15 illustrates the change of the magnetic field during the operating process [59]. As shown in Fig. 2-15(a), the plunger is at the top position, forming a low magnetic resistance path together with the iron core. The bottom path, due to the airgaps, represents a high magnetic resistance. Thus, almost all the magnetic field fluxes run through the top end of the plunger being in contact with the iron core. The high concentration of the magnetic field fluxes generated from the permanent magnet produces a large attracting force to the plunger and latches it at the top position.

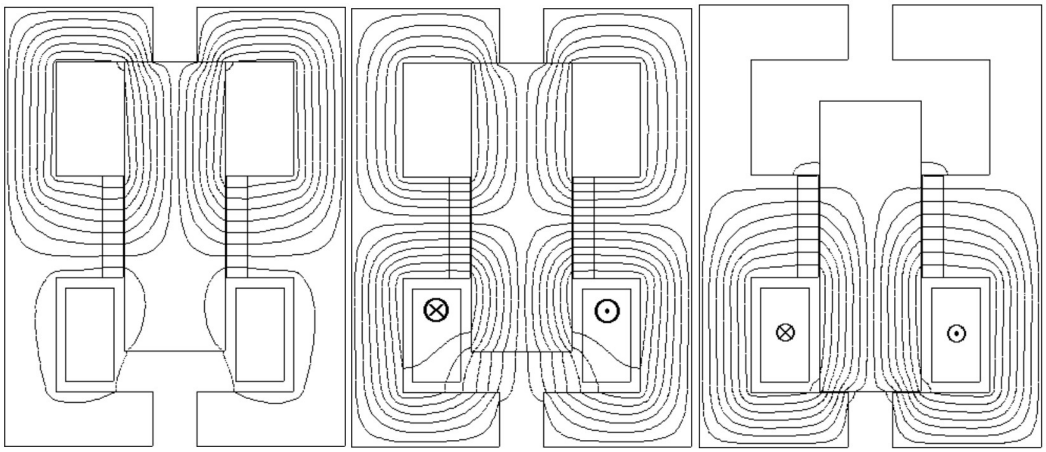

(a) (b) (c)

Fig. 2-15 Magnetic fluxes distribution of a permanent magnet actuator

To switch the actuator, an energised coil is employed to compensate for the magnetic field generated by the permanent magnet, and redirect the magnetic fluxes moving to the bottom path, as shown in Fig. 2-15(b). The bottom coil produces an additional magnetic field, which compensates for the high magnetic resistance of the airgap. Thus, the top retaining force decreases and the bottom attractive force increases. Once the attractive force exceeds the latching force, the plunger starts to move. The plunger moves downwards and reaches the bottom end of the iron core, as shown in Fig. 2-15(c). The electromagnetic force on the plunger, produced by both the permanent magnet and the coil, effectively damps out the mechanical oscillation and ensures the plunger is latched at the bottom end. Once the plunger is in this position, the coil current can be switched off. The plunger will be latched at the bottom position with the static hold-force only generated by the permanent magnet.

A PMA has a simple theoretical design and can generate a large holding force to latch the moving plunger during normal operation. Several researchers have investigated the output characteristic of PMAs and noted that their switching characteristics are similar to vacuum circuit breakers [58]-[61]. In 1998, a PMA was developed for medium voltage

vacuum switchgear [58]. This paper also indicated that a PMA is by its nature better suited for vacuum interrupters than conventional spring-operated actuators with the advantages of superior reliability and cost reduction. A comparison of PMAs, spring mechanism actuators and solenoid actuator was investigated in [62], which indicated that PMAs have the advantages of no noise in the charging process, short recharging time and maintenance-free, but a higher cost compared with the other two types of actuators.

A variable speed PMA designed in [63] was successfully operated with a 320 A, 1.5 kV vacuum switch (DVS10CB type), used in a prototype 300 kVA three-phase tap changer. Benefiting from the high reliability of PMAs, the ABB VM1-type vacuum circuit breaker is the first VCB that achieves maintenance-free status without any auxiliary switches [64]. It has a rated voltage of up to 24 kV and a short-circuit breaking current up to 50 kA. The turn-on operating time is up to 60 ms and the turn-off time is up to 50 ms. A PMA with an easy-controlled system and constant operating time was developed in [60] for vacuum circuit breakers, which achieves 30 ms for the actuator opening process. PMAs also contribute to offshore oil industry drilling and wireline jar applications [65]-[66].

2.3.2. Moving coil actuators

A moving coil actuator (MCA) is an electromagnetic actuator that employs one or more coils in a magnetic field as the moving part. The magnetic field is generally provided by a permanent magnet. Once the coils are energised, there will be a large Lorentz force on the coils to drive the moving part. This Lorentz force is proportional to the magnetic flux density, coil current, and the effective coil length. The MCAs principle has been proposed for decades, which has been used in loudspeakers to drive the mechanism for disk drive read heads [67]-[69], thus, is also called a voice coil actuator [70]. To date, MCAs have been investigated for use in a wide range of applications such as vacuum

circuit breakers.

Fig. 2-16, as an example, presents a MCA topology developed by Siemens [71]. It consists of a permanent magnet, an iron core supporting structure and a moving coil. The permanent magnet supports the magnetic flux path through the magnetic iron core and the airgap. Thus the airgap can be relatively large than for other non-permanent magnet designs. During the static state, the coil stays at a certain position with no current. Once the actuator is triggered, the coil will be energised. The Lorentz force then drives the coil to move upwards or downwards depending on the current direction.

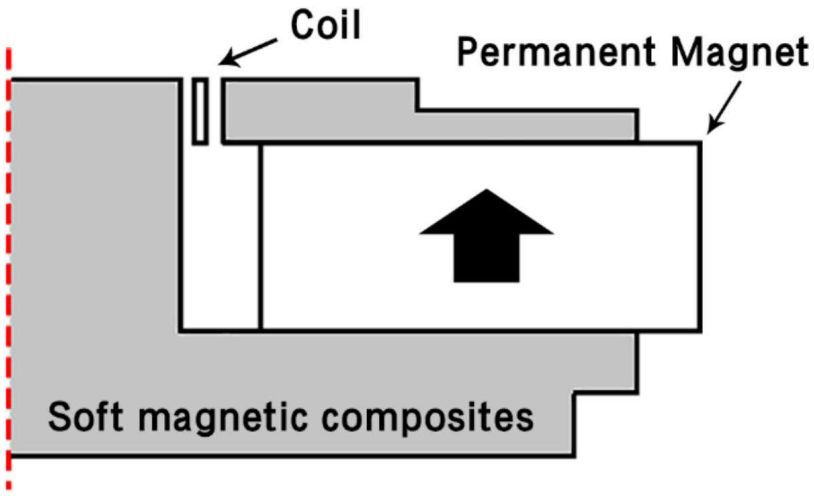

Fig. 2-16 Moving coil actuator [71]

Since the direction of the coil movement is dictated by the voltage polarity across the coil, bi-directional operation can be easily achieved by voltage reversal. However, unlike a PMA, a MCA requires an external latching system, as it does not have an inherent stable position when the power supply is removed. When a vacuum circuit breaker is in the opening or closing process, the Lorentz force on the coils will exceed the latching force so that the actuator releases.

A fast-operating MCA for a vacuum interrupter, which achieved 5 mm displacement within

5 ms was designed and built in [72]. This paper also provided suggestions for the improvement of the MCA design such as minimising the moving mass and increasing the input energy. A novel MCA topology was introduced in [73] with multi permanent magnet pieces in different directions to form a Halbach array structure to augment the magnetic field on one side. An optimisation method for MCAs was introduced in [74], which aimed to achieve a faster operating speed. [75] investigated a design method to reduce the weight of a MCA by including only coils and excluding the core.

In addition to circuit breakers, there is a wide range of MCA applications. [76] investigated MCAs for precision motion applications and proposed a control system for the designed MCA. The experimental test results showed the high performance of the control system in tracking custom periodic signals. [70] highlighted that MCAs are ideal for applications requiring high speed and acceleration, linear force or torque response and tight servo control. MCAs can also be used for printer head design [77], X and Y positioning stages for machine tools [70], semiconductor fabrication and packaging [79], automotive engine valves [80] and smartphone cameras [81].

2.3.3.Moving magnet actuators

A moving magnet actuator (MMA) is a linear electromagnetic actuator, which consists of a permanent magnet assembly attached to a load as a moving part, and a coil assembled on an iron core. Fig. 2-17 shows an example of a MMA topology, developed by a research team at the University of Sheffield [82], which is in axi-symmetric form, showing the radial plane of the structure. The moving part is composed of five permanent magnet annular rings with different magnetisation directions, forming a Halbach array armature. The Halbach array is an arrangement of permanent magnets to enhance the magnetic field on one side while minimising the magnetic field on the other side [83]-[84].

The stator contains an iron core with a slot in the middle to carry the coil. Once the

actuator is triggered, the coil will be energised to produce a magnetic field on the moving permanent magnet through the iron core. The interaction between the magnetic field generated by the permanent magnet and the magnetic field generated by the stator coil results in a strong force to drive the armature movement in both vertical directions. The direction of the movement of the armature is controlled by the voltage polarity across the coil, thus, bi-directional operation can be easily achieved by voltage reversal.

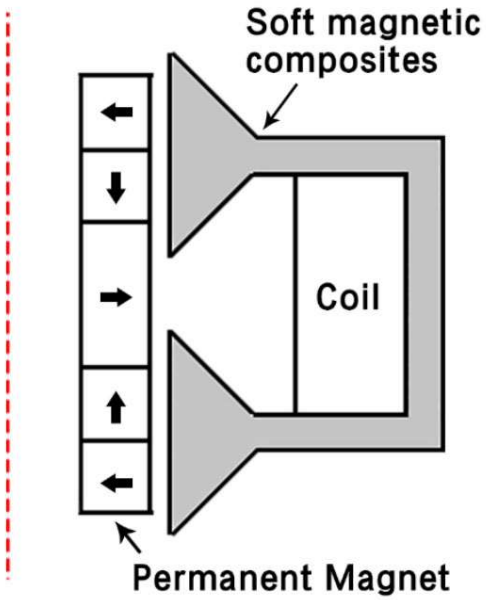

Fig. 2-17 Moving magnet actuator [82]

Compared to MCAs, MMAs have the advantage of no moving wires, therefore, achieve better durability without the risk of damaged wires. Furthermore, full encapsulation can be implemented to enable them to be deployed for use in inhospitable environments. MMAs, as a permanent magnet tubular motor, have no end-windings and are volumetrically efficient [85]-[88]. MMAs also have high force capability per moving mass, which is essential for reciprocating linear compressor applications [82]. The energised coil is attached on the iron core and thus, can be actively water-cooled, which allows a higher force density. The drawbacks of an MMA are the permanent magnet armature has a large moving mass, which means the acceleration speed will be limited. Furthermore,

the large iron core could cause a considerable large eddy current loss with a changing magnetic field. Thus, the designs of MMAs generally use soft magnet composites as the core material.

2.3.4. Thomson coil actuators

A Thomson coil actuator (TCA) is an electromagnetic repulsive drives-based actuator with ultra-fast operating speed, which has been widely investigated for mechanical switches. Fig. 2-18(a) introduced a typical TCA topology, which included energised coils and a metal disk armature [89]. To enable bi-directional operation, two coils are normally applied to drive the armature, where one coil is for the opening process and the other is for the closing process. Once the actuating process is on, one of the coils is excited by a current pulse, which is generally provided by a pre-charged capacitor. This pulse current generates a time-varying magnetic field, which, in turn, induces reversed eddy currents on the conductive metal disk armature. Then, the interaction between the magnetic field produced by the reversed eddy currents and the magnetic field generated by the energised coil develops a strong repulsive force on the disk armature. In another alternative TCA arrangement, as shown in Fig. 2-18(b), the metal disk armature was replaced by a moveable coil, which was wound in an opposite direction to the fixed coil [90]. When a pulse of current was applied to excite the coils, the induced magnetic fields resulted in an opposite repulsing force to drive the coils to separate.

Both of these TCA arrangements use the mutual inductance between two electrical conductors to generate a Lorentz repulse force. This operating principle allows TCAs to achieve a fast and compact design with minimal components. The comparison between the two concepts has been investigated in [91]-[94].

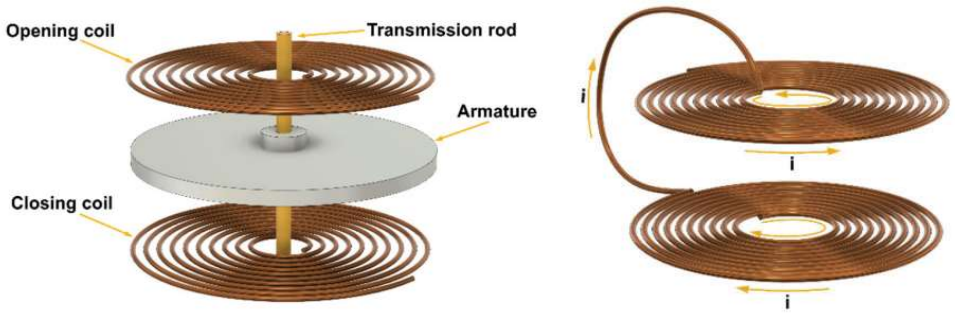

Fig. 2-18 Thomson coil actuator [90]

Due to the advantage of a TCA in operating speed, they have been widely investigated for use in DC circuit breakers [89], [95]. In [96], a TCA achieved a 20 m/s high armature moving speed. In 2018, a TCA was applied to vacuum interrupters to develop a high voltage fast transfer switch [97], where the opening was 0.69 ms. A fast-operation vacuum circuit breaker prototype using a TCA was developed in [98], which achieved a fault current interruption time of less than 5 ms, under a 40.5 kV operating voltage.

The performance of electromagnetic repulsion actuators was compared with PMAs in [99]-[100]. Experimental results have proven that TCAs have advantages in acceleration and overall velocity. It has also been proven that that TCAs can generate a moving force of up to tens of kilonewtons [101]-[102]. Some investigations on TCAs with vacuum interrupters are presented in [103]-[109], where the voltages range from 10 kV up to 40.5 kV, with an average operating speed of the moving armature from 6 to 10 m/s. Although the operating speed is fast, TCAs have the main drawback of low efficiency, as they have no stator core to support the magnetic field. The efficiency of a TCA is generally approximately 5% [89]. A double-coil arrangement TCA exhibits a marked increase in efficiency; however, the overall efficiency is still less than 10% [92]. In addition, TCAs are highly non-linear due to the induced repulsive force. The force on the armature considerably reduces with the displacement [89]. The exciting current for the coils of TCAs can reach hundreds of amps, which is consequently a challenge if they are to be used in a cryogenic environment, for example, a cryogenic aircraft MVDC system.

2.3.5.Comparison of different types of actuators

Table. 2-4 lists the advantages and disadvantages of different types of actuators. The PMA is the most conventional technology with reliable operation. However, due to their relative large moving mass, their operation speed is limited. As with PMAs, MMAs have a large moving mass but can achieve good heat dissipation, as the coils are attached to the iron core. MCAs have a light moving mass with fast operation speed. However, they have moving wires that limit the lifetime. TCAs have an ultra-fast operation speed but need a high pulse current. Furthermore, the efficiency of TCAs can be limited. The general applications for each type of actuator are also summarised in Table. 2-4.

A novel moving coil actuator topology is proposed in this thesis for vacuum circuit breakers, that achieves a fast operating speed with a compact design. This actuator topology can effectively improve the operating speed for hybrid DC circuit breakers.

TABLE 2-4

COMPARISON OF DIFFERENT ACTUATORS

Actuators	Advantages	Disadvantages	Applications	Reference
PMA	●Reliable conventional technology ●Self-latching ●No moving wire ●Long lifetime	●Large moving mass ●Low speed ●Eddy currents losses effect	●Compressors ●Pumps ●Electromagnetic valve actuators ●Active shock absorbers ● Vibrators	●[57]- [66]
MCA	●Light moving mass ●High efficiency ●High speed ●Force linearity ●Compact structure	●Moving wires exist ●Limited lifetime ●Extra latching system	●Loudspeakers ●Circuit breakers ●Printer heads ●Semiconductor fabrication and packaging ●Automotive engine valves ●Smartphone cameras	●[67]- [81]
MMA	●No moving wire ●Heat dissipation ●Compact structure	●Large moving mass ●Extra latching system ●Eddy currents losses effect ●	●Reciprocating linear compressor ●Linear pumps ●Pressure and flow control	●[82]-[88]
TCA	●High speed ●Compact structure	●Low efficiency ●Extra latching system ●High pulse current	●Circuit breakers	●[89]- [109]

2.4. Summary

This chapter introduced multiphase dual wound machines, including their advantages for ship system applications and the significant winding design challenges of magnetic decoupling.

For the DC networks, this chapter presented and compared different types of DC circuit breakers, including mechanical circuit breakers, solid-state circuit breakers, and hybrid circuit breakers. The topology and operating principle of each type of circuit breakers are described, and a comparison of different types of DC circuit breakers is summarized.

Four main kinds of actuators that are used for the mechanical circuit breakers are investigated and compared, which includes permanent magnet actuators, moving coil actuators, moving magnet actuators, and Thomson coil actuators. Each type of actuators are well described with their typical topologies. The advantages, disadvantages, and applications of various actuators were summarised and listed, in terms of operating speed, reliability, and efficiency. The permanent magnet actuator and the moving magnet actuator both have large moving mass, which is not suitable for fast operating applications. The Thomson coil actuator, though has ultra-fast operating speed, needs a high pulse current to excite pancake coils, thus with low efficiency and not idea for working in a cryogenic environment. This research proposes a moving coil actuator to achieve fast operating speed and the potential to work for electric aircraft applications.

2.5. References

[1] E. Levi, “Multiphase electric machines for variable-speed applications,” in IEEE Transactions on Industrial Electronics, vol. 55, no. 5, pp. 1893-1909, May 2008.

[2] Y. Demir and M. Aydin, “A novel asymmetric and unconventional stator winding configuration and placement for a dual three-phase surface PM motor,” IEEE Transactions on Magnetics, vol. 53, 2017.

[3] R. Yang, N. Schofield, N. Zhao, and A. Emadi, “Dual three-phase permanent magnet synchronous machine investigation for battery electric vehicle power-trains,” The Journal of Engineering, vol. 2019, no. 17, pp. 3981–3985, 2019.

[4] E. Mese, M. Tezcan, M. Ayaz, Y. Yasa and K. Yilmaz, “Design considerations for dual winding permanent magnet synchronous machines,” 2012 IEEE Energy Conversion Congr. and Expo. (ECCE), pp. 1894-1901, Sep. 2012.

[5] L. J. Rashkin, J. C. Neely, S. F. Glover, T. J. McCoy and S. D. Pekarek, “Dynamic considerations of power system coupling through dual-wound generators,” 2017 IEEE Electric Ship Technologies Symposium (ESTS), Arlington, VA, 2017, pp. 493-500.

[6] J. C. Neely, L. J. Rashkin, S. F. Glover, D. G. Wilson, N. Doerrty and T. Mccoy, “Dynamic response evaluation of a 20 MW scale dual wound machine based power system,” Advanced Machinery Technology Symposium Conference, Mar. 2018.

[7] J. F. Eastham, T. Cox and J. Proverbs, “Application of planar modular windings to linear induction motors by harmonic cancellation,” IET Electric Power Applications, vol. 4, no. 3, pp. 140-148, Mar. 2010.

[8] C. G. Hodge, J. F. Eastham and A. C. Smith, “The harmonics analysis of machine excitation,” Int. Naval Engineering Conf. (INEC), Edinburgh, May. 2012.

[9] J. F. Eastham and C. G. Hodge “The harmonics analysis of machine phase windings,” Int. Naval Engineering Conf. (INEC), Glasgow, May. 2014.

[10] M. Hudis and J. T. Carroll, “Modeling experiments applied to ceramic air-magnetic ARC chutes,” in IEEE Transactions on Power Apparatus and Systems, vol. PAS-98, no. 5, pp. 1522-1530, Sept. 1979.

[11] V. Kapustin, D. Podolsky and V. Mestcherjakov, “Arc penetration to the arc chute and arc chute plates erosion,” Electrical Contacts - 1996. Proceedings of the Forty-Second IEEE Holm Conference on Electrical Contacts. Joint with the 18th International Conference on Electrical Contacts, 1996, pp. 50-59.

[12] H. Li et al., “Effect of arc chute on DC current interruption by liquid nitrogen in HTS electrical system of distributed propulsion aircraft,” in IEEE Transactions on Applied Superconductivity, vol. 31, no. 5, pp. 1-5, Aug. 2021, Art no. 5601305, doi: 10.1109/TASC.2021.3064515.

[13] H. W. Haberl and O. Jensen, “Mechanical simplicity of air-blast circuit breakers,” in Electrical Engineering, vol. 60, no. 9, pp. 869-874, Sept. 1941.

[14] W. S. Jackson, “The air circuit breaker-50 years of technology,” 1997 IEEE Annual Textile, Fiber and Film Industry Technical Conference, 1997, pp. 4. 2.

[15] E. W. Boehne and L. J. Linde, “Magne-blast air circuit breaker for 5,000-volt service,” in Transactions of the American Institute of Electrical Engineers, vol. 59, no. 4, pp. 202-212, April 1940.

[16] L. J. Linde and B. W. Wyman, “A magnetic-type air circuit breaker for 15,000-volt services,” in Transactions of the American Institute of Electrical Engineers, vol. 63, no. 3, pp. 140-144, March 1944.

[17] Elprocus. Vacuum circuit breaker working and applications. [Online]. Available: https://www.elprocus.com/vacuum-circuit-breaker-working-applications/

[18] C. T. Dervos, P. Vassiliou, “Sulfur hexafluoride (SF6): global environmental effects and toxic byproduct formation,” Journal of the Air Waste Management Association, 2000 Jan. pp. 137-41.

[19] X. Pei, O. Cwikowski, D. S. Vilchis-Rodriguez, M. Barnes, A. C. Smith and R. Shuttleworth, “A review of technologies for MVDC circuit breakers,” IECON 2016

- 42nd Annual Conference of the IEEE Industrial Electronics Society, 2016, pp. 3799-3805.

[20] D. Jovcic, D. V. Hertem, K. Linden, J. P. Taisne, W. Grieshaber, “Feasibility of DC transmission networks,” In Proceedings of the 2011 2nd IEEE PES International Conference and Exhibition on Innovative Smart Grid Technologies, Manchester, UK, 5–7 December 2011; pp. 1–8.

[21] T. Erikksson, M. Backman, S. Halen, “A low loss mechanical HVDC breaker for HVDC Grid applications,” CIGRE, Paris, 24-29 Aug. 2014.

[22] Fuji electric, “For electric railway substations Fuji Electric DC high-speed vacuum circuit breaker,” 23B1-E-0007 datasheet, Jan. 2013.

[23] GE Energy, “Gerapid high speed DC breaker application guide,” DET -739 datasheet, Aug. 2010.

[24] C. Meyer and R. W. De Doncker, “Solid-state circuit breaker based on active thyristor topologies,” in IEEE Transactions on Power Electronics, vol. 21, no. 2, pp. 450–458, Mar. 2006.

[25] L. Q. Zhang, R. Woodley, X. Q. Song, S. Sen, X. Zhao, and A. Q. Huang, “High current medium voltage solid state circuit breaker using paralleled 15kV SiC ETO,” in 2018 IEEE Applied Power Electronics Conference and Exposition (APEC), 2018, pp. 1706–1709.

[26] R. Rodrigues, T. S. Jiang, Y. Du, P. Cairoli, and H. X. Zheng, “Solid state circuit breakers for shipboard distribution systems,” in 2017 IEEE Electric Ship Technologies Symposium (ESTS), 2017, pp. 406–413.

[27] R. Rodrigues, Y. Du, A. Antoniazzi, and P. Cairoli, “A review of solid-state circuit breakers,” in IEEE Transactions on Power Electron, vol. 36, no. 1, pp. 364–377, Jan. 2021.

[28] Z. Miao et al., “A self-powered ultra-fast DC solid state circuit breaker using a normally-on SiC JFET,” in 2015 IEEE Applied Power Electronics Conference and Exposition (APEC), Mar. 2015, pp. 767–773. doi: 10.1109/APEC.2015.7104436.

[29] A. Bhalla, “Market penetration of wide-bandgap SiC and GaN technology in light of silicon superjunction and IGBT technology evolution,” CS MANTECH Conference, Denver, Colorado, USA, pp. 9-12, May. 2014.

[30] K. Tan, P. Liu, X. Ni, C. Peng, X. Song, and A. Q. Huang, “Performance evaluation of multiple Si and SiC solid state devices for circuit breaker application in 380VDC delivery system,” in 2016 IEEE Applied Power Electronics Conference and Exposition (APEC), Mar. 2016, pp. 983–989.

[31] Y. Zhou, Y. Feng, T. Liu, and Z. J. Shen, “A digital-controlled SiC-based solid state circuit breaker with soft-start function for DC microgrids,” in 2018 9th IEEE International Symposium on Power Electronics for Distributed Generation Systems (PEDG), Jun. 2018, pp. 1–7.

[32] Z. J. Shen et al., “First experimental demonstration of solid state circuit breaker (SSCB) using 650V GaN-based monolithic bidirectional switch,” in 2016 28th International Symposium on Power Semiconductor Devices and ICs (ISPSD), Jun. 2016, pp. 79–82.

[33] X. Wu, B. Niu, L. Cheng, Y. Wu, Q. Yi and W. Zhuang, “IGBT-based self-powered bidirectional solid state DC circuit breaker,” 2020 4th International Conference on HVDC (HVDC), 2020, pp. 957-960.

[34] L. Feng, R. Gou, F. Zhuo, X. Yang and F. Zhang, “Development of a 10kV solid-state DC circuit breaker based on press-pack IGBT for VSC-HVDC system,” 2016 IEEE 8th International Power Electronics and Motion Control Conference (IPEMC-ECCE Asia), 2016, pp. 2371-2377.

[35] J. Xi, X. Pei, X. Zeng and L. Niu, “Design, modelling, and test of a solid-state main breaker for hybrid DC circuit breaker,” 2020 22nd European Conference on Power Electronics and Applications (EPE'20 ECCE Europe), 2020, pp. 1-10.

[36] R. F. Schmerda, S. Krstic, E. L. Wellner and A. R. Bendre, “IGCTs vs. IGBTs for circuit breakers in advanced ship electrical systems,” 2009 IEEE Electric Ship Technologies Symposium, 2009, pp. 400-405.

[37] R. R. Boudreaux and R. M. Nelms, “A comparison of MOSFETs, IGBTs, and MCTs for solid state circuit breakers,” Proceedings of Applied Power Electronics Conference. APEC '96, 1996, pp. 227-233 vol.1.

[38] A. Mokhberdoran, A. Carvalho, H. Leite, and N. Silva, “A review on HVDC circuit breakers,” in 3rd Renewable Power Generation Conference (RPG 2014), Sep. 2014, pp. 1–6.

[39] K. Sano and M. Takasaki, “A surgeless solid-state DC circuit breaker for voltage-source-converter-based HVDC systems,” in IEEE Transactions on Industry Applications, vol. 50, no. 4, pp. 2690–2699, Jul. 2014.

[40] K. A. Corzine and R. W. Ashton, “A new Z-source DC circuit breaker,” in IEEE Transactions on Power Electronics, vol. 27, no. 6, pp. 2796–2804, Jun. 2012.

[41] M. Callavik, A. Blomberg, J. Häfner, and B. Jacobson, “The hybrid HVDC breaker,” ABB Grid Systems Technical Paper, vol. 361, pp. 143-152, 2012.

[42] J. A. Martinez, et al., “EMTP modeling of hybrid HVDC breakers,” 2015 IEEE PES General Mtg., Jul. 2015.

[43] D. Peftitsis, et al., “Design considerations and performance evaluation of hybrid DC circuit breakers for HVDC grids,” 18th Eur. Conf. Power Electron. App., Sep. 2016.

[44] X. Su, et al., “Modeling DC circuit breaker in MTDC for wind farms based on delay slope method,” 42nd Annu. Conf. of IEEE Ind. Electron. Soc., Oct. 2016.

[45] N. Lin, et al., “Detailed device-level electrothermal modeling of the proactive hybrid HVDC breaker for real-time hardware-in-the-loop simulation of DC grids,” in IEEE Transactions on Power Electronics, Vol. 33(2), Feb. 2018.

[46] J. Hafner, ¨ et al., “Proactive hybrid HVDC breakers—a key innovation for reliable HVDC grids,” CIGRE Intl. Symp.: Electric Power System of the Future—Integrating Supergrids and Microgrids, Sep. 2011.

[47] C. Peng, A. Q. Huang and X. Song, "Current commutation in a medium voltage hybrid DC circuit breaker using 15 kV vacuum switch and SiC devices," 2015

IEEE Applied Power Electronics Conference and Exposition (APEC), 2015, pp. 2244-2250.

[48] C. C. Davidson, et al., “A new ultra-fast HVDC circuit breaker for meshed DC networks,” 11th IET Intl. Conf. AC DC Power Trans., Feb. 2015.

[49] NARI, “SGRI launches world’s first 200kV DC Circuit Breaker,” C-EPRI, Jan. 2015.

[50] J. Liu, et al., “A hybrid current-limiting circuit for DC line fault in multiterminal VSC-HVDC system,” in IEEE Transactions on Industrial Electronics, Vol. 64(7), Jul. 2017.

[51] C Meyer, M Kowal, R W. Decker. “Circuit breaker concept for future high-power DC appliactions,”. IEEE-IAS conference, 2005, v2:860-866.

[52] Y. Bingjian, et al., “A hybrid circuit breaker for DC-application,” 2015 IEEE 1st Intl. Conf. DC Microgrids, Jun. 2015.

[53] H. Yu, S. Chi, and E. Li, “Forced current commutation hybrid DC circuit breaker based on full-controllable power electronic devices,” Automation of Electric Power Systems. 41. 168-172 and 187.

[54] Y. Wu, M. Rong, Y. Wu, F. Yang, M. Li, Y. Li, “Development of a new topology of dc hybrid circuit breaker,” Electric Power Equipment – Switching Technology (ICEPE-ST), 2013 2nd Int. Conf. on, 2013, pp. 1–4.

[55] L. Liu, J. Zhuang, C. Wang, Z. Jiang, J. Wu and B. Chen, “A hybrid DC vacuum circuit breaker for medium voltage: principle and first measurements,” in IEEE Transactions on Power Delivery, vol. 30, no. 5, pp. 2096-2101, Oct. 2015.

[56] Y. F. Wu, Y. Wu, M. Rong, F. Yang, C. Niu, M. Li, and Y. Hu, “Research on a novel two-stage direct current hybrid circuit breaker,” AIP Rev. Sci. Instrum., 2014, 85,

[57] R. B. Ummaneni, C. Jaillot, R. Nilssen and J. E. Brennvall, “Experimental characterisation of linear permanent magnet actuator with gas springs,” 2009 IEEE International Electric Machines and Drives Conference, 2009, pp. 369-372.

[58] A. J. W. Lammers, P. P. Leeufkens and G. C. Schoonenberg, “MV vacuum switchgear based on magnetic actuators,” 1998 Fifth International Conference on Trends in Distribution Switchgear: 400V-145kV for Utilities and Private Networks (Conf. Publ. No. 459), 1998, pp. 86-90.

[59] E. Dullni, “A vacuum circuit-breaker with permanent magnetic actuator for frequent operations,” Proceedings ISDEIV. 18th International Symposium on Discharges and Electrical Insulation in Vacuum (Cat. No.98CH36073), 1998, pp. 688-691 vol.2.

[60] Z. Huang, X. Duan, J. Zou and M. Chen, “A permanent magnetic actuator with scheduled stroke curve for vacuum circuit breakers,” 24th ISDEIV 2010, 2010, pp. 162-165.

[61] X. Duan, M. Liao, F. Ding, et al, “Application and key technology analysis of controlled switching,” High Voltage Aparatus, China, 2007, 43(2):113-117.

[62] E. J. Choi and J. Ma, “Development of Permanent Magnetic Actuator for a solid insulated vacuum circuit breaker,” 2015 3rd International Conference on Electric Power Equipment – Switching Technology (ICEPE-ST), 2015, pp. 462-465.

[63] H. Jiang, R. Shuttleworth, B. A. T. Al Zahawi and A. Power, “Variable speed latching magnetic actuator for a vacuum switch,” 1997 Eighth International Conference on Electrical Machines and Drives (Conf. Publ. No. 444), 1997, pp. 105-108.

[64] ABB, “VM1 Vacuum circuit-breaker with magnetic actuator mechanism,” Leaflet no. DEABB 2233 03 E Printed in Germany (06.05-500-PPI).

[65] R. B. Ummaneni, J. E. Brennvall, and R. Nilssen, “Applications of linear permanent magnet actuators in offshore applications,” AEE, 2-4 July 2008, Trondheim, Norway.

[66] R. B. Ummaneni, J. E. Brennvall, and R. Nilssen, “Concept of linear permanent magnet actuator with gas springs in drilling applications,” ICEMS, 20-23 Nov 2006, Nagasaki, Japan

[67] J. A. Wagner, “The choice of steel in a moving coil actuator for disk drives,” Conference Record of the 1991 IEEE Industry Applications Society Annual Meeting, 1991, pp. 133-137 vol.1.

[68] J. Borwick, “Loudspeaker and Headphone Handbook,” London: Butterworths, 1988.

[69] M. Colloms, “High Performance Loudspeakers,” 5th Ed. New York: John Wiley and Sons, 1997.

[70] X. M. Feng, Z. J. Duan, Y. Fu, A. L. Sun, and D. W. Zhang, “The technology and application of voice coil actuator,” In Proc. 2nd International Conference on Mechanic Automation and Control Engineering, 2011, pp. 892-895.

[71] Siemens Report, “Loudspeaker optimization: minimal mass with 1.8 T flux density,” Tech. Report. 2018.

[72] X. Pei, A. C. Smith, R. Shuttleworth, D. S. Vilchis-Rodriguez and M. Barnes, “Fast operating moving coil actuator for a vacuum interrupter,” in IEEE Transactions on Energy Conversion, vol. 32, no. 3, pp. 931-940, Sept. 2017.

[73] L. Liu and S. Chang, “A moving coil electromagnetic valve actuator for camless engines,” 2009 International Conference on Mechatronics and Automation, 2009, pp. 176-180.

[74] A. B. J. Sung and B. D. S. Kim, “A design method of voice coil type high speed actuator for valve operation,” 2012 15th International Conference on Electrical Machines and Systems (ICEMS), 2012, pp. 1-5.

[75] H. Kim, M. Yoon and J. Hong, “Design and performance analysis of moving-coil type linear actuator,” 2011 International Conference on Electrical Machines and Systems, 2011, pp. 1-4.

[76] S. Saeedi, A. Sadighi and M. S. Panahi, “Robust repetitive control of a cylindrical voice-coil actuator,” 2021 9th RSI International Conference on Robotics and Mechatronics (ICRoM), 2021, pp. 281-286.

[77] Y. Yabuuchi, M. Kobayashi, M. Watada, D. Ebihara, T. Takura and T. Okada,

"Application of a cylindrical moving coil linear DC motor to printer head," in IEEE Transactions on Magnetics, vol. 32, no. 5, pp. 5028-5030, Sep. 1996.

[78] X.Z.Wang, F.Xie, M.X.Zeng, "The design of light-stylus displacement sensor's focused servo control system ," Automation and Instrumentatiuon, 2000. pp.1~5.

[79] H.W.Park, H.S.Yang, Y.P.Park, S.H.Kim, "Position and vibration control of a flexible robot manipulator using hybrid controller," Robotics and Autonomous System,1999. pp. 31~41.

[80] H. Muamer, L. Chen and S. Liu, "Design and simulation of a moving coil linear actuator for automotive applications," 2004 IEEE International Conference on Industrial Technology, 2004. IEEE ICIT '04., 2004, pp. 1023-1027 Vol. 2.

[81] C. L. Hsieh and C. S. Liu, "Design of a voice coil motor actuator with L-shape coils for optical zooming smartphone cameras," in IEEE Access, vol. 8, pp. 20884-20891, 2020.

[82] J. Wang, Z. Lin, and D. Howe, "Analysis of a short-stroke, single-phase, quasi-Halbach magnetised tubular permanent magnet motor for linear compressor applications," IET Electric Power Applications, vol. 2, no. 3, May., pp. 193-200, 2008.

[83] S. Jang, J. Choi, H. Cho and S. Lee, "Thrust analysis and measurements of tubular linear actuator with cylindrical halbach array," in IEEE Transactions on Magnetics, vol. 41, no. 5, pp. 2028-2031, May 2005.

[84] S. M. Jang, J. Y. Choi, H. Cho and S. Lee, "Dynamic characteristic analysis and experiments of moving-magnet linear actuator with cylindrical Halbach array," in IEEE Transactions on Magnetics, vol. 41, no. 10, pp. 3814-3816, Oct. 2005.

[85] A. W. van Zyl, C. G. Jeans, R. J. Cruise and C. F. Landy, "Comparison of force to weight ratios between a single-sided linear synchronous motor and a tubular linear synchronous motor," IEEE International Electric Machines and Drives Conference. IEMDC'99. Proceedings (Cat. No.99EX272), 1999, pp. 571-573.

[86] N. Bianchi, S. Bolognani, D. D. Corte and F. Tonel, "Tubular linear permanent

magnet motors: an overall comparison," in IEEE Transactions on Industry Applications, vol. 39, no. 2, pp. 466-475, March-April 2003.

[87] J. F. Eastham, "Novel synchronous machines: linear and disc," IEE Proceedings B (Electric Power Applications), 1990, 137, (1), pp. 49– 58.

[88] J. Wang, G. W. Jewell and D. Howe, "A general framework for the analysis and design of tubular linear permanent magnet machines," in IEEE Transactions on Magnetics, vol. 35, no. 3, pp. 1986-2000, May 1999.

[89] M. Barnes, D. S. Vilchis-Rodriguez, X. Pei, R. Shuttleworth, O. Cwikowski and A. C. Smith, "HVDC circuit breakers–a review," in IEEE Access, vol. 8, pp. 211829-211848, 2020.

[90] A. Bissal, J. Magnusson, and G. Engdahl, "Electric to mechanical energy conversion of linear ultra-fast electro-mechanical actuators based on stroke requirements," in Proc. Int. Conf. Electr. Mach. (ICEM), Berlin, Germany, Sep. 2014, pp. 509–515.

[91] A. Bissal, J. Magnusson and G. Engdahl, "Comparison of two ultra-fast actuator concepts," in IEEE Transactions on Magnetics, vol. 48, no. 11, pp. 3315-3318, Nov. 2012.

[92] Y. Zhao, Y. Xinlin, W. Xiaoguang, "Comprehensive optimization of coil-coil electromagnetic repulsive actuators," High Volt. Eng. 2015, 41, pp. 4207–4212.

[93] D. S. Vilchis-Rodriguez, R. Shuttleworth and M. Barnes, "Double-sided Thomson coil based actuator: finite element design and performance analysis," 8th IET International Conference on Power Electronics, Machines and Drives (PEMD 2016), 2016, pp. 1-6.

[94] Z. Nanxun, F. Chun-en, G. Pan, L. Wei, Z. Bi-de and R. Xiao, "Comparison of two types of electromagnetic repulsive force actuators," 2017 4th International Conference on Electric Power Equipment - Switching Technology (ICEPE-ST), 2017, pp. 916-919.

[95] M. Al-Dweikat, J. Cui, S. Sun, M. Yang, G. Zhang, and Y. Geng, "A review on

Thomson coil actuators in fast mechanical switching," Actuators, vol. 11, no. 6, p. 154, Jun. 2022.

[96] M. Steurer, K. Frohlich, W. Holaus and K. Kaltenegger, "A novel hybrid current-limiting circuit breaker for medium voltage: principle and test results," in IEEE Transactions on Power Delivery, vol. 18, no. 2, pp. 460-467, Apr. 2003.

[97] L. Qin, H. Jiang, X. Zhao, H. Quan, X. Huang, T. Liao, J. Zhou, D. Qiu, and Y. Ban, "Research on 10kv quick vacuum circuit breaker with double opening and closing coils," 2nd International Symposium on Resource Exploration and Environmental Science, IOP Conference Series: Earth and Environmental Science, 2018, Vol. 170.

[98] X. Xiaodong, L. Zhibing, Y. Xianlgian, L. Beiyang and T. Yang, "Design and test of vacuum circuit breaker with hybrid fast operating mechanism," 2017 4th International Conference on Electric Power Equipment - Switching Technology (ICEPE-ST), 2017, pp. 939-946.

[99] E. Dong, L. Bo, J. Zou, "Comparison Analysis of Experiment Performance between High-speed Repulsion Mechanism and Permanent Magnetic Mechanism," High Voltage Apparatus, 2007, 43(2):125-126.

[100] E. Dong, Y. Wang, J. Cong, J. Zou, "The analysis of high-speed repulsion actuator and performance comparisons with permanent magnetic actuator in vacuum circuit breaker," In Proceedings of the 2008 23rd International Symposium on Discharges and Electrical Insulation in Vacuum, Bucharest, Romania, Sep. 2008.

[101] B. Roodenburg, B. H. Evenblij, "Design of a fast linear drive for (hybrid) circuit breakers–development and validation of a multi domain simulation environment," Mechatronics 2008, 18, pp. 159–171.

[102] P. Skarby, U. Steiger, "An ultra-fast disconnecting switch for a hybrid HVDC breaker—a technical breakthrough," In Proceedings of the CIGRE 265, Calgary, Alberta, pp. 9–11. Sep. 2013.

[103] X. Song, C. Peng and A. Q. Huang, “A medium-voltage hybrid DC circuit breaker, part I: solid-state main breaker based on 15 kV SiC emitter turn-off thyristor,” in IEEE Journal of Emerging and Selected Topics in Power Electronics, vol. 5, no. 1, pp. 278-288, Mar. 2017.

[104] C. Peng, X. Song, A. Q. Huang and I. Husain, “A medium-voltage hybrid DC circuit breaker—part II: ultrafast mechanical switch,” in IEEE Journal of Emerging and Selected Topics in Power Electronics, vol. 5, no. 1, pp. 289-296, Mar. 2017.

[105] C. Peng, I. Husain, A. Q. Huang, B. Lequesne and R. Briggs, “A fast mechanical switch for medium-voltage hybrid DC and AC circuit breakers,” in IEEE Transactions on Industry Applications, vol. 52, no. 4, pp. 2911-2918, Aug. 2016.

[106] H. Chunguang, W. Jinjin, H. Ying, C. Yundong and C. Yuchen, “Design and research of high stability repulsion mechanism of 12kV vacuum circuit breaker,” 2016 27th International Symposium on Discharges and Electrical Insulation in Vacuum (ISDEIV), 2016, pp. 1-4.

[107] W. Wen et al., “Research on operating mechanism for ultra-fast 40.5-kV vacuum switches,” in IEEE Transactions on Power Delivery, vol. 30, no. 6, pp. 2553-2560, Dec. 2015.

[108] L. Ren et al., “Development of an electromagnetic repulsion mechanism for a 40.5kV fast vacuum circuit breaker,” 2017 4th International Conference on Electric Power Equipment - Switching Technology (ICEPE-ST), 2017, pp. 929-933.

[109] J. Jiang et al., “Research on the Coordination of 40.5kV Fast Vacuum Switch Driven by Electromagnetic Repulsion Mechanism and Oil Damper,” 2019 5th International Conference on Electric Power Equipment - Switching Technology (ICEPE-ST), 2019, pp. 652-657.

[110] B. Yin, X. Pei, J. F. Eastham, H. Wang, C. Hodge, O. Simmonds, C. Vagg and X. Zeng, “Magnetic Decoupling of Winding Design in Dual Wound

Generators," in IEEE Transactions on Energy Conversion, 2022.

[111] B. Yin, X. Zeng, J. F. Eastham, D. Vilchis-Rodriguez and X. Pei, "Novel fast operating moving coil actuator with compensation coil for HVDC circuit breakers," in CSEE Journal of Power and Energy Systems, vol. 7, no. 5, pp. 1041-1050, Sep. 2021.

[112] B. Yin, X. Pei, J. F. Eastham, X. Zeng, "Analysis of stator end-winding in a dual wound machine using Biot-Savart law," PEMD 2022: The 11th International Conference on Power Electronics, Machines and Drives.

Chapter 3.

Magnetic decoupling of winding design in dual wound generators

Chapter contents:

This chapter develops a fully magnetic decoupled dual wound generator for electric ship systems. An analytical harmonic calculation based on algebraic method is presented. A 2D finite element model in COMSOL is simulated. The experimental test results further verify that there is no electromagnetic coupling between the two outputs from the two sets of stator windings

3.1. Chapter summary

Traditional large cruise ships and naval warships require a set of diesel engines for the propulsion system, and another separate generator set for ship services such as the domestic/hotel loads (navigation, lighting, air-conditioning, etc). This direct diesel-drive system performs at low efficiency and uses up a lot of onboard space. Electric propulsion for ship systems has been investigated and proven to have the advantages of lower fuel consumption, better dynamic performance and higher reliability. An IFEP system further integrates the propulsion and ship services, building an all-electric network, which provides more flexible commercial solutions for maintenance and thus, reduces the capital and running costs. A dual wound generator with only one prime mover can further reduce the number of generators, which can save onboard volume and mass while still achieving the same total power ratings.

This chapter investigates a 2-pole and a 6-pole dual wound generator for IFEP ships system applications. The proposed stator winding arrangements eliminate the electromagnetic coupling between the two windings, to avoid cross-coupling of the two outputs. A harmonics analysis method is used to ensure there is no common harmonic field between the rotor and stator windings. The 2D finite element modelling method is used in COMSOL to simulate the magnetic fields and dynamic performance of the dual wound generator. A prototype dual wound generator is proposed in this chapter to further verify that there is no electromagnetic coupling between the two windings. This is important as the end-winding fields are included, which are not considered in the 2D simulations.

The remainder of this chapter is cited from the author's published article in IEEE Transactions on Energy Conversion [110]. The structure of this chapter is organised in an alternative-based format, where the indices, equations, tables, figures, titles and references are numbered independently.

Statement of Authorship

<table>
<tr><td colspan="4">This declaration concerns the article entitled:</td></tr>
<tr><td colspan="4">Magnetic decoupling of winding design in dual wound generators</td></tr>
<tr><td colspan="4">Publication status (tick one)
Draft manuscript [ ] Submitted [ ] In review [ ] Accepted [ ] Published [√]</td></tr>
<tr><td>Publication details (reference)</td><td colspan="3">B. Yin, X. Pei, J. F. Eastham, H. Wang, C. Hodge, O. Simmonds, C. Vagg, X. Zeng, “Magnetic Decoupling of Winding Design in Dual Wound Generators,” in IEEE Transactions on Energy Conversion, 2022, doi: 10.1109/TEC.2022.3191952.</td></tr>
<tr><td colspan="4">Copyright status (tick the appropriate statement)
I hold the copyright for this material [ ] Copyright is retained by the publisher, but I have been given permission to replicate the material here [√]</td></tr>
<tr><td>Candidate’s contribution to the paper (provide details, and also indicate as a percentage)</td><td colspan="3">The candidate contributed to / considerably contributed to / predominantly executed the…
Formulation of ideas:
● 80%
● Magnetic decoupling of winding design for the proposed dual wound generator used in IFEP ship systems to save onboard volume and space. This research is guided and supervised by Dr. Xiaoze Pei and Prof. John Frederic Eastham.
Design of methodology:
● 100%
● A harmonics analysis using the algebraic method and analytical equations is used for the winding design. A 2D finite element model is built in COMSOL to investigate the magnetic field distribution and dynamic performance.
Experimental work:
● 100%
● The dual wound generator prototype was built by rewinding an existing machine frame following the designed winding arrangement. The experimental test is carried out to further verify the decoupled design.
Presentation of data in journal format:
● 80%
● Organising and writing this article, revised by Dr Xiaoze Pei and other co-authors</td></tr>
<tr><td>Statement from Candidate</td><td colspan="3">This paper reports on original research I conducted during the period of my Higher Degree by Research candidature.</td></tr>
<tr><td>Signed</td><td>Boyuan Yin</td><td>Date</td><td>25/11/2022</td></tr>
</table>

Magnetic Decoupling of Winding Design in Dual Wound Generators

Boyuan Yin[1], Xiaoze Pei[1*], John Frederic Eastham[1], Han Wang[2], Chris Hodge[3], Oliver Simmonds[3], Christopher Vagg[2], Xianwu Zeng[2]

1 Dept. of Electronics & Electrical Engineering, University of Bath, United Kingdom
2 Dept. of Mechanical Engineering, University of Bath, United Kingdom
3 BMT Defence & Security UK Ltd.

Abstract: A general shipboard power system contains multiple electrical machine sets to provide electrical power with different ratings for both the propulsion system and the ship service. In order to achieve the most compact design and maximize the weight reduction, a study of using a single dual wound generator to replace the electrical machine sets is presented in this paper. It consists of dual two-layer windings of different pole numbers which use the same slots and share one prime mover, producing two independent power supplies. This paper verifies a dual wound machine designed for no electromagnetic coupling by algebraically analyzing the spatial harmonic magnetic field distribution. Further verification of the absence of electromagnetic coupling due to both the airgap and slot leakage fluxes is provided by 2D finite element modeling. The dual wound generator prototype using the principle is designed, built and experimentally tested. The experimental results match well with the simulation results, validating the independence of the two power outputs and showing that the winding end-turns also do not couple. The results are significant for applications where multiple independent power supplies are needed, or where an auxiliary power supply is needed which could be drawn from an existing traction motor.

Index terms: Dual wound machine, Electric ship, Harmonic decoupling, Independent power supplies.

3.2. Introduction

Traditional large cruise ships and naval warships contain a set of diesel generators for ship service systems, and another separate set of prime movers for propulsion systems [1]-[2]. This direct-drive diesel system can occupy a large space on the ships with low power efficiency. Electric propulsion has emerged to be the most efficient arrangement for several vessel types [3]-[4], and the number of electrically propelled ships has grown rapidly over the last ten years [5]. Compared with direct-drive diesel systems, electric propulsion systems have great potential to reduce fuel consumption, enhance dynamic performance and increase the system reliability [6]-[8]. Integrated full electric propulsion (IFEP) systems remove the direct mechanical coupling between the prime mover and propeller, building an all-electric network, which can provide power for both the ship services and the propulsion [9]. All the engines in IFEP systems are used to generate electrical power, rather than to provide mechanical propulsion, so the total number of engines can be reduced, which contributes to the reduction of the weight and volume for the ship, as well as noise and vibration. IFEP systems can also achieve more flexible ship engine arrangements by eliminating the mechanical connections between the diesel generators and the propulsion. The independent engine groups and propulsion machines provide more flexible commercial solutions for maintenance and thus reduce the capital costs. In summary, the IFEP systems can provide significant benefits for the ship structures. The primary purpose of a dual wound generator is to supply different subsystems with only one compact machine. Compared with the general IFEP system, a dual wound machine only needs one prime mover, which takes less volume and mass than two separate prime movers to achieve the same total power rating, saving space on the ship [10]. With only one electric machine, there are no integration problems between the generators.

Dual wound generators are shown to have great potential to provide better power quality

[11], better torque quality [12] and reduced losses [13]. The different winding strategies that can be applied to dual wound machines are described in references [11], [14]. Some studies of the dual wound machine generators have been performed in [15]-[16] using the same winding pole numbers and therefore being magnetically coupled. However, in these machines the change of operation condition of one output would fully impact the operation of the other [15]-[16]. Based on the principle of the IFEP system, this paper is based on the design of a dual wound generator having the novel feature that each winding uses a different pole number, providing the electric power for both the propulsion and ship services simultaneously without any electromagnetic coupling [17]-[18]. The two outputs of the dual wound generator are from two windings on the stator, which mechanically share the same slots but can be windings of different forms. The proposed stator winding arrangements have the benefit of eliminating the electromagnetic coupling between them to avoid cross-coupling between the power supplies. In addition, each of the two rotor windings should only couple with its corresponding stator winding. By developing a dual wound generator prototype, it is possible to experimentally investigate if the windings are coupled and this paper designs a prototype 2-pole and 6-pole dual wound generator operating at 1500 rpm based on an existing machine frame. An analytical harmonic calculation based on the airgap fields is presented showing that there is no electromagnetic coupling between the two stator windings. A harmonics analysis using the algebraic method and analytical equations developed in [19]-[21] is used in this paper. A 2D finite element model has been used for simulation in COMSOL to demonstrate the magnetic flux density distribution and the dynamic performance. The detailed simulation results are published in a previous research paper [18] to show that there is no coupling due to both the airgap fields and the slot leakage flux. The designed dual wound machine is experimentally tested in this paper and the results further verify that there is no electromagnetic coupling between the two outputs from the two sets of stator windings; this not only includes the airgap and stator slot leakage fields but importantly also the end-winding fields which have not been considered previously.

The structure of this paper is as follows. Section II introduces the dual wound generator topology and design based on the existing machine frame, including the rotor winding distributions and the magnetic flux density in the air gap; Section III presents the stator electromagnetic decoupling performance and the winding harmonic analysis; Section IV presents the operation of the dual wound generator with resistive load using COMSOL finite element modelling. Section V demonstrates the experimental results compared with the simulation results and further validates the independence of the two power outputs. Section VI discusses the system aspects and the potential applications of the dual wound generator.

3.3. Generator design and air gap flux density

3.3.1. Dual wound generator topology

The prototype dual wound generator designed in this paper is a synchronous machine with a separately excited wound rotor using the existing machine frame. Table 3-1 presents its key dimensions.

TABLE 3-1

GENERATOR DIMENSIONS

Item	Stator	Rotor
Number of slots	36	24
Diameter	190.5 mm	186.5 mm
Axial length	123.6 mm	139.5 mm
Slot opening	2.7 mm	3.5 mm
Airgap	2 mm	
Stator outer diameter	295 mm	

This existing machine was in the lab at the University of Bath, manufactured by Mawdsley's LtD. It has 36-slot stator, 24-slot rotor, four slip rings and several open terminals. The existing windings are removed. The dimensions of the machine frame is

measured in the aspects of axial length, both rotor and stator diameters, and slot areas. The proposed magnetic decoupled winding design in this paper is based on this existing machine frame with the measured dimensions.

The stator has 36 slots and the rotor 24. To achieve a sinusoidal form of airgap magnetic field, the rotor windings use concentrically distributed windings. Based on the slot dimensions, the total number of turns of the 2-pole rotor is 1100 and the 6-pole rotor has the total number of turns of 1000. The design provides maximum airgap flux density without saturation in the frame structures. Considering the maximum exciting current and the packing factors, the wire used for the rotor is SWG 27 with a diameter of 0.4166 mm. The 2-pole and 6-pole rotor windings are excited through four slip rings and brushes. The 2-pole stator has 20 turns in each slot, and the 6-pole stator has 12 turns. Considering the slot packing area and the rated current, the 2-pole stator uses SWG 21 wire and the 6-pole stator uses SWG 19 wire.

3.3.2. Air gap flux density produced by the rotor windings

The machine operating performance highly depends on the air gap flux density distribution generated by the rotor windings. In this dual wound generator design, concentric windings are used to produce a good approximation to a sinusoidal magnetic field in the airgap. Due to the different number of conductors in each slot, the rotor winding can generate a good approximation to the sine wave air gap flux density required if the slot conductors are themselves sinusoidally distributed. It will be appreciated that the number of slots in a wavelength is finite and, in the case of the 6-pole winding, small. However, even in this case, careful design can lead to a reasonably sinusoidal air gap field.

The rotor machine frame has 24 slots. The 2-pole winding has a pole pitch of 12 slots while the 6-pole winding has 4. The coil distributions are shown in Fig. 3-1, which shows

the 2-pole distribution (one coil set out of two) in Fig. 3-1(a) and the six-pole distribution (one coil set out of six) in Fig. 3-1(b). Each of these coil sequences is repeated with arrows showing the current directions.

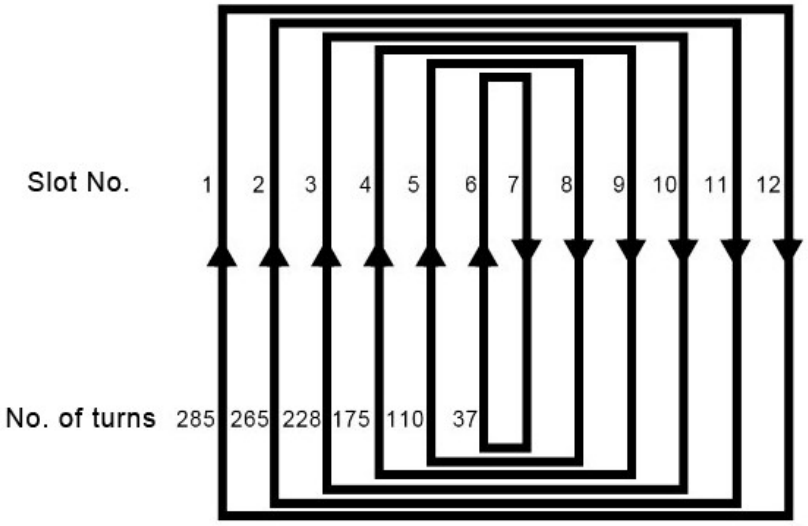

(a) 2-pole rotor winding diagram (one coil set of two)

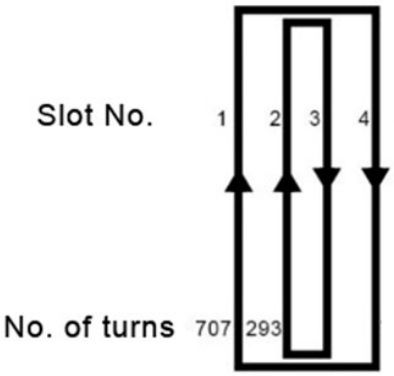

(b) 6-pole rotor winding diagram (one coil set of six)

Fig. 3-1 Rotor winding diagram

For a single general machine winding which consists of a group of coils in a series connection, the conductor distribution can be expressed as a Fourier expansion as shown below in equation (3-1).

$$n = \sum_{p=1}^{p=\infty} N_p \cos(p\theta + \varphi_p) \qquad (3-1)$$

The slot configuration can be replaced by a thin patch of current the width of the slot opening on an iron surface, then if a general slot at θ_s contains N_s conductors and has a slot opening of 2δ the conductor distribution produced by the slot is given by equation (3-2).

$$\overline{N}_p = \frac{1}{\pi}\int_{\theta_s-\delta}^{\theta_s+\delta} \frac{N_s}{2\delta}\varepsilon^{-jp\theta_s} \qquad (3-2)$$

$$\overline{N}_p = \frac{1}{\pi}\frac{sin\ p\delta}{p\delta} N_s\varepsilon^{-jp\theta_s} \qquad (3-3)$$

If the assumption of point conductors is made then

$$\frac{sin\ p\delta}{p\delta} \Rightarrow 1\ as\ \ \delta \Rightarrow 0 \qquad (3-4)$$

$$\overline{N}_p = \frac{1}{\pi} N_s\varepsilon^{-jp\theta_s} \qquad (3-5)$$

Assuming that the winding has S slots and there are N_s conductors in the general s^{th} slot, then the winding distributions are given by equation (3-6)

$$\overline{N}_p = \frac{1}{\pi}\sum_{s=1}^{s=S} N_s\varepsilon^{-jp\theta_s} = N_p\varepsilon^{j\Phi_s} \qquad (3-6)$$

The rotor windings of the dual wound machine use concentrically distributed windings as shown in Fig. 3-1. The harmonics distribution can be calculated using equation (3-6).

The magnetic field harmonic distribution of the 2-pole and 6-pole rotor windings are calculated and presented in Table 3-2 and Table 3-3 based on equation (3-6) , with the

harmonics ranged from the fundamental up to the 35th harmonic. It clearly indicates that there is no common harmonic field between the two windings, which means there is no mutual electromagnetic coupling between them due to the air-gap flux. This is important since it implies that during the transient change of the field current in one winding, there will be no back-emf induced in the other winding.

TABLE 3-2

2-POLE ROTOR MAGNETIC FIELD HARMONICS DISTRIBUTION

Harmonics	Magnetic field (T)
1	0.603
23	0.026
25	0.024

TABLE 3-3

6-POLE ROTOR MAGNETIC FIELD HARMONICS DISTRIBUTION

Harmonics	Magnetic field (T)
3	0.536
21	0.077
27	0.060

Fig. 3-2 shows the 2D FEA simulation results of the magnetic field distribution around the airgap with rotor excitation current of 1 A. The approximate sinusoidal magnetic field is the result of the combination of the square waves generated by each rotor coil. The 2-pole rotor magnetic field in the air gap (Fig. 3-2(a)) better approximates a sinusoid than the 6-pole rotor winding (Fig. 3-2(b)) because the 2-pole winding has more slots per pole. The peak magnetic field for 2-pole and 6-pole are similar, and around 0.5 T, because the total number of turns are almost the same. The ripples appearing on the magnetic flux density along the airgap are because of the slotting.

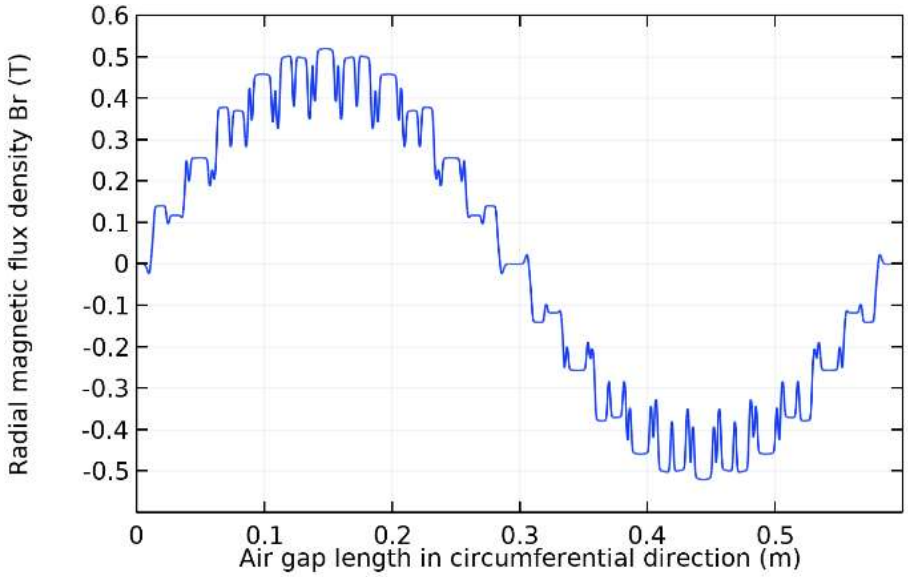

a) 2-pole rotor magnetic flux density

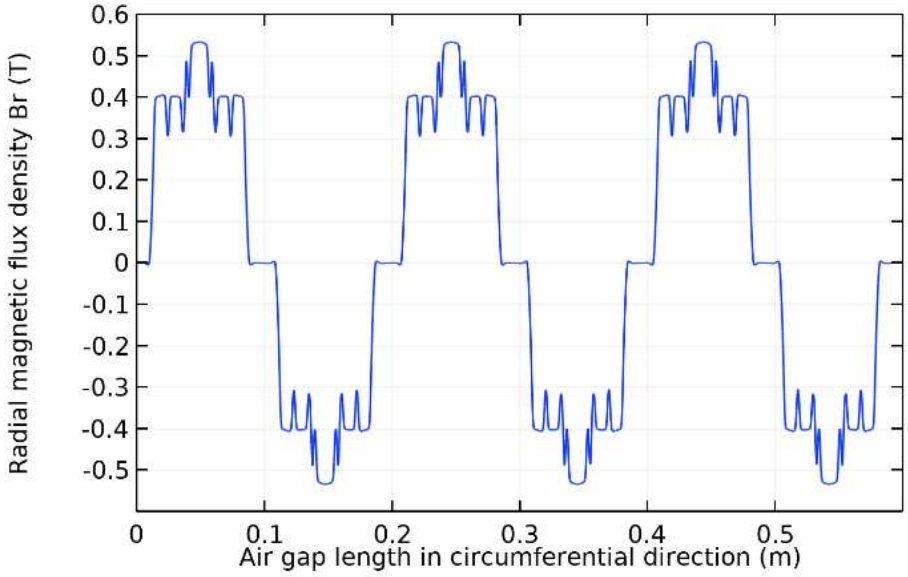

(b) 6-pole rotor magnetic flux density

Fig. 3-2 Rotor magnetic flux density distribution in the air gap

The two rotor winding distributions can start from any phase position with respect to each other. The best position can be taken as that which produces the smallest peak magnetic field when both rotor windings are excited and a simulation has been done to change the relative position between the two windings by one slot at a time. Fig. 3-3 shows the total

field at the best position when the 2-pole and 6-pole windings are aligned, i.e. where the 2-pole and the 6-pole windings start in the same slot. The following finite element modelling results presented in this paper are based on this aligned rotor winding distribution.

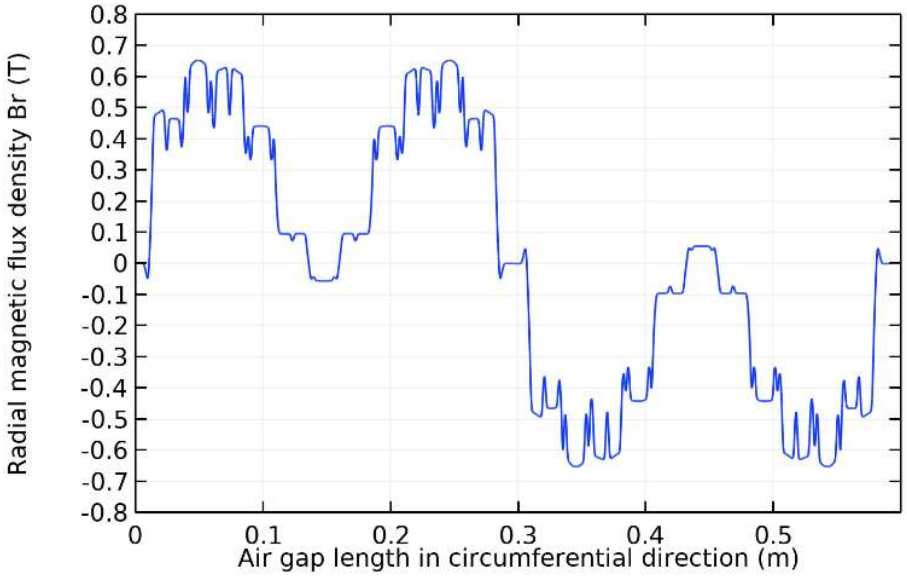

Fig. 3-3 2-pole and 6-pole magnetic flux density when it is aligned

3.4. Winding harmonics & electro-magnetic coupling

The stator windings generate induced emf from the airgap magnetic field produced by the rotor windings. The frequency of the output voltage is proportional to the pole number. The 6-pole winding produces a frequency that is 3 times higher than that produced by the 2-pole winding. The stator machine frame has 36 slots, for which the 2-pole and 6-pole stator winding distribution is as shown in Fig. 3-4. Each pole winding is distributed in two layers, where the 2-pole stator windings are above the 6-pole stator windings, thus there are four layers in total. This design aims to maximize the induced voltage and minimize the spatial harmonics from the windings whilst ensuring that there is no electromagnetic coupling between them. The 2-pole and 6-pole windings are both short-pitched: the 2-pole has a pitch angle of 120° and the 6-pole has 150°. Two terminals for

each phase (R, Y and B) are connected to a terminal panel so that the load can be connected to each phase.

Slot	1	2	3	4	5	6	7	8	9	10	11	12	13	14	15	16	17	18	19	20	21	22	23	24	25	26	27	28	29	30	31	32	33	34	35	36
2 Pole	R	R	R	R	R	R	-B	-B	-B	-B	-B	-B	Y	Y	Y	Y	Y	Y	-R	-R	-R	-R	-R	-R	B	B	B	B	B	B	-Y	-Y	-Y	-Y	-Y	-Y
	-B	-B	-B	-B	-B	-B	Y	Y	Y	Y	Y	Y	-R	-R	-R	-R	-R	-R	B	B	B	B	B	B	-Y	-Y	-Y	-Y	-Y	-Y	R	R	R	R	R	R
6 Pole	R	R	-B	-B	Y	Y	-R	-R	B	B	-Y	-Y	R	R	-B	-B	Y	Y	-R	-R	B	B	-Y	-Y	R	R	-B	-B	Y	Y	-R	-R	B	B	-Y	-Y
	R	-B	-B	Y	Y	-R	-R	B	B	-Y	-Y	R	R	-B	-B	Y	Y	-R	-R	B	B	-Y	-Y	R	R	-B	-B	Y	Y	-R	-R	B	B	-Y	-Y	R

Fig. 3-4 Stator winding distribution

It is worth noting that since the 2-pole and 6-pole fields rotate at the same speed as the rotor, the relative position between the air gap fluxes of the 2-pole and 6-pole windings, which depends on the power factor of the loads, remains fixed. The stator windings therefore use the same aligned position as the rotor windings assuming that the load power factor is the same. Further study could be done if the load power factors are known for the two loads.

The dual wound generator is designed to provide two independent power supplies. The 2-pole rotor windings can only produce 2-pole magnetic fluxes that couple with the 2-pole stator windings. The 6-pole rotor windings can only generate 6-pole magnetic flux that couples with the 6-pole stator windings. At the same time, the current in a winding can only produce fluxes corresponding to its winding harmonics. This ensures that there is no electromagnetic coupling between the 2-pole and 6-pole windings, so that there are no common winding harmonics.

Phase 'R' of a general machine winding which consists of a group of coils each of N turns connected in series gives a conductor distribution for the p^{th} harmonic of:

$$\overline{N}_{pR} = \frac{1}{\pi}\sum_{s=1}^{s=S} N_{sR} e^{-jp\theta_{sR}} = N_{pR} e^{-jp\theta_{pR}} \qquad (3-7)$$

Similarly, the conductor distribution for the 'B' phase is shown in equation (3-8) and 'Y'

phase is shown in equation (3-9).

$$\overline{N}_{pB} = N_{pB} e^{-jp\theta_{pB}} \quad (3-8)$$

$$\overline{N}_{pY} = N_{pY} e^{-jp\theta_{pY}} \quad (3-9)$$

The three-phase stator windings of the dual wound machine use the double layer distributed winding as shown in Fig. 3-4. The top layer formed by the leading coil sides has 6, π/3 length phase bands. The bottom layer formed by the second coil sides is reverse repeat of the top layer displaced by α π. The angle between the m coil sides in a phase band for the general case is π/3m. The conductor distribution on the p^{th} harmonic for the R phase top layer taking both phase bands is shown in equation (3-10).

$$\overline{N}_{pRT} = \frac{N}{\pi} \sum_{k=0}^{k=m-1} e^{-jp\frac{k\pi}{3m}} - e^{-jp\left(\frac{k\pi}{3m}+1\right)} \quad (3-10)$$

where m is the number of coils per phase band.

If p is an even number, then:

$$\overline{N}_{pRT} = 0 \quad (3-11)$$

If p is an odd number, then:

$$\overline{N}_{pRT} = 0 \quad (3-11)$$

If p is an odd number, then:

$$\overline{N}_{pRT} = \frac{2N}{\pi} \sum_{k=0}^{k=m-1} e^{-jp\frac{k\pi}{3m}} \quad (3-12)$$

Hence the conductor distribution can be written as equation (3-13).

$$\overline{N}_{pRT} = \frac{2N}{\pi}\left[\frac{\left(1-e^{-jp\frac{\pi}{3}}\right)}{\left(1-e^{-jp\frac{\pi}{3m}}\right)}\right] = \frac{2N}{\pi}\left[e^{-jp\frac{\pi(m-1)}{6m}}\right]\left[\frac{sin\{\frac{p\pi}{6}\}}{sin(\frac{p\pi}{6m})}\right] \quad (3-13)$$

Since the bottom layer is a reverse repeat of the top displaced by απ (α is the coil short-pitched angle) the R phase winding conductor distribution is as shown in equation (3-14).

$$\overline{N}_{pR} = \overline{N}_{pRT}\left(1-e^{-jp\alpha}\right) = 2\overline{N}_{pRT}\, je^{\frac{-jp\alpha}{2}} sin\left(\frac{\alpha p}{2}\right) \quad (3-14)$$

hence

$$\left|N_{pR}\right| = \frac{4N}{\pi}\left[\frac{sin\{\frac{p\pi}{6}\}}{sin(\frac{p\pi}{6m})}\right]\left[sin\left(\frac{\alpha p}{2}\right)\right] \quad (3-15)$$

In this formula, m times the expression $\left[\frac{sin\{p\pi/6\}}{sin(p\pi/6m)}\right]$ is called the distribution factor and the expression $[sin(\alpha p/2)]$ is the pitch or chording factor. The conductor distribution for the red phase can be written as

$$\overline{N}_{pR} = N_p \quad (3-16)$$

Then since the winding is symmetrical the conductor distribution for the blue phase is as shown in equation (3-17) and the yellow phase is as shown in equation (3-18).

$$\overline{N}_{pB} = N_p e^{-\frac{2\pi p}{3}} \quad (3-17)$$

$$\overline{N}_{pY} = N_p e^{\frac{2\pi p}{3}} \quad (3-18)$$

The winding distributions of a 3-phase winding may be represented by positive, negative and zero phase sequence sets each having three balanced windings. For a balance current input, the zero-sequence set can be ignored. The sets for the balanced double layer winding are given by:

The positive sequence $n_{fp} = N_p$ if p =1, 7, 13 … and is zero for all other odd values.

The negative sequence $n_{np} = N_p$ if p =5, 11,17 … and is zero for all other odd values.

The winding harmonic distributions of the 2-pole and 6-pole stator windings are shown in Table 3-4 and Table 3-5. The winding harmonics are separately calculated into three components: the positive phase sequence (PPS), negative phase sequence (NPS) and zero phase sequence (ZPS). When the windings are supplied by 3-phase currents, the three phase sequences can correspondingly produce forward, backward and stationary fields. Table 3-4 and Table 3-5 show that there is no common harmonic term appearing between the 2-pole and 6-pole stator windings, which verifies that there is no electromagnetic coupling between them due to the airgap field. From the results shown in Table 3-2 and Table 3-5, there is also no common harmonic component between the 2-pole rotor winding and 6-pole stator winding. Similarly, examining Table 3-3 and Table 3-4 it is apparent that the 6-pole rotor windings have no mutual harmonics with the 2-pole stator windings. The harmonics analysis therefore shows that the rotor windings only couple with their corresponding stator winding.

TABLE 3-4

2-POLE STATOR WINDING HARMONICS DISTRIBUTION

Harmonics	PPS	NPS	ZPS
1	0.83	0.00	0.00
5	0.00	0.17	0.00
7	0.13	0.00	0.00
11	0.00	0.09	0.00
13	0.08	0.00	0.00
17	0.00	0.07	0.00
19	0.07	0.00	0.00
23	0.00	0.08	0.00
25	0.09	0.00	0.00
29	0.00	0.13	0.00
31	0.17	0.00	0.00
35	0.00	0.83	0.00

TABLE 3-5

6-POLE STATOR WINDING HARMONICS DISTRIBUTION

Harmonics	PPS	NPS	ZPS
3	0.93	0.00	0.00
9	0.00	0.00	0.50
15	0.00	0.07	0.00
21	0.07	0.00	0.00
27	0.00	0.00	0.50
33	0.00	0.93	0.00

3.5. Modelling of performance

3.5.1. Rotor excitation under no-load condition

A non-linear 2D finite element simulation using COMSOL has been performed to verify the results presented in Section III for both the airgap fluxes considered by the harmonic analysis and the slot leakage fluxes. It should be noted that the flux density levels in the stator and rotor cores and teeth are in the linear range (no saturation). When the 2-pole rotor winding is excited and the 6-pole rotor winding is open-circuit, the magnetic flux density and the induced voltage are shown in Fig. 3-5 and Fig. 3-6. The magnetic flux density and the magnetic vector potential distributions on the cross-sectional plane are shown in Fig. 3-5. The induced voltage generated by the 2-pole stator winding is shown in Fig. 3-6. The 6-pole stator winding has zero induced voltage.

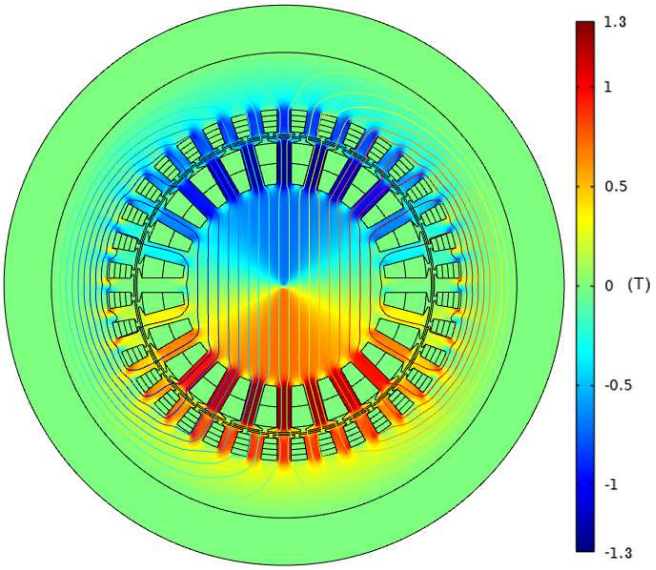

Fig. 3-5 2-pole magnetic field distribution

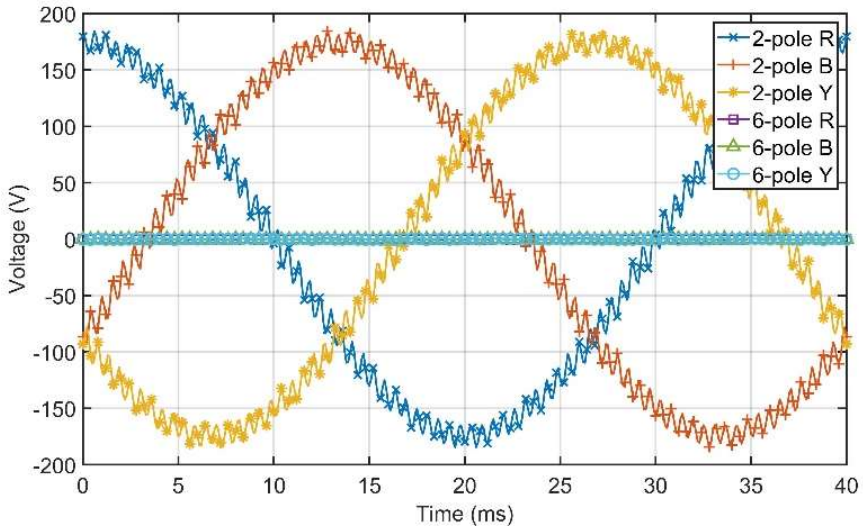

Fig. 3-6 2-pole and 6-pole stator voltage with 2-pole excitation

Fig. 3-7 and Fig. 3-8 present the condition when only the 6-pole rotor winding is excited and the 2-pole rotor winding is open-circuit. Fig. 3-7 presents the 6-pole magnetic flux and magnetic vector potential distributions. It is clearly shown in Fig. 3-8 that 2-pole winding has no induced emf, while the 6-pole winding produces sinusoidal induced emf only when 6-pole rotor winding is excited.

Fig. 3-9 and Fig. 3-10 present the condition when both the 2-pole and 6-pole rotor

windings are excited. Fig. 3-10 presents the 2-pole and 6-pole stator induced voltages, and shows that the 2-pole and 6-pole voltages are independently generated without influence from the other rotor winding. It is to be concluded that the excitation of 6-pole rotor winding has a negligible impact on 2-pole stator winding, and vice versa.

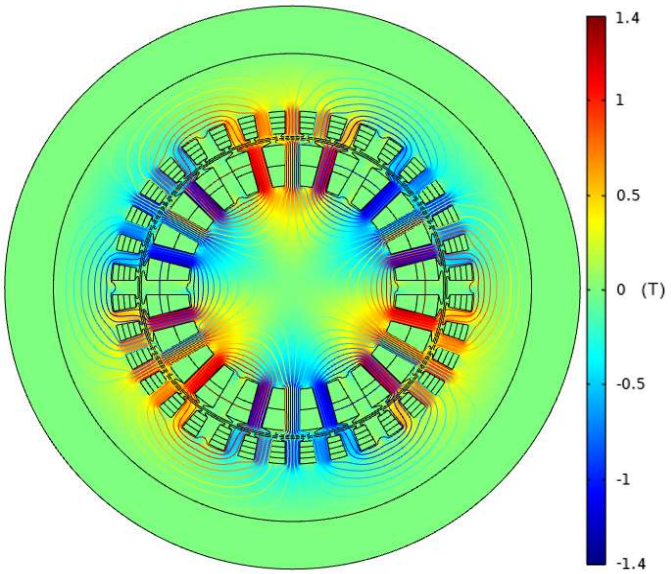

Fig. 3-7 6-pole magnetic field distribution

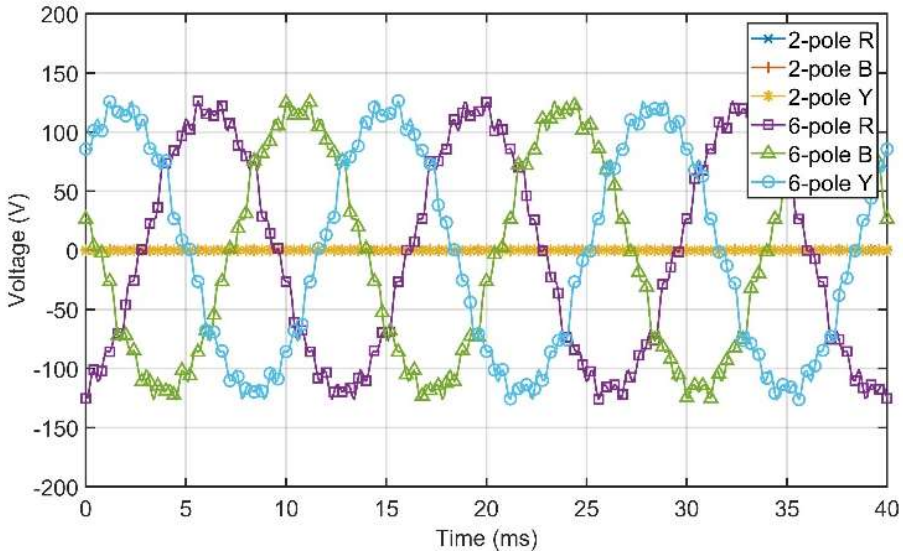

Fig. 3-8 2-pole and 6-pole stator voltage with 6-pole excitation

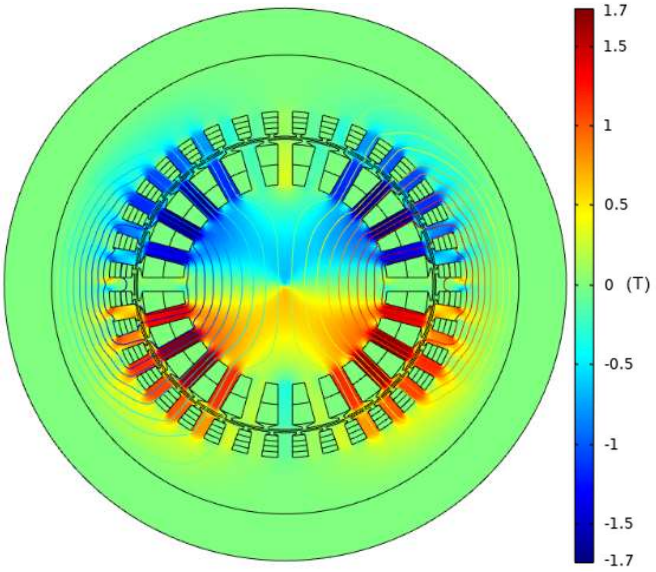

Fig. 3-9 2-pole and 6-pole magnetic field distribution

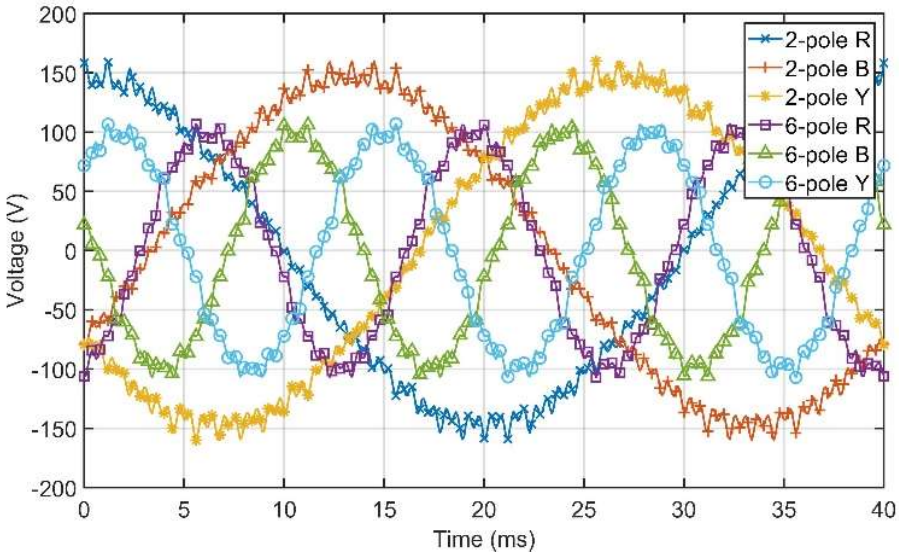

Fig. 3-10 2-pole and 6-pole stator voltage with 2-pole and 6-pole excitation

3.5.2.Simulation performance with resistive load

To investigate the performance under load and further demonstrate the fully decoupled winding properties, a simulation of the dual wound machine with resistive load condition has been studied. This simulation aims to verify that the 2-pole and 6-pole windings operate independently when both 2-pole and 6-pole rotor windings are energized. The power rating of the 2-pole generator is designed to be 560 W at 1500 rpm. The peak

phase voltage and current are assumed to be 150 V and 2.5 A. The load resistance that connected for each phase of the 2-pole generator is therefore 60 Ω. For the 6-pole generator, the power rating is designed to be 220 W. The peak phase voltage and current are assumed to be 106 V and 1.4 A, so that the load resistance that connected for each phase of the 6-pole generator is 80 Ω. Fig. 3-11 presents the phase voltage and current for both windings when the 2-pole stator winding is supplying a 60 Ω resistive load and 6-pole stator winding is open circuit. It can be observed that the 2-pole winding operates at rated condition while 6-pole winding produces induced voltage but has no current. The voltage and current for the 2-pole stator winding in Fig. 3-11 do not exhibit ripples because the 2-pole generator is loaded and the winding is connected to the circuit, where the winding acts as a filter inductor.

Fig. 3-12 shows the equivalent condition with the 2-pole winding in open circuit and the 6-pole winding with a resistive load of 80 Ω. Considering the results of Fig. 3-11 and Fig. 3-12 it is confirmed that the 2-pole and 6-pole windings can operate independently when either one is operating at its rated condition.

The case where both sets of windings are operating simultaneously at their respective rated loads is shown in Fig. 3-13. The stator voltages and currents with dual load are similar to the results with the single load conditions (Fig. 3-11, Fig. 3-12) which again shows that the 2-pole generator does not affect 6-pole generator and vice versa.

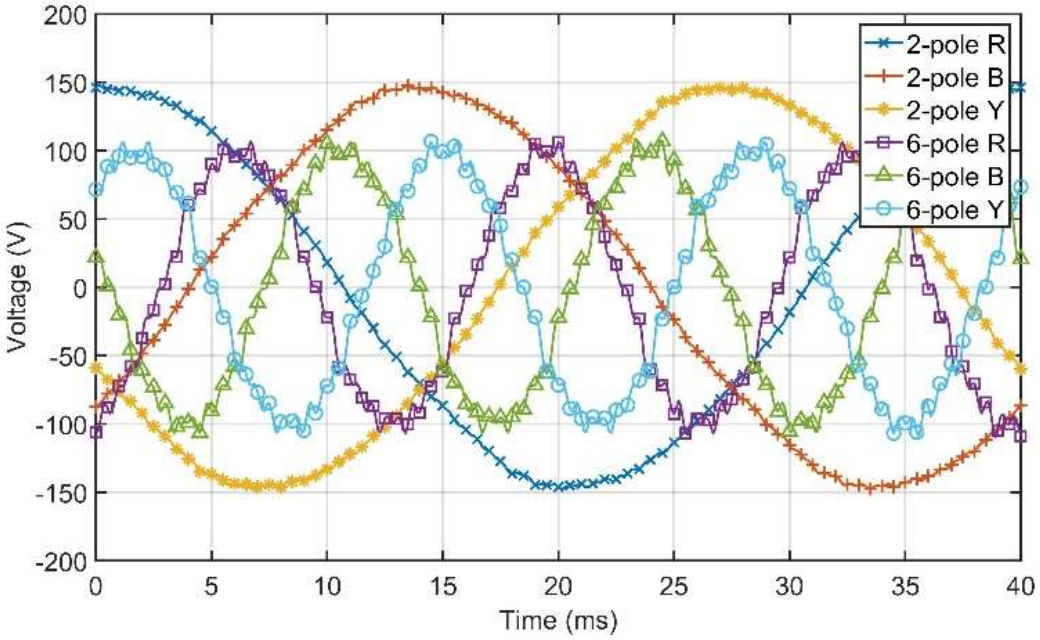

(a) 2-pole and 6-pole stator phase voltage with 2-pole loaded

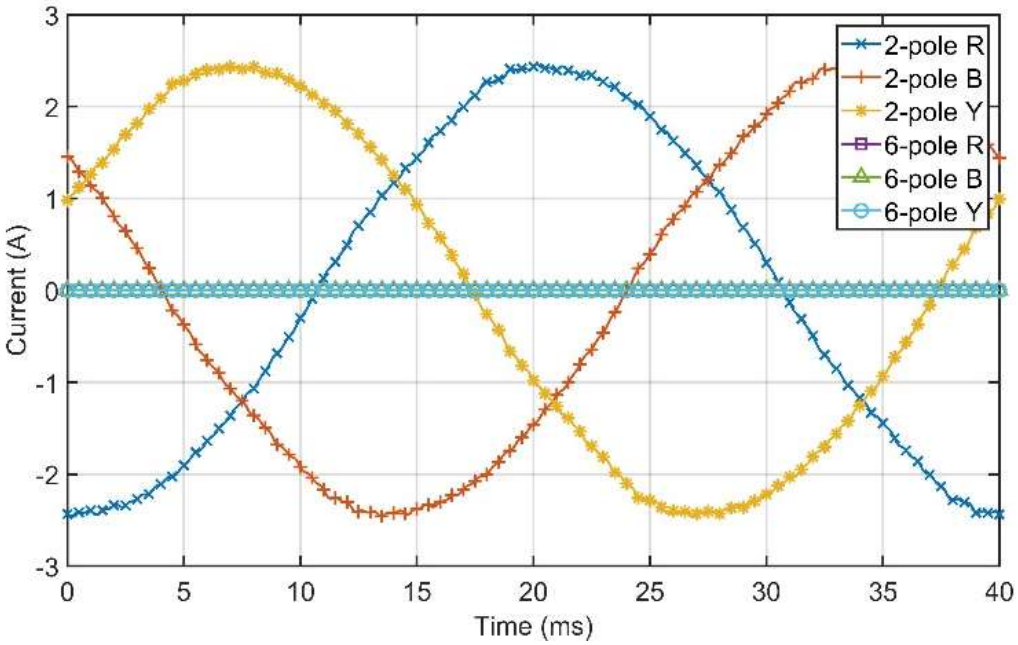

(b) 2-pole and 6-pole stator terminal current with 2-pole loaded

Fig. 3-11 Phase voltage & current with 2-pole loaded

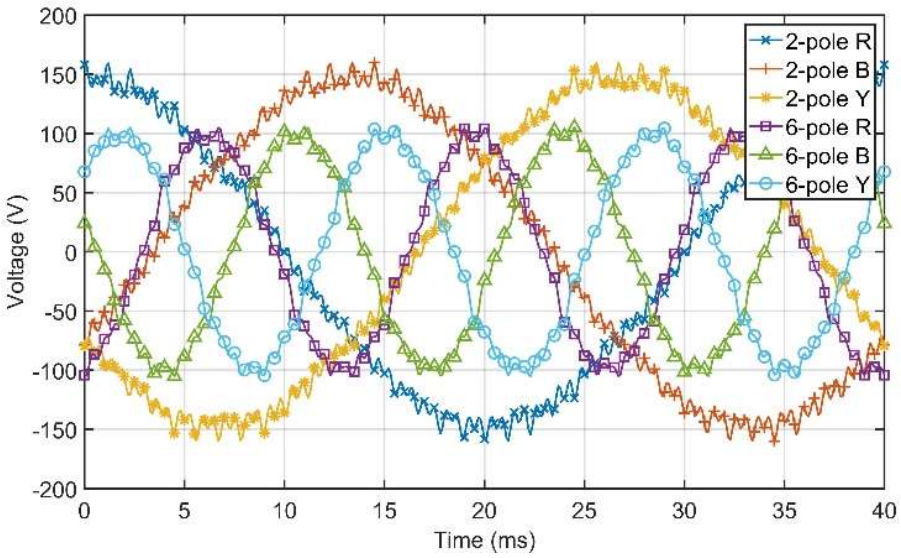

(a) 2-pole and 6-pole stator terminal voltage with 6-pole loaded

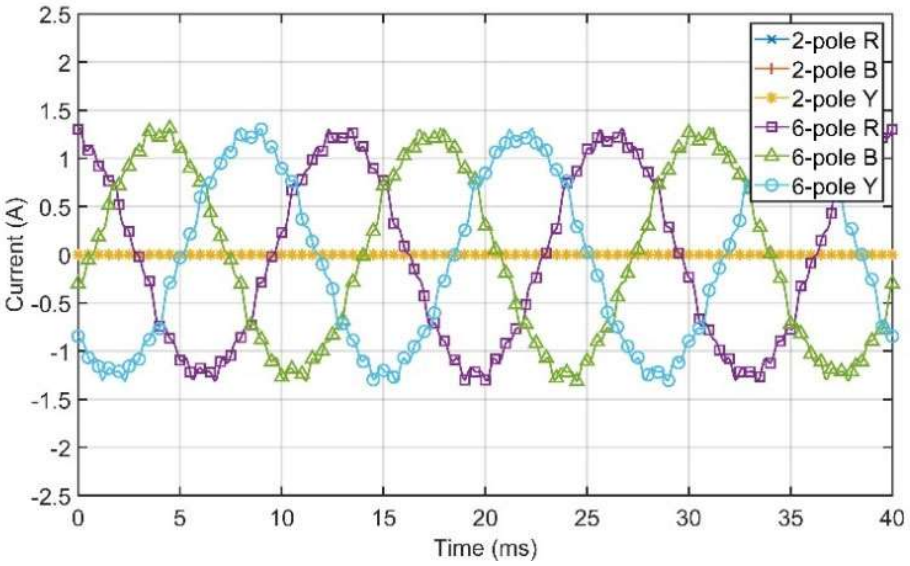

(b) 2-pole and 6-pole stator terminal current with 6-pole loaded

Fig. 3-12 Phase voltage & current with 6-pole loaded

This section shows the simulation results when either and both windings are loaded at rated operation conditions, and confirms that they are fully decoupled due to both the airgap and slot leakage fields. The peak voltage of the 2-pole winding is 146 V and the peak current is 2.5 A, which means the power is 547.5 W at 1500 rpm. The peak voltage

of the 6-pole winding is 105 V and the peak current is 1.4 A, which shows the power is 220.5 W.

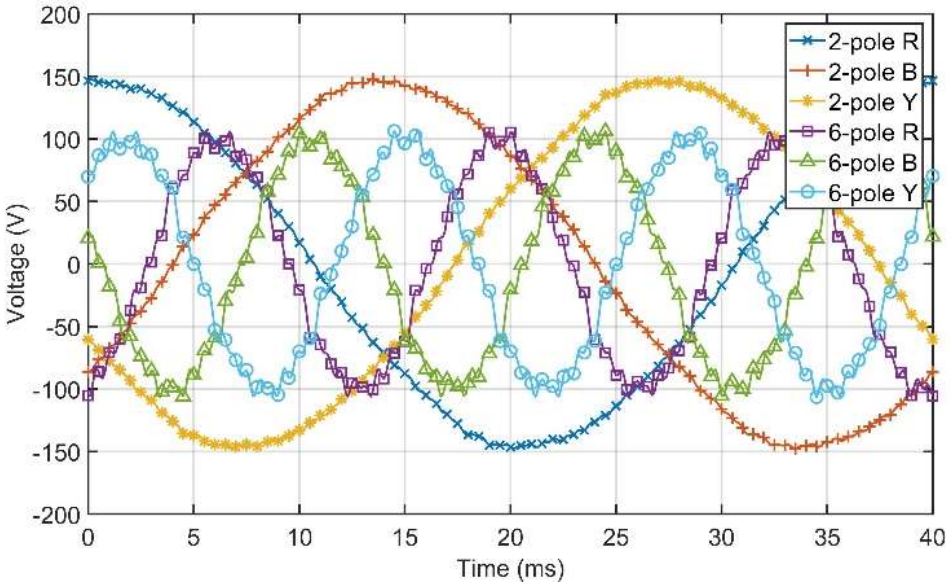

(a) 2-pole and 6-pole stator terminal voltage with 2-pole and 6-pole loaded

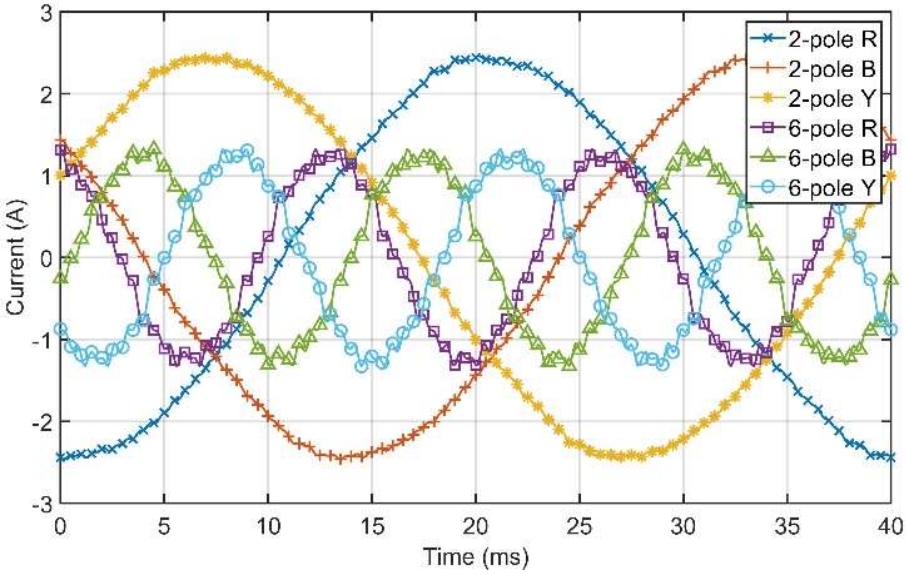

(b) 2-pole and 6-pole stator terminal current with 2-pole and 6-pole loaded

Fig. 3-13 Phase voltage & current with 2-pole and 6-pole loaded

3.6. Experimental tests

3.6.1. Test platform

In order to further validate the concept, the proposed winding scheme is implemented and tested to confirm agreement between experimental results and simulation. The electric connection diagram of the dual wound generator is shown in Fig. 3-14. Fig. 3-15 shows a schematic of the experimental test platform. The dual wound generator winding process is recorded and shown in Fig. 16. It shows the slot arrangements and end-winding distributions. Large end-winding areas may cause potential magnetically decoupling problems and mechanical vibration problems. Fig. 3-17 shows the experimental test platform at the University of Bath (U.K.), which is composed of the dual wound generator prototype, a DC motor, resistive loads, power sources and data acquisition equipment. The DC motor is used as the prime mover, representing the prime mover in the electric ship application. The DC motor is rated at 5 kW and has a rated rotating speed of 3000 rpm. The DC motor has a rated field voltage of 200 V, with the field current of 1.1 A. The maximum armature current is 36.5 A. A LAB/SMS630 DC power supply is used to provide field current to the DC motor and a LAB/SMS5300 DC power supply to provide armature current. The torque of the DC motor can be controlled by changing the armature current, which is adjusted so as to achieve the target speed of up to 1500 rpm, monitored by a tachometer. On the generator side, the 2-pole and 6-pole rotor windings are supplied by EA-PS 8360-15 and LAB-SMP11200 DC power supplies to provide a one amp excitation current for the rotor windings. The two outputs of the dual wound generator are separately connected with their rated three-phase resistive loads. An oscilloscope is used to monitor and record the output voltage and current.

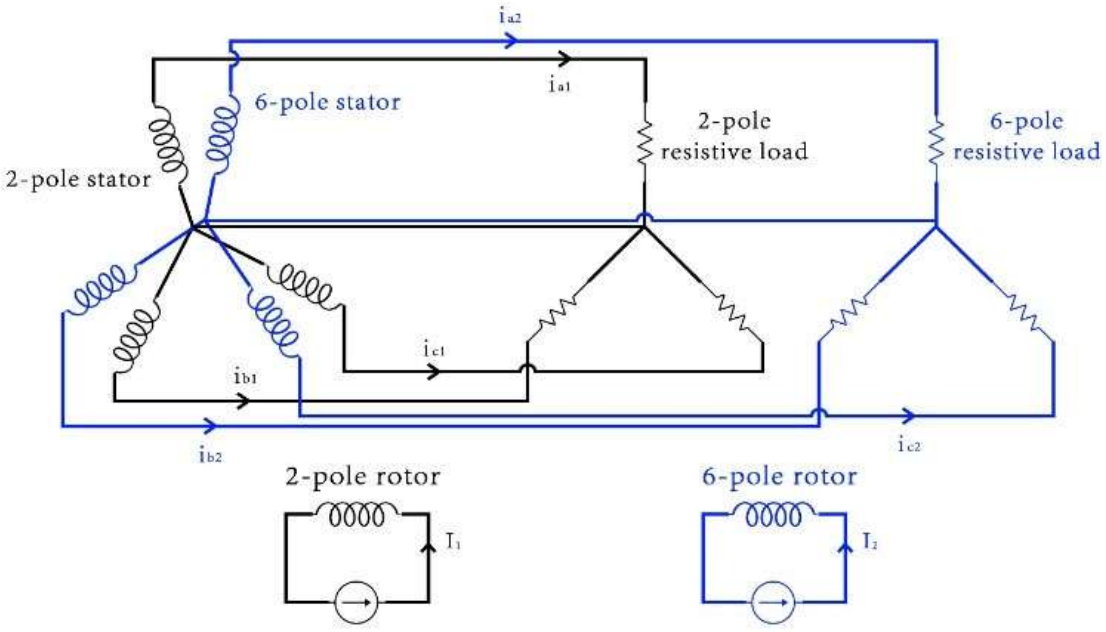

Fig. 3-14 Electric connection of dual wound generator

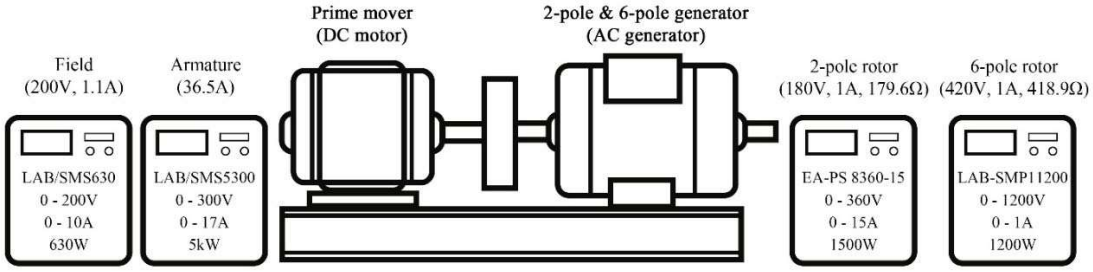

Fig. 3-15 Schematic of experimental test platform

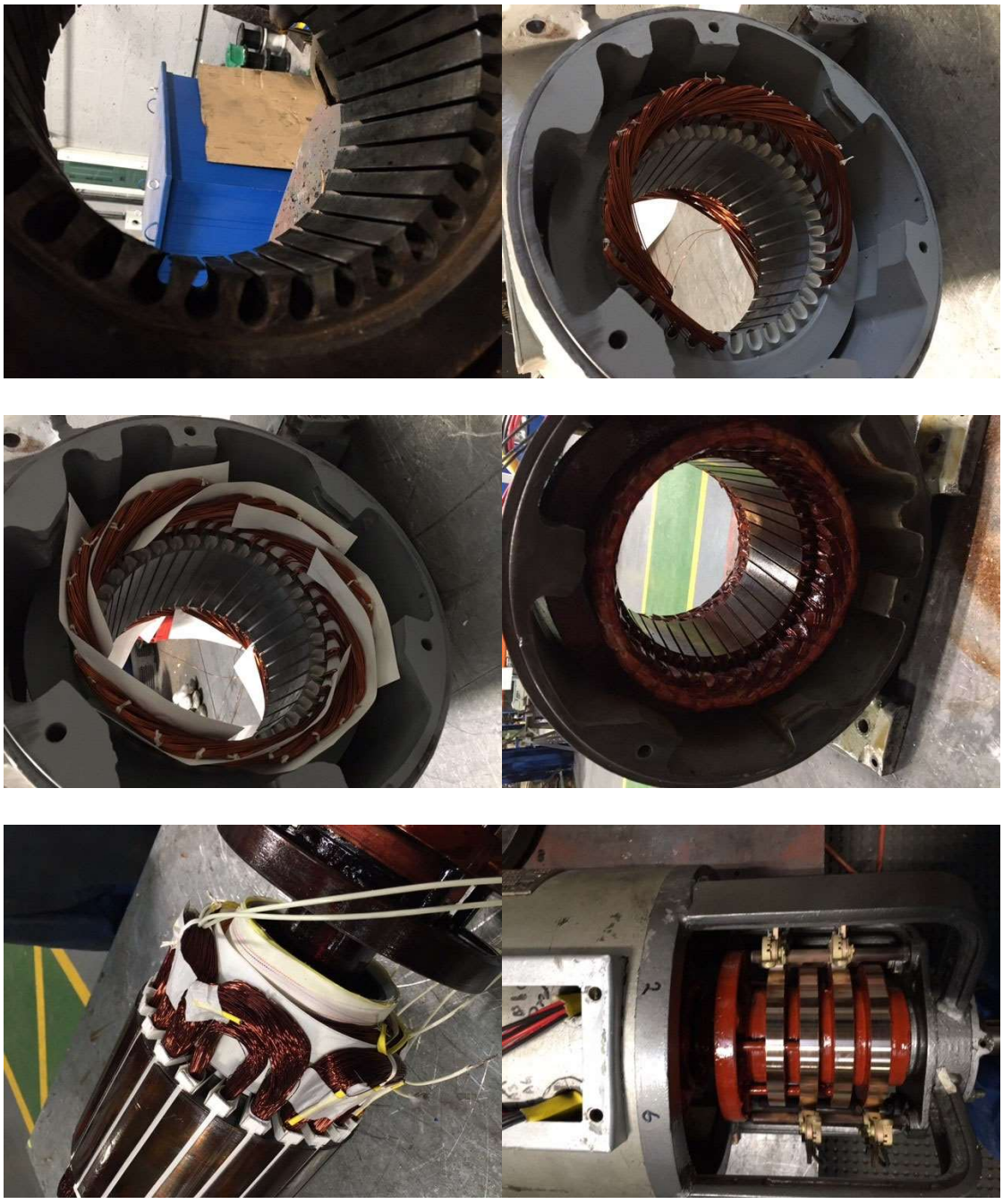

Fig. 3-16 Dual wound generator winding process

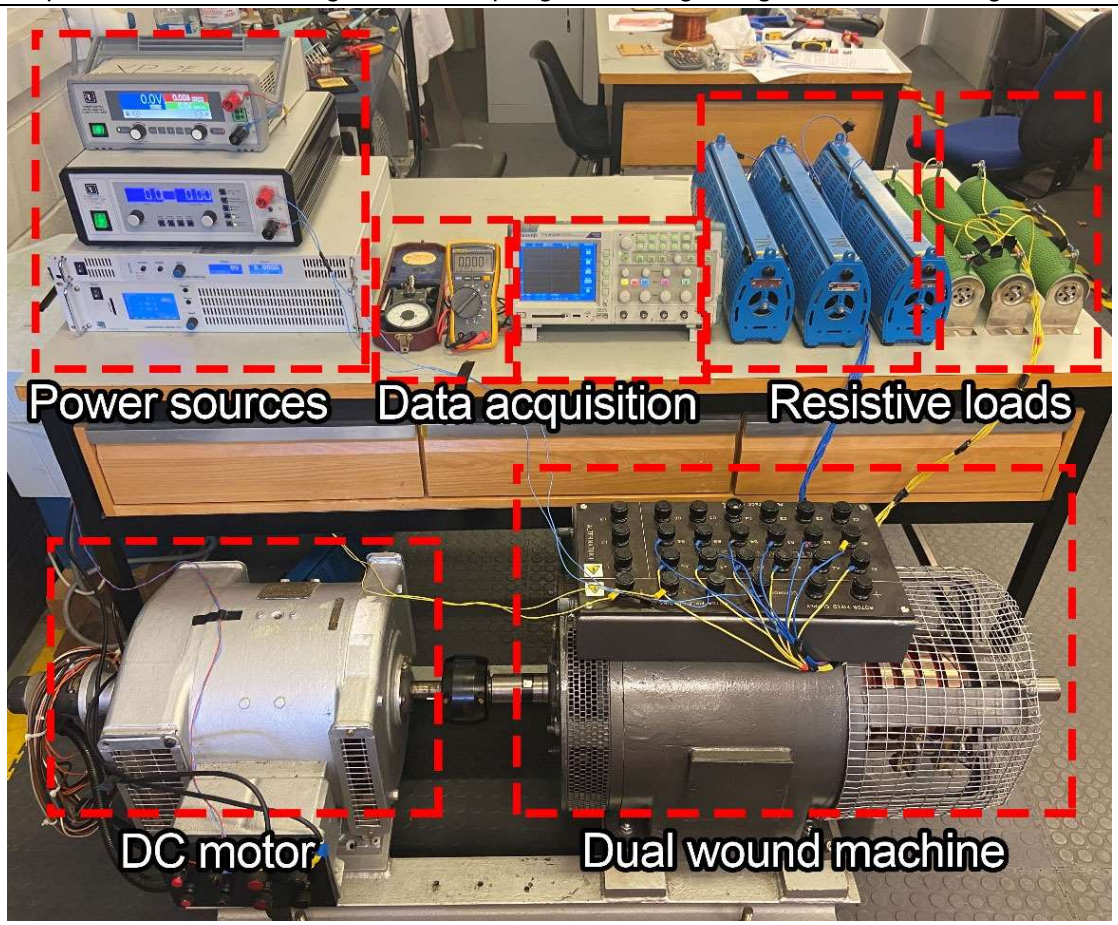

Fig. 3-17 Experimental test platform

3.6.2. Experimental performance with rotor excitation under no-load condition

In order to investigate whether one rotor winding would couple with the other stator winding the dual wound generator prototype is tested at no-load condition when only the 2-pole winding is excited, only the 6-pole winding is excited and when both rotor windings are excited.

Fig. 3-18 shows the stator terminal voltage of 2-pole winding and 6 pole-winding when only the 2-pole rotor winding is excited. The 2-pole stator winding generates a peak voltage of 170 V and the voltage of the 6-pole stator winding is negligible, though not exactly zero. It is worth mentioning that the end-winding resistance and reactance are

not considered in the 2D finite element modelling as it requires a 3D model. However, the experimental test includes end-winding effects for the first time for this class of machine, and the small induced voltage on the 6-pole stator winding may be due to this coupling.

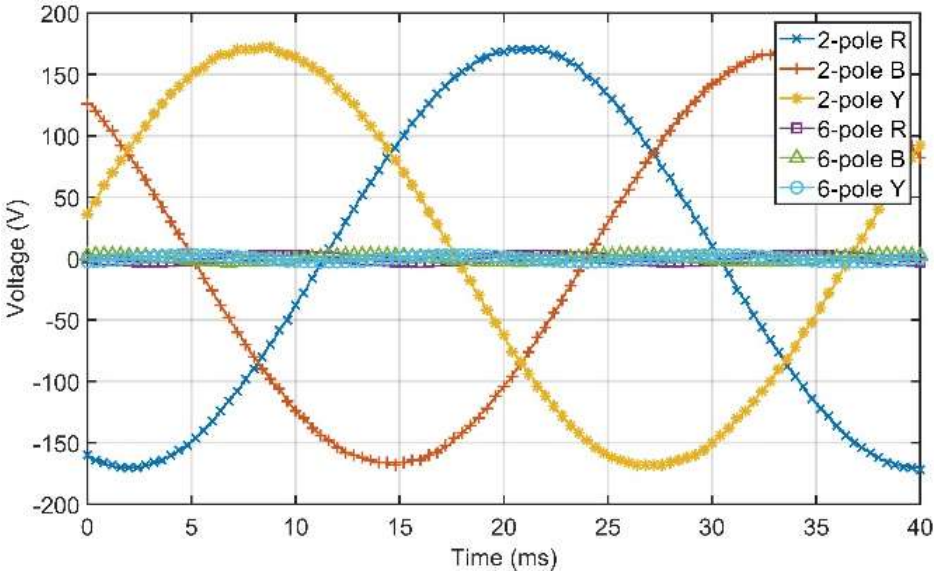

Fig. 3-18 2-pole and 6-pole stator voltage with 2-pole excitation

Fig. 3-19 shows the stator terminal voltage with only the 6-pole rotor winding excited. The 6-pole stator winding generates a peak voltage of 132 V and the voltage of 2-pole stator winding is negligible.

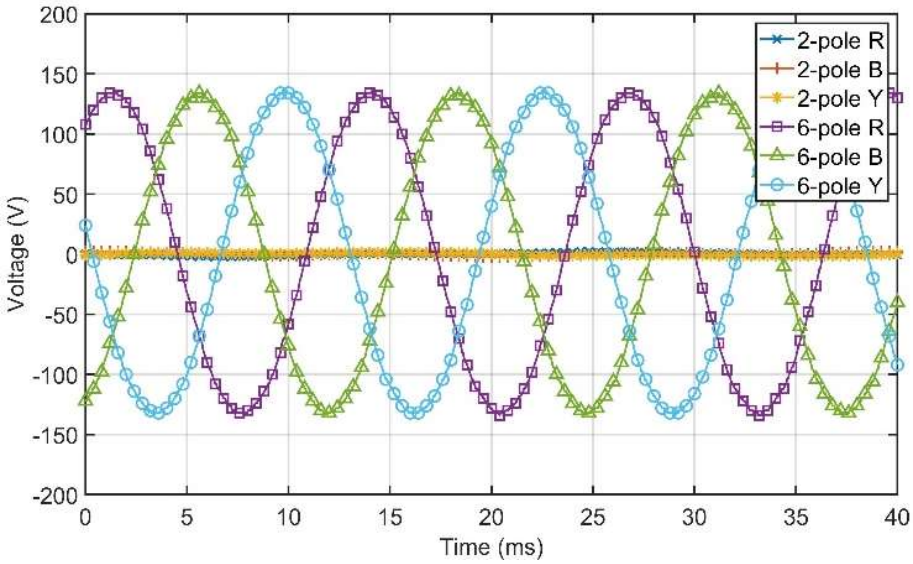

Fig. 3-19 2-pole and 6-pole stator voltage with 6-pole excitation

When both 2-pole and 6-pole rotor windings are excited as shown in Fig. 3-20, the 2-pole winding has a peak induced voltage of 154 V and 6-pole winding has a peak voltage of 112 V. The voltage is slightly reduced compared with the results shown in Figs. 3-18 and 3-19, which shows 3.7% reduction for 2-pole voltage and 18.8% for 2-pole voltage. This can be due to the saturation of the rotor and stator electrical steel, especially near the slot areas. This no-load experiment also indicates that the three-phase outputs are balanced without the influence of the other winding.

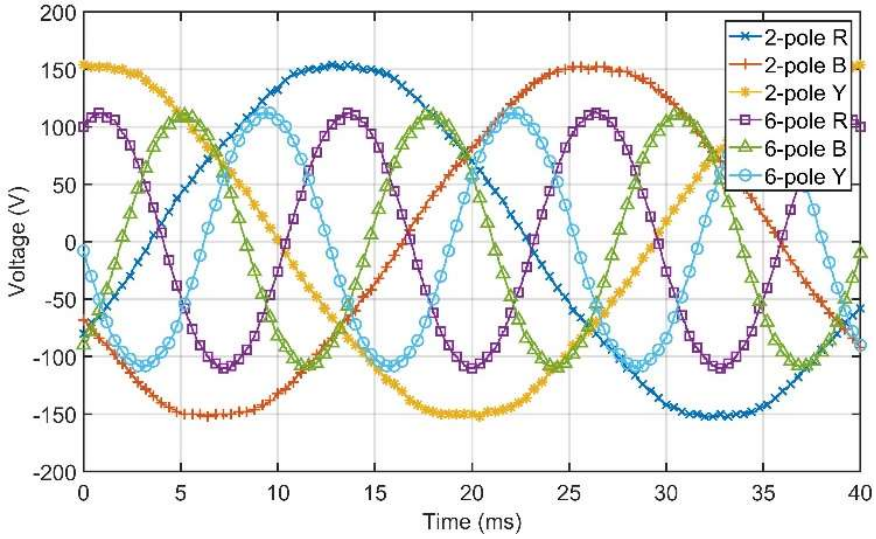

Fig. 3-20 2-pole and 6-pole stator voltage with 2-pole and 6-pole excitation

3.6.3. Experimental performance with resistive load

In order to confirm the performance of the system when either one or both windings are loaded, and whether each will affect the operation of the other, a resistive load of 60 Ω is used for 2-pole generator and a resistive load of 80 Ω for the 6-pole generator, as in the simulations. The three scenarios as in Section IV-B are tested: only the 2-pole generator loaded, only the 6-pole generator loaded and both 2-pole and 6-pole generators are loaded.

Fig. 3-21 and Fig. 3-22 show the condition when the 2-pole generator is connected to 60 Ω resistive load and the 6-pole stator winding is in open circuit. The 2-pole generator generates peak voltage of 144 V and peak current of 2.32 A, which is 501.1 W at 1500 rpm. Fig. 3-23 and Fig. 3-24 present the generator voltage when the 2-pole generator is open circuit and the 6-pole generator is connected to 80 Ω resistive load. The 6-pole generator generates peak voltage of 106 V and peak current of 1.28 A, which is 203.5 W at 1500 rpm. Fig. 3-25 and Fig. 3-26 show the results with the 2-pole generator connected to 60 Ω resistive load and the 6-pole generator connected to 80 Ω resistive load. The results show that the 2-pole and 6-pole generators can generate individual outputs with the resistive load without any influence from the other generator, demonstrating that they are electromagnetically decoupled.

The comparison between the simulation and experimental results are shown in Table 3-6 for 2-pole stator voltage and Table 3-7 for 6-pole stator voltage. The 2-pole and 6-pole simulation results match well with the experimental results. This again demonstrates that the 2-pole and 6-pole generator is substantially electromagnetically decoupled and therefore the change of load for one generator does not impact the operation of the other generator. The small changes can be due to end-winding coupling or due to the saturation effect.

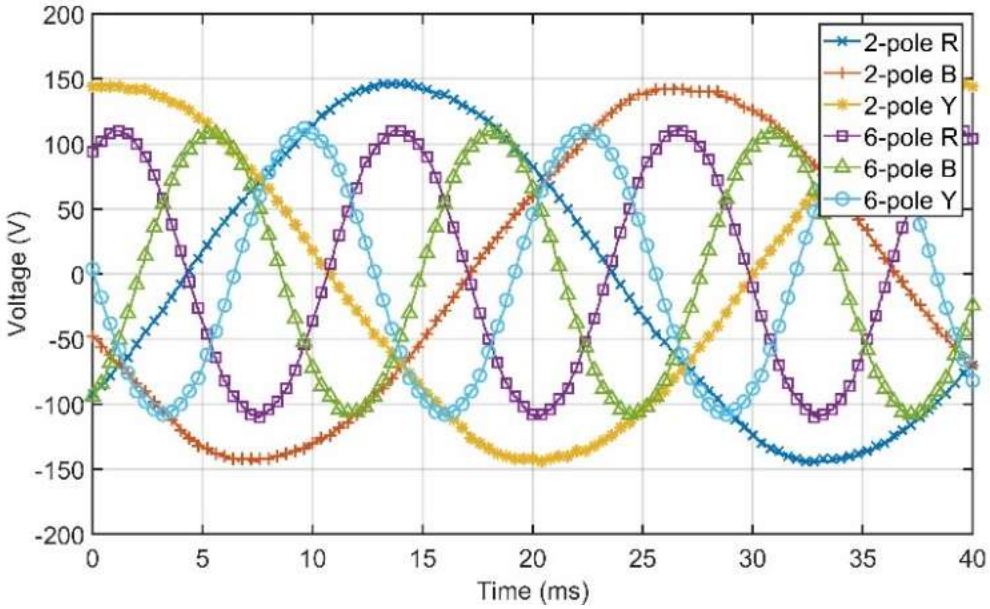

Fig. 3-21 2-pole and 6-pole stator voltage with 2-pole loaded and 6-pole open circuit

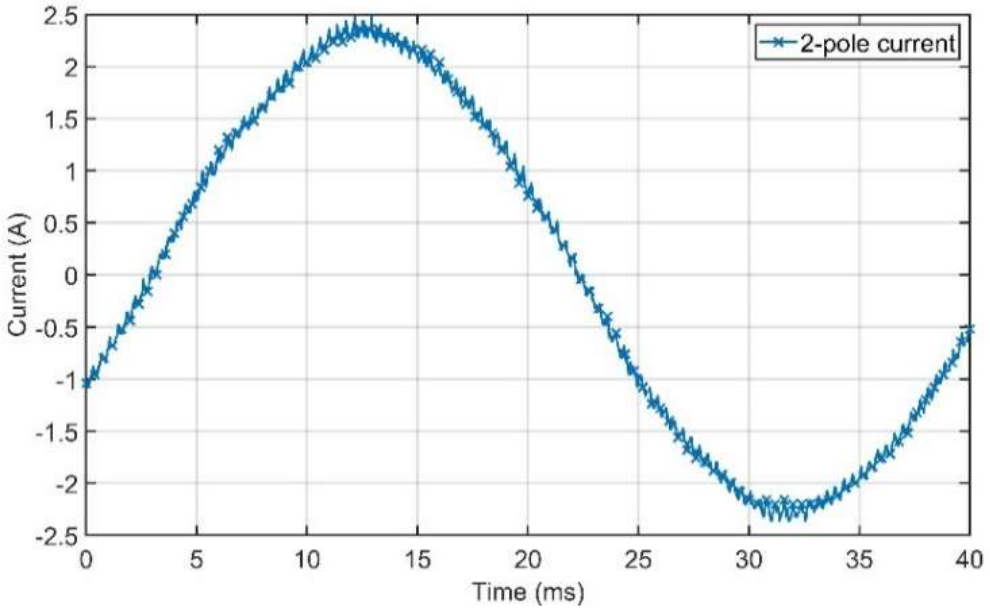

Fig. 3-22 2-pole stator current with 2-pole loaded and 6-pole open circuit

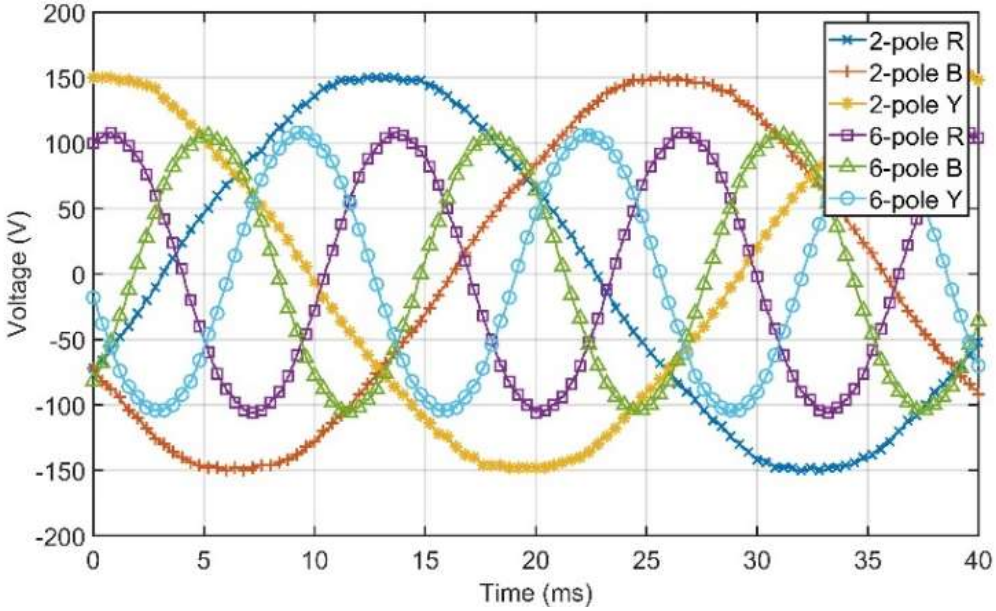

Fig. 3-23 2-pole and 6-pole stator voltage with 2-pole open-circuit and 6-pole loaded

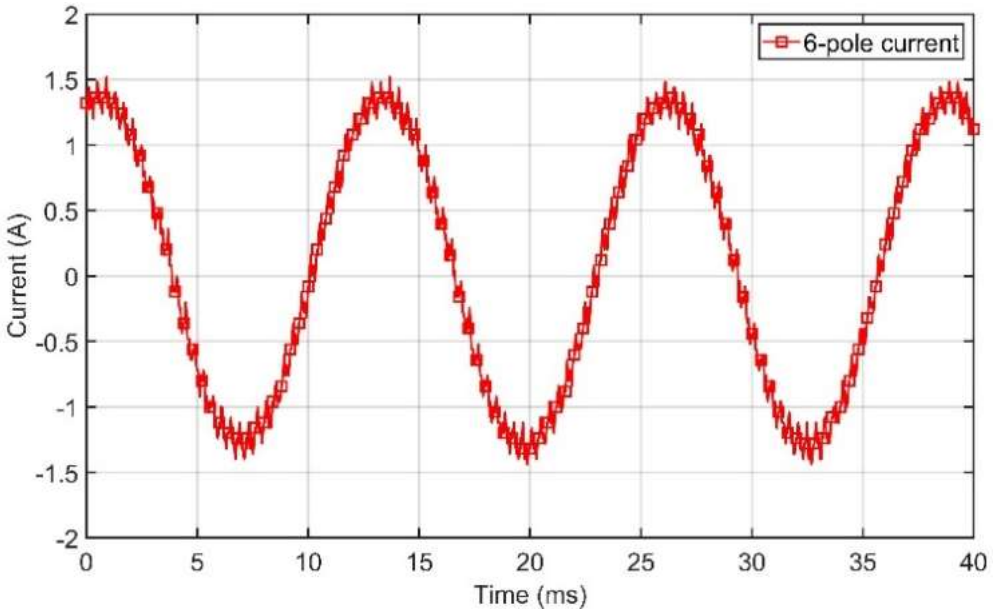

Fig. 3-24 6-pole stator current with 2-pole open-circuit and 6-pole loaded

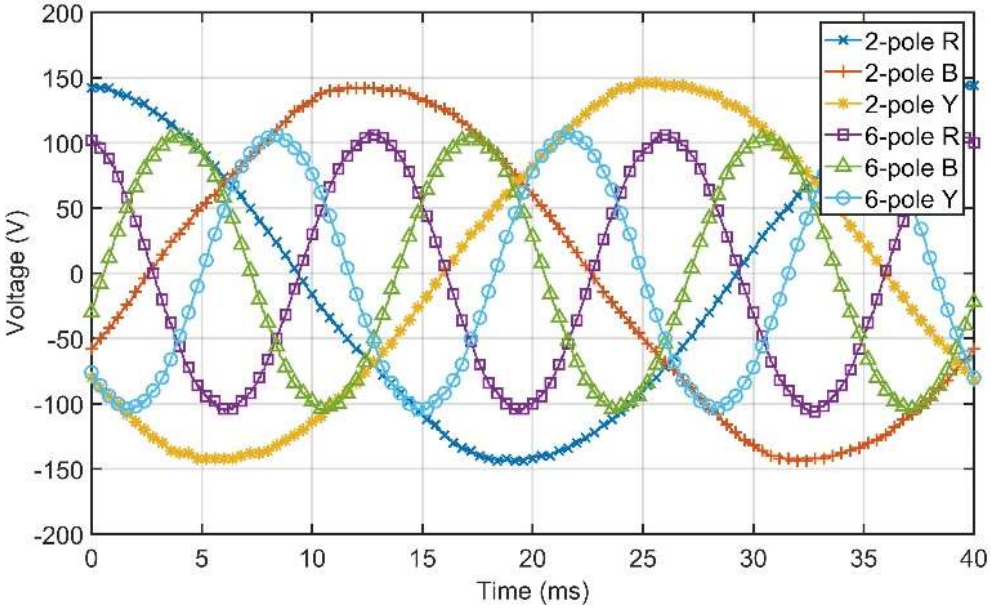

Fig. 3-25 2-pole and 6-pole stator voltage with 2-pole and 6-pole loaded

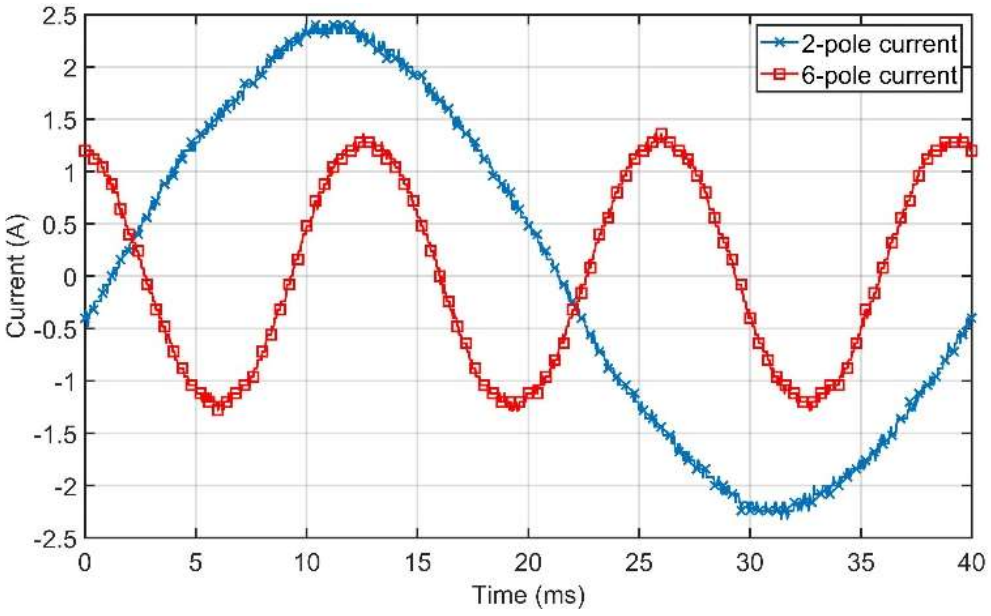

Fig. 3-26 2-pole and 6-pole stator current with 2-pole and 6-pole loaded

TABLE 3-6

SUMMARY OF 2-POLE STATOR VOLTAGE UNDER DIFFERENT CONDITIONS

Operating condition	Simulation (V)	Experimental (V)	Difference $(\frac{Simulation-Experimental}{Experimental})$
2-pole rotor winding excited	175	170	2.94%
Both rotor windings excited open circuit	150	154	2.59%
2-pole winding loaded 6-pole open-circuit	146	146	0.00%
6-pole winding loaded 2-pole open-circuit	147	148	0.67%
Both stator windings loaded	146	144	1.39%

TABLE 3-7

SUMMARY OF 6-POLE STATOR VOLTAGE UNDER DIFFERENT CONDITIONS

Operating condition	Simulation (V)	Experimental (V)	Difference $(\frac{Simulation-Experimental}{Experimental})$
6-pole rotor winding excited	125	132	-5.30%
Both rotor windings excited. Open circuit.	107	112	-1.82%
2-pole winding loaded 6-pole open-circuit	106	108	1.89%
6-pole winding loaded 2-pole open-circuit	105	108	2.88%
Both stator windings loaded	105	106	2.86%

3.7. System aspects and discussion

There are several options for integrating the dual wound generator into an overall electric ship IFEP power system. The choices considered for this paper are as follows.

The system must supply high power to the propulsion and low power to the ships services, with a power ratio between 5 and 10 to 1. The total power required is of the order of tens of Mega Watts and in a warship application will need to be supplied by a gas turbine at a speed of the order of 3600 rpm. It will therefore be convenient to use the 2-pole output

to supply the high-power propulsion at the usual frequency of 60 Hz. The supply for the ship services will then be at 180 Hz from the 6-pole winding.

However, the ship services supply will need to be either 60 Hz or any frequency if the supply is feeding power electronics conditioning equipment. The choice is then between converting the supply immediately at the generator output to 60 Hz via an electronic converter to give an AC supply or rectifying it to form a DC supply. The choice between AC and DC systems is application specific and is the subject of debate but it is believed that the DC system is a strong contender. However, in either case the current supplied by the generator output will be balanced.

The propulsion power will be conditioned by power electronic converters for control of the propulsion motors. The supply choice is to either rectify at the dual wound machine to form a DC supply or to supply the motor converters directly. In either case the current supplied by the generator will again be balanced. The test results in the paper are therefore all for balanced loads. However other conditions such as unbalanced loads will be considered in future work.

In this paper, the dual wound generator using wound-rotor is presented and experimentally verified. It is promising to extend the design methodology to a permeant magnet dual wound generator.

Outside of the proposed marine application the magnetically decoupled dual-wound generator has several potential applications, with the general case being any scenario where two independent power supplies are required, e.g. at different voltage and frequency levels. This scenario is especially widespread in the transport sector where an electric propulsion system requires high voltage power supply and auxiliary systems or ‘hotel loads’ require low voltage supply, typically 12 V, 24V or 48 V. In this case the dual wound generator could be especially relevant in the ‘series’ hybrid-electric powertrain

architecture in which the transient vehicle power requirement is met by a small capacity high voltage battery pack, with the average power requirement being met by a high voltage generator powered by a prime mover (internal combustion engine or micro gas turbine) to maintain the charge of the battery pack. In this architecture the existing generator could have a secondary winding introduced to supply the low voltage systems, replacing the need for an alternator or DC-DC converter. The series hybrid-electric powertrain seems likely to fade in popularity as many governments introduce policy to pushing the passenger car sector towards full Battery Electric Vehicles (BEVs) and away from hybrid vehicles. However, the case for the haulage sector is less clear cut as the high energy requirements make BEVs less practical, and in this case the proposed system could be especially interesting as significant hotel loads often exist, for example for refrigeration.

For pure BEVs it should be noted that, since the two windings are completely decoupled, it is also possible to simultaneously operate them in different quadrants. This opens the possibility of dual wound traction motors in which the electric traction motor also contains a secondary winding which allows power take-off, replacing the alternator or DC-DC converter in the same manner described for the dual-wound generator.

3.8. Conclusions

This paper presents a dual wound generator with 2-pole and 6-pole windings, which can generate two independent power supplies of different frequencies for an IFEP ship system. Previous studies on dual wound machines used same pole numbers for the two windings without the consideration of harmonic decoupling. The machine designed in this paper ensures that the two generators can operate independently. Both analytical calculations and 2D finite element COMSOL simulations validated by test results are applied to investigate the generator performance. The harmonic analysis and finite element modelling results show that the two outputs are fully electromagnetically decoupled as far as the airgap and slot leakage fields are concerned. A dual wound generator prototype is built and experimentally tested to validate the design and show that the end-winding leakage fields also do not couple. The dual wound generator prototype demonstrates that the 2-pole and 6-pole windings can generate individual power outputs without influence from the other winding. When the dual wound generator is integrated into an electric ship system, the power supply for the propulsion system can be independent from the power supply for the ship service system. Other potential applications, such as in electric cars, busses and trains are highlighted.

3.9. References

[1] R. T. Meyer, R. A. DeCarlo, S. Pekarek, and C. J. Doktorcik, “Gas turbine engine behavioral modeling,” Journal of Engineering for Gas Turbines and Power, Dec. 2015.

[2] A. K. Adnanes, “Maritime electrical installations and diesel electric propulsion,” ABB report/Lecture note NTNU, 2003.

[3] J. F. Hansen and F. Wendt, “History and state of the art in commercial electric ship propulsion, integrated power systems, and future trends,” Proceedings of the IEEE, vol. 103, no. 12, pp. 2229-2242, Dec. 2015.

[4] N. Doerry, J. Amy and C. Krolick, “History and the status of electric ship propulsion, integrated power systems, and future trends in the U.S. navy,” Proceedings of the IEEE, vol. 103, no. 12, pp. 2243-2251, Dec. 2015.

[5] H. Pestana, “Future trends of electrical propulsion and implications to ship design,” Maritime Technology and Engineering, pp. 797-803, 2014.

[6] J. M. Apsley, A. Gonzalez-Vill asenor, M. Barnes, A. C. Smith, S. Williamson, J. D. Schuddebeurs, P. J. Norman, C. D. Booth, G. M. Burt and J. R. McDonald, “Propulsion drive models for full electric marine propulsion systems,” IEEE Transactions on Industry Applications, vol. 45, no. 2, pp. 676-684, Mar. 2009.

[7] G. Sulligoi, A. Vicenzutti and R. Menis, “All-electric ship design: from electrical propulsion to integrated electrical and electronic power systems,” IEEE Transactions on Transportation Electrification, vol. 2, no. 4, pp. 507-521, Dec. 2016.

[8] W. A. Hill, G. Creelman and L. Mischke, “Control strategy for an icebreaker propulsion system,” IEEE Transactions on Industry Applications, vol. 28, no. 4, pp. 887-

892, Jul. 1992.

[9] I. M. Elders, P. J. Norman, J. D. Schuddebeurs, C. D. Booth, G. M. Burt, J. R. McDonald, J. Apsley, M. Barnes, A. Smith, S. Williamson, S. Loddick and I. Myers, “Modelling and analysis of electro-mechanical interactions between prime-mover and load in a marine IFEP system,” 2007 IEEE Electric Ship Technologies Symposium, Arlington, VA, 2007, pp. 77-84.

[10] J. D. Schuddebeurs, P. J. Norman, C. D. Booth, G. M. Burt and J. R. McDonald, “Emerging research issues regarding integrated-full-electric-propulsion,” In Proc. the 41st International Universities Power Engineering Conference, Newcastle-upon-Tyne, 2006, pp. 669-673.

[11] E. Mese, M. Tezcan, M. Ayaz, Y. Yasa and K. Yilmaz, “Design considerations for dual winding permanent magnet synchronous machines,” 2012 IEEE Energy Conversion Congr. and Expo. (ECCE), pp. 1894-1901, Sep. 2012.

[12] Y. Demir and M. Aydin, “A novel asymmetric and unconventional stator winding configuration and placement for a dual three-phase surface PM motor,” IEEE Transactions on Magnetics, vol. 53, 2017.

[13] Y. Li, Z. Zhu, X. Wu, A. S. Thomas and Z. Wu, “Comparative study of modular dual 3-phase permanent magnet machines with overlapping/non-overlapping windings,” IEEE Transactions on Industry Applications, vol. 55, no. 4, pp. 3566-3576, Jul. 2019.

[14] E. Mese, M. Ayaz, M. Tezcan, K. Yilmaz and E. Ozdemir, “A permanent magnet synchronous machine with motor and generator functionalities in a single stator core,” Compumag, Jul. 2013.

[15] L. J. Rashkin, J. C. Neely, S. F. Glover, T. J. McCoy and S. D. Pekarek, “Dynamic

considerations of power system coupling through dual-wound generators," 2017 IEEE Electric Ship Technologies Symposium (ESTS), Arlington, VA, 2017, pp. 493-500.

[16] J. C. Neely, L. J. Rashkin, S. F. Glover, D. G. Wilson, N. Doerrty and T. Mccoy, "Dynamic response evaluation of a 20 MW scale dual wound machine based power system," Advanced Machinery Technology Symposium Conference, Mar. 2018.

[17] C. G. Hodge and J. F. Eastham, "Dual wound machines for electric ship power systems," 2015 IEEE Electric Ship Technologies Symposium (ESTS), Alexandria, VA, 2015, pp. 62-67.

[18] B. Yin, X. Pei, X. Zeng, F. Eastham, C. Hodge and O. Simmonds, "Design and analysis of dual wound machine for electric ships," 2020 International Conference on Electrical Machines (ICEM), 2020, pp. 104-110.

[19] J. F. Eastham, T. Cox and J. Proverbs, "Application of planar modular windings to linear induction motors by harmonic cancellation," IET Electric Power Applications, vol. 4, no. 3, pp. 140-148, Mar. 2010.

[20] C. G. Hodge, J. F. Eastham and A. C. Smith, "The harmonics analysis of machine excitation," Int. Naval Engineering Conf. (INEC), Edinburgh, May. 2012.

[21]J. F. Eastham and C. G. Hodge "The harmonics analysis of machine phase windings," Int. Naval Engineering Conf. (INEC), Glasgow, May. 2014.

Chapter 4.

Experimental testing of the dynamic performance of a magnetic decoupled dual wound generator

Chapter contents:

This chapter presents the experimental test results of the dual wound generator dynamical operation with resistive, inductive and rectifier load conditions.

4.1. Chapter summary

IFEP systems remove the direct mechanical coupling between a prime mover and a propeller, building an all-electric onboard network to supply both a ship's services and propulsion systems, which can reduce fuel consumption, increase system reliability and also reduce maintenance and capital costs. However, both the propulsion system and ship services have flexible power demands, which means that the loads of the generator can be dynamically changed in a practical application. This can bring more challenges to a designed dual wound generator.

Chapter 3 investigated the proposed dual wound generator's performance under no-load and rated resistive load continuous operating conditions. To further verify the independence of the two outputs of the proposed dual wound generator design, this chapter investigates the dynamical operation under resistive, inductive and rectified load conditions.

The experimental tests including the change of rotor excitation current, resistance of loads, inductance of loads and rectified DC loads are demonstrated, and the results indicate that the two windings are not influenced by a sudden change of load from the other winding.

The rest of this chapter is cited from the author's submitted article in IEEE Transactions on Energy Conversion. The structure of this chapter is organised in an alternative-based format, where the indices, equations, tables, figures, titles and references are numbered independently.

Statement of Authorship

<table>
<tr><td colspan="4">This declaration concerns the article entitled:</td></tr>
<tr><td colspan="4">Experimental testing of the dynamic performance of a magnetic decoupled dual wound generator</td></tr>
<tr><td colspan="4">Publication status (tick one)
Draft manuscript [ ] Submitted [√] In review [ ] Accepted [ ] Published [ ]</td></tr>
<tr><td>Publication details (reference)</td><td colspan="3">B. Yin, X. Pei, J. F. Eastham, H. Wang, X. Zeng, “Experimental testing of the dynamic performance of a magnetic decoupled dual wound generator,” in IEEE Transactions on Energy Conversion</td></tr>
<tr><td colspan="4">Copyright status (tick the appropriate statement)
I hold the copyright for this material [√] Copyright is retained by the publisher, but I have been given permission to replicate the material here [ ]</td></tr>
<tr><td>Candidate’s contribution to the paper (provide details, and also indicate as a percentage)</td><td colspan="3">The candidate contributed to / considerably contributed to / predominantly executed the…
Formulation of ideas:
● 80%
● The research further investigates the decoupling between the two outputs of the dual wound generator prototype under more complex operating conditions. This research is guided by Dr. Xiaoze Pei.
Design of methodology:
● 100%
● 2D finite element modelling is used to analyse the magnetic field distribution and the operating conditions of the dual wound generator with resistive and inductive load. Experimental tests are carried out to further verify the design.
Experimental work:
● 100%
● The experimental tests demonstrate the two windings are not influenced by the sudden change of load from the other winding under different operating conditions.
Presentation of data in journal format:
● 80%
● Organising and writing this article, revised by Dr Xiaoze Pei, Prof. John Fred Eastham, and other co-authers</td></tr>
<tr><td>Statement from Candidate</td><td colspan="3">This paper reports on original research I conducted during the period of my Higher Degree by Research candidature.</td></tr>
<tr><td>Signed</td><td>Boyuan Yin</td><td>Date</td><td>25/11/2022</td></tr>
</table>

Experimental testing of the dynamic performance of a magnetic decoupled dual wound generator

Boyuan Yin, Xiaoze Pei, John Frederic Eastham, Han Wang, Xianwu Zeng

Abstract— The electric propulsion ship system removes the direct mechanical coupling between the diesel engines and the propellers. An all-electric network is introduced to increase system efficiency and reduce emissions. Considering a more compact and integrated design, a dual wound generator is proposed and designed to provide independent power supplies for ship propulsion and ship services. The two sets of windings physically share the same slots in one machine frame but electromagnetically are fully decoupled. This avoids the impact from the change of one output onto the other. The paper investigates this effect by considering load dynamical change between the two outputs. Different types of loads including resistive, resistive-inductive and rectified are experimentally tested and it is shown that the designed dual wound generator is a fully decoupled machine so that the change of load for one winding output for all cases does not have an impact on the other. This indicates that the machine has great potential for use in electric ships, electric aircraft and heavy-duty vehicles.

Index Terms— Dynamic performance, Dual wound machine, Magnetic decoupling, Independent power supplies

4.2. Introduction

Naval warships and large cruise ships require a high-power rating supply for the propulsion system and a medium power rating supply for the onboard services. The traditional solution contains a set of diesel generators for the ship service system, and separate prime movers for the propulsion system [1]-[2]. This direct diesel-power ship system can occupy a large onboard space with lower power efficiency. The electric propulsion system has emerged to be the most efficient arrangement for several vessel types [3]-[4], and the number of electrically-propelled ships has grown rapidly over the decade [5]. Compared with the diesel ship systems, the electrical propulsion system has a great potential to reduce fuel consumption, enhance dynamic performance and increase the system reliability [6]-[8]. The integrated full electric propulsion (IFEP) system removes the direct mechanical coupling between the prime mover and the propeller, introducing an all-electric onboard system to supply both the ship services and the propulsion system [9]-[10]. By using electrical distribution rather than mechanical distribution, the IFEP system eliminates the need for clutches and the gearbox. It offers flexibility in the locations of the engines to achieve acoustic decoupling between the engines and the hull. The IFEP system also has the benefits of reducing fuel consumption, increasing reliability, and reducing maintenance costs [6], [11].

Most electric propulsion ships are operating with AC power distribution systems. With the advancement of semiconductor devices and the improvement of the capacity in power converters and DC circuit breakers, the onboard DC distribution systems become more attractive for electric ship manufacturers. The benefits of using DC networks on electric ships are investigated in terms of economic and environmental considerations [12]. The DC networks on an electric propulsion ship can increase the system efficiency, and improve carbon dioxide emission and fuel consumption [12].

A dual wound machine provides a redundant system and enables several interconnection permutations [16]. It is also one of a range of multiphase machines that attracted attention in electric vehicle applications with high power and fault-tolerance capability [17]. A dual wound machine can provide better power quality [13], torque quality [14], and higher efficiency [15]. A dual three-phase machine with an interior permanent magnet rotor is developed and proved to have better torque density and torque quality without compromising efficiency compared with the Nissan Leaf IPM machine [18].

A dual wound generator is developed to provide two power supplies for the systems with different operating conditions. It consists of two sets of windings in one machine frame driven by one prime mover. On the electric propulsion ship systems, a dual wound generator can supply both the propulsion and onboard service at the same time with only one prime mover. This achieves a more compact design due to the reduction of the number of diesel engines, generators and transformers. The primary challenge of the design of a dual wound generator for electric propulsion systems is the independence of the two outputs. The two sets of windings physically share the same slots in one machine frame, but the winding distributions are different. The winding strategy on a dual wound generator allows the two outputs to have individual power ratings and frequencies. Through the arrangements of the windings, the electromagnetic coupling between the two windings can be eliminated. Different winding strategies applied to dual wound machines are described in [13], [19]. Previous studies on the dual wound machines commonly used the same pole number for each winding and therefore were magnetically coupled [20]-[21]. Thus, the change of the operation condition for one output would impact the operation on the other winding. The analysis in [22]-[25] theoretically proved the possibility of designing an uncoupled dual wound machine but the results are not experimentally verified, and only the in-slot windings are considered.

A dual wound generator with both 2-pole and 6-pole windings has been proposed, which can provide the power for both the propulsion and the onboard service simultaneously [26]. Previous research has shown the independence of the two sets of windings under static operation conditions. Both analytical harmonic calculation and 2D finite element modelling are used to verify that there is no electromagnetic coupling between the two sets of windings. The end-winding effect in a dual wound machine is analysed mathematically using a simplified 2D model in [27], where the results are calculated by the Biot-Savart Law. A prototype of the designed dual wound generator is built by rewinding an existing machine frame. The experimental test results have shown that the 2-pole generator and the 6-pole generator can independently generate outputs without the influence from the other winding under both no-load and rated resistive load continuous operating conditions. Both propulsion and onboard service have flexible power demands, thus the load can be dynamically changed in practical applications. This brings more challenges to the independence of the dual wound generator outputs. This paper investigates the dual wound generator dynamical operation with resistive, inductive and rectifier load conditions, and experimental dynamic tests using the designed dual wound generator prototype are presented. Firstly, a static test with resistive and inductive load is presented, showing that the 2-pole and 6-pole windings have no electromagnetic coupling. Secondly dynamic tests including the change of rotor excitation current, resistive loads, resistive and inductive loads, and the rectifier loads. The dynamic tests are carried out to demonstrate the two windings are not influenced by the sudden change of load from the other winding under different operating conditions.

This paper is structured as follows: Section II introduces the dual wound generator design topology. Section III presents the simulation results based on the dual wound generator design. Section IV shows the experimental test results on the dual wound generator prototype under different types of loads.

4.3. Dual wound generator design

4.3.1. Dual wound generator topology

The dual wound generator designed in this paper is a wound rotor synchronous generator with 2-pole and 6-pole windings. Two groups of windings share the same slots but rotor windings can be separately excited. The machine prototype is built based on an existing machine frame, where the machine dimension is shown in Table. 4-1.

This existing machine was in the lab at the University of Bath, manufactured by Mawdsley's LtD. It has 36-slot stator, 24-slot rotor, four slip rings and several open terminals. The existing windings are removed. The dimensions of the machine frame is measured in the aspects of axial length, both rotor and stator diameters, and slot areas. The proposed magnetic decoupled winding design in this paper is based on this existing machine frame with the measured dimensions.

The detailed design method was introduced in [26], where the air gap magnetic field harmonics distributions are calculated and the results indicate that there are no common harmonics between the two windings, fulfilling the condition for no mutual coupling, and ensuring that the two outputs are independent.

TABLE 4-1

GENERATOR DIMENSIONS

Item	Stator	Rotor
Number of slots	36	24
Diameter	190.5 mm	186.5 mm
Axial length	123.6 mm	139.5 mm
Slot opening	2.7 mm	3.5 mm
Airgap	2 mm	
Stator outer diameter	295 mm	

4.3.2.Rotor winding distribution

To produce a sinusoidal air-gap magnetic field, the rotor windings are arranged in the concentric form . The number of conductors in each slot are sinusoidally distributed to generate an approximation to a sinusoidal magnetic flux in the airgap. The dual wound generator has 24 slots in the rotor frame. Thus the 2-pole rotor winding has a pole pitch of 12 slots and the 6-pole rotor winding, 4 slots. Fig. 4-1 illustrates the 2-pole rotor winding distribution, which shows one of the two 2-pole coil sets. Fig. 4-2 illustrates the 6-pole rotor winding distribution, which shows the one coil set out of six. The rotor winding conductors are connected and excited through four slip rings and brushes.

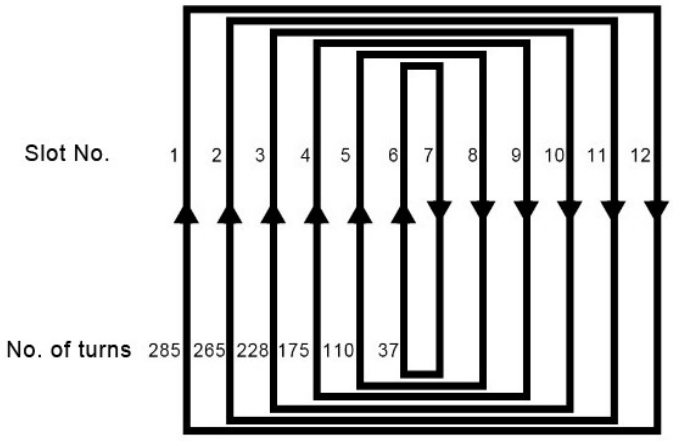

Fig. 4-1 2-pole rotor winding distribution

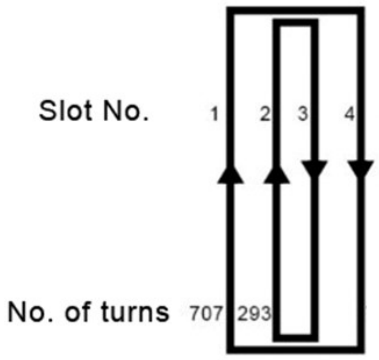

Fig. 4-2 6-pole rotor winding distribution

The sinusoidal winding distribution is arranged considering the machine slot space and the rotor excitation current, which aims to maximize the usage of each slot and minimize the saturation in the machine frame. The 2-pole rotor has a total number of turns of 1100, and the 6-pole rotor has a total number of turns of 1000. Thus, the number of turns in each slot is as shown in the above figures. The wire type for the rotor windings is SWG27 with a diameter of 0.4166 mm, which depends on the excitation current of 1 A and the fill factor.

4.3.3. Stator winding distribution

The rotor of the dual wound generator produces a rotating magnetic field, which generates an induced voltage in the stator windings. To propose a fully decoupled machine design, the 2-pole rotor winding only produces a magnetic field that couples with the 2-pole stator winding. In the same way, the 6-pole rotor winding only produces a magnetic field that couples with the 6-pole stator winding. The stator frame has 36 slots with four layers in each slot, where the 2-pole and 6-pole windings each occupy 2 layers. The 2-pole winding is above the 6-pole winding. This is the same order as in the rotor. Following the previous study in [26], the designed dual wound generator stator winding distribution is shown in Fig. 4-3. The winding distribution design principle aims to maximize the induced voltage and minimize the spatial harmonics. Both the 2-pole and 6-pole windings are short-pitched distributed windings. The 2-pole stator winding has a pitch angle of 120 degrees, while the 6-pole winding has a pitch angle of 150 degrees.

Slot	1	2	3	4	5	6	7	8	9	10	11	12	13	14	15	16	17	18	19	20	21	22	23	24	25	26	27	28	29	30	31	32	33	34	35	36
2 Pole	R	R	R	R	R	R	-B	-B	-B	-B	-B	-B	Y	Y	Y	Y	Y	Y	-R	-R	-R	-R	-R	-R	B	B	B	B	B	B	-Y	-Y	-Y	-Y	-Y	-Y
	-B	-B	-B	-B	-B	-B	Y	Y	Y	Y	Y	Y	-R	-R	-R	-R	-R	-R	B	B	B	B	B	B	-Y	-Y	-Y	-Y	-Y	-Y	R	R	R	R	R	R
6 Pole	R	R	-B	-B	Y	Y	-R	-R	B	B	-Y	-Y	R	R	-B	-B	Y	Y	-R	-R	B	B	-Y	-Y	R	R	-B	-B	Y	Y	-R	-R	B	B	-Y	-Y
	R	-B	-B	Y	Y	-R	-R	B	B	-Y	-Y	R	R	-B	-B	Y	Y	-R	-R	B	B	-Y	-Y	R	R	-B	-B	Y	Y	-R	-R	B	B	-Y	-Y	R

Fig. 4-3 Stator winding distribution

The winding harmonics distribution of the 2-pole and 6-pole stator windings are calculated and analysed in the previous paper [26], which indicates that there is no common harmonic component between the 2-pole and 6-pole stator windings. Also, the 2-pole rotor windings have no mutual harmonics with the 6-pole stator windings and vice versa. The harmonics analysis shows that the rotor windings only couple with their corresponding stator winding

4.4. Finite element modelling

2D finite element modelling is used to analyse the magnetic field distribution and the airgap magnetic field distribution. The FEM analysis in [26] has verified the harmonic analysis and the slot leakage fluxes at a steady-state operation. This section presents the simulation results of resistive and inductive load conditions for the 2-pole and 6-pole generators to further investigate the decoupling between the two generators under different load conditions.

Fig. 4-4 shows the simulation results that the 2-pole stator is loaded with 60 Ω resistive load and 100 mH inductive loads, while the 6-pole is loaded with a rated 80 Ω resistive load. The peak voltage for the 2-pole output is 150 V with a peak current of 2.2 A. The peak voltage for the 6-pole generator is 140 V with a peak current of 1.7 A.

Fig. 4-5 shows the 6-pole generator resistive and inductive load test simulation results. The 2-pole stator is loaded with a rated 60 Ω resistive load, while the 6-pole stator is loaded with 80 Ω resistive and 100 mH inductive loads. The peak voltage for the 2-pole output is 150 V with a peak current of 2.5 A. The peak voltage for the 6-pole generator is 140 V with a peak current of 1.3 A.

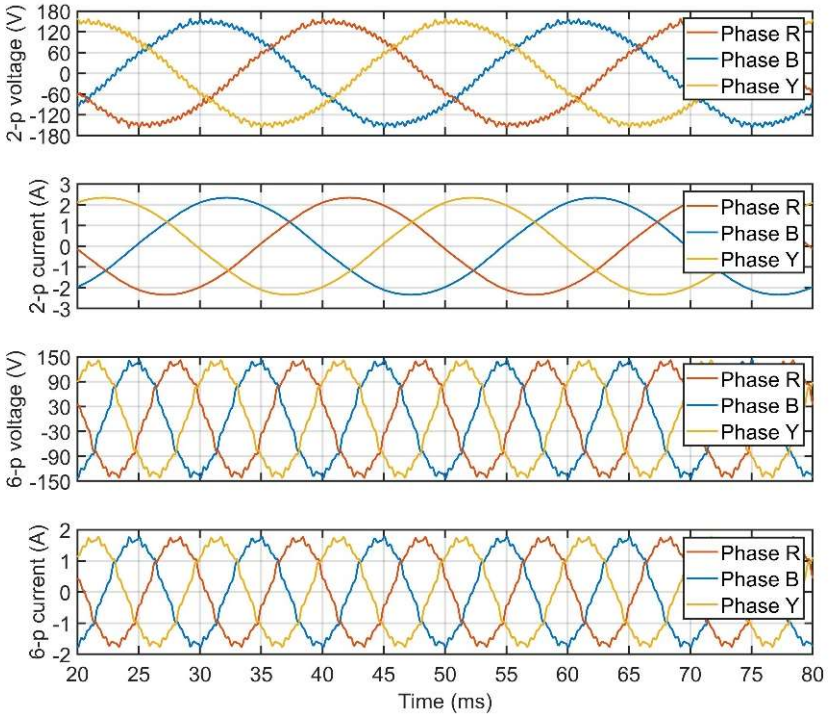

Fig. 4-4 2-pole and 6-pole outputs with 2-pole RL load

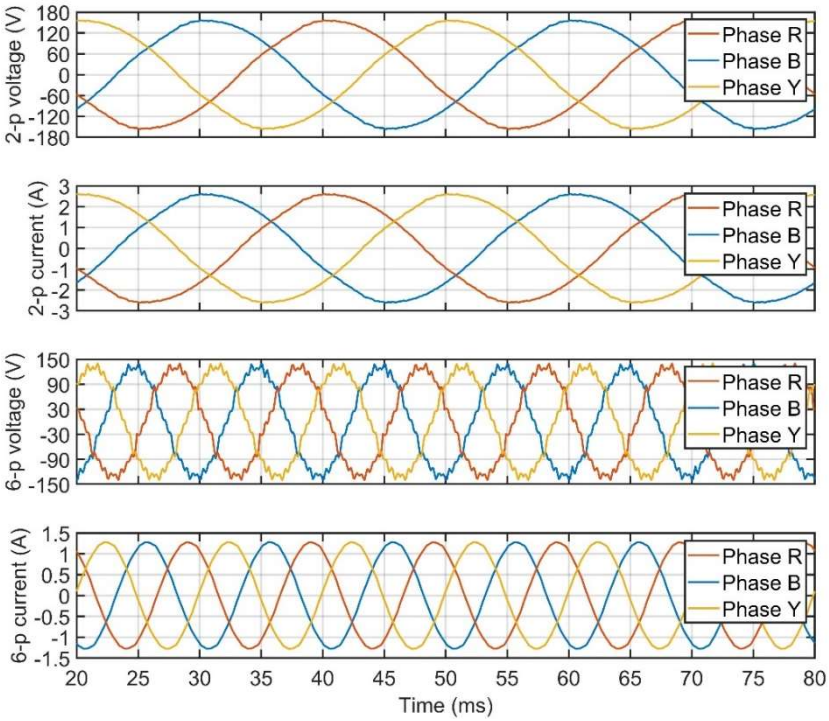

Fig. 4-5 2-pole and 6-pole outputs with 6-pole RL load

It can be seen that the peak voltage stays the same with or without the inductive load for both the 2-pole and 6-pole generators, including the phase angle. However, the inductive load brings more ripples to the voltage curve. The peak current for both generators is reduced with the 3-phase inductive load as the non-idea inductors bring extra load resistance. The current phase angle is changed as well. The difference on the output of the 6-pole generator when the load is inductive is more obvious as it operates at a higher frequency.

4.5. Experimental test and discussion

4.5.1. Test platform

A dual wound generator prototype has been built following the design principle to verify the decoupled winding design. The schematic of the experimental test platform is shown in Fig. 4-6. A DC motor is coupled with the dual wound generator through the shaft, representing a diesel engine prime mover in the electric propulsion systems. The DC motor has a rated power of 5 kW and a rated rotating speed of 3000 rpm. The field voltage of the DC motor is 200 V, with a field current of 1.1 A. The armature current is up to 36.5 A. A LAB/SMS630 DC power supply is used to provide the field current to the DC motor and a LAB/SMS5300 DC power supply to provide armature current. The operation speed can be adjusted by changing the DC motor terminal voltage to achieve the proposed testing speed of 2000 rpm. The rotating speed of the prime mover is monitored by a tachometer.

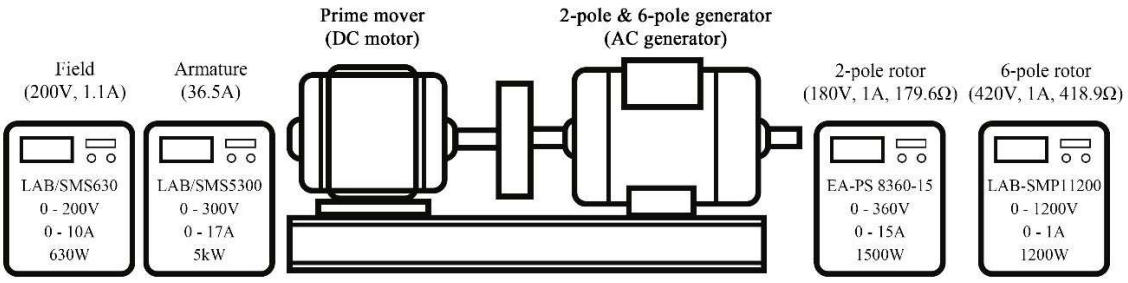

Fig. 4-6 Schematic of experimental test platform

The dual wound generator is a wound rotor synchronous machine. The 2-pole and 6-pole rotor windings are excited DC windings. The rated rotor winding excitation current is 1 A. The 2-pole rotor winding resistance is 179.6 Ω, and the 6-pole rotor winding resistance is 418.9 Ω. The 2-pole and 6-pole rotor windings are separately supplied by the EA-PS 8360-15 and LAB-SMP11200 power sources, that are capable to provide the 1 A excitation current.

The 2-pole and 6-pole three-phase outputs on the stator windings can be connected to different loads through the terminals. In this paper, 3-phase resistive loads, resistive and inductive loads and rectified DC loads are experimentally tested. The electric connection diagram for the experimental test is shown in Fig. 4-7. The voltage and current are monitored and recorded by an oscilloscope.

The experimental test platform is shown in Fig. 4-8, which consists of the dual wound generator prototype, the DC drive motor, electric loads, power sources and data acquisition equipment.

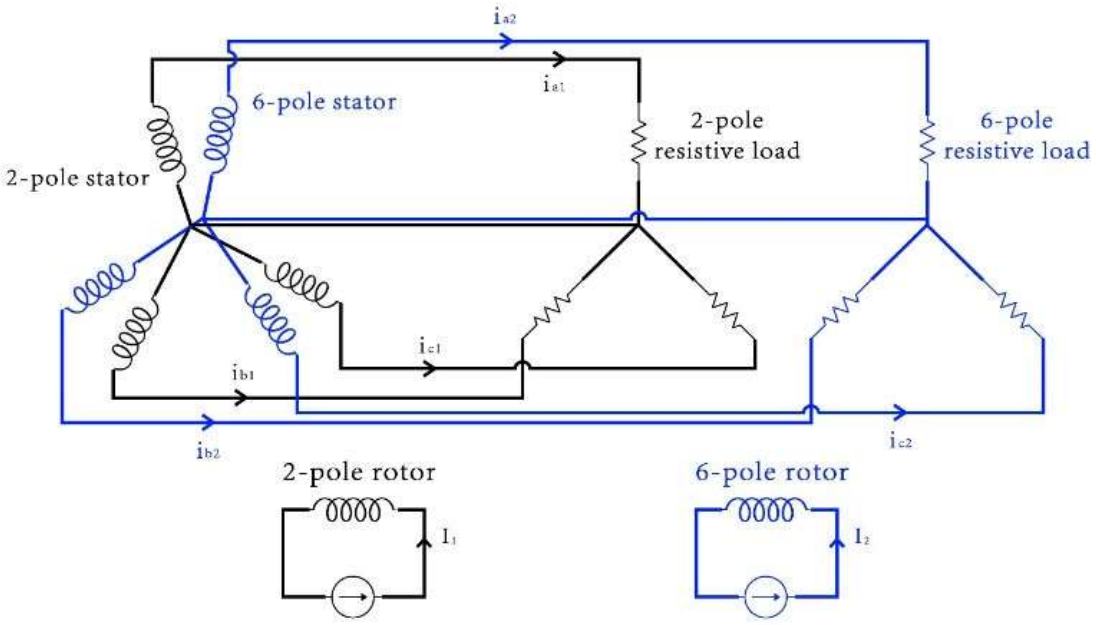

Fig. 4-7 Electric connection of dual wound generator

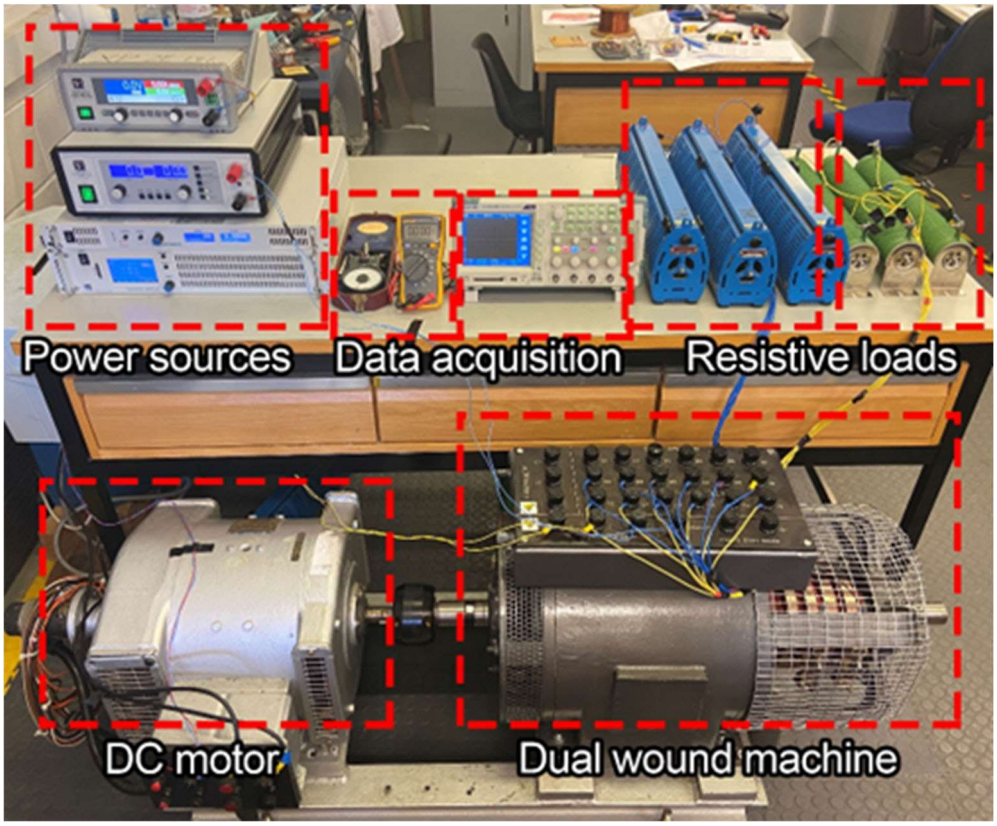

Fig. 4-8 Experimental test platform

4.5.2. Rotor current dynamic change

The output voltage of the generator can be controlled through the rotor excitation current at a fixed operating speed. To investigate whether the change of one of the rotor excitation currents would impact the other generator, the dual wound generator is tested with the rotor excitation current increasing. In this test, the two stator windings are loaded with their rated resistance, which is 60 Ω for the 2-pole generator and 80 Ω for the 6-pole generator. As shown in Fig. 4-9, a resistor is series connected in the rotor excitation circuit to provide a low initial rotor current. A circuit breaker is used to short-circuit the resistor to increase the rotor excitation current to 1 A. The external resistor has the same resistance as the corresponding rotor winding; thus, the rotor current will be doubled by switching the circuit breaker.

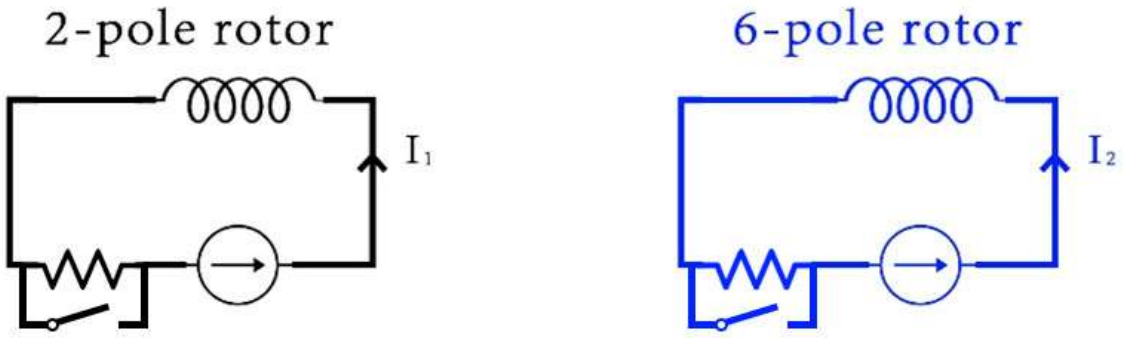

(a) 2-pole rotor test circuit (b) 6-pole rotor test circuit

Fig. 4-9 Rotor current dynamic change test circuit

Fig. 4-10 shows the 2-pole and 6-pole stator voltage dynamic change when the 2-pole rotor current is increased from 0.5 A to 1 A. As the 2-pole rotor excitation current increases, the 2-pole stator voltage increases. Since the input power of the DC motor is constant, it causes a rotating speed drop of the prime mover. This rotating speed variation due to load changes happens for any type of generators. The prime mover

diesel engine will recover the rotating speed to the set point with a speed control system. It is noted that the peak voltage of the 2-pole stator at 1 A rotor current is smaller than the two times that at 0.5 A rotor current, which is due to the drop of the rotating speed. The 6-pole voltage as shown in Fig. 4-10 is slightly decreased with the 2-pole rotor excitation current increasing because of the decreased rotating speed.

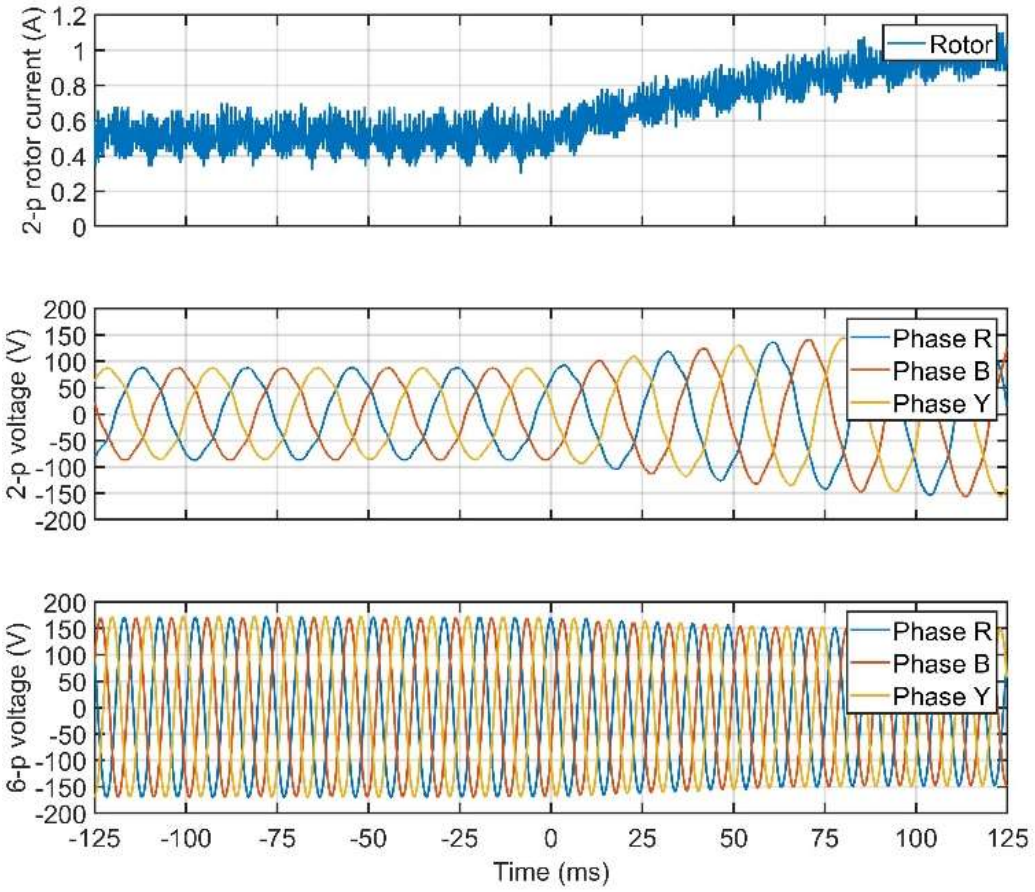

Fig. 4-10 2-pole rotor current dynamic test

Fig. 4-11 shows the experimental test results that the 6-pole rotor current increased from 0.6 A to 1 A. The 6-pole stator output voltage increases as the 6-pole rotor excitation current increases. In the same way as the 2-pole rotor current change effect, the prime mover rotating speed decreases slightly with the 6-pole rotor current increases. Thus the 2-pole stator output voltage decreases.

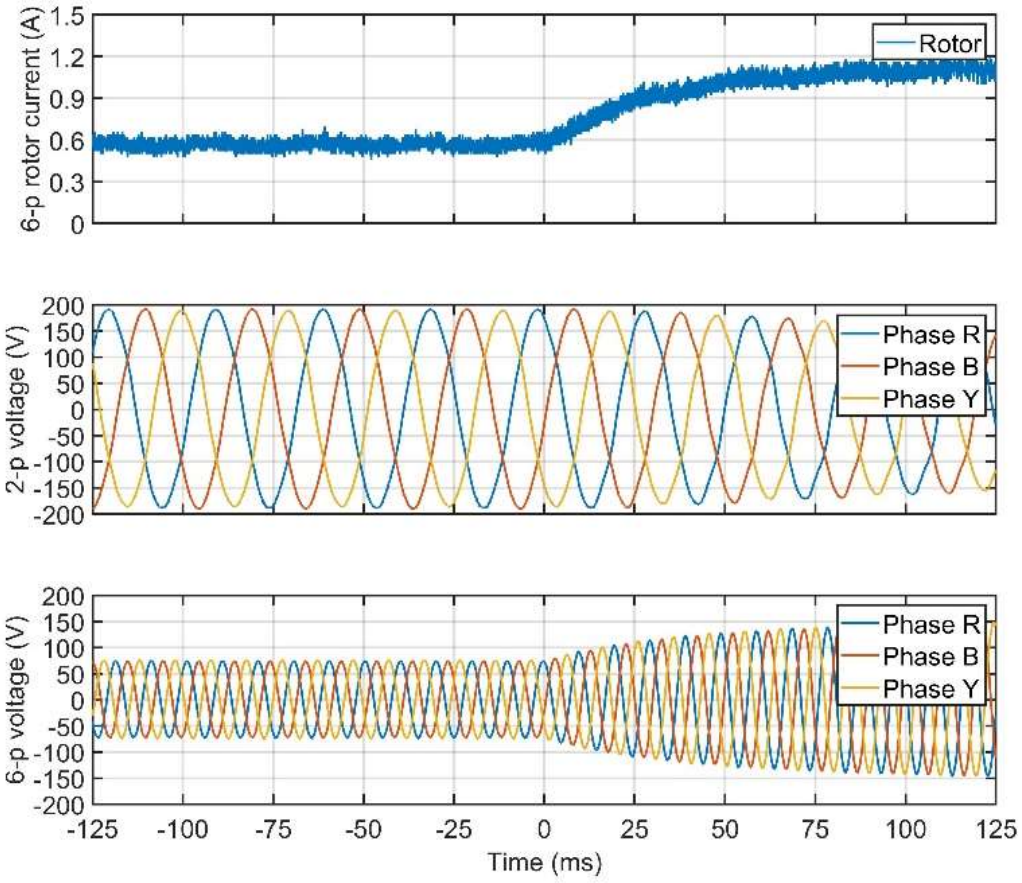

Fig. 4-11 6-pole rotor current dynamic test

It can be observed that in the dynamic change test of the 6-pole rotor current, the range of the change of the 2-pole stator voltage is less than the range of the change of the 6-pole stator voltage, which indicates the rotor current only affects the corresponding stator winding. This is also applies to the 2-pole rotor current dynamic test.

4.5.3. Resistive load dynamic change

In an all-electric propulsion system, the propulsion and service power can change under different operations. Therefore, it is important to make sure that the change of the load of one generator will not affect the other generator. Fig. 4-12 and Fig. 4-13 show the resistive load dynamic change test results.

The 2-pole dynamic load testing process is initiated to operate the 2-pole generator at a no-load condition. Then the rated 3-phase resistive load is switched on to the 2-pole generator, while the 6-pole generator is always at a rated load condition. The 2-pole generator dynamic load test results are shown in Fig. 4-12. The 2-pole stator current starts to increase from zero to its rated current. The 2-pole stator voltage shows instability when the load is connected and soon recovers to the rated 3-phase sinewave, while the 6-pole stator voltage is completely stable and not influenced.

With the same test process as the 2-pole dynamic load test, the 6-pole resistive load dynamic test results are shown in Fig. 4-13. The 6-pole stator has no current at the beginning of the test as it is a no-load condition. The current starts to increase to its rated level when the load is connected. A few ripples appear on the 6-pole stator voltage during the switching process, which is soon recovered to the normal voltage waveform.

The experimental test results for the resistive load dynamic change in this section shows that the change of the resistive load of the 2-pole generator has no impact on the 6-pole generator and vice versa.

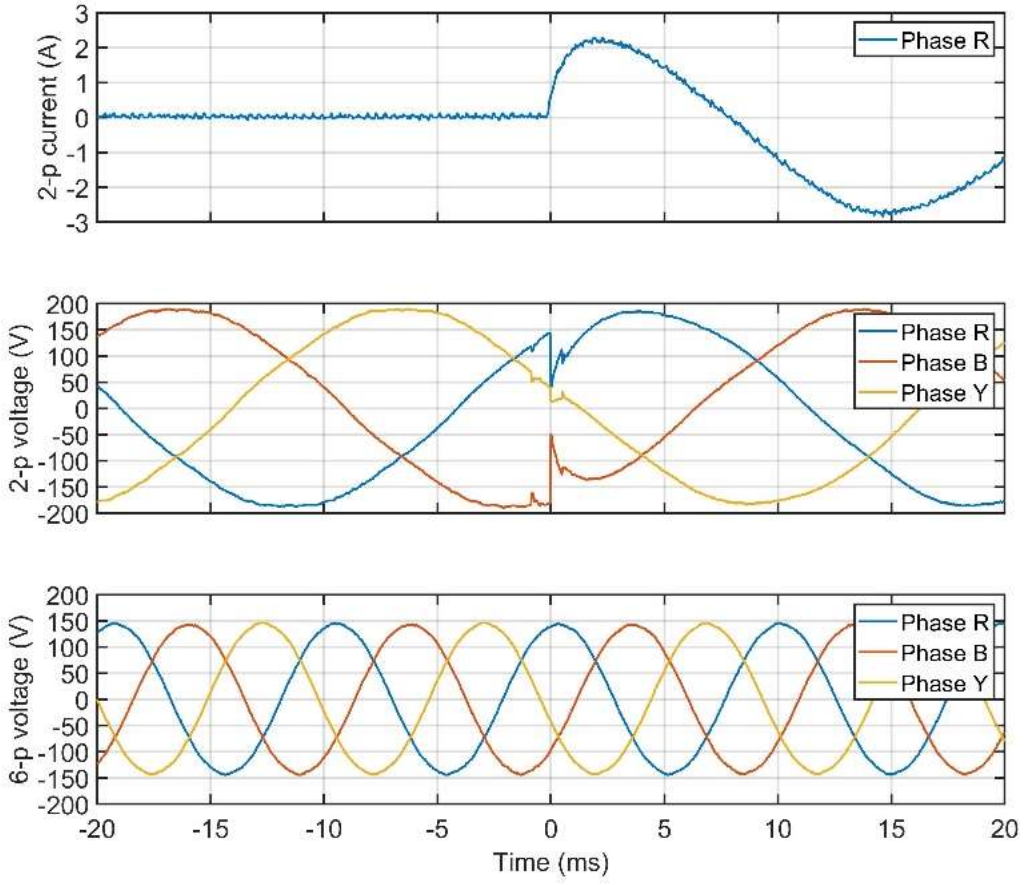

Fig. 4-12 2-pole resistive load dynamic test

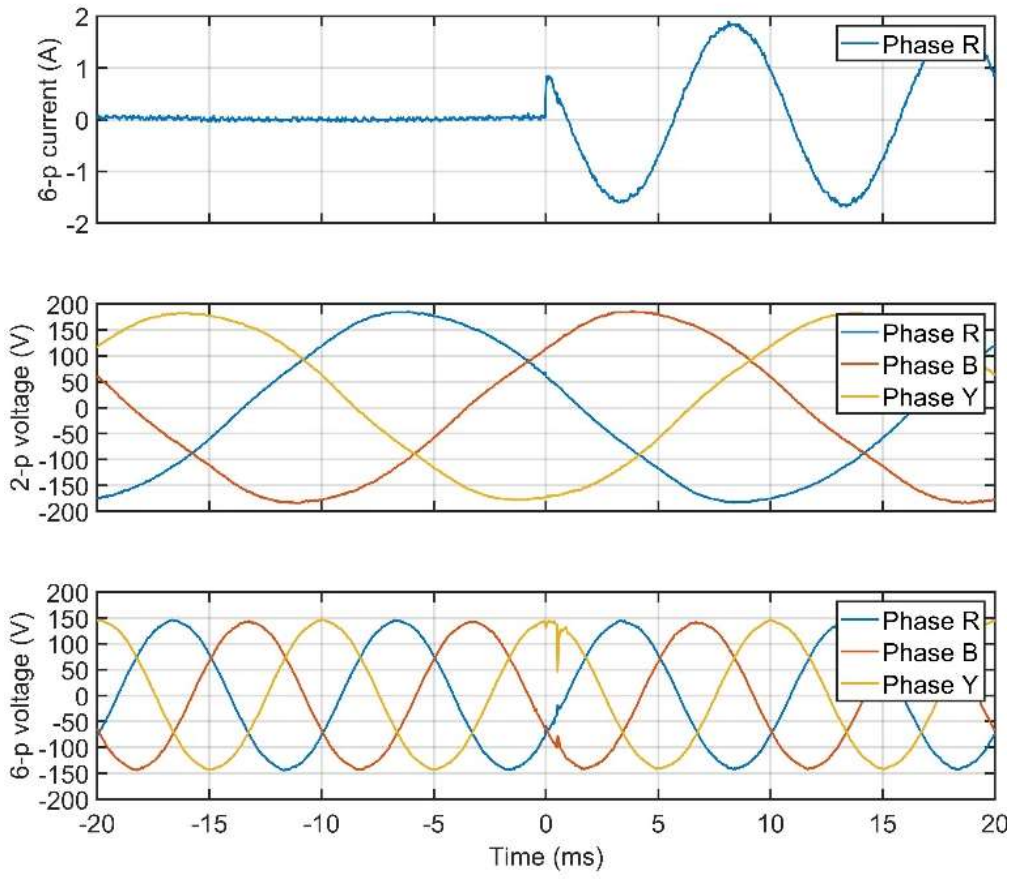

Fig. 4-13 6-pole resistive load dynamic test

4.5.4.RL load dynamic change

Since the resistive load dynamic change test proves the decoupling of the two generators in that situation, considering a more complex operation condition, the inductive load test is apt.

In the dynamic change of resistive and inductive load test procedure, the load for the 2-pole generator is 60 Ω resistive load with 100 mH inductive loads. And the 6-pole generator has 80 Ω resistive load with 100 mH inductive loads. The test process is the same as the resistive load dynamic test. At the beginning, the generator operated at a no-load condition. Then the load is switched to the tested generator. The other generator

is at the rated 3-phase resistive load condition during the testing process.

Fig. 4-14 presents the 2-pole generator resistive and inductive load dynamic test results. The 2-pole stator current starts to increase when the load is connected. The first peak value does not reach the rated peak current because of the inductive load. It is noticed that the 2-pole stator voltage is affected when the 2-pole loads are switched in the circuit. But the 6-pole voltage is stable constantly, which indicates the decoupling of the two generators under the inductive load condition.

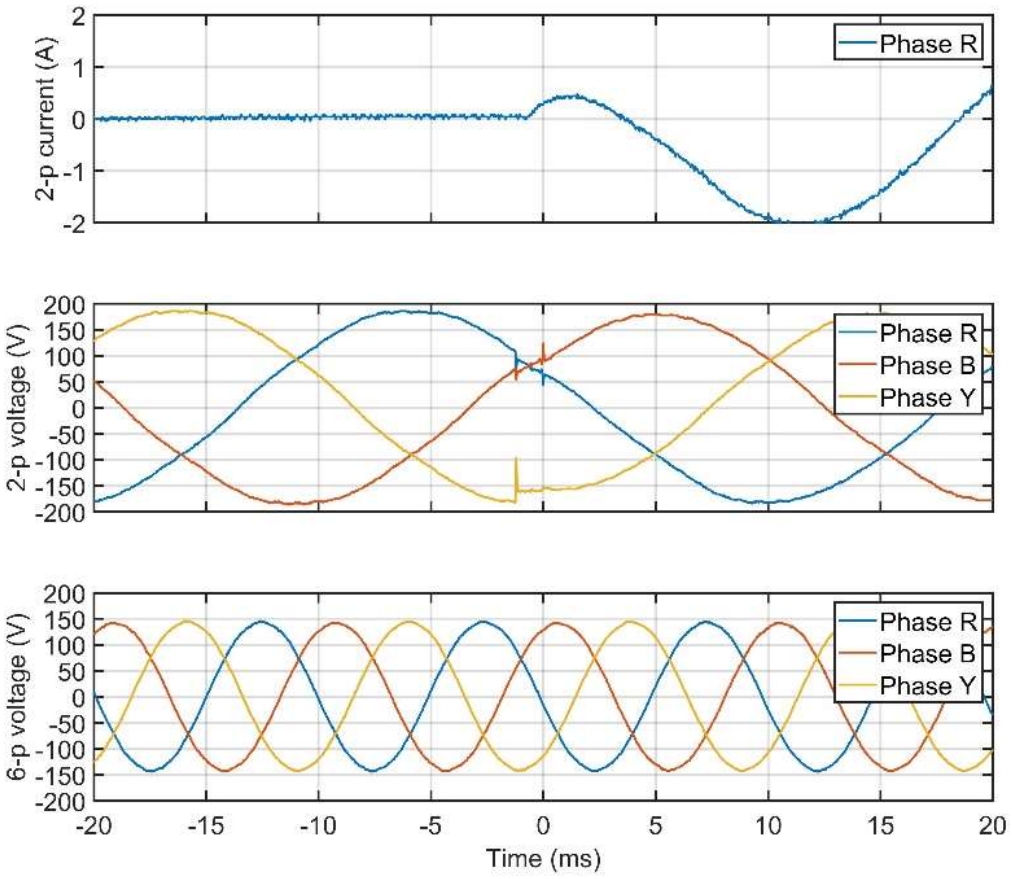

Fig. 4-14 2-pole resistive and inductive load dynamic test

The resistive and inductive load dynamic test for the 6-pole generator is shown in Fig. 4-15. In the same way as in the 2-pole generator test, the load switching only effect the 6-

pole voltage itself, without any impact on the 2-pole generator output. The results shown in this section further proves the independence of the two generators under a more complex load condition with the dynamic operation.

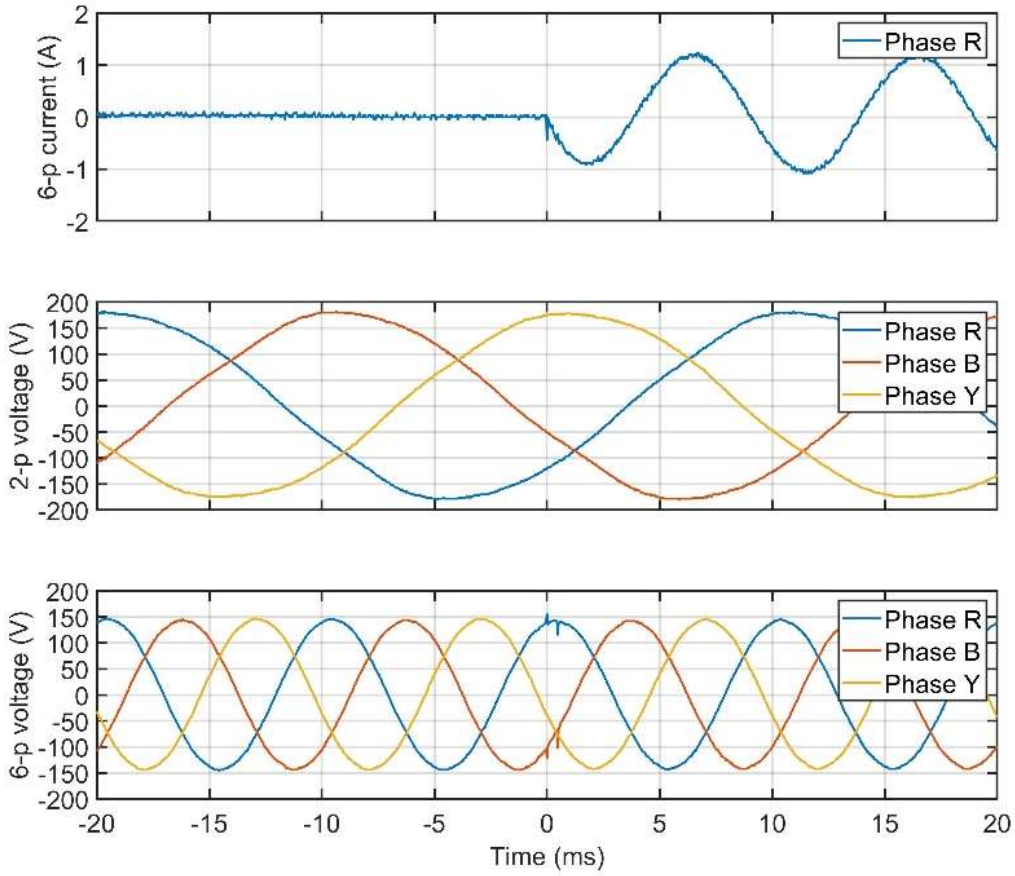

Fig. 4-15 6-pole resistive and inductive load dynamic test

4.5.5.Rectifier DC load dynamic change

Increasing use is being made of DC distribution networks for all-electric propulsion ship systems. Therefore, in this section, a rectifier load test on the dual wound machine is investigated by using a full-bridge rectifier VS-36MT120 to produce a DC bus on the 2-pole and 6-pole stator side for a resistive load. The dynamic change of load is also considered to verify the full decoupling of the two generator outputs under a dynamic

rectifier condition. The DC resistive loads used in this test are a 1000 Ω resistor for the 2-pole winding output and a 500 Ω resistor for the 6-pole generator. The generator output under test is initially operating in a no-load condition. Then the DC resistive load is switched into the DC bus. The other generator keeps the rated 3-phase loaded condition.

Fig. 4-16 shows the 2-pole rectifier load dynamic change test results. The 2-pole stator rectified DC voltage is increased from zero to 320 Vdc after switching on. There are ripples that appear on each switching point on the primary side of the 2-pole stator voltage. There is almost no effect on the 6-pole stator at the switching point.

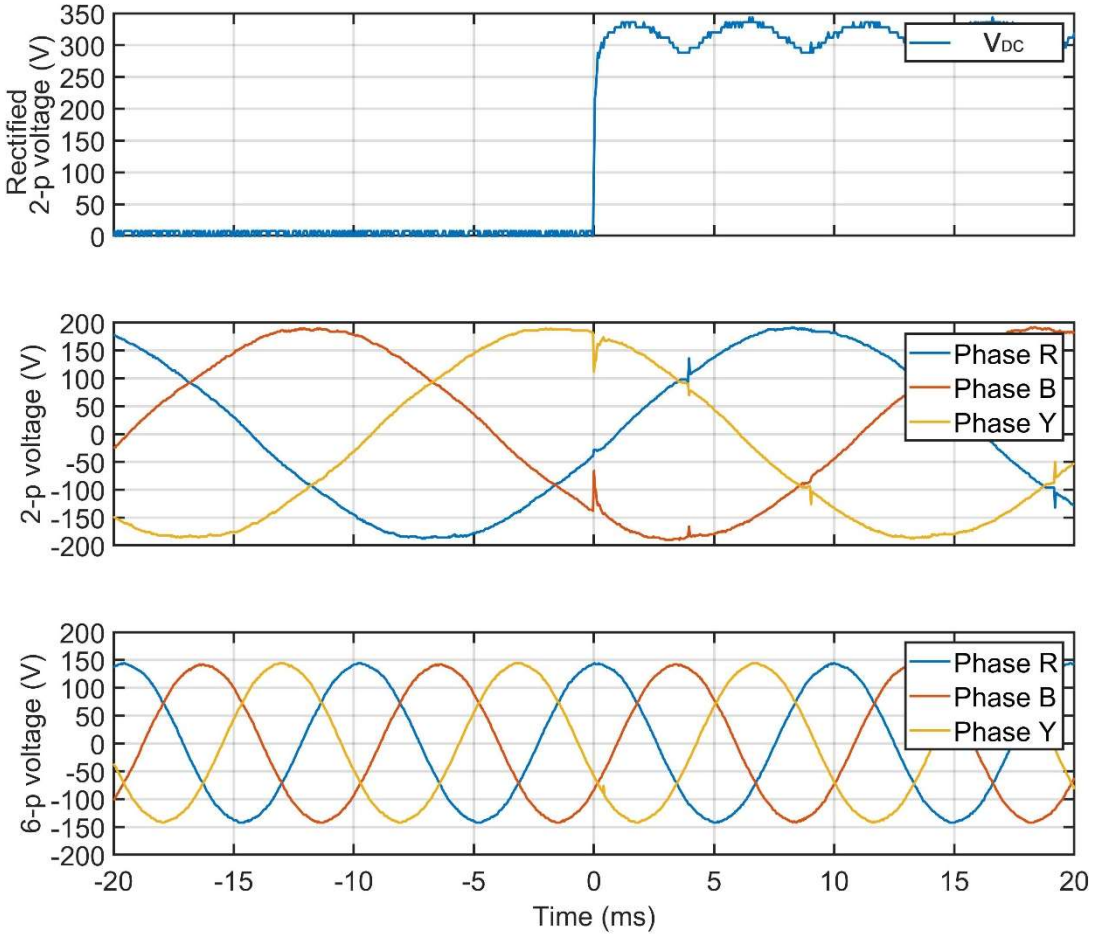

Fig. 4-16 2-pole rectifier load dynamic test

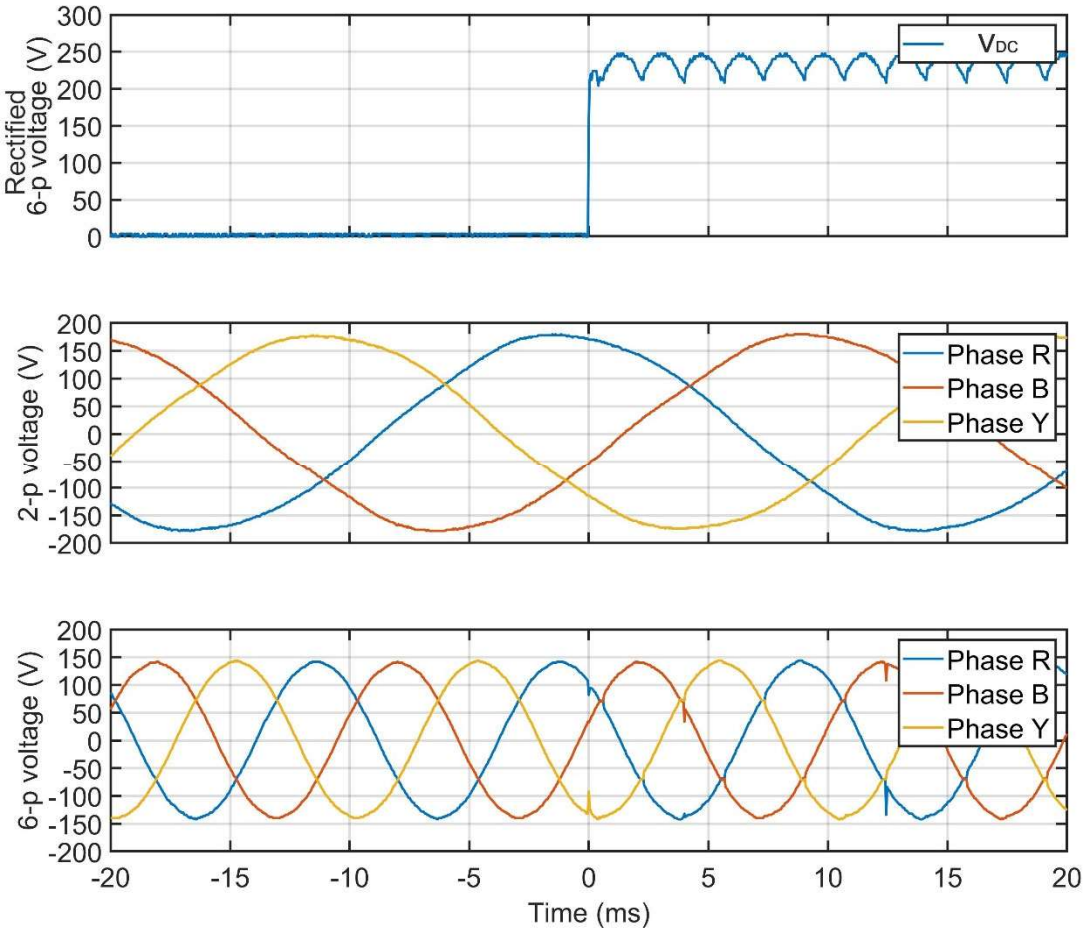

Fig. 4-17 6-pole rectifier load dynamic test

4.6. Conclusions

This paper designed and built a 2-pole and 6-pole dual wound generator for the IFEP systems. The arrangements of the 2-pole and 6-pole windings are investigated to eliminate the electromagnetic coupling based on the airgap and slot leakage fields. Considering the practical full-electric propulsion ship system applications, the propulsion and ship service loads can be more complex and dynamically changed. Therefore, this paper investigated the resistive load, inductive load and rectified load dynamic performance of the designed dual wound generator prototype to verify the fully decoupling of the two generators. 2D finite element analysis is applied to verify the machine decoupling performance of resistive and inductive loads. Experimental tests on the dual wound generator prototype are performed, including the rotor excitation current dynamically increasing, the resistive load dynamically changing, the resistive and inductive loads dynamically changing and the rectified circuit DC load dynamically changing. These tests of the dual wound generator further demonstrate that the two generators outputs including the end-windings are fully decoupled under more complex load conditions. The dual wound generator prototype demonstrates that the 2-pole and 6-pole windings can generate independent power supplies with no impact on the other generator, which ensures the power supplies for the electric propulsion and the ship service segment is independent. This application can also be applied to electric aircrafts, trains, busses, and heavy-duty trucks.

4.7. References

[1] R. T. Meyer, R. A. DeCarlo, S. Pekarek, and C. J. Doktorcik, “Gas turbine engine behavioral modeling,” Journal of Engineering for Gas Turbines and Power, Dec. 2015.

[2] A. K. Adnanes, “Maritime electrical installations and diesel electric propulsion,” ABB report/Lecture note NTNU, 2003.

[3] J. F. Hansen and F. Wendt, “History and state of the art in commercial electric ship propulsion, integrated power systems, and future trends,” Proceedings of the IEEE, vol. 103, no. 12, pp. 2229-2242, Dec. 2015.

[4] N. Doerry, J. Amy and C. Krolick, “History and the status of electric ship propulsion, integrated power systems, and future trends in the U.S. navy,” Proceedings of the IEEE, vol. 103, no. 12, pp. 2243-2251, Dec. 2015.

[5] H. Pestana, “Future trends of electrical propulsion and implications to ship design,” Maritime Technology and Engineering, pp. 797-803, 2014.

[6] J. M. Apsley, A. Gonzalez-Vill asenor, M. Barnes, A. C. Smith, S. Williamson, J. D. Schuddebeurs, P. J. Norman, C. D. Booth, G. M. Burt and J. R. McDonald, “Propulsion drive models for full electric marine propulsion systems,” IEEE Transactions on Industry Applications, vol. 45, no. 2, pp. 676-684, Mar. 2009.

[7] G. Sulligoi, A. Vicenzutti and R. Menis, “All-electric ship design: from electrical propulsion to integrated electrical and electronic power systems,” IEEE Transactions on Transportation Electrification, vol. 2, no. 4, pp. 507-521, Dec. 2016.

[8] W. A. Hill, G. Creelman and L. Mischke, “Control strategy for an icebreaker propulsion system,” IEEE Transactions on Industry Applications, vol. 28, no. 4, pp. 887-

892, Jul. 1992.

[9] I. M. Elders, P. J. Norman, J. D. Schuddebeurs, C. D. Booth, G. M. Burt, J. R. McDonald, J. Apsley, M. Barnes, A. Smith, S. Williamson, S. Loddick and I. Myers, “Modelling and analysis of electro-mechanical interactions between prime-mover and load in a marine IFEP system,” 2007 IEEE Electric Ship Technologies Symposium, Arlington, VA, 2007, pp. 77-84.

[10] C. G. Hodge, and D. J. Mattick, “The electric warship”, Trans IMarE, Vol 108, Part 2, pp 109-125, The Institute of Marine Engineers, 1995.

[11] J. D. Schuddebeurs, P. J. Norman, C. D. Booth, G. M. Burt and J. R. McDonald, “Emerging research issues regarding integrated-full-electric-propulsion,” 41st International Universities Power Engineering Conference, 2006, pp. 669-673.

[12] S. Kim and H. Jeon, “Comparative analysis on AC and DC distribution systems for electric propulsion ship,” Journal of Marine Science and Engineering, vol. 10, no. 5, p. 559, Apr. 2022.

[13] E. Mese, M. Tezcan, M. Ayaz, Y. Yasa and K. Yilmaz, “Design considerations for dual winding permanent magnet synchronous machines,” 2012 IEEE Energy Conversion Congr. and Expo. (ECCE), pp. 1894-1901, Sep. 2012.

[14] Y. Demir and M. Aydin, “A novel asymmetric and unconventional stator winding configuration and placement for a dual three-phase surface PM motor,” IEEE Transactions on Magnetics, vol. 53, 2017.

[15] Y. Li, Z. Zhu, X. Wu, A. S. Thomas and Z. Wu, “Comparative study of modular dual 3-phase permanent magnet machines with overlapping/non-overlapping windings,” IEEE Transactions on Industry Applications, vol. 55, no. 4, pp. 3566-3576, Jul. 2019.

[16] L. Rashkin, R. Matthews, J. Neely and N. Doerry, “Dynamic response comparison of dual-wound and single-wound machines in multi-bus power system architectures,” 2020 IEEE Transportation Electrification Conference & Expo (ITEC), 2020, pp. 784-788.

[17] N. Schofield, X. Niu and O. Beik, “Multiphase machines for electric vehicle traction,” 2014 IEEE Transportation Electrification Conference and Expo (ITEC), 2014, pp. 1-6.

[18] R. Yang, N. Schofield, N. Zhao, and A. Emadi, “Dual three-phase permanent magnet synchronous machine investigation for battery electric vehicle power-trains,” The Journal of Engineering, vol. 2019, no. 17, pp. 3981–3985, 2019.

[19] E. Mese, M. Ayaz, M. Tezcan, K. Yilmaz and E. Ozdemir, “A permanent magnet synchronous machine with motor and generator functionalities in a single stator core,” Compumag, Jul. 2013.

[20] L. J. Rashkin, J. C. Neely, S. F. Glover, T. J. McCoy and S. D. Pekarek, “Dynamic considerations of power system coupling through dual-wound generators,” 2017 IEEE Electric Ship Technologies Symposium (ESTS), Arlington, VA, 2017, pp. 493-500.

[21] J. C. Neely, L. J. Rashkin, S. F. Glover, D. G. Wilson, N. Doerrty and T. Mccoy, “Dynamic response evaluation of a 20 MW scale dual wound machine based power system,” Advanced Machinery Technology Symposium Conference, Mar. 2018.

[22] B. Yin, X. Pei, X. Zeng, F. Eastham, C. Hodge and O. Simmonds, “Design and analysis of dual wound machine for electric ships,” 2020 International Conference on Electrical Machines (ICEM), 2020, pp. 104-110.

[23] J. F. Eastham, T. Cox and J. Proverbs, “Application of planar modular windings to linear induction motors by harmonic cancellation,” IET Electric Power Applications, vol. 4, no. 3, pp. 140-148, Mar. 2010.

[24] C. G. Hodge, J. F. Eastham and A. C. Smith, “The harmonics analysis of machine excitation,” Int. Naval Engineering Conf. (INEC), Edinburgh, May. 2012.

[25]J. F. Eastham and C. G. Hodge “The harmonics analysis of machine phase windings,” Int. Naval Engineering Conf. (INEC), Glasgow, May. 2014.

[26] B. Yin, X. Pei, J. F. Eastham, H. Wang, C. Hodge, O. Simmonds, C. Vagg and X. Zeng, “Magnetic decoupling of winding design in dual wound generators,” IEEE Transactions on Energy Conversion, 2022.

[27] B. Yin, X. Pei, J. F. Eastham and X. Zeng, “Analysis of stator end-winding in a dual wound machine using Biot-Savart law,” The 11th International Conference on Power Electronics, Machines and Drives (PEMD), Newcastle, Jun. 2022.

Chapter 5.

A novel fast operating moving coil actuator with a compensation coil for HVDC circuit breakers

Chapter contents:

This chapter introduces a novel design of a moving coil actuator topology with compensation coils for DC circuit breakers. The compensation coils eliminate the saturation in the magnetic core, reduce system equivalent inductance, thus increase the operating speed.

5.1. Chapter summary

Conventional AC systems have a lower efficiency and higher cost when considering long-distance power transmissions [1]-[3]. With the development of DC transmission networks, a more economical and energy-efficient solution for long-distance power transmission is achievable, which is important for the development of renewable energy systems deployment [1], [5]. However, the design of DC circuit breakers is regarded as the main limitation to the implementation of DC transmission systems [6]. The design of a DC circuit breaker is generally more complex than an AC circuit breaker due to no natural zero-crossing point and the high rate of rise of a fault current.

This chapter proposes a novel moving coil actuator topology for DC circuit breakers, which applies additional compensation coils to an original moving coil actuator design. The compensation coils generate an opposite magnetic field against the magnetic field produced by the moving coils, which effectively eliminates the saturation in the magnetic core. This topology significantly reduces the system equivalent inductance, and therefore achieves a higher rate of rising excitation current in the moving coils, which results in a faster actuating speed. The dynamic performance is compared between an original moving coil actuator and the actuators with compensation coils. 2D finite element analysis is used to investigate the actuators performance in terms of magnetic field, excitation current, moving force and efficiency.

The rest of this chapter is cited from the author's published article in CSEE Journal of Power and Energy Systems [111]. The structure of this chapter is organised in an alternative-based format, where the indices, equations, tables, figures, titles and references are numbered independently.

Statement of Authorship

<table>
<tr><td colspan="4">This declaration concerns the article entitled:</td></tr>
<tr><td colspan="4">A Novel Fast Operating Moving Coil Actuator with a Compensation Coil for HVDC Circuit Breakers</td></tr>
<tr><td colspan="4">Publication status (tick one)
Draft manuscript [ ] Submitted [ ] In review [ ] Accepted [ ] Published [√]</td></tr>
<tr><td>Publication details (reference)</td><td colspan="3">B. Yin, X. Zeng, J. F. Eastham, D. Vilchis-Rodriguez and X. Pei, "Novel fast operating moving coil actuator with compensation coil for HVDC circuit breakers," in CSEE Journal of Power and Energy Systems, vol. 7, no. 5, pp. 1041-1050, Sept. 2021, doi: 10.17775/CSEEJPES.2020.06910.</td></tr>
<tr><td colspan="4">Copyright status (tick the appropriate statement)
I hold the copyright for this material [ ] Copyright is retained by the publisher, but I have been given permission to replicate the material here [√]</td></tr>
<tr><td>Candidate's contribution to the paper (provide details, and also indicate as a percentage)</td><td colspan="3">The candidate contributed to / considerably contributed to / predominantly executed the…
Formulation of ideas:
● 80%
● Introducing a novel moving coil actuator topology with compensation coils for DC circuit breakers, guided and supervised by Dr Xiaoze Pei.
Design of methodology:
● 100%
● A 2D finite element model is built and simulated in COMSOL, investigating the dynamic performance of the moving coil actuator with compensation coils, guided by Dr Xiaoze Pei.
Experimental work:
● 100%
Presentation of data in journal format:
● 80%
● Organising and writing this article, revised by Dr Xiaoze Pei and other co-authers</td></tr>
<tr><td>Statement from Candidate</td><td colspan="3">This paper reports on original research I conducted during the period of my Higher Degree by Research candidature.</td></tr>
<tr><td>Signed</td><td>Boyuan Yin</td><td>Date</td><td>25/11/2022</td></tr>
</table>

B. Yin, X. Zeng, J. F. Eastham, D. Vilchis-Rodriguez and X. Pei, "Novel fast operating moving coil actuator with compensation coil for HVDC circuit breakers," in CSEE Journal of Power and Energy Systems, vol. 7, no. 5, pp. 1041-1050, Sept. 2021, doi: 10.17775/CSEEJPES.2020.06910. Published open access with a CC BY-NC-ND licence.

A Novel Fast Operating Moving Coil Actuator with a Compensation Coil for HVDC Circuit Breakers

Boyuan Yin, Xianwu Zeng, John F. Eastham, Damian Vilchis-Rodriguez and Xiaoze Pei

Abstract— DC circuit breakers are major enabling components for multi-terminal HVDC systems. Their key design targets are operating speed and efficiency. This paper proposes a novel moving coil actuator using a compensation coil topology to operate mechanical circuit breakers. This topology aims to significantly improve the magnetic field saturation and reduce the system inductance, so that the operating speed is increased. Four possible connection methods for the compensation coils are proposed and analyzed using finite element modelling, ensuing simulation results are compared and discussed. The operating speed of the moving coil actuator with compensation coils is significantly improved compared with the original moving coil actuator. The moving coil actuator with compensation coils can open a distance of 5 mm within 2.8 ms and the peak efficiency is 47%.

Index Terms— Compensation coil, DC circuit breaker, HVDC, mechanical circuit breaker, moving coil actuator.

5.2. Introduction

High voltage direct current (HVDC) systems provide an economical and energy-efficient solution for long-distance bulk power transmission [1]–[3]. This significantly supports the development of renewable energy, transmitting abundant power from remote resources to the cities with high power demands. Offshore wind power is an important means for realizing energy structure reforms, and HVDC transmission technology is the key solution to enable offshore wind power grid connections. Large numbers of offshore wind farms have been established based on HVDC remote power transmissions [4]. The United Kingdom currently has more than one hundred offshore wind farms under operation, which provide significant energy for industrial use [5]. In China, Zhangbei, the multi-terminal VSC-HVDC project in the Beijing – Tianjin – Hebei area operating at +/- 500 kV and up to 4500 MW, enables the integration of renewable energy in a transmission ring and ensures the optimization of power flow [6]. A 535 kV HCB has been developed by NR Electric Co., Ltd. for Zhangbei project, which introduces the first commercial HCB at 500 kV level [7], [8].

The HVDC circuit breaker, as an important component in the system, which faces the challenge of providing strong fault-clearance capability within a short period of time. The solid-state circuit breaker based on IGBT components is able to break the fault current in less than a few hundred micro-seconds [9]-[11]. However, it has limited overcurrent capability [1], and high conduction losses under normal operating conditions [12]-[16]. In contrast, the mechanical circuit breaker has low conduction losses, which reduces the power losses during normal operations. The mechanical circuit breaker uses a pre-charged capacitor to create the artificial zero-crossing point. The operating speed of the mechanical circuit breaker is limited especially for small current interruptions, caused by the pre-charged capacitor [17], [18]. The hybrid circuit breaker is designed to achieve fast HVDC current interruption with less losses than the solid state HVDC breaker under

normal operations [19], [20]. Research is proposed to investigate new circuit breaker topologies [21]–[23], control methods [23], and consider the application of superconductor materials [25], [26]. Since the semiconductor circuit breakers are much faster than the mechanical, the breaking time of hybrid DC circuit breakers largely depends on the operating speed of the mechanical breaker. It is therefore important to design a fast-operating actuator with high efficiency and high reliability.

Typical actuators, such as the permanent magnet actuator, the Thomson coil actuator, the moving magnet actuator, and the moving coil actuator are commonly used for circuit breakers. The permanent magnet actuator is a typical linear actuator that is widely used in various industrial processes with low manufacturing and maintenance costs [27]–[30]. However, the operational speed of the permanent magnet actuator is limited. The Thomson coil actuator is used for ultra-fast operations [31]–[33], however, the operating efficiency is limited due to the decreasing linked magnet flux density and force between the coil and armature as the gap increases [34]–[36]. Given its relatively low moving mass and constant air-gap design, the moving coil actuator has great potential to achieve fast operating speeds. The excited coil produces an electromagnetic force in a magnetic field produced by permanent magnets following Lorenz's law. The moving coil actuator has been proved to have better dynamic performance than the moving magnet actuator due to its higher force density, which makes it more suitable for vacuum interrupter applications [37], [38]. However, the moving coil actuator has a large coil inductance, which limits the rise of current in the coil and therefore the operating speed. Also, the high operating current produces a high magnetic field, which leads to saturation in the magnetic core. In addition, the magnetic field changes when the coil is energized, which produces eddy current losses in the magnetic core.

This paper proposes a novel moving coil actuator topology, which applies a group of compensation coils to the original moving coil actuator. The compensation coils generate

an opposing magnetic field, which reduces the impact of the magnetic field produced by the moving coils when they are energized. The equivalent coil inductance is significantly reduced by the compensation coils and therefore, the rise of current in the coil is much faster and so is the actuation. By implementing the compensation coils, the magnetic field in the magnetic core does not change when the moving coil is energized during the opening and closing operations. This idea is similar to the compensation winding in DC machines to eliminate armature reaction. A similar design was investigated by Mikhail Godkin in 2004, this applied three compensating coils with different power supplies, and a position sensor to accurately control the current in the coils [39]. Passive compensation with closed-loop supplied coils placed next to the moving coils is proposed in this paper for the first time. The closed-loop coils can also be replaced by solid copper rings to achieve a similar effect. Four possible connection methods for compensation coils are proposed, namely, passive compensation, series connection, parallel connection, and hybrid connection. The current, force, efficiency, operational speed, and displacement are compared for these connections.

The remainder of this paper is structured as follows. Section II introduces the operating principle of moving coil actuators with compensation coil topology. Section III employs finite element modeling to compare the actuator operating performance for the four different connection methods with the original actuator. Section IV discusses the simulation results and summarizes the advantages and disadvantages of the moving coil actuator with compensation coils. Section V provides our conclusions.

5.3. Moving coil actuator with compensation coils for hybrid DC circuit breakers topology

5.3.1. Vacuum interrupter specification

Air, oil, and sulfur hexafluoride (SF_6) are commonly used in circuit breakers. However, vacuum breakers have become the most widely used because they are more environmentally friendly [40]. A vacuum interrupter is basically a mechanical switch as shown in Fig. 5-1. A moving contact and a fixed contact are located at the ends of a ceramic high vacuum arcing chamber. This is supported by ceramic insulators, one of which encloses bellows to support the movement of the contact [41]. An external actuator is used to connect with and operate the moving contact. This controls the opening and closing operation of the interrupter and is able to hold it in the open and closed positions.

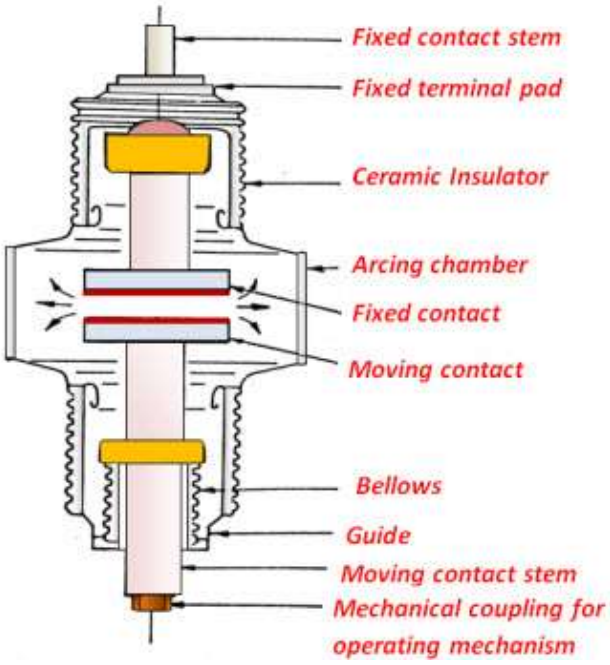

Fig. 5-1 Vacuum interrupter diagram [45]

The vacuum interrupter used in this paper is the TJC241-type, supplied by Shanxi

Baoguang Electric Device Company, which has voltage and current ratings of 3.6 kV and 1.25 kA. The separation distance between the two contacts is 2 mm. The weight of the moving part is 0.3 kg and the force required to hold contacts open at full stroke is 175 N. It is important that the actuator designed for the duty should be able to avoid contact popping, bounce, rebound, and welding. The operating distance for the actuator is 5 mm when the mechanical connections between the vacuum interrupter and the actuator are taken into account. This extra operating distance can be buffered and absorbed by the auxiliary mechanical structure.

5.3.2. Original moving coil actuator

The moving coil actuator has the same operating principle as a loudspeaker, and is also called a voice coil actuator [42]. Fig. 5-2 shows the radial plane of the axisymmetric topology. The actuator comprises a permanent magnet, two moving coils, and three soft magnetic composite (SMC) blocks. The two moving coils make full use of the magnetic field in both air gaps and achieve a more compact design when compared with a single coil. The permanent magnet generates the magnetic field in both upper and lower air gaps through the SMC cores. During normal operations, there is no current through the moving coils, so the vacuum interrupter maintains an open or closed position. When the coils are energized by a pre-charged capacitor, a Lorentz force, which is proportional to the current, is induced in the coils. This force can drive the actuator's moving parts in either direction, depending on the direction of the injected current. In Fig. 5-2, for example, the moving coils have a force to move downwards according to Fleming's left-hand rule.

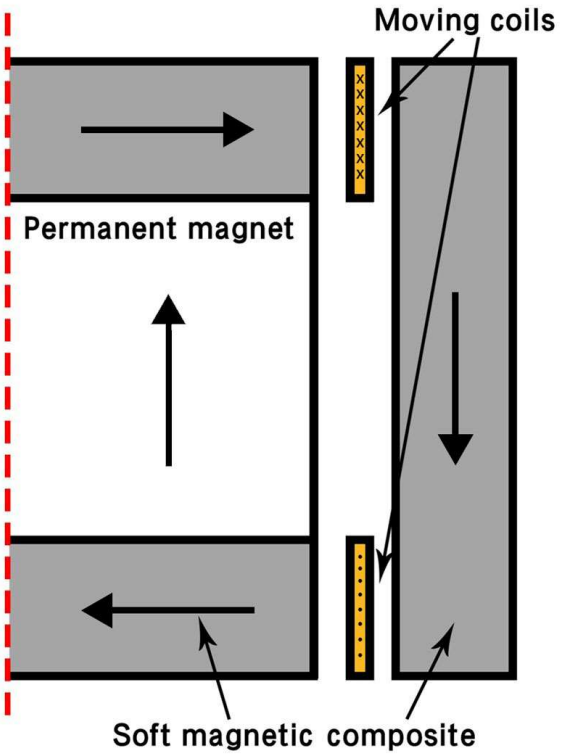

Fig. 5-2 Original moving coil actuator topology

The operating speed of a moving coil actuator depends on the electromagnetic force, which can be expressed as:

$$F_{mag} = B_g I l \qquad (5-1)$$

Where:

B_g: the air gap flux density produced by the magnet

I: the current through the coil

l: the coil length

R_c: the coil resistance

The coil length for this model is defined as the wire length that formed the coil, which can be expressed as:

$$l = 2\pi rN \qquad (5-2)$$

Where:

r: the coil radius

N: the coil number of turns

The B_g and l are both constants depending on the design. The coil current, therefore, is the key factor to change the force on the coil and therefore the operating speed. The coil voltage can be expressed as:

$$V_L(t) = L\frac{di_L}{dt} + R_c i_L \qquad (5-3)$$

In order to increase the rate of rise of current, one method is to reduce the coil inductance. Based on the moving coil actuator topology, there are three ways to reduce the coil inductance. The first is to reduce the number of turns, which in turn reduces the electromagnetic force. The second is to reduce the coil radius, which again reduces the force. The third method that is proposed here is to provide a compensation coil group to oppose and reduce the magnetic field produced by the moving coils. This is similar in concept to that of bifilar wound non-inductive coils.

5.3.3. Moving coil actuator with compensation coil topology

The compensated moving coil actuator topology includes two compensation coils as shown in Fig. 5-3. The two compensation coils are fixed to the top and bottom SMC blocks and have the same number of turns as the moving coils.

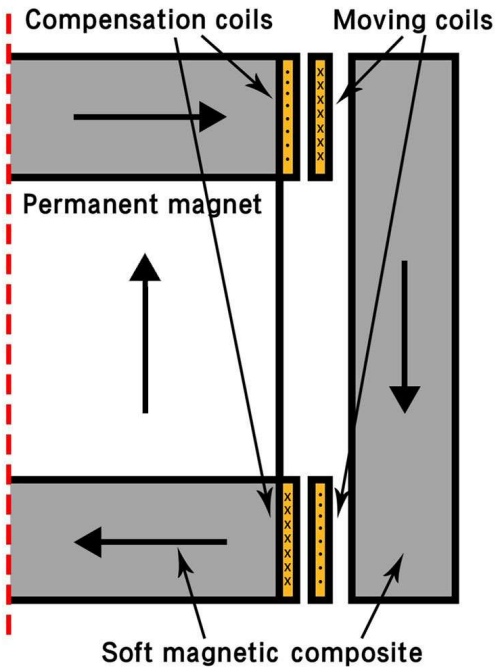

Fig. 5-3 Moving coil actuator with compensation coils topology.

The current through the compensation coils follows that in the moving coils but in the opposite direction, and produces an opposing magnetic field to oppose and reduce the magnetic field generated by the moving coils. The magnetic field in the SMC blocks is therefore maintained at the value produced by the permanent magnets to eliminate saturation. The action of the compensation coils can also be explained by their generation of mutual inductance with the moving coils which reduces the total system equivalent inductance, to achieve a higher rate of rise of current during the opening and closing operations. In summary, the proposed moving coil actuator with compensation coils has the following advantages. The magnetic field in the magnetic core does not change and the effective coil inductance is reduced. This leads to increased rate of rise of current and therefore operating speed of the moving coil actuator with compensation coils.

To generate current in the compensation coils, there are four possible connection methods. The first is passive compensation, in which the two compensation coils are

short-circuited as shown in Fig. 5-4 (a). When the moving coils are energized, there will be induced current generated in the compensation coils reducing the magnetic field.

The second and third connection methods are series connection as shown in Fig. 5-4 (b) and parallel connection as shown in Fig. 5-4 (c). The benefit of series connection is that the current in the compensation coil is the same as the moving coil, which provides excellent magnetic field cancellation. However, the inductance of the series connection is higher than that of the parallel connection. The parallel connection can achieve the smallest system inductance, but cannot guarantee that the currents in the moving and compensation coils are the same, which means that the changing magnetic field is not fully compensated. It also requires a capacitor with a higher current rating to support the large total current through the four coils.

Another method is the hybrid connection as shown in Fig. 5-4 (d), which connects the compensation coil and the corresponding moving coil in series, then connects the two groups in parallel. This connection method can ensure each coil group has the same current and reduces the system inductance by parallel connection.

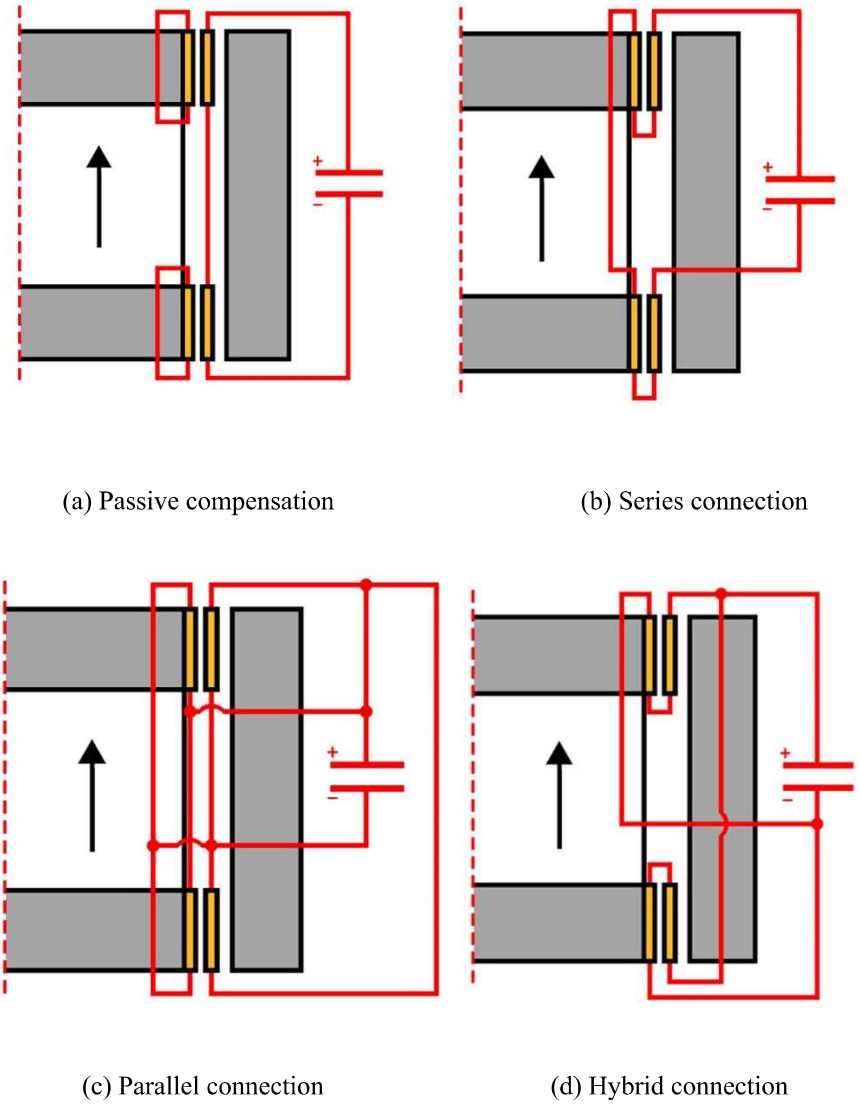

(a) Passive compensation (b) Series connection

(c) Parallel connection (d) Hybrid connection

Fig. 5-4 Connection method for moving coils and compensation coils

5.4. Finite element modelling and results analysis

5.4.1. Modelling method

Finite element analysis (FEA) was carried out by a 2-D axisymmetric model in COMSOL, using partial differential equations (PDE). FEA simulation had shown excellent agreement between numerical and experimental results in original moving coil actuators [35]. The COMSOL model simulation is built based on Maxwell's field equations (5-4) –

(5-7):

$$\nabla \cdot E = \frac{\rho}{\varepsilon_0} \quad (5-4)$$

$$\nabla \cdot B = 0 \quad (5-5)$$

$$\nabla \times E = -\frac{\partial B}{\partial t} \quad (5-6)$$

$$\nabla \times B = \mu_0 \left(J + \varepsilon_0 \frac{\partial E}{\partial t} \right) \quad (5-7)$$

where E is the electrical field, ρ is charge density, B is magnetic flux, and J is charge density in the coils.

During the operational process, the energy stored in the capacitor is used to inject a large current pulse in the coils. The equivalent circuit includes a capacitor (C) and moving coils (R_c L_c) coupled with compensation coils (R_w L_w) as shown in Fig. 5-5. The circuit equation can be expressed as:

$$R_c I_c + L_c \frac{dI_c}{dt} + M \frac{dI_w}{dt} = U_c \quad (5-8)$$

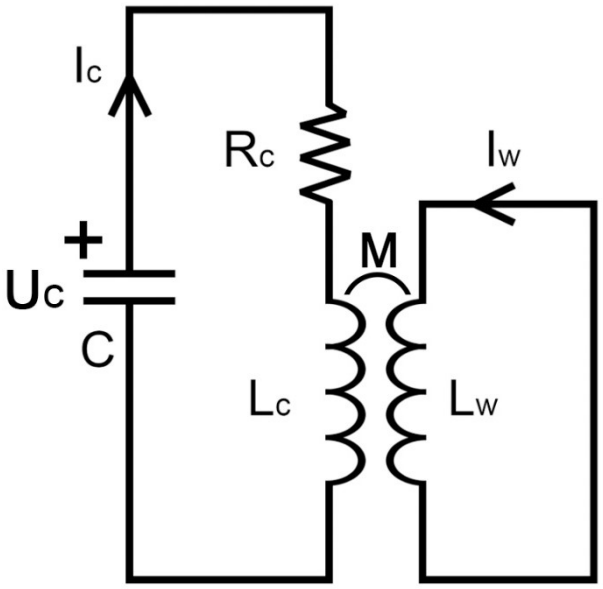

Fig. 5-5 Equivalent circuit of moving coil actuator with compensation coil

The electromagnetic force can be derived using the Lorentz force as:

$$F = \int_0^l \vec{B} \times \vec{J}\, dl \qquad (5-9)$$

The efficiency of the actuator is defined as the increase of the kinetic energy over the decrease of the energy stored in the capacitor, which is as shown in equation (5-10).

$$\eta = \frac{\Delta E_k}{\Delta E_c} = \frac{\frac{1}{2} m({v_t}^2 - {v_0}^2)^2}{\frac{1}{2} C\left({U_t}^2 - {U_0}^2\right)} \qquad (5-10)$$

Where E_k is the kinetic energy of the moving part. E_c is the energy stored in the capacitor. m is the mass of the moving part. v is the velocity of the moving part. U is the voltage across the capacitor.

5.4.2. Finite element modelling

The essential topology of the moving coil actuator with compensation coils is introduced

in Fig. 5-3, where the magnetic field is fully used by the coils in the two airgaps. The size of the actuator is not significant for this prototype design but is determined by the magnetic field saturation in the magnetic core. A large cylindrical permanent magnet is applied, which means more steel is required. A larger magnetic steel generally provides a greater efficient area to support the magnetic fluxes, which can reduce the saturation. For this prototype, the size of the magnetic steel is designed to minimize the saturation. However, the size of the magnetic cores also determines the size of the coils, which affects the coil length, coil inductance, and even the mass of the moving part. Thus the FEM simulation should be analysed to investigate the reasonable sizes of the topology.

The total weight of the proposed prototype is not concerned in this design. The material used for the actuator should be considered to have the potential to operate in a cryogenic electric aircraft environment.

A common ground is established by using the same topology, size, materials, and external supply to investigate the performance of the moving coil actuator with compensation coils and compare the different connection methods. The actuators are designed for a TJC241-type vacuum interrupter supplied by Shanxi Baoguang Electric Device Company as introduced in the previous section, the key parameters of which are shown in Table 5-1. The actuator designed is expected to separate the two contacts by 5 mm considering the rebound and buffer structures.

The moving coil actuator was broadly optimized and has a height of 90 mm, and a radius of 70 mm. Neodymium Iron Boron (NdFeB) N50-type from the Eclipse Magnetics company was used for the design, which has a remanent flux density, Br, of 1.4 T [43]. The cylindrical permanent magnet has a height of 50 mm and a radius of 45 mm. The soft magnetic composite used is Symmco's Somaloy 1000-SP [44]. In order to compare the moving coil actuators with differently connected compensation coils, the air gap is increased to 7 mm to allow space for the compensation coils and the supporting structure.

The magnetic field in the air gap is designed to be 0.85 T at steady state. The compensation coils and moving coils are both double-layered with 37 turns. The two compensation coils are fixed onto the top and bottom SMC cores. The moving coils are fixed on the moving structure carrying the moving contact of the vacuum interrupter. A 20 mF capacitor is pre-charged to 50 V to provide the excitation current for the moving coils and the compensation coils when they are used. Table 5-1 lists key parameters of the actuator.

TABLE 5-1

ACTUATOR KEY PARAMETERS

Parameter	Value
Actuator height	90 mm
Actuator radius	70 mm
Permanent magnet height	50 mm
Permanent magnet radius	45 mm
Permanent magnet remanent flux density	1.4 T
Air gap length	7 mm
Magnetic field in the air gap	~0.85 T
Moving coil number of turns	37
Compensation coil number of turns	37
Coil wire cross-section area	1 mm2
External capacitance	20 mF
Capacitor voltage	50 V

5.4.3.Magnetic field analysis

During the actuator opening and closing process, the current through the moving coils generates a changing magnetic field, which is superimposed on the constant magnetic field produced by the permanent magnet. This changing magnetic field could cause additional saturation. The compensation coil groups can eliminate this influence by opposing and reducing the changing magnetic field.

Fig. 5-6 (a) shows the initial steady state magnetic field distribution produced by the permanent magnet. When the current flows into the moving coils and reaches 60 A, the magnetic field distribution for the original moving coil actuator is shown in Fig. 5-6 (b). It can be seen that the magnetic field around the SMCs core edges is significantly enhanced and saturated. To improve this saturation, a pair of passive compensation coils are added in the corresponding location of the two moving coils as shown in Fig. 5-6 (c). The induced current in the passive compensation coils generates an opposite magnetic field to reduce the moving coil magnetic field. It can be seen that the edges of the SMCs core are less saturated. Fig. 5-6 (d) displays the magnetic field using the series connection. The compensation coils and moving coils are series connected to ensure that they have the same current and fully compensate the magnetic field produced by the moving coils. Fig. 5-6 (e) shows the magnetic field with the parallel connected compensation coils. Due to the small differences between the radius of compensation coils and moving coils, they present different inductances, which results in the magnetic field being not fully compensated. Fig. 5-6 (f) shows the magnetic field distribution of the hybrid connection. Due to the corresponding compensation coil and moving coil being series connected, compensation magnetic fields are generated respectively on the top and the bottom coil regions. The changing magnetic field is effectively eliminated. It is clear that the moving coil actuators with compensation coils, in general, shows less saturation in the SMC cores compared with the original one when the moving coil is energized with the same current of 60 A.

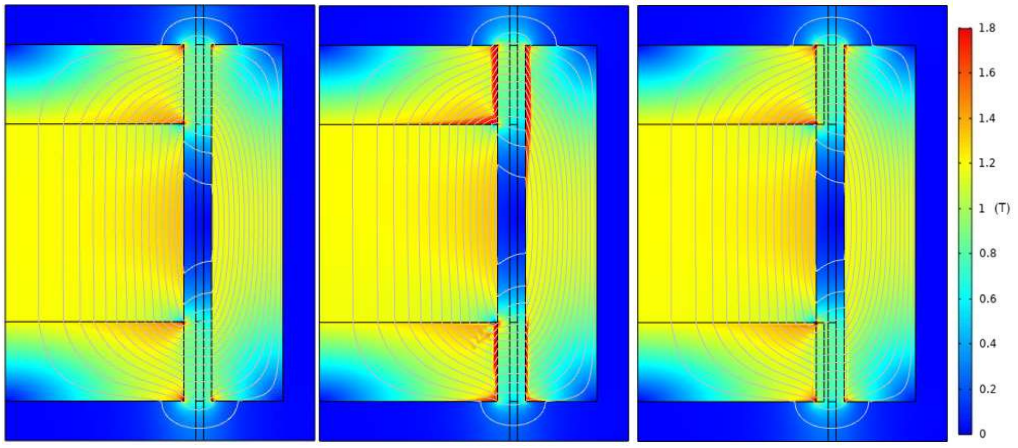

(a) (b) (c)

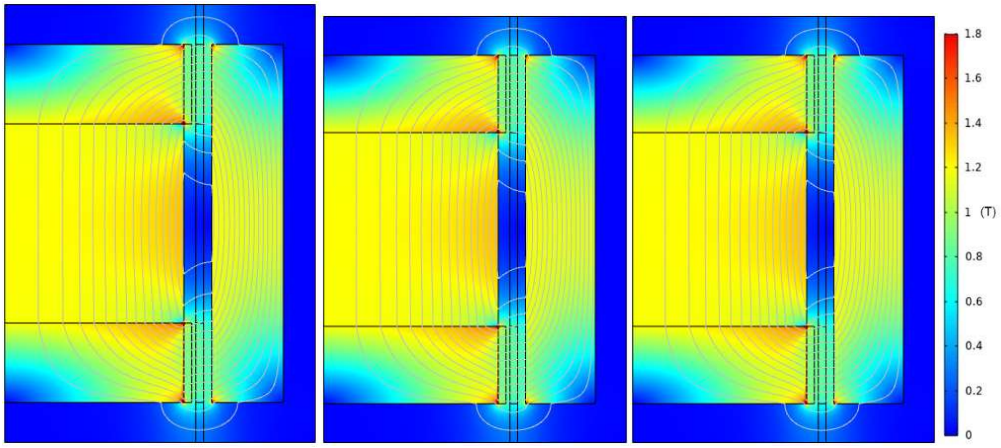

(d) (e) (f)

(a) Steady state magnetic field produced by the permanent magnet

(b) Original moving coil actuator

(c) Passive connection moving coil actuator with compensation coils

(d) Series connection moving coil actuator with compensation coils

(e) Parallel connection moving coil actuator with compensation coils

(f) Hybrid connection moving coil actuator with compensation coils

Fig. 5-6 Magnetic field distribution with coil current of 60A

In summary, the compensation coils are able to reduce the impact of the magnetic field

produced by the moving coil when energized, this effectively reduces the moving coil inductance and avoids saturation of the core. The passive compensation and parallel connections reduce the magnetic field from the moving coils even though the current in them is not exactly the same, while the series connection and hybrid connection can fully compensate.

5.4.4. Current analysis

The electromagnetic force is the key factor to determine the actuator operating speed. The force is decided by the current through the moving coils. Fig. 5-7 shows the simulation results of the moving coil current in the first 4 ms. It can be seen that the original moving coil actuator has the lowest rate of rise of current. The passive connection and series connection actuator have almost the same rate of rise of current. The hybrid connection actuator has a fast rate of rise of current and high peak current. The current in the parallel connection coils rises fastest with the highest peak current value.

The compensation coils and moving coils form a non-inductive coil. With lower equivalent inductance, the rate of rise of the current and peak current are both increased. The parallel connection not only provides high excited current for the compensation coils, but also reduces the circuit equivalent inductance. In this case, the parallel connection actuator has the smallest inductance, which makes it have the fastest rate of rise of current with the highest peak current value. It is noted that the current through the parallel compensation coils decreases very quickly. The current is lower than the hybrid connection at t = 1 ms, and then lower than the three other connections at t = 1.4 ms. The parallel connection, although it has a fast rate of rise and high peak current, only has better performance in the first time period because the total energy in the pre-charged capacitor is the same for all cases. The parallel coil resistance will quickly consume the energy from the capacitor. The parallel connection actuator would have

better performance if the energy in the capacitor were increased.

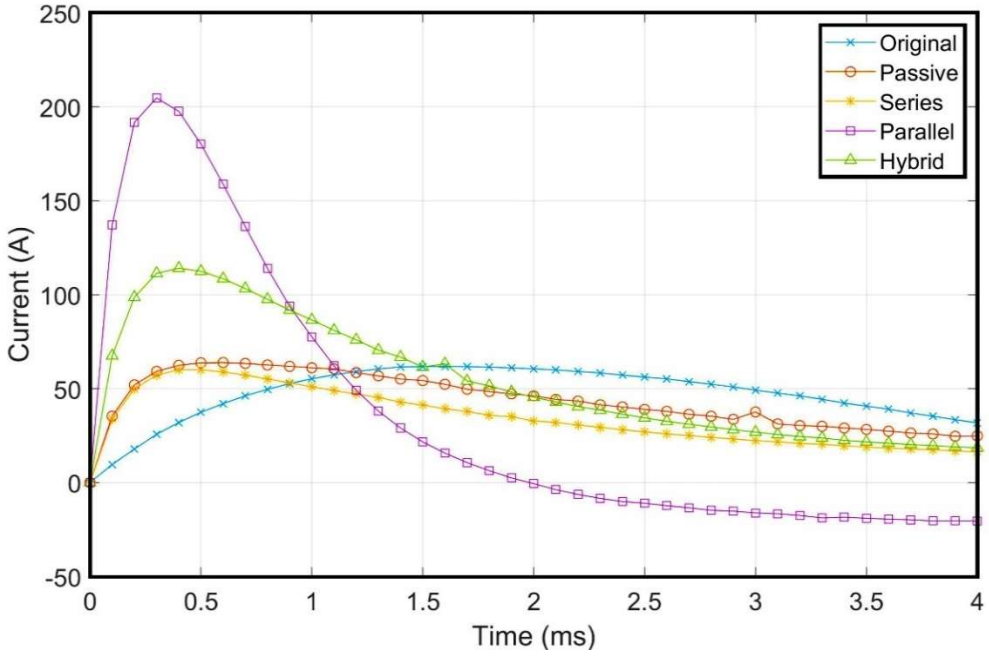

Fig. 5-7 Current in the moving coils against time

Compared with the original moving coil actuator, it can be seen that the rates of rise of current in the moving coils is improved by the compensation coils. Meanwhile, the series connection has the same rate of rise of current as the passive connection but with a lower peak current. After 1.2 ms, the current of both passive compensation and series connections is lower than the original actuator, which means that the compensation coils for these two connections are only effective in the first period, after which the acceleration will be slower than in the original actuator. If the capacitor energy is increased, the actuator with compensation coils will achieve longer acceleration time and better dynamic performance.

5.4.5.Force analysis

The electromagnetic force on the moving coils is determined by the current in the coil and magnetic field produced by the permanent magnet in the air gap. It is important to

investigate if compensation coils would reduce the electromagnetic force on the moving coils. A static test has been investigated by fixing the coils at their initial position, while a current from 0 A to 100 A is applied to the coils. The static electromagnetic force on the moving coils is as shown in Fig. 5-8.

It can be seen that the force for passive compensation coils is slightly higher than the original moving coil actuator. The increased electromagnetic force with compensation coils is due to less saturation in the magnetic core, leading to a slightly higher permanent magnet field in the air gap. The force for series, parallel and hybrid connected compensation coils is similar to the original moving coil actuator. This is a combined effect of less saturation in the magnetic core and the force from the magnetic field produced by the compensation coils.

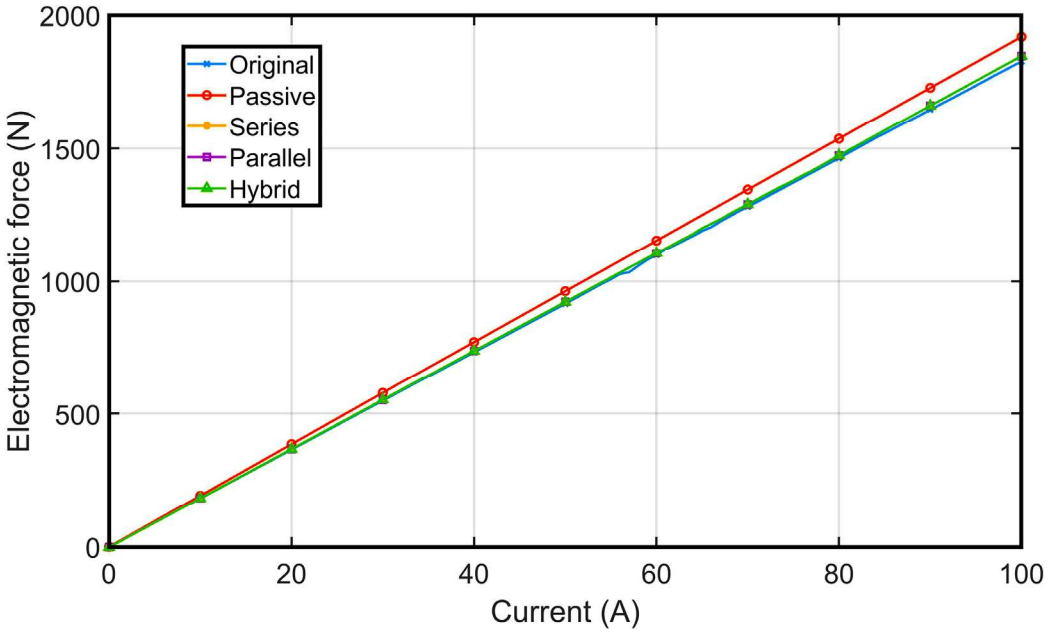

Fig. 5-8 Force on the moving part with linear current

Fig. 5-9 shows the force on the moving part during the dynamic opening operating process under the same conduction as the results shown in Fig. 5-7. The force has the same trend as the current in the moving coil. The actuator with parallel connected

compensation coils provides the fastest rate of rise of the force and the highest force due to the fast current rise. It is noted that the force on the parallel connection actuator reduces quickly and even has a negative force after t = 2 ms. This is because there is a negative current in the moving coil due to low current from the capacitor and slightly imbalanced coil inductance between the moving coil and compensation coil.

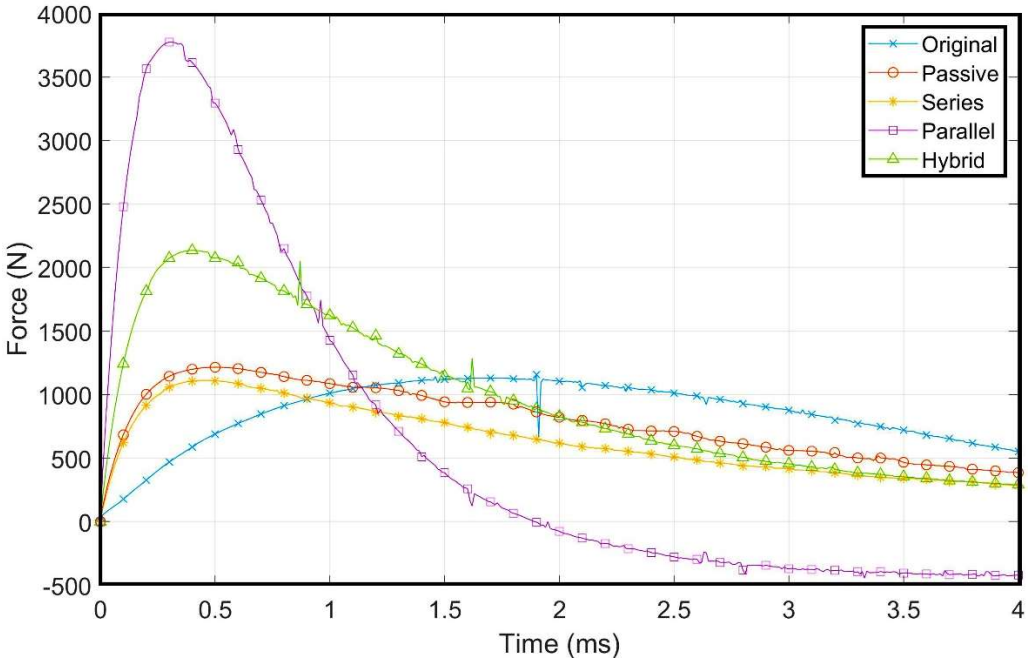

Fig. 5-9 Force on the moving part against time

5.4.6. Displacement analysis

The displacement of the actuators with time is simulated for 4 ms, as shown in Fig. 5-10. The actuators with compensation coils generally have better performance than the original moving coil actuator. The parallel connection and hybrid connection actuators have a faster operational speed than the other three actuators because of the relatively high operating current. As previously mentioned, the operating distance for the designed actuator is 5 mm considering the mechanical connections between the vacuum interrupter and the actuator. The original moving coil actuator and the series connection

actuator each need more than 4 ms to achieve 5 mm displacement, the original moving coil actuator is the slightly faster of the two. The passive compensation actuator reaches 5mm within 3.8 ms. The hybrid connection actuator achieves 5 mm within 3 ms and the parallel connection actuator within 2.8 ms. According to these results, the parallel connection actuator has the best displacement performance for this vacuum interrupter.

The displacement performance in Fig. 5-10 illustrates that the selection of the actuators can be different depending on the proposed operating distance. The parallel connection actuator achieves 6.2 mm at t = 3.5 ms, then it is exceeded by the hybrid connection actuator, this is because the parallel connection coil current reaches the peak in the first 0.5 ms and then drops very quickly. The overall performance of passive and series connection actuators is similar to the original moving coil actuator. It is noted that the original moving coil actuator operates slowly at the beginning, but exceeds the passive connection actuator at t = 3 ms, having the potential to surpass the series connection actuator in the later part of the action.

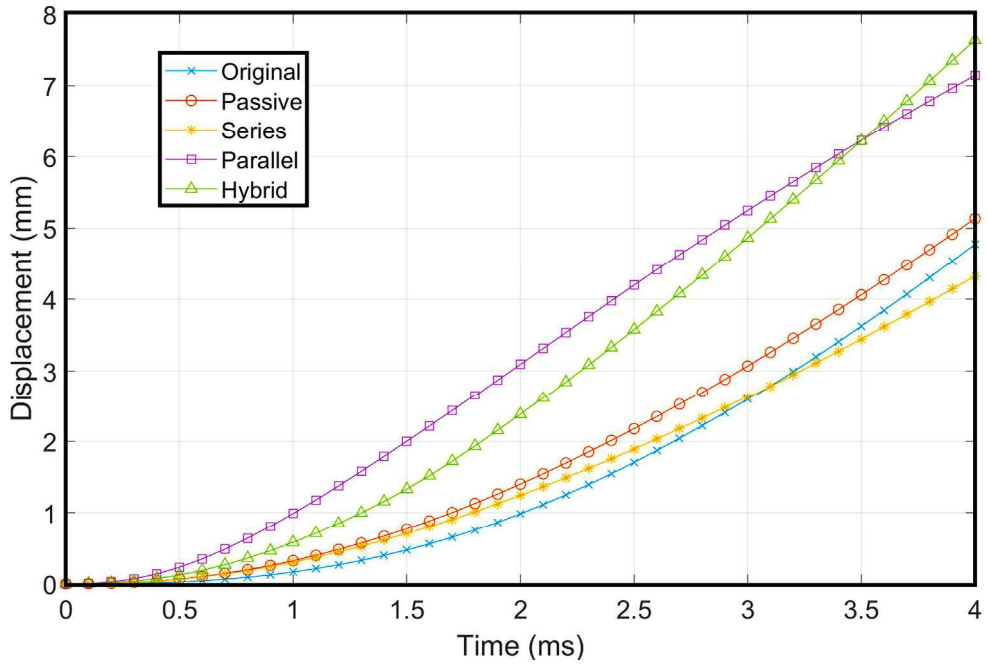

Fig. 5-10 Moving part displacement against time

5.4.7. Efficiency analysis

A high-efficiency actuator is preferred for the HVDC circuit breakers due to the challenge of energy harvesting. The efficiency of the actuator determines how many times the actuator can operate after each charge of the capacitor. Fig. 5-11 shows the comparison of efficiency between the five actuator topologies. The moving coil actuators with compensation coils have higher efficiency in the first 2 ms. The parallel connection actuator has a relatively low efficiency below 15%, which is due to the energy consumption by the high current in the compensation coils. The series and hybrid connection actuators have similar efficiency performances, which are better than the original actuator in the first 2 ms. The passive compensation actuator has the highest efficiency until t = 3 ms.

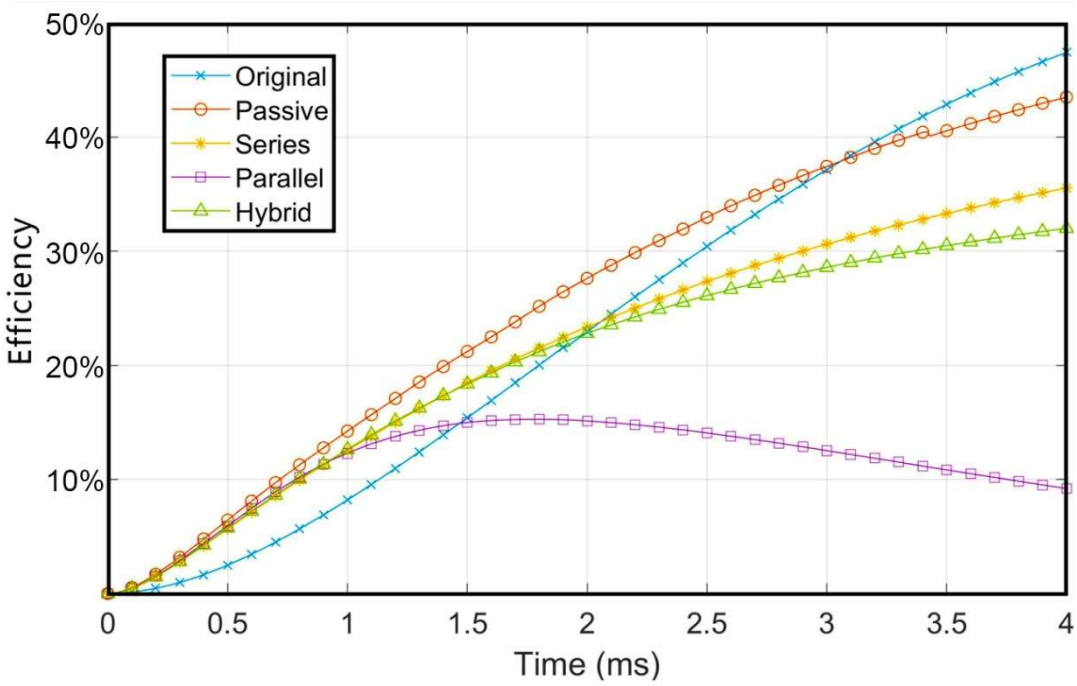

Fig. 5-11 Actuator efficiency against time

According to the results in the time domain, the passive compensation actuator has better efficiency performance if it is only required for a short operational time, while the

original moving coil actuator has higher efficiency when the operational time is longer.

In practical applications, there is more concern about the efficiency against the actuator displacement, rather than against time. Fig. 5-12 shows the efficiency against the displacement. It can be seen that the passive compensation and the original moving coil actuators have the highest efficiency. And the parallel connection actuator performs with the lowest efficiency. The efficiency of the passive compensation actuator is almost 4 times higher than the parallel connection actuator for the displacement of 5 mm.

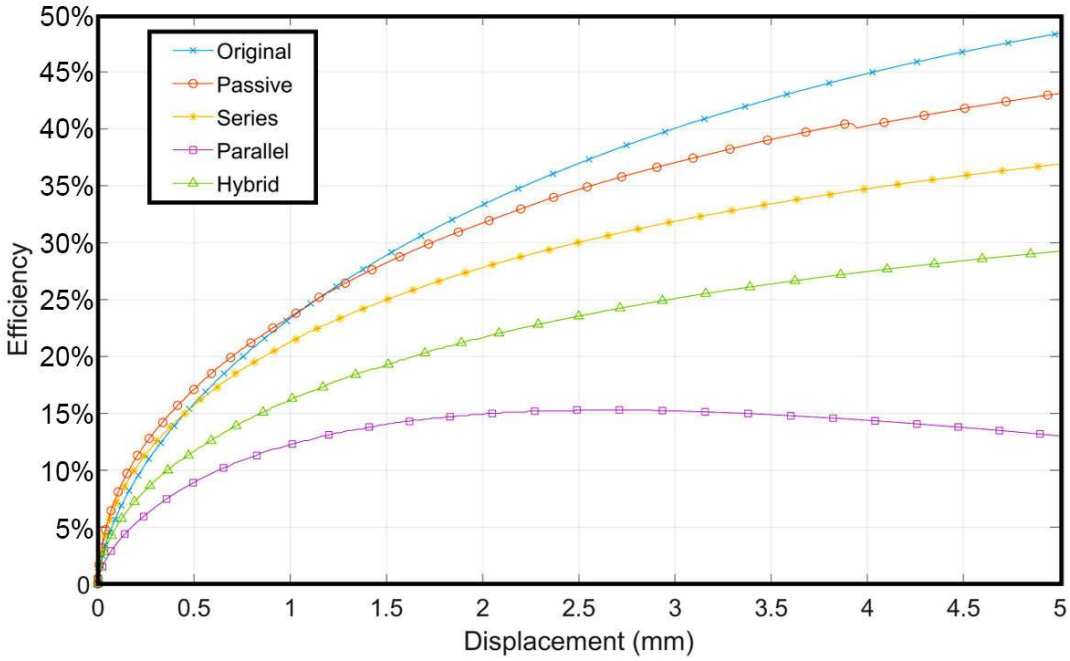

Fig. 5-12 Actuator efficiency against displacement

The breaking process consumes the energy stored in the pre-charged capacitor. Large energy consumption during the operational process requires frequent recharging for the capacitor, which is not preferred. Fig. 5-13 shows the capacitor voltage reduction during the operational process. The passive connection, series connection, and original moving coil actuators complete the breaking operation using the lowest energy from the capacitor. The hybrid connection actuator uses 43.1% of the capacitor energy, while the parallel

connection actuator uses 82.5% of the capacitor energy for one operation.

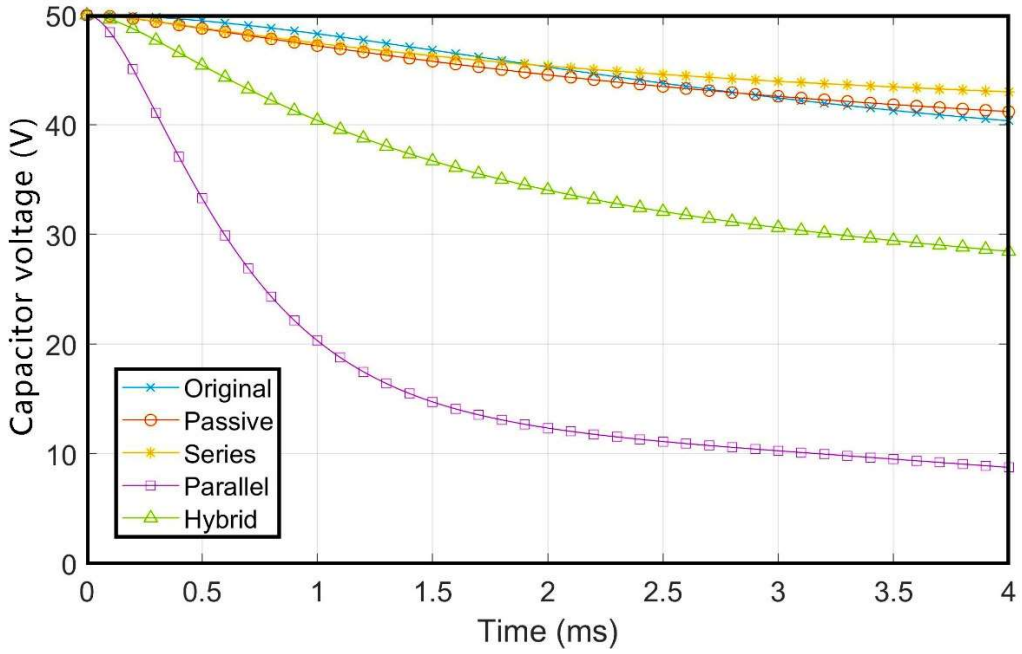

Fig. 5-13 Capacitor voltage against time

5.5. Performance comparison

The moving coil actuators with compensation coils have advantages and disadvantages compared with the original moving coil actuator. Overall, the moving coil actuators with compensation coils have faster operational speeds than the original moving coil actuator. The compensation coils effectively reduce the magnetic field generated by the moving coils, which can reduce saturation and eddy current loss in the SMCs. At the same time, the compensation coils significantly reduce the coil equivalent inductance, providing a faster rate of rise of the current in the coil. The moving coil actuators with compensation coils can achieve the target displacement within a shorter period of time.

Table 5-2 shows the quantitative comparison of the performance of actuators in terms of the rate of rise of current, peak current, peak force, opening time, energy consumption and efficiency for one operation.

The passive connection actuator is slightly faster than the original moving coil actuator and has higher operating efficiency, this makes it a good solution for the replacement of the original moving coil actuator. The series connection actuator provides the best magnetic field compensation, and achieves no changing flux from the moving coils when energized. However, the performance is not as good as the passive compensation in terms of both operating speed and efficiency. The parallel connection actuator has the fastest operation speed, but the lowest efficiency. The high operating current requires a capacitor with a higher current rating. Also, the energy consumed by the parallel connection for each operation is the highest, which means the capacitor needs to be recharged more frequently. The operational speed of the hybrid connection is lower than the parallel connection but much higher than the other actuators, while the operating current is relatively small, reducing the pressure on the system. The hybrid connection actuator maintains high efficiency without too much energy consumption in one operation. In summary, the passive connection moving coil actuator with compensation coils can be an alternative option giving faster speed than the original moving coil actuator. The parallel connection actuator can be used for an ultra-fast linear actuator.

TABLE 5-2

PERFORMANCE COMPARISON

	Original	Passive	Series	Parallel	Hybrid
Rate of rise of current (A/ms)	36.9	113.9	132.7	675.1	286.7
Peak current (A)	61.8	63.9	60.1	204.7	114.1
Peak force (N)	1159.2	1215.3	1111.5	3775.2	2135.0
Opening time (ms)	4.1	3.9	4.3	2.8	3.1
Energy consumption	19.5%	17.3%	14.5%	82.5%	43.1%
Efficiency	48.4%	43.1%	36.9%	13.0%	29.3%

5.6. Conclusions

This paper aims to investigate a fast-operating and highly efficient actuator for a vacuum interrupter. A new type of moving coil actuator with compensation coils is proposed. Finite element analysis results show the performance of the moving coil actuator using compensation coils is significantly improved. The compensation coils are able to increase the operating speed, and at the same time to eliminate the saturation of the core by reducing the moving coil magnetic field. Four possible connection methods for the compensation coils: passive connection, series connection, parallel connection and hybrid connection are investigated in this paper. In summary, the following conclusions can be drawn:

1) The compensation coils can effectively reduce the effective coil inductance, which achieves a faster rate of rise of the current in the moving coil and hence a faster operating speed. The compensation coils can also reduce the magnetic field produced by the moving coils to avoid eddy current loss and saturation.

2) The current in the compensation coils consumes energy, but the overall operating efficiency is still competitive. The passive connection actuator has the highest efficiency of 43.1%.

3) The moving coil actuator with parallel connected compensation coils offers the fastest operational speed of 2.8 ms opening time for displacement of 5 mm, which also has the largest operating force, reaching peak value of 3775.2 N.

The analysis of the moving coil actuator with compensation coils presented in this paper develops a new idea for actuator design, which has the potential to improve the actuator performance when applied to HVDC hybrid circuit breakers.

5.7. References

[1] N. Flourentzou, V. G. Agelidis, and G. D. Demetriades, “VSC-based HVDC power transmission systems: an overview,” IEEE Transactions on Power Electronics, vol. 24, no. 3, pp. 592–602, Mar. 2009.

[2] G. Li, T. An, J. Liang, W. Liu, T. Joseph, J. J. Lu, M. Szechtman, B. R. Andersen, and Y. L. Lan, “Power reversal strategies for hybrid LCC/MMC HVDC systems,” CSEE Journal of Power and Energy Systems, vol. 6, no. 1, pp. 203–212, Mar. 2020.

[3] G. Li, J. Liang, F. Ma, C. E. Ugalde-Loo, and H. F. Liang, “Analysis of single-phase-to-ground faults at the valve-side of HB-MMCs in HVDC systems,” IEEE Transactions on Industrial Electronics, vol. 66, no. 3, pp. 2444–2453, Mar. 2019.

[4] J. De Decker and P. Kreutzkamp. (2020, Jul.). Offshore electricity grid infrastructure in Europe. Brussels, Belgium. [Online]. Available: http://www.offshoregrid.eu

[5] 4Coffshore Database. (2020, Jul.). Offshore wind farms in the United Kingdom. [Online]. Available: https://www.4coffshore.com/windfarms/united-kingdom/

[6] ABB News. (2020, Jul.). ABB enables world’s first HVDC grid in China. Zurich, Switzerland. [Online]. Available: https://new.abb.com/news/detail/10464/abb-enables-worlds-first-hvdc-grid-in-china

[7] C. Dongming and Y. Bing, “500 kV commutation-based hybrid HVDC circuit breaker” Automation of Electric Power Systems, vol. 42, no. 7, pp. 102-107, 2018.

[8] B. Yang, D. Cao, W. Shi, W. Lv, W. Wang, and B. Liu, “A novel commutation-based hybrid HVDC circuit breaker,” in CIGRE Winnipeg Colloquium, 2017, pp. A3-15.

[9] C. Meyer and R. W. De Doncker, “Solid-state circuit breaker based on active thyristor topologies,” IEEE Transactions on Power Electronics, vol. 21, no. 2, pp. 450–458, Mar. 2006.

[10] L. Q. Zhang, R. Woodley, X. Q. Song, S. Sen, X. Zhao, and A. Q. Huang, “High current medium voltage solid state circuit breaker using paralleled 15kV SiC ETO,” in 2018 IEEE Applied Power Electronics Conference and Exposition (APEC), 2018, pp. 1706–1709.

[11] R. Rodrigues, T. S. Jiang, Y. Du, P. Cairoli, and H. X. Zheng, “Solid state circuit breakers for shipboard distribution systems,” in 2017 IEEE Electric Ship Technologies Symposium (ESTS), 2017, pp. 406–413.

[12] C. Meyer and R. W. De Doncker, “LCC analysis of different resonant circuits and solid-state circuit breakers for medium-voltage grids,” IEEE Transactions on Power Delivery, vol. 21, no. 3, pp. 1414–1420, Jul. 2006.

[13] R. Wang, B. Zhang, S. S. Zhao, L. Liang, and Y. Chen, “Design of an IGBT-series-based solid-state circuit breaker for battery energy storage system terminal in solid-state transformer, ” in IECON 2019-45th Annual Conference of the IEEE Industrial Electronics Society, Lisbon, Portugal, 2019, pp. 6677–6682.

[14] H. Pang, G. F. Tang, and Z. Y. He, “Evaluation of losses in VSC-HVDC transmission system,” in IEEE Power and Energy Society General Meeting-Conversion and Delivery of Electrical Energy in the 21st Century, Pittsburgh, PA, USA, Jul. 2008, pp. 1–6.

[15] J. Häfner and B. Jacobson, “Proactive hybrid HVDC breakers-A key innovation for reliable HVDC grids,” in CIGRE Session, Sep. 2011, pp. 1–9.

[16] C. Peng and A. Q. Huang, “A protection scheme against DC faults VSC based DC

systems with bus capacitors," in 2014 IEEE Applied Power Electronics Conference and Exposition-APEC 2014, Mar. 2014, pp. 3423–3428.

[17] R. Bini, M. Backman, and A. Hassanpoor, "Interruption technologies for HVDC transmission: State-of-art and outlook," in 2017 4th International Conference on Electric Power Equipment-Switching Technology (ICEPE-ST), Xi'an, 2017, pp. 318–323.

[18] S. Kamtip and K. Bhumkittipich, "Comparison between mechanical circuit breaker and solid state circuit breaker under abnormal conditions for low voltage systems," in 2015 18th International Conference on Electrical Machines and Systems (ICEMS), Pattaya, Thailand, Oct. 2015, pp. 1091–1096.

[19] J. M. Meyer and A. Rufer, "A DC hybrid circuit breaker with ultra-fast contact opening and integrated gate-commutated thyristors," IEEE Transactions on Power Delivery, vol. 21, no. 2, pp. 646–651, Apr. 2006.

[20] M. Callavik, A. Blomberg, J. Häfner, and B. Jacobson, "The hybrid HVDC breaker," ABB Grid Systems, Nov. 2012.

[21] A. Maistrello, E. Gaio, A. Ferro, M. Perna, C. Panizza, F. Soso, L. Novello, M. Matsukawa, and K. Yamauchi, "Experimental qualification of the hybrid circuit breaker developed for JT-60SA quench protection circuit," IEEE Transactions on Applied Superconductivity, vol. 24, no. 3, pp. 3801505, Jun. 2014.

[22] A. Shukla and G. D. Demetriades, "A survey on hybrid circuit-breaker topologies," IEEE Transactions on Power Delivery, vol. 30, no. 2, pp. 627–641, Apr. 2015.

[23] D. Keshavarzi, E. Farjah, and T. Ghanbari, "Hybrid DC circuit breaker and fault current limiter with optional interruption capability," IEEE Transactions on Power Electronics, vol. 33, no. 3, pp. 2330–2338, Mar. 2018.

[24] A. Mokhberdoran, O. Gomis-Bellmunt, N. Silva, and A. Carvalho, “Current flow controlling hybrid DC circuit breaker,” IEEE Transactions on Power Electronics, vol. 33, no. 2, pp. 1323–1334, Feb. 2018.

[25] X. Z. Pei, O. Cwikowski, A. C. Smith, and M. Barnes, “Design and experimental tests of a superconducting hybrid DC circuit breaker,” IEEE Transactions on Applied Superconductivity, vol. 28, no. 3, pp. 5000205, Apr. 2018.

[26] U. A. Khan, J. G. Lee, F. Amir, and B. W. Lee, “A novel model of HVDC hybrid-type superconducting circuit breaker and its performance analysis for limiting and breaking DC fault currents,” IEEE Transactions on Applied Superconductivity, vol. 25, no. 6, pp. 5603009, Dec. 2015.

[27] G. Krebs, A. Tounzi, B. Pauwels, D. Willemot, and F. Piriou, “Modeling of a linear and rotary permanent magnet actuator,” IEEE Transactions on Magnetics, vol. 44, no. 11, pp. 4357–4360, Nov. 2008.

[28] P. Jin, Y. Yuan, G. Jian, H. Y. Lin, S. H. Fang, and H. Yang, “Static characteristics of novel air-cored linear and rotary halbach permanent magnet actuator,” IEEE Transactions on Magnetics, vol. 50, no. 2, pp. 7024204, Feb. 2014.

[29] J. Wang, G. W. Jewell, and D. Howe, “Development of a novel spherical permanent magnet actuator,” in IEE Colloquium on New Topologies for Permanent Magnet Machines, London, UK, Jun. 1997.

[30] P. Jin, S. H. Fang, H. Y. Lin, Z. Q. Zhu, Y. K. Huang, and X. B. Wang, “Analytical magnetic field analysis and prediction of cogging force and torque of a linear and rotary permanent magnet actuator,” IEEE Transactions on Magnetics, vol. 47, no. 10, pp. 3004–3007, Oct. 2011.

[31] D. S. Vilchis-Rodriguez, R. Shuttleworth, and M. Barnes, “Experimental validation of a finite element 2D axial thomson coil model with inductance and resistance compensation,” in 13th IET International Conference on AC and DC Power Transmission (ACDC 2017), Manchester, May 2017, pp. 1–6.

[32] D. S. Vilchis-Rodriguez, R. Shuttleworth, and M. Barnes, “Finite element analysis and efficiency improvement of the Thomson coil actuator,” in 8th IET International Conference on Power Electronics, Machines and Drives (PEMD 2016), Glasgow, Apr. 2016, pp. 1–6.

[33] Y. Wu, Y. Wu, M. Z. Rong, F. Yang, J. Y. Zhong, M. Li, and Y. Hu, “A new thomson coil actuator: principle and analysis,” IEEE Transactions on Components, Packaging and Manufacturing Technology, vol. 5, no. 11, pp. 1644–1655, Nov. 2015.

[34] A. Bissal, J. Magnusson, and G. Engdahl, “Comparison of two ultra-fast actuator concepts,” IEEE Transactions on Magnetics, vol. 48, no. 11, pp. 3315–3318, Nov. 2012.

[35] A. Bissal, J. Magnusson, and G. Engdahl, “Electric to mechanical energy conversion of linear ultrafast electromechanical actuators based on stroke requirements,” IEEE Transactions on Industry Applications, vol. 51, no. 4, pp. 3059–3067, Jul./Aug. 2015.

[36] D. S. Vilchis-Rodriguez, R. Shuttleworth, and M. Barnes, “Double-sided Thomson coil based actuator: Finite element design and performance analysis,” in 8th IET International Conference on Power Electronics, Machines and Drives (PEMD 2016), Apr. 2016.

[37] X. Z. Pei, A. C. Smith, R. Shuttleworth, D. S. Vilchis-Rodriguez, and M. Barnes, “Fast operating moving coil actuator for a vacuum interrupter,” IEEE Transactions on Energy Conversion, vol. 32, no. 3, pp. 931–940, Sep. 2017.

[38] B. Y. Yin, X. Z. Pei, X. W. Zeng, and F. Eastham, “A comparison between moving magnet and moving coil actuators for vacuum interrupters,” in IECON 2019-45th Annual Conference of the IEEE Industrial Electronics Society, Lisbon, Portugal, Oct. 2019, pp. 5651–5656.

[39] M. Godkin, “Linear voice coil actuator with compensating coils,” U.S. Patent 6 713 904, Mar. 30, 2004.

[40] Y. Tian, J. Y. Xu, Y. Deng, Y. X. Wang, E. Dong and J. Y. Zou, “Development and type test of ZW-126/D2000-40 vacuum circuit breaker with controlled switching technology, ” CSEE Journal of Power and Energy Systems, Feb. 2020.

[41] Elprocus. Vacuum circuit breaker working and applications. [Online]. Available: https://www.elprocus.com/vacuum-circuit-breaker-working-applications/

[42] X. M. Feng, Z. J. Duan, Y. Fu, A. L. Sun, and D. W. Zhang, “The technology and application of voice coil actuator,” in 2011 Second International Conference on Mechanic Automation and Control Engineering, Hohhot, 2011, pp. 892–895.

[43] Eclipse Magnetics Ltd., “N38”, NdFeB magnets/neodymium iron boron magnets datasheet. [Online]. Available: https://www.eclipsemagnetics.com/site/assets/files/2418/ndfeb_neodymium_iron_boron-standard_ndfeb_range_datasheet_rev1.pdf

[44] Symmco INC., “Somaloy 1000-SP”, Soft magnetic composites (SMC) datasheet. [Online]. Available: https://629ea6a8-e6fb-47d9-a626-714ee3e565d5.filesusr.com/ugd/57a430_f04b6c55ec65496487d85762af87294d.pdf

[45] Electrical4U, “Vacuum circuit breaker or VCB and vacuum interrupter,” Oct. 2020.

Chapter 6.

A fast operating moving coil actuator with compensation coils for vacuum interrupters

Chapter contents:

This chapter proposes a design of a novel fast operating moving coil actuator with compensation coil topology for DC circuit breakers. A prototype of the designed actuator is built and experimentally tested with a vacuum interrupter. The performance of the moving coil actuator is demonstrated in terms of operating speed, capacitor voltage, coil current, displacement and energy consumption.

6.1. Chapter summary

Decarbonisation has been identified as one of the most significant targets by many countries and institutions. The development of hydrogen-powered electric aircraft, which can achieve zero emissions during flight, is significant to meet decarbonisation and sustainability targets. Onboard DC electric networks face a challenge of high and fast-rising DC fault currents caused by the large energy stored in capacitors and batteries. Reliable and fast-operating DC circuit breakers are therefore urgently needed. The operating speed of a hybrid DC circuit breaker, with low on-state losses, is depended on its mechanical switch.

This chapter proposes the design of a novel fast operating moving coil actuator with compensation coil topology for circuit breaker applications. The actuator topology is simulated in 2D finite element modelling using COMSOL, to investigate the magnetic field distribution and dynamical performance. A prototype of the moving coil actuator is designed, built, and experimentally tested with a vacuum interrupter.

The results demonstrate that the compensation coils can effectively increase the rate of rise of the excitation current in the coils, thus increase the actuating speed. This novel topology can also eliminate the saturation in the magnetic core. Further potential improvements for the designed moving coil actuator are presented and analysed.

The rest of this chapter is cited from the author's submitted article in IEEE Transactions on Industrial Electronics. The structure of this chapter is organised in an alternative-based format, where the indices, equations, tables, figures, titles and references are numbered independently.

Statement of Authorship

<table>
<tr><td colspan="4">This declaration concerns the article entitled:</td></tr>
<tr><td colspan="4">A fast operating moving coil actuator with compensation coils for vacuum interrupters</td></tr>
<tr><td colspan="4">Publication status (tick one)
Draft manuscript [ ] Submitted [√] In review [ ] Accepted [ ] Published [ ]</td></tr>
<tr><td>Publication details (reference)</td><td colspan="3">B. Yin, X. Pei, J. F. Eastham, Emelie Nilsson, Jean-francois Rouquette, Jean Rivenc, Ludovic Ybanez, X. Zeng, “A fast operating moving coil actuator with compensation coils for vacuum interrupters,” in IEEE Transactions on Industrial Electronics</td></tr>
<tr><td colspan="4">Copyright status (tick the appropriate statement)
I hold the copyright for this material [√] Copyright is retained by the publisher, but I have been given permission to replicate the material here [ ]</td></tr>
<tr><td>Candidate’s contribution to the paper (provide details, and also indicate as a percentage)</td><td colspan="3">The candidate contributed to / considerably contributed to / predominantly executed the…
Formulation of ideas:
● 80%
● The novel moving coil actuator with compensation coils topology is proposed for circuit breaker applications. The compensation coils can eliminate the saturation in the magnetic core, increase the rate of rising of excitation current and increase the actuating speed. This research is guided by Dr. Xiaoze Pei.
Design of methodology:
● 100%
● A 2D finite element modelling is simulated using COMSOL to investigate the magnetic field distribution and dynamical performance of the designed moving coil actuator.
Experimental work:
● 100%
● A prototype of the moving coil actuator is designed, built, and experimentally tested with a vacuum interrupter to demonstrate the actuator performance in terms of operating speed, capacitor voltage, coil current, displacement and energy consumption
Presentation of data in journal format:
● 80%
● Organising and writing this article, revised by Dr Xiaoze Pei, Prof. John Fred Eastham, and Dr. Xianwu Zeng.</td></tr>
<tr><td>Statement from Candidate</td><td colspan="3">This paper reports on original research I conducted during the period of my Higher Degree by Research candidature.</td></tr>
<tr><td>Signed</td><td>Boyuan Yin</td><td>Date</td><td>25/11/2022</td></tr>
</table>

A fast operating moving coil actuator with compensation coils for vacuum interrupters

Boyuan Yin, Xiaoze Pei, John Frederick Eastham, Emelie Nilsson, Jean-francois Rouquette, Jean Rivenc, Ludovic Ybanez, Xianwu Zeng

Abstract—In recent years hydrogen-powered electric aircraft have attracted significant interest aiming to achieve sustainability and decarbonization targets. The onboard DC electric networks are facing a great challenge in DC fault protection requirements. Vacuum interrupters are widely used in low voltage and medium voltage networks as they are environmentally friendly with low maintenance. This paper designs and builds a fast operation moving coil actuator, with compensation coils, for a vacuum interrupter as part of a hybrid DC circuit breaker. The compensation coils induce a magnetic field which acts against the magnetic field from the moving coils, thus reducing the saturation in the electric steel. It also reduces the coil inductance so that the rate of rise of current and the operating speed are improved. Four possible connections are proposed and compared with the original moving coil actuator. A vacuum interrupter actuator prototype is built and tested to verify the performance of the moving coil actuator. The actuator structure is designed to latch the moving contact in an open or closed position without energy consumption and avoid the effects of bouncing, rebounding and welding. The experimental results show comparisons between different connections of the actuator coils in terms of opening time, coil current, and pre-charged capacitor voltage. The dynamic performance of each actuator connection is also compared. The overall fastest operation is the parallel connection actuator within 3.5 ms when the capacitor is pre-charged to 50 V. The actuator with compensation coils is shown to have a higher current rising rate and faster opening speed.

Index Terms—Moving coil actuator, Compensation coil, Vacuum interrupter, Circuit breaker.

6.2. Introduction

Decarbonization is one of the most urgent global challenges for industrial applications, especially in the aviation industry. Most institutions propose to complete decarbonization and meet the net zero target by 2050[1]. The development of electric aircraft is significant in achieving sustainability and decarbonization targets. The research on hydrogen-powered aircraft has been widely discussed [2-5]. Airbus UpNext has launched an advanced superconducting and cryogenic experimental powertrain demonstrator (ASCEND) project to develop a superconducting full-electric aircraft propulsion system in 2021 [6]. The power electronics for aviation must be reliable and efficient to meet the electric aircraft propulsion protection requirements. The onboard electric networks can suffer from high and fast-rising DC fault current due to the large energy storage in capacitors and batteries [7]. The development of onboard DC circuit breakers is urgently needed.

The design of a DC circuit breaker is generally more complex than an AC breaker. The mechanical DC circuit breakers have a reliable mechanical structure with low conduction resistance, reducing the joule losses during normal operation. It needs a pre-charged capacitor to generate the artificial zero-crossing point [8]. However, the interruption time of a mechanical circuit breaker is limited, in the order of milliseconds [9]. The solid-state DC circuit breaker is a power semiconductor-based device that has a fast interruption ability. It can break the fault current in less than 100 us [10-12]. However, the limited overcurrent capability and high conduction losses can not be neglected [13]. Hybrid DC circuit breakers, which combine mechanical and solid-state circuit breakers, are proposed to achieve a fast fault-interruption speed with lower on-state losses [14-15]. Since the semiconductor devices have a much faster-operating speed than the mechanical switches, the operating time of the hybrid circuit breaker highly depends on the mechanical switch. A mechanical switch includes an interrupter and its operating

actuator.

A vacuum interrupter is a widely used electrical component in medium-power applications. Compared with sulfur hexafluoride (SF6), vacuum is environmentally friendly and can provide high insulation strength due to its superior arc quenching properties [16]. In a closed environment like an electric aircraft application, the vacuum interrupter becomes the only option. A vacuum interrupter is a mechanical switch using two electric contacts in a vacuum chamber [17-20]. The fixed contact and the moving contact are located at the two ends of the vacuum chamber, with a comparatively short contact stroke. The moving contact is supported by a ceramic bellow, which is used for external actuator operation through a mechanical coupling. The design of the fast-operation actuator for vacuum interrupters is very important for hybrid direct current circuit breakers [21], superconducting fault current limiters [22-23] and other system protection.

To meet the electric aircraft propulsion fault protection requirement, the actuator should be able to separate the moving contact and the fixed contact with a considerable force and operating speed. There are a few typical actuators for vacuum interrupters, the permanent magnet actuator [24-27], Thomson coil actuator [28-30], moving magnet actuator [31-32] and moving coil actuator [33-35]. The permanent magnet actuator employs energized coil and a permanent magnet for force production, this has the benefits of compact design, reliable operation and mature technology. However, due to the heavy armature and considerable eddy current loss, the operating speed is limited. Alternatively, the Thomson coil actuator, as the novel design for ultra-fast operation circuit breakers, has been investigated with a vacuum interrupter [36-38]. It accelerates the moving armature with pancake coils. But the efficiency can be limited [28], [30], [39-40]. A moving magnetic actuator applies energized coil to generate a magnetic field driving the permanent magnet armature. It performs well in terms of durability and efficiency as

it has no moving wires. However, the heavy permanent magnet armature limits the operating speed. Compared with the moving magnet actuator, a moving coil actuator has less moving mass as the moving part is a coil. The moving coil actuator is also known as a loud- speaker actuator with the benefits of low moving mass and high efficiency. The comparison of the performance between the moving magnet actuator and the moving coil actuator is investigated in [41], which proves the moving coil actuator has better dynamic performance and higher force density. The moving coil actuator can be improved by minimizing the moving mass, increasing input energy, and reducing the coil resistance and inductance.

This paper proposes a design of a novel fast operating moving coil actuator with compensation coil topology. The compensation coils are employed to generate a magnetic field in the opposite direction to the magnetic field produced by the original moving coils, so that the equivalent coil inductance is significantly reduced. Therefore, the rate of current rise in the coils is much faster increasing the operating speed. Four possible connections between the moving coils and the compensation coils, including the passive compensation, series connection, parallel connection and hybrid connection, are investigated in this paper. The finite element modelling of the moving coil actuator with compensation coils has been investigated in the previous published paper [33]. A moving coil actuator prototype is designed, built, and experimentally tested with a vacuum interrupter. The performance is compared with the original moving coil actuator in terms of operating speed, displacement and energy consumption.

The structure of this paper is as follows. Section II introduces the vacuum interrupter specifications and the moving coil actuator topology designed for the vacuum interrupter. Section III shows the experimental test results and analysis of the moving coil actuator prototype with a vacuum interrupter. Section IV compares and discusses the actuator performance between different coil connections for the moving coil actuator. Both the

opening and closing processes are analyzed.

6.3. Vacuum interrupter specifications and actuator topology

6.3.1. Vacuum interrupter specifications

TJC-241 type vacuum interrupter, manufactured by Shanxi Baoguang Electric Device Company, is investigated in this paper. It has a rated voltage of 3.6 kV and a rated current of 1.25 kA. The stroke between the two contacts is 2 mm. During the normal operation, the contact resistance is 30 μΩ. The mass of the moving part is 0.3 kg and the closing force of the moving contact is 110 N. The detailed specifications of TJC-241is listed in Table 6-1.

TABLE 6-1

VACUUM INTERRUPTER SPECIFICATIONS

Parameter	Value
Rated Voltage	3.6 kV
Maximum Voltage (1 min)	20 kV
Rated current	1.25 kA
Maximum Current (2 s)	15 kA
Stroke	2 ± 0.6 mm
Contact resistance	30 μΩ
Mass of moving part	0.3 kg
Closing force	110 ± 30 N

6.3.2. Moving coil actuator electro-magnetic design

The actuator designed for the vacuum interrupter should be based on its mechanical parameters, not only to ensure the reliable opening and closing process, but also to avoid contact popping, bounce, rebound, and welding [9]. The actuator designed in this paper

is proposed to achieve a 4.5 mm operating distance, which includes the 2 mm moving contact stroke and an additional 2.5 mm distance to provide contact wear compensation.

The actuator for the vacuum interrupter proposed in this paper is a moving coil actuator, operating using the same principle as a loudspeaker, it is also called a voice coil actuator. Fig. 6-1 (a) shows the 2D axisymmetric topology of the original moving coil actuator, which contains two moving coils in the top and bottom airgaps to utilize fully the magnetic field generated by the permanent magnet. The arrows show the directions of the magnetic flux. The moving coils position shown in Fig. 6-1 (a) is at the closed position, which aligns with the top and bottom magnetic steel. Once the fault happens, the moving coils will be energized by a pre-charged capacitor. Then a large Lorentz force will be induced on the moving coils, driving the moving part of the actuator to separate the two contacts of the vacuum interrupter. In Fig. 6-1 (a), the current direction in the moving coils generates force to move them downwards.

The moving coil actuator with compensation coil topology is shown in Fig. 6-1 (b) [33]. Two fixed compensation coils are located on the top and bottom magnetic steel, aligning with the moving coils at the closed position. When the actuator is active, an opposite-direction current will flow into the compensation coils to compensate the magnetic field produced by the moving coils. The magnetic field, therefore, is maintained at the same level to avoid saturation in the magnetic core. Because the compensation coils are wound in the opposite direction to the moving coils, the equivalent coil inductance is significantly reduced, so that the exciting current in the moving coils has a higher rate of rise, and the actuator operating speed is increased.

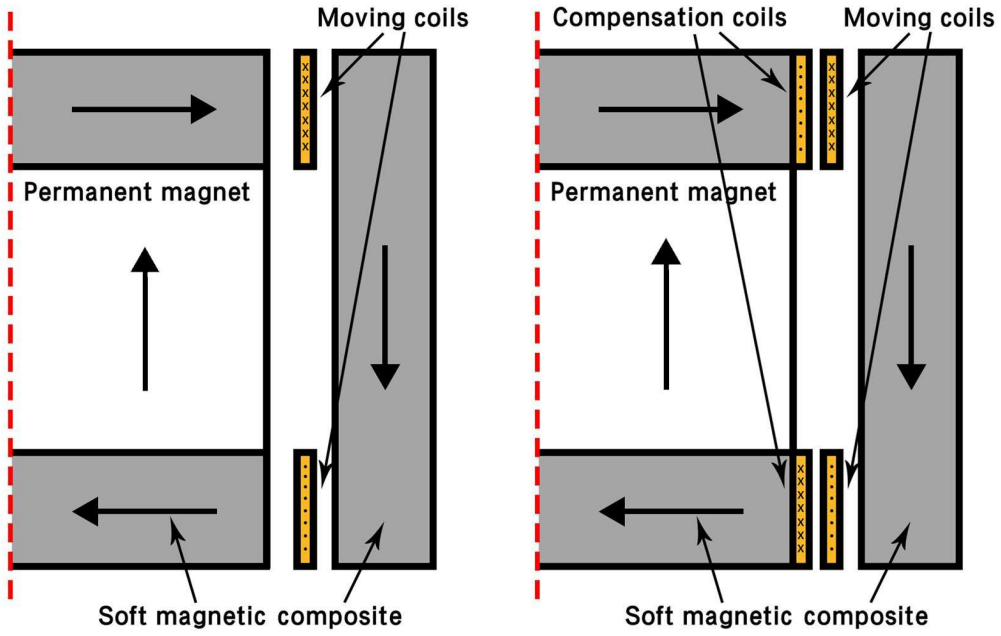

(a) Original moving coil actuator (b) Moving coil actuator with compensation coils

Fig. 6-1 Moving coil actuator 2D topology

The actuator is energized by a pre-charged capacitor during the opening and closing process. There are four possible connections for the moving coils and the compensation coils as shown in Fig. 6-2. The passive compensation actuator is shown in Fig. 6-2 (a), in which the moving coils are connected with the capacitor and the compensation coils are short-circuited. The compensation coils can also be replaced by annular copper rings in this connection. Fig. 6-2 (b) shows the series connection actuator topology, where all the moving coils and the compensation coils are series connected. This connection ensures that the current flowing into the four coils are the same, maximizing the magnetic field compensation.

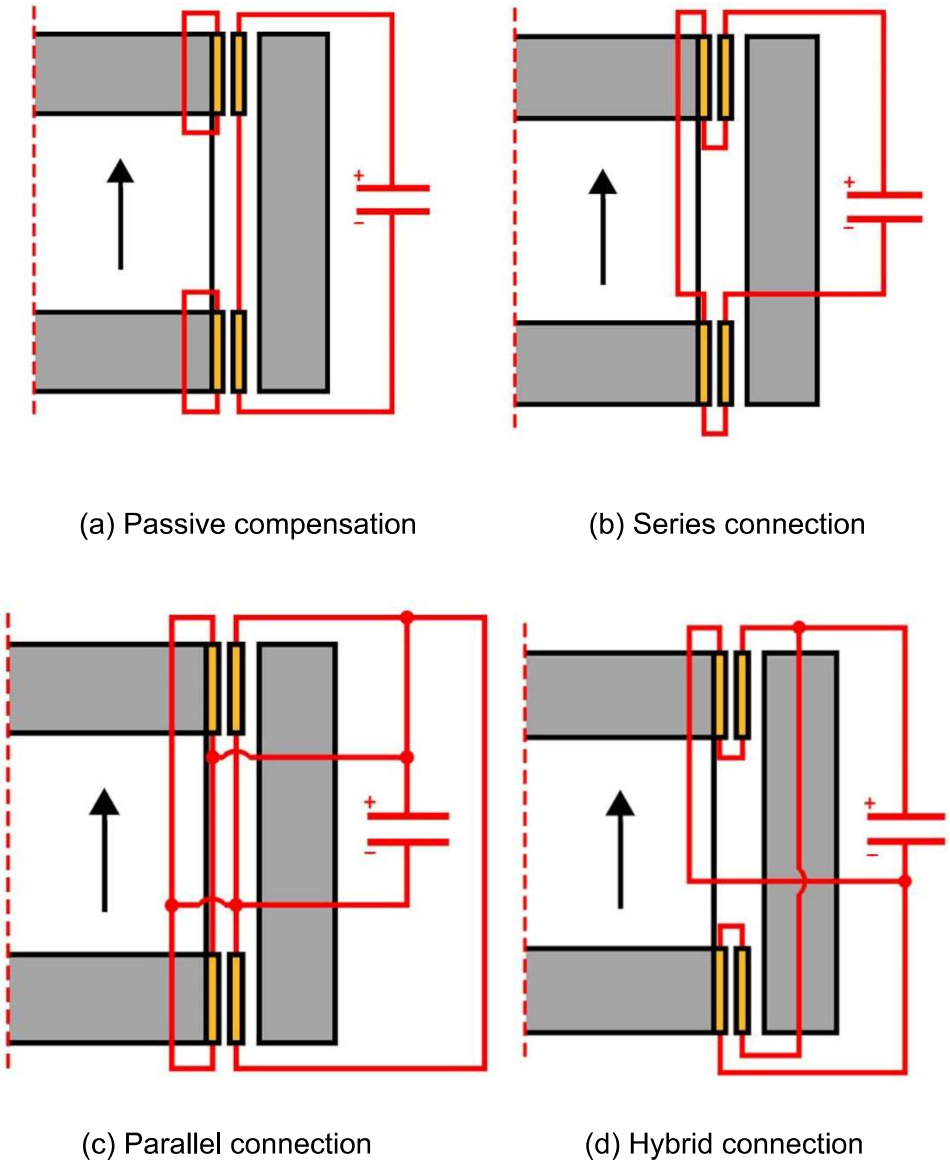

(a) Passive compensation (b) Series connection

(c) Parallel connection (d) Hybrid connection

Fig. 6-2 Different connections of moving coil actuator with compensation coils

Fig. 6-2 (c) shows the parallel connection actuator topology. The moving coils and the compensation coils are parallel connected to minimize the equivalent resistance and the inductance. The hybrid connection actuator topology is shown in Fig. 6-2 (d), where the top moving coil and the top compensation coil are series connected to ensure they have the same exciting current to fully compensate the magnetic field. So does the coil in the bottom. Meanwhile, the top and bottom coil groups are parallel connected to reduce the

coil inductance and resistance.

6.3.3. Vacuum interrupter actuator mechanical design

To achieve a reliable and high-performed vacuum circuit breaker design, the mechanical structure needs to be considered to avoid bouncing, rebounding, contacts popping and welding [9].

The arcing between the two contacts cannot be avoided due to the bouncing and popping during the opening and closing process, which may cause the contact to melt and fuse, forming dynamic welding on the surface. Arcing and welding will degrade and burn the contacts, reducing the device lifetime and bringing difficulties in separating the two contacts. To eliminate the welding effect and against the welding force, the moving plate of the actuator is coupled with the moving contact through a wipe spring. The actuator moving plate actuating distance is 4.5 mm, which is 2.5 mm further than 2 mm vacuum interrupter stroke. Two 'L-shaped' stoppers are applied to avoid the moving contact moving further, exceeding the allowed stroke limitation. A wipe spring is applied between the moving contact and the actuator moving plate. A supporting spring is located at the top of the vacuum interrupter connecting the top plate and the fixed contact. During the opening process, the moving plate already travels 2.5 mm before it drives the moving contact. When the two contacts start to separate, there has been a large amount of the kinetic energy accumulating on the moving actuator, which effectively againsts the welding force. During the closing process, the moving plate travels the first 2 mm together with the moving contact, then it compresses the wipe spring and the supporting spring for another 2.5 mm to provide the holding force avoiding the contact bouncing and rebounding.

Once the actuating process is finished, the current in the moving coils is removed. Then the moving part must hold at the opening or closing position securely. Thus, four

permanent magnets are employed on the moving plate of the actuator. A steel plate above the moving plate and another steel block at the bottom of the moving plate are employed to latch the moving part of the actuator at a stable position after the actuating process.

The final designed 3D topology of the moving coil actuator with vacuum interrupter is shown in Fig. 6-3, including the mechanical parts of magnetic latches, driving shaft, contact stoppers, rubber absorbers, and supporting steel rods.

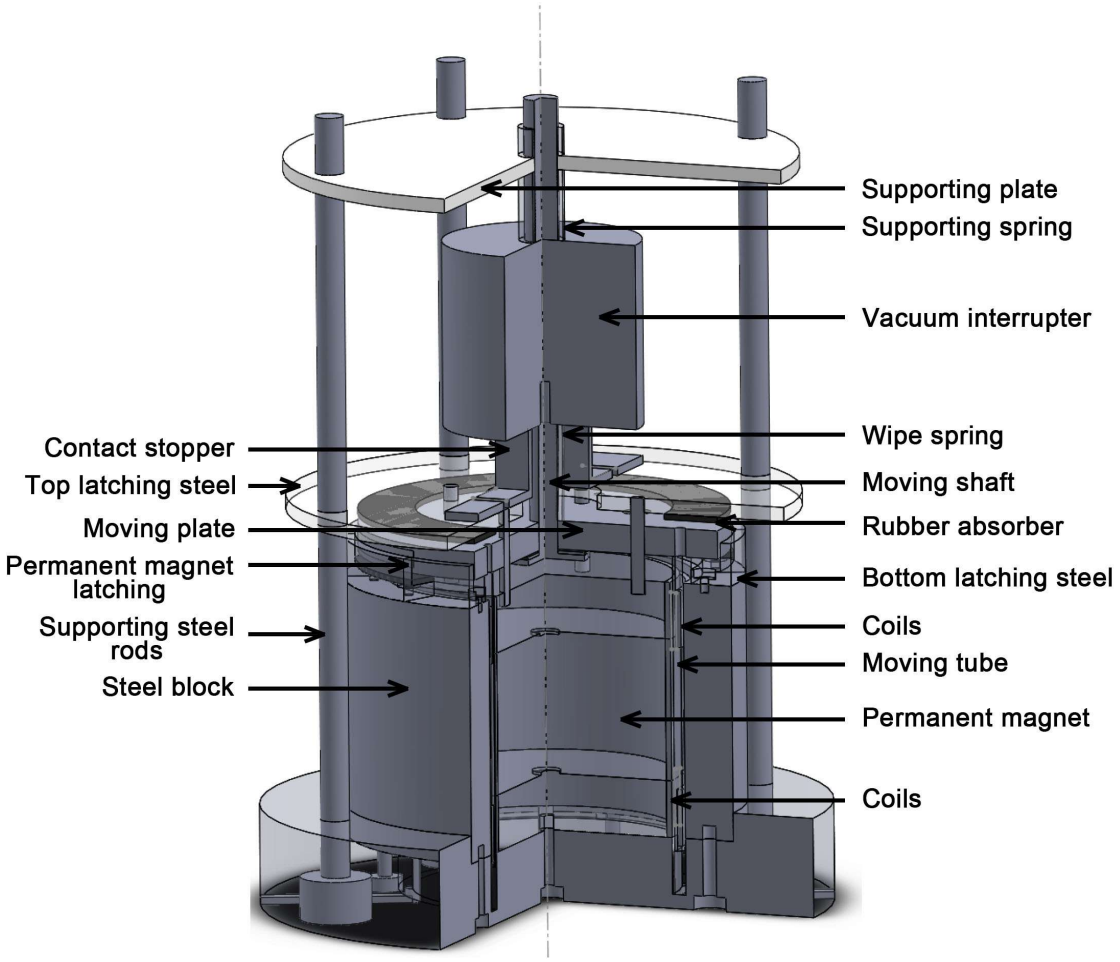

Fig. 6-3 Moving coil actuator 3D topology

6.4. Experimental investigation

A moving coil actuator with compensation coils prototype was built and assembled with the TJC241 vacuum interrupter in this section as shown in Fig. 6-4. Fig. 6-4 (a) shows the top and bottom moving coils wound on a G10 tube with epoxy coating. The tube is directly attached with the moving plate with latching permanent magnets. Fig. 6-4 (b) shows the magnetic core frame. The permanent magnet and compensation coils are placed in the magnetic core frame. Neodymium iron boron (NdFeB) N50 type is used in the actuator. The moving tube as shown in Fig. 6-4 (a) is placed in the airgap shown in Fig. 6-4 (b). The complete actuator with vacuum interrupter is shown in Fig. 6-4 (c). The coil terminals at the front provide flexible connections for the moving coils and the compensation coils. Therefore, the comparison tests can be investigated by using different coil connections.

(a)

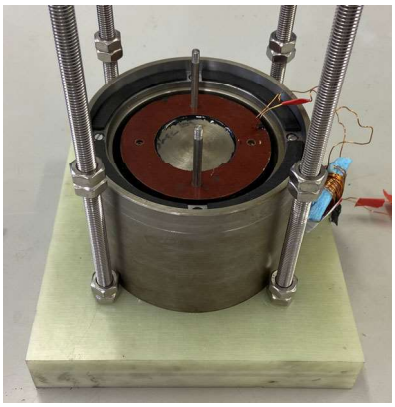

(b)

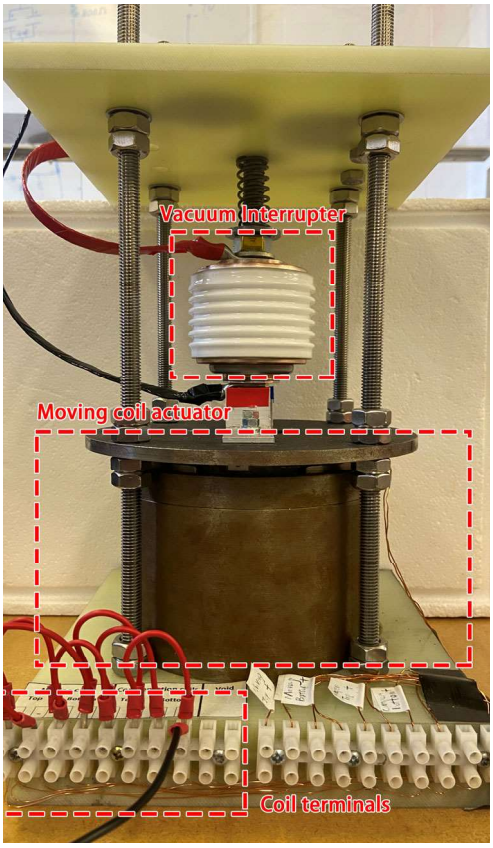

(c)

(a) Moving plate and moving coils on the G10 tube

(b) Steel frame with the permanent magnet and compensation coils

(c) Prototype actuator with vacuum interrupter

Fig. 6-4 Moving coil actuator prototype

To control the actuating process, a control circuit is designed with a 20 mF pre-charged capacitor, to provide power for moving coil actuator operations. The capacitors are connected to the coils through an H-bridge, which includes four MOSFETs. The H-bridge circuit can control the exciting current in both directions, which drives the actuator to open and close. The open and close signals are generated by a control board, which is also functions to control the current energizing time by adjusting the duration of the signal

pulse. The open pulse period is set to be 10 ms and the closing pulse period is 14 ms, where both are longer than the operating time, in order to hold the moving contact in position after the opening or closing operation.

The test platform for the actuator with vacuum interrupter is shown in Fig. 6-5. A Phontron SA3-type fast camera is employed to capture the accurate dynamic position of the actuator moving parts with a high sampling rate of 15000 frames per second. The resolution is up to 256 × 256 pixels. A high sampling rate oscilloscope is used to record the coil voltage and current waveforms. DC power supplies are used to support the control circuit and charge the capacitors.

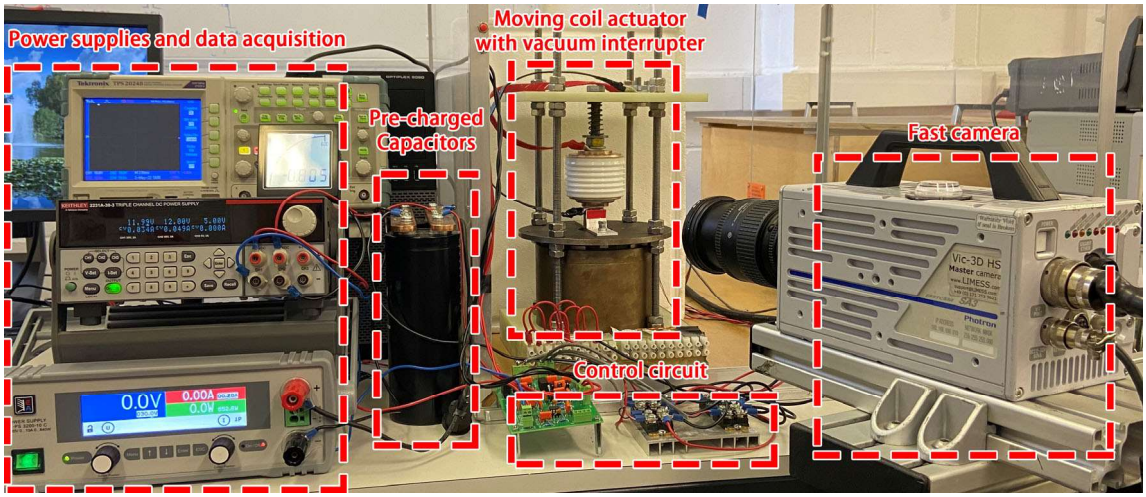

Fig. 6-5 Actuator with vacuum interrupter test platform

6.4.1.Static magnetic field distribution

The permanent magnet generates a high magnetic field in the top and bottom airgaps through the magnetic steel frame. The magnetic field is distributed evenly through the cylinder steel piece and changed along the vertical direction. A gauss meter is used to measure the magnetic field distributed along the vertical direction as shown in Fig. 6-6. The peak flux density is 0.85 T, produced at the top and bottom airgaps, where the coils

are located.

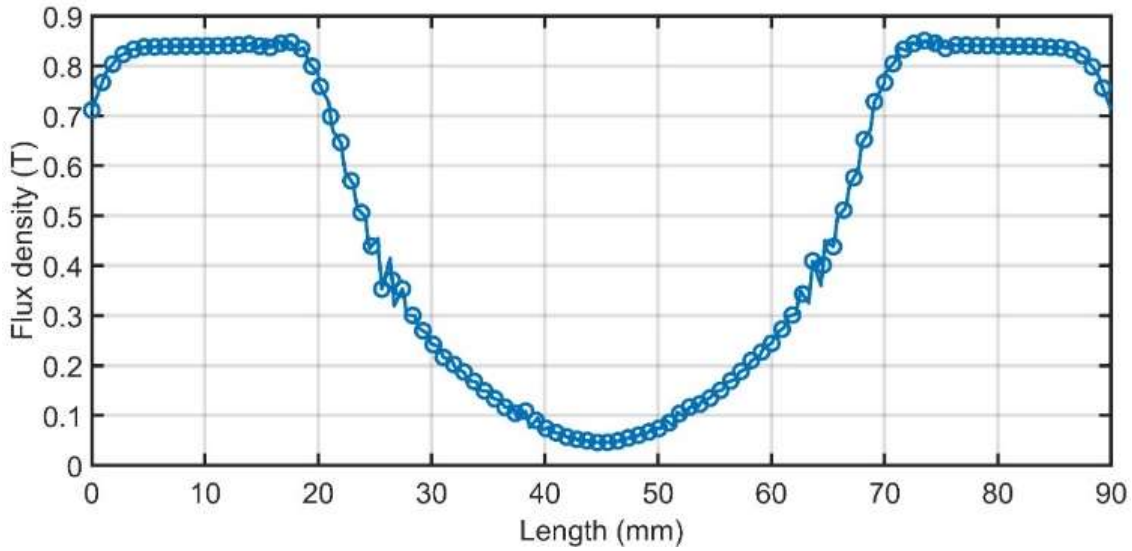

Fig. 6-6 Flux density distribution in the airgap produced by the permanent magnets (along the vertical path)

6.4.2. Static electro-magnetic force on the moving coils

The electro-magnetic force on the moving part is directly related to the coil current. The static test in this section uses a load cell mechanically connected to the moving plate and stabled at a certain position that is aligned with the airgaps. When the constant current flows into the moving coils, the force measured by the load cell is recorded. The change of electro-magnetic force against the coil current is shown in Fig. 6-7, where the current ranges from 0 to 10 A. The theoretical force is calculated by equation F = BIL, where B is the magnetic field in the airgap, I is the coil current, and L is the total length of the conductors of the moving coils.

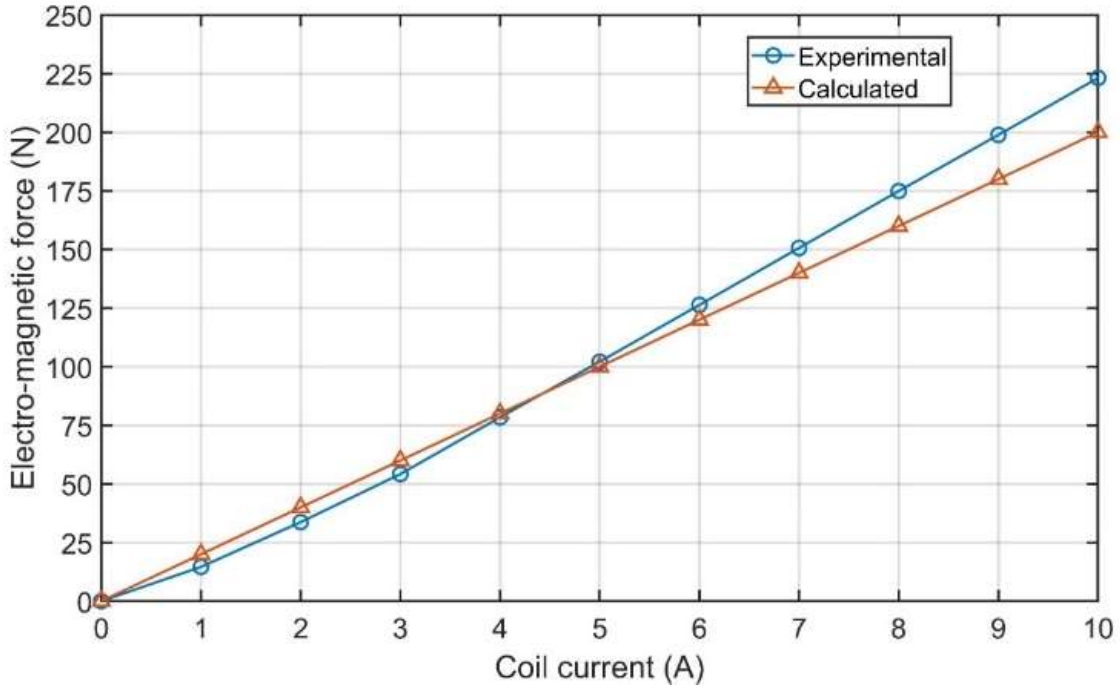

Fig. 6-7 Electro-magnetic force on the moving plate

6.4.3.Actuator opening and closing process

6.4.3.1 Opening process

The moving part of the designed vacuum circuit breaker includes an actuator moving plate and a vacuum interrupter moving contact. Fig. 6-8 shows the moving plate and moving contact opening process of the passive compensation actuator with a capacitor voltage of 80 V. The displacement is a negative value as the open process for the actuator is moving downwards. The moving plate displacement is up to 4.2 mm. The moving contact displacement is up to 2.5 mm, as a mechanical stopper is applied to protect the bellow in the vacuum interrupter. The rated stroke of the vacuum interrupter is 2 mm, therefore, once the contact travels over 2 mm, the actuator is opened. There is a time delay before the moving contact acts because of the 2.5 mm gap between the moving plate and the moving contact. From the time zero, the moving plate starts to move downwards. It starts to pull the moving contact to open at t1. Then the moving plate

and the moving contact are moving downwards together, until the moving plate is stopped by the bottom absorbing rubber at t2 and the moving contact hits the stopper at t3. Both the moving plate and the moving contact have a minor rebounding effect, but soon achieve the stabilized position.

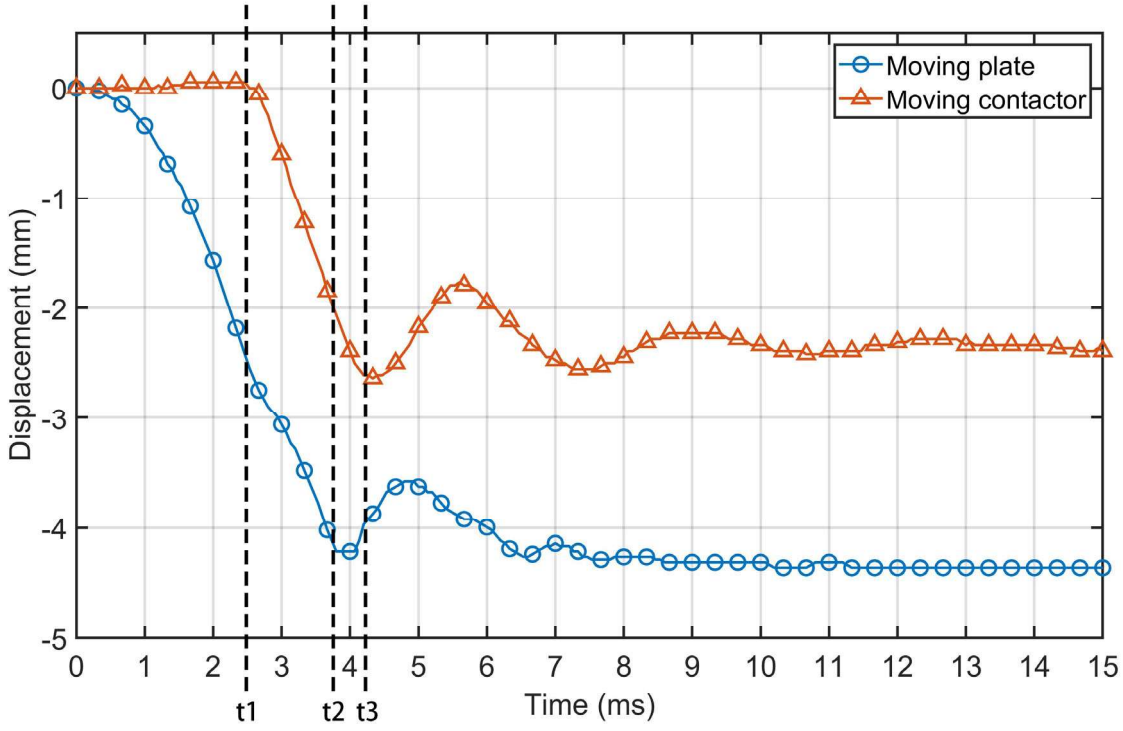

Fig. 6-8 Moving plate and moving contact opening displacement of passive compensation actuator with capacitor voltage of 80V

6.4.3.2 Closing process

For the vacuum interrupt circuit breaker, the closing time is of less concern when compared with the opening time. Due to the mechanical structure of the vacuum circuit breaker, a supporting spring is used to provide the holding force and eliminate the contact bouncing and rebounding effect. Thus, unlike the opening process, the vacuum interrupter will not stay stationary but will move upwards and compress the supporting spring. Therefore, there are three positions that need to be monitored during the closing process: the actuator moving plate, the moving contact and the fixed contact of the

vacuum interrupter. Fig. 6-9 shows an example of the closing process of the passive compensation coil actuator with the initial capacitor voltage of 60 V. Once the actuator receives the closing signal, the moving plate starts to move upwards with the moving contact from time zero and reaches a position of 2 mm at time t1 when the moving contact touches the fixed contact in the vacuum chamber. The moving plate then separates with the moving contact. The moving plate will continue to move upwards until hitting the top absorbing rubber to stop at time t2, which has a little rebound after t2 and then stays steady. The moving contact moves upwards together with the fixed contact since time t1 to compress the supporting spring, during which time period the two contacts are kept closed. After time t3, the moving plate, moving contact and the fixed contact become stable at the closed position. The closed time for the passive compensation actuator under 60 V is 4 ms.

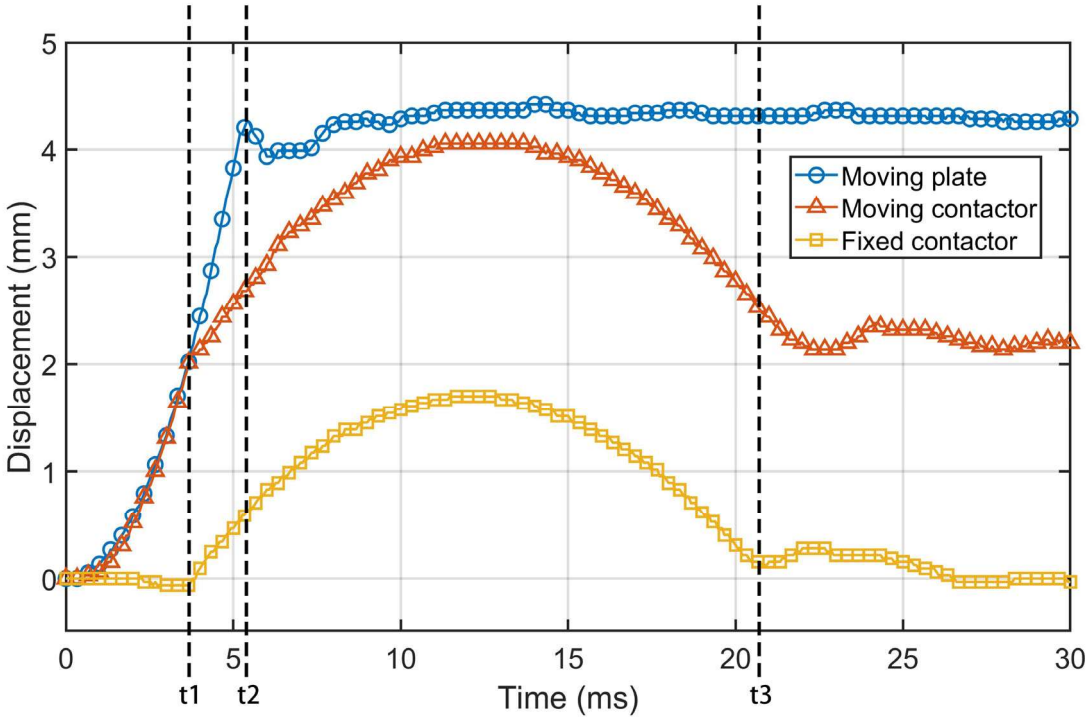

Fig. 6-9 Closing process of passive compensation actuator with capacitor voltage of 60 V

6.4.4. Dynamic performance during the opening process

A circuit breaker is used to interrupt the current and clear the fault in a short period. Therefore the opening process of the actuator is more important than the closing process. This section therefore first concentrates on analyzed the dynamic opening performance of each actuator under different initial capacitor voltages. Both the electrical and mechanical properties of each actuator are tested to identify the best operating point. According to the actuator design in section II. B, there is a 2.5 mm difference between the actuator's moving plate displacement and the vacuum interrupter's moving contact displacement. Therefore, the displacement for the moving plate and the moving contact are recorded, separately. The coil current and capacitor voltage are measured by an oscilloscope and the displacement is recorded by the high-speed camera.

6.4.4.1 Original moving coil actuator

Fig. 6-10 presents the original moving coil actuator opening dynamic performance with the initial test voltage from 30 V to 80 V. The coil current is increased with a higher capacitor voltage. There are two stages of the coil current with each capacitor voltage: at the first stage, the current is rising from zero and reaches its first and second plateau. Then in the second stage, the current is increased to the overall peak value, holds for a period, then decreases to zero. In the first stage, the actuator receives the opening signal. The current starts flowing into the moving coils and increasing. The current reaches the first peak at 1.4 ms because of the circuit inductance. Then the current starts decreasing to its first valley, at which point the moving plate starts to pull the moving contact open. The moving plate speed suddenly decreases, resulting in the reduction of the induced voltage in the coils. Therefore, the coil current starts to increase again. The current then reaches the second plateau due to the circuit inductance. The coil current then decreased to the second valley, where the moving plate arrives at the fully open position.

Then in the second stage, the moving coil speed decreases to zero, so that the induced voltage is also reduced to zero. The current then increases to its highest value and lasts for a period, which produces the holding force on the moving parts to eliminate the bouncing effect.

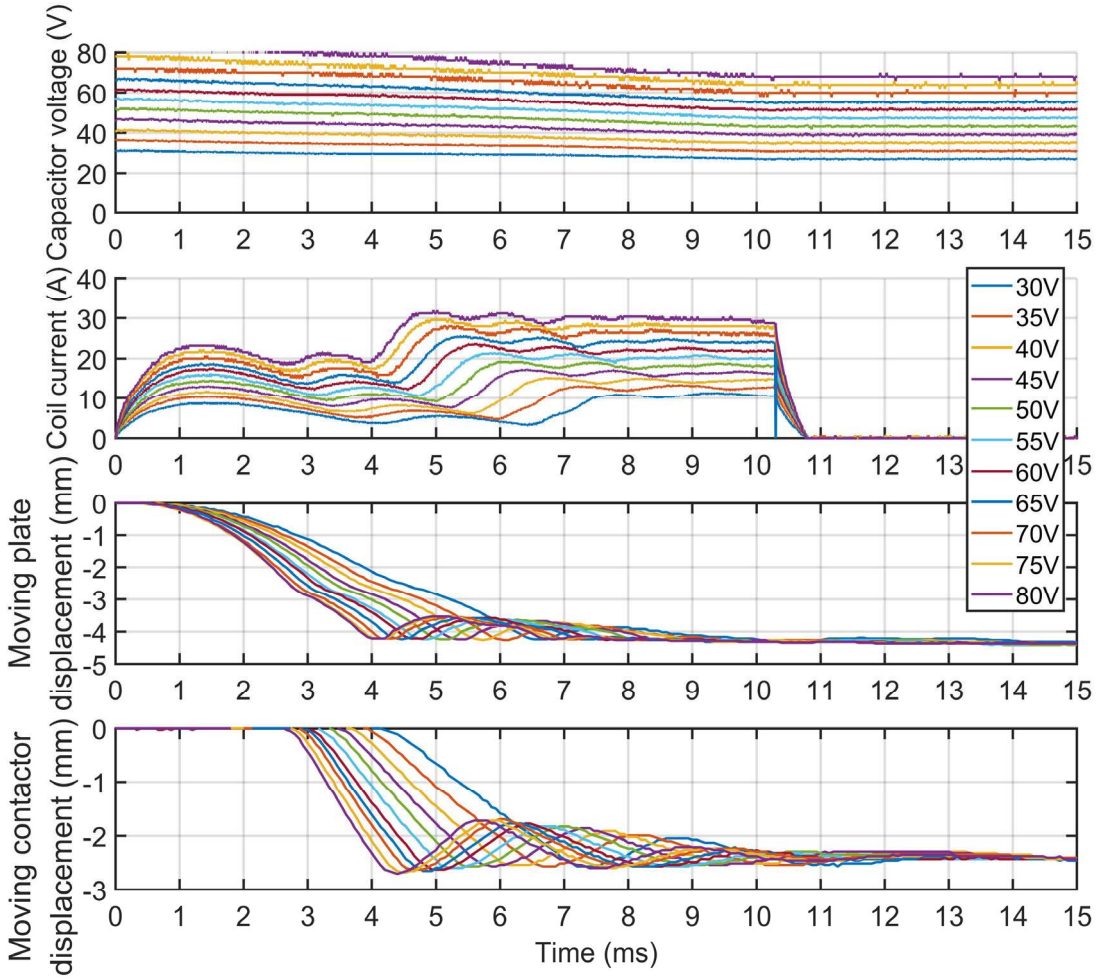

Fig. 6-10 Original moving coil actuator dynamic performance

6.4.4.2 Passive compensation actuator

Fig. 6-11 shows the passive compensation actuator dynamic performance with the initial capacitor voltage from 30 V to 80 V. Compared with the original moving coil actuator, the rate of rising of coil current at the beginning is much higher. This is because the

compensation coils significantly reduce the coil inductance. The coil current increases to the peak value in a very short period, which is less than 0.4 ms. The coil current increases quickly producing higher acceleration for the moving parts. Thus, the moving plate moves faster in the first milliseconds compared with the original moving coil actuator.

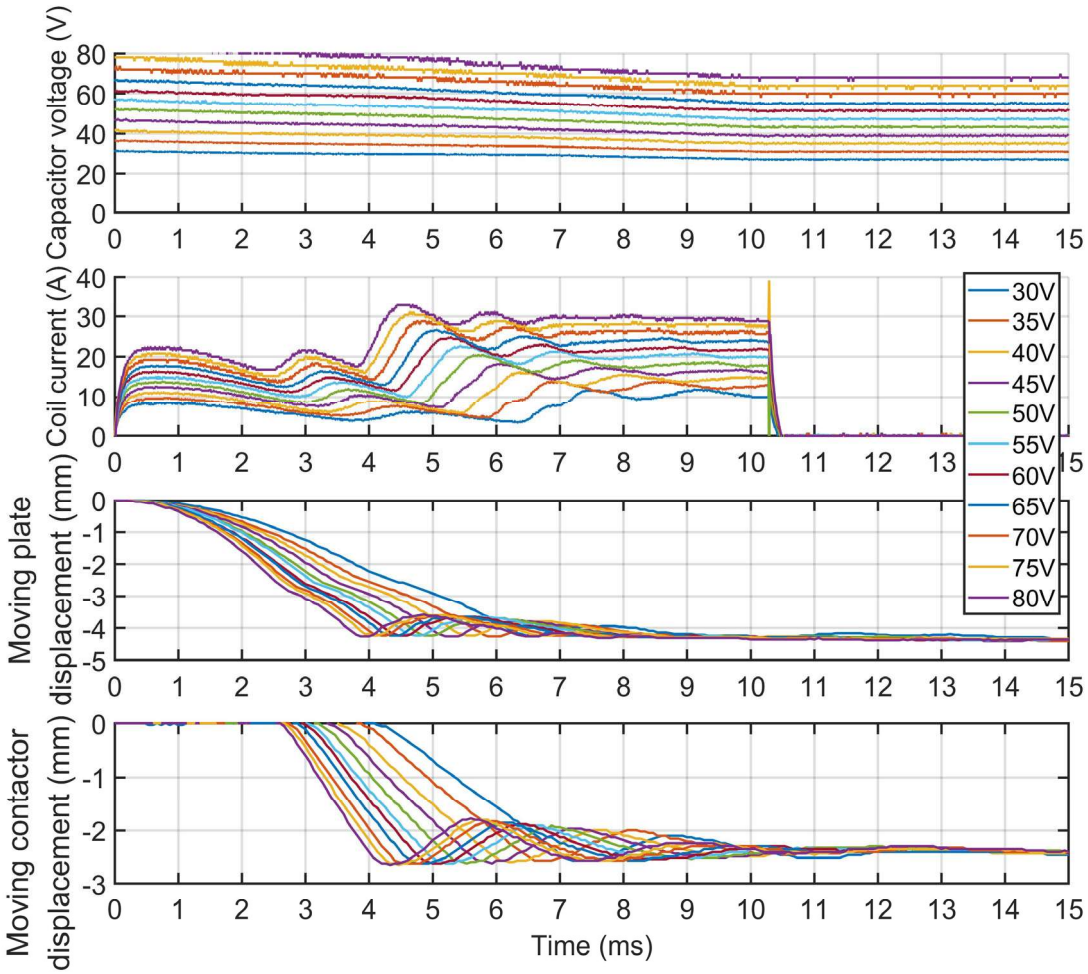

Fig. 6-11 Passive compensation actuator dynamic performance

6.4.4.3 Series connection actuator

The series connection actuator dynamic performance is shown in Fig. 6-12. The tested initial capacitor voltage is from 30 V to 100 V, which has a wider range as the high series connected resistance needs a higher voltage to generate an exciting current for coils. It

can be seen that the capacitor voltage remains at a relatively high level after each operation. Although the four series connected coils bring high circuit inductance, the compensation coils cancel most of the coil inductance. Therefore, the rate of rising of current in the moving coils is still very fast. It takes the series connection actuator 3.8 ms to open with a capacitor voltage of 100 V where the peak current is 22 A

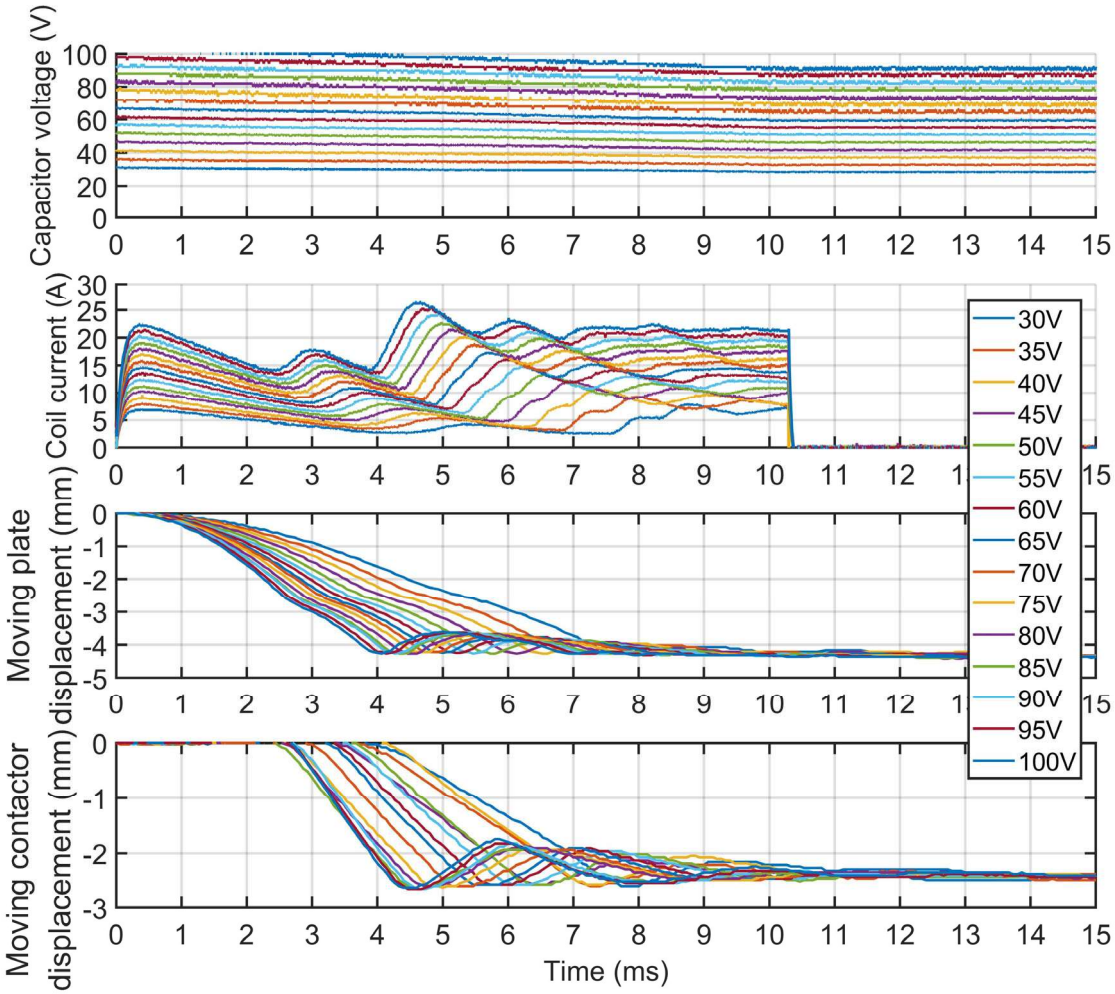

Fig. 6-12 Series connection actuator dynamic performance

6.4.4.4 Parallel connection actuator

Fig. 6-13 shows the dynamic performance of the parallel connection actuator, with the initial capacitor voltage from 10 V to 50 V. The parallel connected coils achieve the lowest

coil equivalent inductance, thus the highest rate of current rise. The peak current can reach up to 35 A within 0.3 ms. The parallel connection actuator has the highest coil current and the rate of rising of current, but the energy consumption is also high. It is noted that the capacitor voltage drops very quickly from the beginning, which makes the coil current decrease quickly at the end of the operation. The holding force, therefore, becomes lower. The rebound effect is more obvious than that in other types of coil connections.

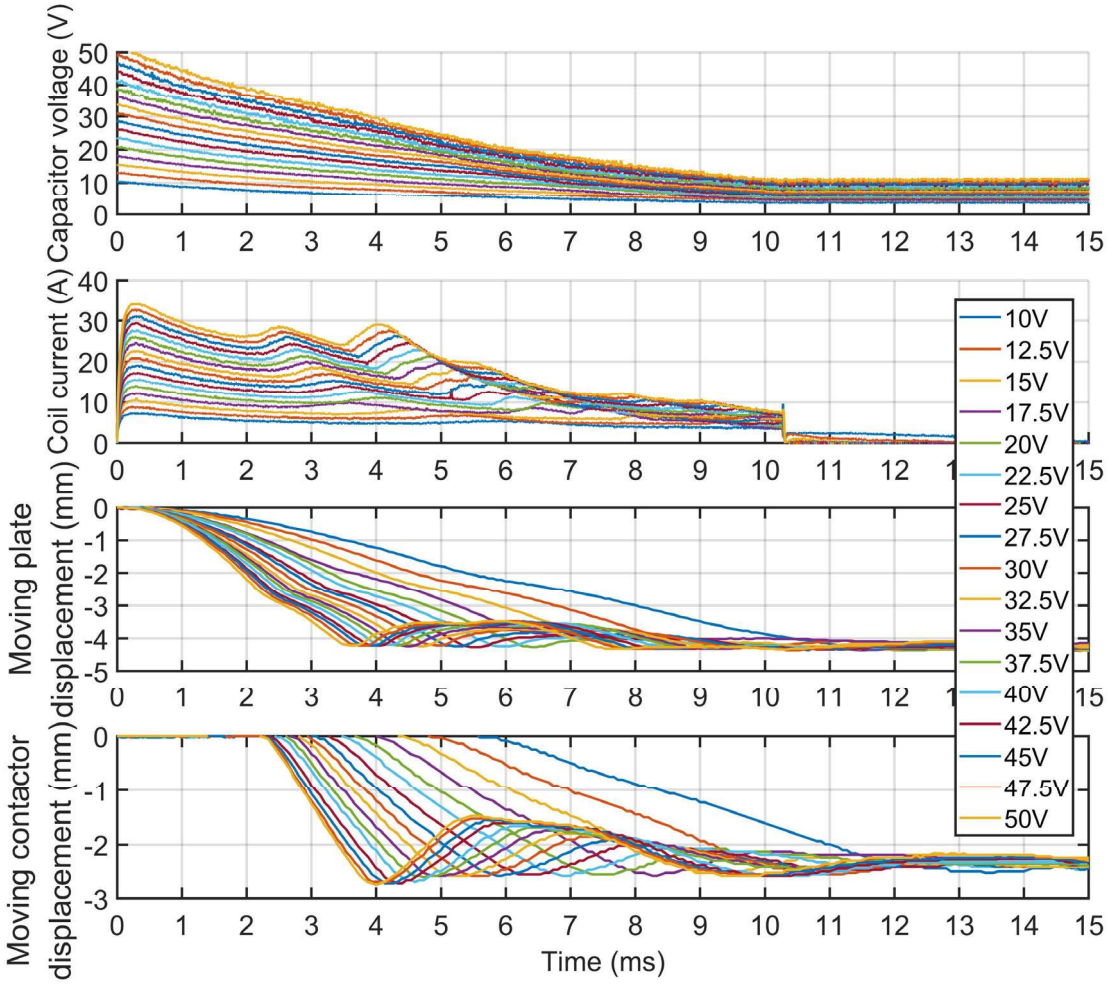

Fig. 6-13 Parallel connection actuator dynamic performance

6.4.4.5 Hybrid connection actuator

The dynamic performance of the hybrid connection actuator is shown in Fig. 6-14 with the initial capacitor voltage from 20 V to 60 V. The hybrid connection actuator combines the advantages of low circuit inductance from the parallel connection and low mutual inductance from the series connection. The coil current can reach a higher level with a reasonable capacitor voltage and remain at a steady level for the holding force. The moving contact has some rebound effect but the contact opening distance is over 2mm, which is acceptable.

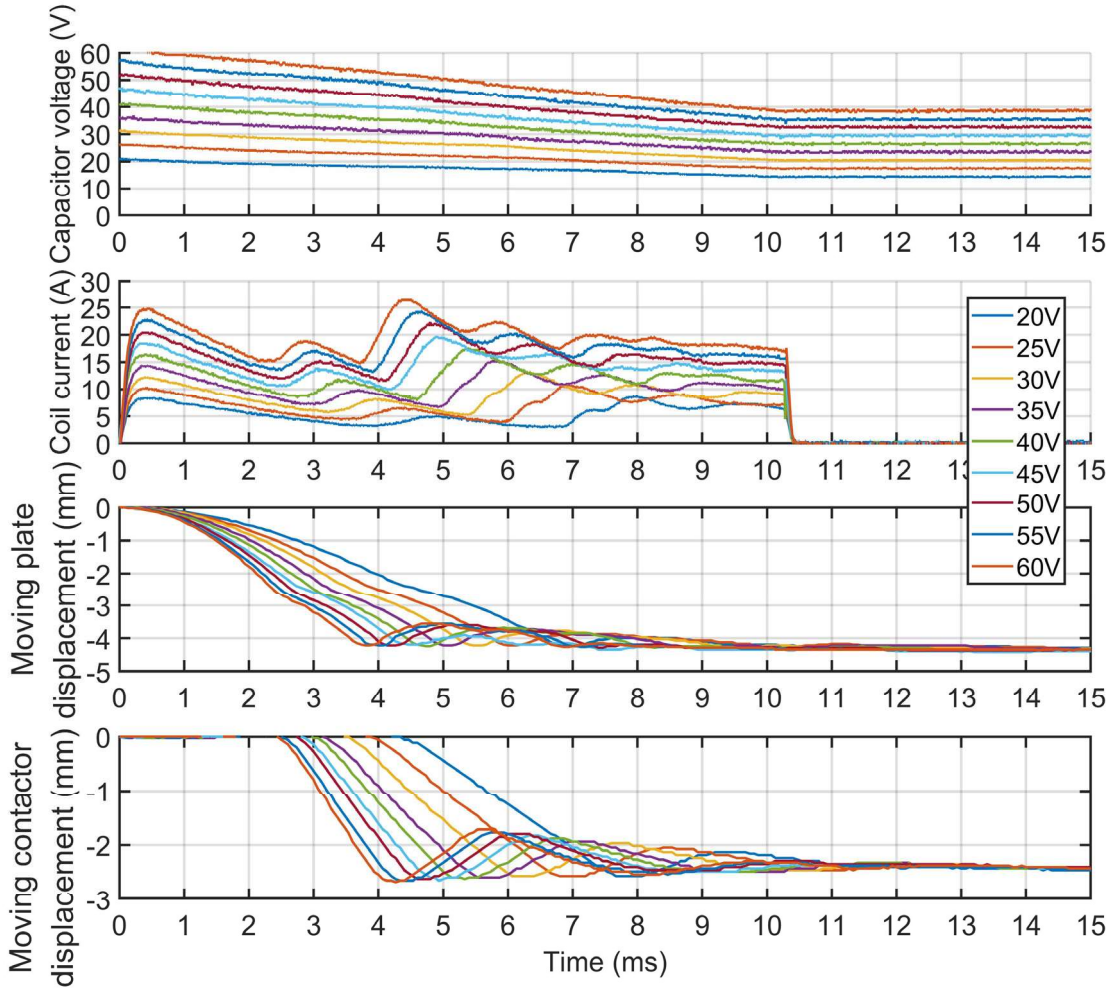

Fig. 6-14 Hybrid connection actuator dynamic performance

6.4.5. Comparison of different coil connections during the open process

To compare the performance of the different connections, the actuator performance is investigated at different initial capacitor voltages, in terms of the actuator opening time, the peak current in the moving coils, and the energy consumption for one operation.

Fig. 6-15 and Fig. 6-16 show the opening performance of the original moving coil actuator, passive compensation actuator, series connection actuator, parallel connection actuator and hybrid connection actuator. Fig. 6-15 compares the opening time, coil peak current, and energy consumption against the initial capacitor voltage. The parallel connection actuator has the fastest operating speed as it has the lowest coil equivalent inductance and resistance. Correspondingly, the peak current in the moving coils is also the highest, as well as the energy consumption for one operation. The hybrid connection actuator has twice the equivalent inductance and resistance when compared with the parallel connection, thus the coil peak current is lower than the parallel connection actuator but higher than other actuators. The passive compensation actuator is similar to the original moving coil actuator, but employs two compensation coils to reduce the coil inductance. The overall circuit resistance is almost the same. The series connection actuator has the largest coil inductance and resistance, which decides its lowest coil peak current and energy consumption, thus the opening time is longer than other actuators at certain initial capacitor voltages. But the series connection actuator has a great potential to have multi operations after one charge.

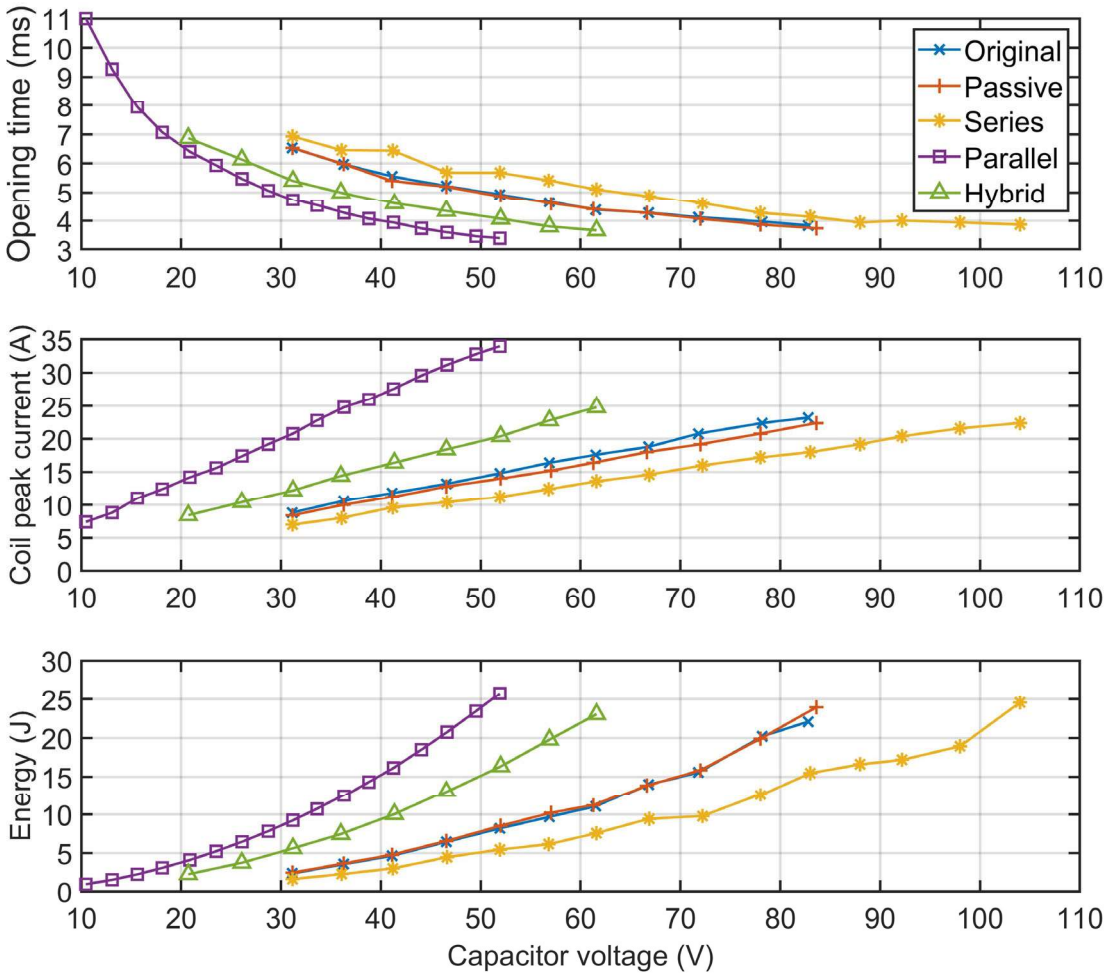

Fig. 6-15 Actuator performance on different capacitor voltage for different connections

The overall fastest operating actuator is the parallel connection actuator at an initial capacitor voltage of 50 V, which can reach 3.5 ms. It also has the highest coil peak current of 35 A, which brings a challenge to the coils' overcurrent ability and the requires high current rating of the capacitor. The opening speed from fastest to slowest is parallel, hybrid, passive, original, and series with the same capacitor voltage. The coil peak current and energy are in opposite sequence.

The force from the moving coil actuator is proportional to the current in the coil. Fig. 6-16 compares the five actuators in terms of the peak coil current. The opening speeds for the original, passive, series, and hybrid connection actuator are almost the same at a

certain peak moving coil current, but the parallel connection actuator is slower. Correspondingly, the energy consumption for the parallel connection actuator is the lowest with the same coil current.

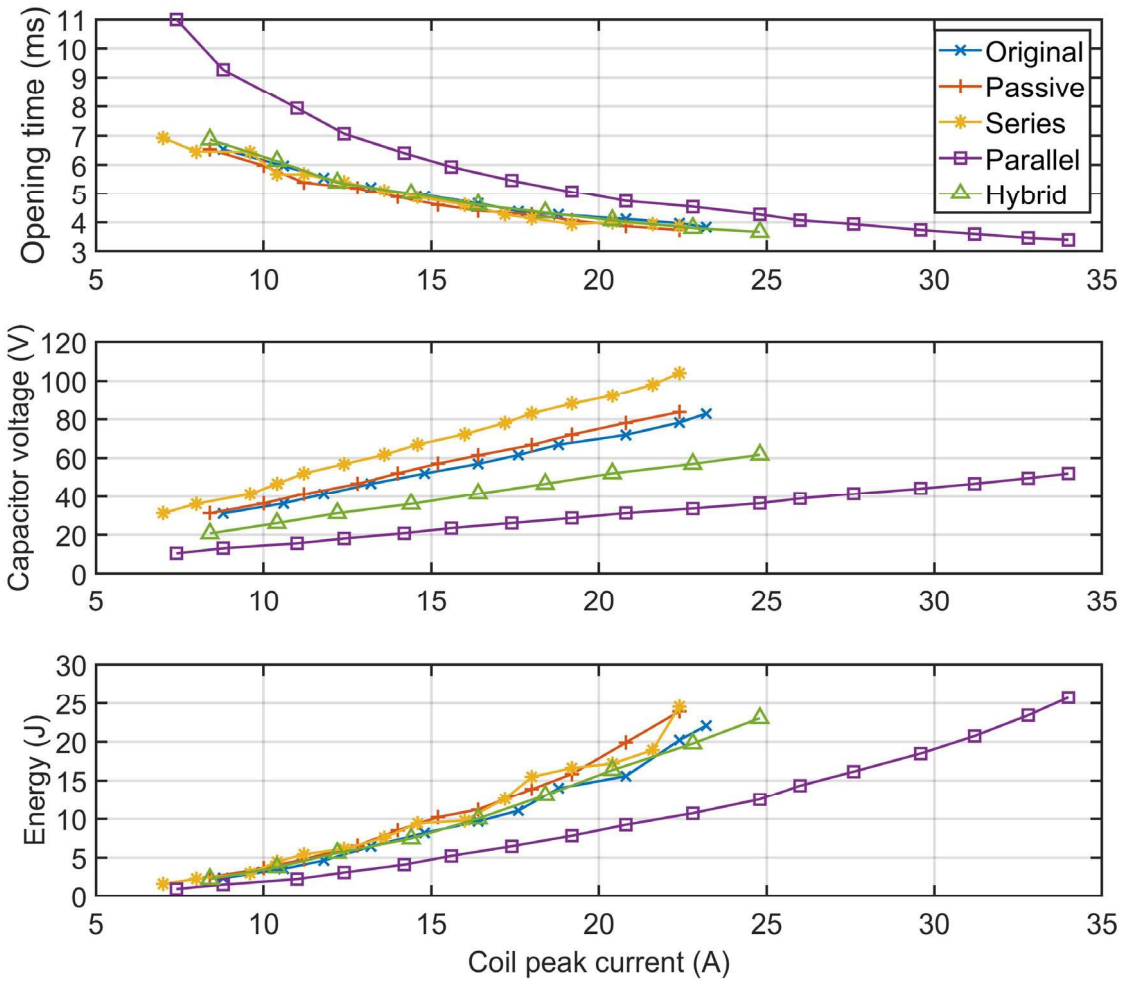

Fig. 6-16 Actuator performance with different coil peak currents for different connections

6.5. Discussion and potential improvements

The moving coil actuator with compensation coils is investigated in this paper with passive compensation, series connection, parallel connection and parallel connection. The simulation results in the previous published paper [33] have verified the magnetic field saturation in the magnetic core is significantly improved by the compensation coils and the rate of rise of current is significantly increased. The actuator performance with the vacuum interrupter and necessary supporting structures is further investigated experimentally. The overall experimental results demonstrated in this paper show that the compensation coils can bring benefits to reduce the coil equivalent inductance and improve operating speed. The passive compensation actuator has a similar operating speed to the original moving coil actuator, but has lower system inductance, it also has the simplest structure compared with other connections. The series connection actuator can withstand higher capacitor voltage, which allows higher energy stored in the pre-charged capacitor. Therefore, the series connection actuator can operate multiple times after each charge. The parallel connection actuator performs the fastest operating speed with the lowest capacitor voltage, but the energy consumption is high for one operation. The holding force is less as the coil current drops very quickly. The hybrid connection actuator balances the performance of the series and parallel connection with reasonable coil current and holding force. The closing operation is reliable and as expected.

The potential improvements of the proposed actuator can be:

1) Increase the capacitor voltage level to achieve a higher coil current. This may pose a challenge to the capacitor and coil current capability but will achieve faster operating speed.

2) Increase the number of turns in the coils which brings a higher Lorentz force. The coil inductance is fully compensated, but the longer conductor will increase the coil

resistance and reduce the peak coil current.

3) Reduce the moving part mass. Since the moving force is generated on the moving part, the acceleration depends on the moving mass. Minimizing the moving mass can efficiently increase the operating speed.

4) With a higher operating speed, the coil current flow time should be extended to provide the necessary holding force.

6.6. Conclusions

This paper proposed a novel moving coil actuator with compensation coil topology. The moving coil actuator with a vacuum interrupter prototype is designed, built and experimentally tested in this paper. Four possible connections for the compensation coils are presented. The passive compensation actuator has the most compact design. The series connection actuator supports high capacitor voltage and small energy consumption for each operation, thus having a great potential for multi-operation after each charge. The parallel connection actuator has the smallest circuit inductance and resistance, which gives the fastest rate of current rise. However, the energy consumption is large and the coil current decreases too fast to generate a holding force. The hybrid connection actuator balances the series and parallel connection, achieving small coil inductance and a performance that is between the original moving coil and the parallel connection actuator.

The actuator can hold the moving contact at the open or closed position with the magnetic latch. The springs and supporting structures are designed to help to eliminate the effect of bouncing, rebounding and welding. The dynamic performance of each actuator is investigated, and the global comparison is analyzed.

This paper demonstrates that the moving coil actuator with the compensation coils has a higher current rising rate than the original moving coil actuator. The parallel connection actuator achieves the highest operating speed at 50 V capacitor voltage in less than 3.5 ms, however, with a high rebound effect. The most reliable operation is the passive compensation actuator, which can separate the two contacts within 3.7 ms at a capacitor voltage of 80 V. The high-speed moving coil actuator with compensation coils actuator has great potential with applications in high voltage DC circuit breakers.

6.7. References

[1] J. Huete, D. Nalianda, B. Zaghari and P. Pilidis, “A strategy to decarbonize civil aviation: a phased innovation approach to hydrogen technologies,” in IEEE Electrification Magazine, vol. 10, no. 2, pp. 27-33, Jun. 2022.

[2] P. J. Ansell, “Hydrogen-electric aircraft technologies and integration: enabling an environmentally sustainable aviation future,” in IEEE Electrification Magazine, vol. 10, no. 2, pp. 6-16, Jun. 2022.

[3] S. Njoya Motapon, L. -A. Dessaint and K. Al-Haddad, “A comparative study of energy management schemes for a fuel-cell hybrid emergency power system of more-electric aircraft,” in IEEE Transactions on Industrial Electronics, vol. 61, no. 3, pp. 1320-1334, Mar. 2014.

[4] Y. Gao, C. Jausseme, Z. Huang and T. Yang, “Hydrogen-powered aircraft: hydrogen–electric hybrid propulsion for aviation,” in IEEE Electrification Magazine, vol. 10, no. 2, pp. 17-26, Jun. 2022.

[5] S. Sirimanna, T. Balachandran, N. Salk, J. Xiao, D. Lee and K. Haran, “electric propulsors for zero-emission aircraft: partially superconducting machines,” in IEEE Electrification Magazine, vol. 10, no. 2, pp. 43-56, Jun. 2022.

[6] “Cryogenics and superconductivity for aircraft, explained | Airbus,” www.airbus.com,Sep.01,2021. https://www.airbus.com/en/newsroom/stories/2021-03-cryogenics-and-superconductivity-for-aircraft-explained

[7] F. F. Wang, R. Chen and Z. Dong, “Power electronics: a critical enabler of future hydrogen–electric systems for aviation,” in IEEE Electrification Magazine, vol. 10, no. 2, pp. 57-68, Jun. 2022.

[8] T. Erikksson, M. Backman, S. Halen, “A low loss mechanical HVDC breaker for HVDC Grid applications”, CIGRE, Paris, 24-29 Aug. 2014.

[9] A. Greenwood, “Vacuum switchgear,” London: Institution Of Engineering And Technology, 2007.

[10] C. Meyer and R. W. De Doncker, “Solid-state circuit breaker based on active thyristor topologies,” in IEEE Transactions on Power Electronics, vol. 21, no. 2, pp. 450–458, Mar. 2006.

[11] L. Q. Zhang, R. Woodley, X. Q. Song, S. Sen, X. Zhao, and A. Q. Huang, “High current medium voltage solid state circuit breaker using paralleled 15kV SiC ETO,” in 2018 IEEE Applied Power Electronics Conference and Exposition (APEC), 2018, pp. 1706–1709.

[12] R. Rodrigues, T. S. Jiang, Y. Du, P. Cairoli, and H. X. Zheng, “Solid state circuit breakers for shipboard distribution systems,” in 2017 IEEE Electric Ship Technologies Symposium (ESTS), 2017, pp. 406–413.

[13] C. Meyer and R. W. De Doncker, “LCC analysis of different resonant circuits and solid-state circuit breakers for medium-voltage grids,” in IEEE Transactions on Power Delivery, vol. 21, no. 3, pp. 1414–1420, Jul. 2006.

[14] J. M. Meyer and A. Rufer, “A DC hybrid circuit breaker with ultra-fast contact opening and integrated gate-commutated thyristors,” in IEEE Transactions on Power Delivery, vol. 21, no. 2, pp. 646–651, Apr. 2006.

[15] M. Callavik, A. Blomberg, J. Häfner, and B. Jacobson, “The hybrid HVDC breaker,” ABB Grid Systems, Nov. 2012.

[16] W. Li, L. G. Campbell, G. Balasubramanian, and L. D. Loud, “Measuring external dielectric strength of the vacuum interrupter envelope,” 2018 28th International Symposium on Discharges and Electrical Insulation in Vacuum (ISDEIV), 2018, pp. 531-534.

[17] Z. Liu et al., “Development of high-voltage vacuum circuit breakers in china,” in IEEE Transactions on Plasma Science, vol. 35, no. 4, pp. 856-865, Aug. 2007.

[18] P.G. Slade, The Vacuum Interrupter: Theory, Design, and Application, New York: CRC Press, 2008, p23.

[19] L. T. Falkingham and W. Molan, “Arc control systems for AMF high voltage vacuum interrupters — modeling the contact gap,” 2014 International Symposium on Discharges and Electrical Insulation in Vacuum (ISDEIV), 2014, pp. 125-128.

[20] X. Godechot, S. Chakraborty, A. Girodet, and P. Vinson, “Design and tests of vacuum interrupters for high voltage circuit breakers,” in Proc. 26th Int. Symp. Discharges Elect. Insul. Vac. (ISDEIV), Mumbai, India, September 2014, pp. 417-420.

[21] X. Pei, O. Cwikowski, D. S. Vilchis-Rodriguez, M. Barnes, A. C. Smith and R. Shuttleworth, “A review of technologies for MVDC circuit breakers,” IECON 2016 - 42nd Annual Conference of the IEEE Industrial Electronics Society, 2016, pp. 3799-3805.

[22] X. Pei and A. C. Smith, “Experimental tests of a resistive SFCL integrated with a vacuum circuit breaker,” in IEEE Transactions on Applied Superconductivity, vol. 26, no. 3, Apr. 2016.

[23] X. Pei, O. Cwikowski, A. C. Smith and M. Barnes, “Design and experimental tests of a superconducting hybrid DC circuit breaker,” in IEEE Transactions on Applied Superconductivity, vol. 28, no. 3, pp. 1-5, Apr. 2018.

[24] R. B. Ummaneni, C. Jaillot, R. Nilssen and J. E. Brennvall, “Experimental characterisation of linear permanent magnet actuator with gas springs,” 2009 IEEE International Electric Machines and Drives Conference, 2009, pp. 369-372.

[25] J. Jiang, H. Lin, S. Fang, “Multi-objective optimization of a permanent magnet actuator for high voltage vacuum circuit breaker based on adaptive surrogate modeling technique,” MDPI Energies, 2019.

[26] S. Fang, H. Lin and S. L. Ho, “Transient co-simulation of low voltage circuit breaker with permanent magnet actuator,” in IEEE Transactions on Magnetics, vol. 45, no. 3, pp. 1242-1245, Mar. 2009.

[27] S. Fang, M. Xia, H. Lin, S. Ho, “Analysis and design of a high-speed permanent magnet characteristic actuator using eddy current effect for high-voltage vacuum circuit breaker,” in IET Electric Power Applications 2016.

[28] D. S. Vilchis-Rodriguez, R. Shuttleworth, A. C. Smith and M. Barnes, “Design, construction, and test of a lightweight Thomson coil actuator for medium-voltage vacuum switch operation,” in IEEE Transactions on Energy Conversion, vol. 34, no. 3, pp. 1542-1552, Sep. 2019.

[29] Y. Wu et al., “A new Thomson coil actuator: principle and analysis,” in IEEE Transactions on Components, Packaging and Manufacturing Technology, vol. 5, no. 11, pp. 1644-1655, Nov. 2015.

[30] D. S. Vilchis-Rodriguez, R. Shuttleworth and M. Barnes, “Modelling Thomson coils with axis-symmetric problems: practical accuracy considerations,” in IEEE Transactions on Energy Conversion, vol. 32, no. 2, pp. 629-639, Jun. 2017.

[31] S. Kim, M. Song, N. Park, J. Yoo, Y. Park and K. Park, “Optimal design of moving-

magnet type actuators for optical disk drives considering effect of coil electromagnet," in IEEE Transactions on Magnetics, vol. 45, no. 5, pp. 2228-2231, May. 2009.

[32] R. E. Clark, D. Howe and G. W. Jewell, "The influence of magnetization pattern on the performance of a cylindrical moving-magnet linear actuator," in IEEE Transactions on Magnetics, vol. 36, no. 5, pp. 3571-3574, Sep. 2000.

[33] B. Yin, X. Zeng, J. F. Eastham, D. Vilchis-Rodriguez and X. Pei, "Novel fast operating moving coil actuator with compensation coil for HVDC circuit breakers," in CSEE Journal of Power and Energy Systems, vol. 7, no. 5, pp. 1041-1050, Sep. 2021.

[34] X. Pei, A. C. Smith, R. Shuttleworth, D. S. Vilchis-Rodriguez and M. Barnes, "Fast operating moving coil actuator for a vacuum interrupter," in IEEE Transactions on Energy Conversion, vol. 32, no. 3, pp. 931-940, Sep. 2017.

[35] D. S. Vilchis-Rodriguez, R. Shuttleworth, and M. Barnes, "Finite element assessment of moving coil actuator for HVDC breaker applications," in Proc. IECON-42nd Annu. Conf. IEEE Ind. Electron. Soc., Florence, Italy, Oct. 2016, pp. 4281–4286.

[36] C. Peng, I. Husain, A. Q. Huang, B. Lequesne, and R. Briggs, "A fast mechanical switch for medium-voltage hybrid DC and AC circuit breakers," IEEE Trans. Ind. Appl., vol. 52, no. 4, pp. 2911–2918, Jul. 2016.

[37] W. Wen et al., "Research on operating mechanism for ultra-fast 40.5-kVvacuum switches," in IEEE Transactions on Power Delivery, vol. 30, no. 6, pp. 2553–2560, Dec. 2015.

[38] E. Dong, P. Tian, Y. Wang, and W. Liu, "The design and experimental analysis of high-speed switch in 1.14kV level based on novel repulsion actuator," in Proc. 4th Int. Conf. Elect. Utility Deregulation Restruct. Power Technol., Weihai, Shandong, 2011, pp.

767–770.

[39] A. Bissal, J. Magnusson, and G. Engdahl, “Electric to mechanical energy conversion of linear ultrafast electromechanical actuators based on stroke requirements,” in IEEE Transactions on Industrial Applications, vol. 51, no. 4, pp. 3059–3067, Jul. 2015.

[40] A. Bissal, J. Magnusson, and G. Engdahl, “Comparison of two ultra-fast actuator concepts,” in IEEE Transactions on Magnet, vol. 48, no. 11, pp. 3315–3318, Nov. 2012.

[41] B. Yin, X. Pei, X. Zeng and F. Eastham, “A comparison between moving magnet and moving coil actuators for vacuum interrupters,” IECON 2019 - 45th Annual Conference of the IEEE Industrial Electronics Society, 2019, pp. 5651-5656.

Chapter 7.

Conclusions and future works

Chapter contents:

This chapter presents the thesis conclusions and discusses the potential future works.

7.1. Conclusions

This PhD research project developed a magnetically decoupled dual wound generator and a novel fast-operation moving coil actuator topology. Onboard electric propulsion systems have been proven to be an effective and environmental-friendly solution for large ships and hydrogen-electric aircraft. This Thesis makes intensive efforts into two aspects. Firstly, for the power side, a dual wound generator with decoupled outputs providing power supplies for both ship services and propulsion systems independently was designed and analysed. Secondly, for fault protection devices, the novel design of a moving coil actuator with compensation coils was proposed as a promising protection component for hybrid DC circuit breakers.

7.1.1. Magnetically decoupled design for a dual wound generator

This Thesis developed a dual wound generator for IFEP ship systems, which provided dual outputs from the 2-pole and 6-pole windings. The objectives have been achieved including:

- Designed the winding arrangement for a 2-pole and a 6-pole dual wound generator, to achieve magnetic decoupling between the two outputs. (presented in Chapter 3)

- Built a 2D finite element model of the proposed dual wound generator in COMSOL, to simulate the magnetic field distribution and operational performance. Investigated the output voltage and current to verify the magnetic decoupling design. (presented in Chapter 3)

- Built a prototype of the proposed dual wound generator design and experimentally tested its practical performance, to validate the full decoupling between the two outputs. (presented in Chapter 3 and Chapter 4)

The design achieved a fully decoupled winding arrangement by magnetic field harmonics analysis. The harmonics distributions of the 2-pole stator, 6-pole stator, 2-pole rotor and 6-pole rotor were calculated and cross-checked to ensure there was no common harmonic components between the 2-pole and the 6-pole windings. The dual wound generator topology was simulated in COMSOL using finite element modelling analysis. The magnetic field distribution and dynamical performance under resistive load conditions was also presented. The results further demonstrated the fully decoupled windings properties.

A prototype of the dual wound generator was designed, built and tested operating at 1,500 rpm (Chapter 3), and 2,000 rpm (Chapter 4). The static operating performance was demonstrated, showing no impact between the two outputs. Considering more complex practical operating conditions, sudden changes of resistive load, inductive load and rectified DC load were performed to further challenge the independence of the two outputs. All the experimental testing results proved that the magnetic decoupling design of the dual wound generator was achieved.

The dual wound generator design developed in this Thesis and experimentally validated for its decoupled windings design is achieved for the first time. This is important since in previous studies, using decoupled designs, were only performed entirely using 2D FEA, and did not include the effects of the end windings. In addition, most of the dual wound generators introduced previously used the same pole number for both windings, therefore, they were electromagnetically coupled, which means that a change in operating condition of one output would impact the operation of the other output. This is not ideal for electric ship applications. The dual wound generator proposed in this PhD research project achieves a fully magnetic decoupled design, where the change of operation of one output will not impact the operation of the other output.

7.1.2. Novel design of moving coil actuator topology with compensation coils

As fault currents in onboard DC electric networks have a high peak and rising rate, the key feature of the design of a hybrid circuit breaker used actuator is the operating speed. A novel design using compensation coils for the moving coil actuators was proposed in this Thesis. The objectives have been achieved including:

- Developed a novel moving coil actuator with compensation coils topology, and built a 2D finite element model in COMSOL to simulate the actuating performance. (presented in Chapter 5)

- Built and experimentally tested a prototype of the moving coil actuator design using a vacuum interrupter. (presented in Chapter 6)

The designed moving coil actuator topology has two air gaps to fully use the magnetic field generated by the permanent magnet. Four possible connections between the moving coils and compensation coils were introduced, including the passive compensation, series connection, parallel connection and hybrid connection.

The designed moving coil actuator topology was simulated using finite element modelling in COMSOL, to investigate the compensation coils' impact on the magnetic field distributions and the compensating performance. The simulation results showed the actuator's performance with compensation coils was significantly improved. The compensation coils generate an opposite-direction magnetic field against the magnetic field generated by the moving coils, avoiding the core saturation and eddy current losses effect. The compensation coils also effectively reduce the system equivalent inductance, thus increasing the rate of rise of the excitation current.

A prototype of the moving coil actuator with the designed compensation coils topology was built and experimentally tested with a vacuum interrupter. A pre-charged capacitor was used to provide energy for coil excitation. A 'H-bridge' circuit using four MOSFETs controlled the excitation current in both directions, which drove the actuator to open and close. The mechanisms were designed to operate with the actuating process including the latching system, springs and other supporting structures, which helped to eliminate the effects of bouncing, rebounding and welding.

The manufacture of the prototype actuator considered operation in a cryogenic environment for hydrogen electric aircraft applications. Cryogenic materials such as G10 and epoxy were used. The experimental tests investigated the dynamical performance of each actuator, and further analysed the global comparison between them. The key findings of the actuator performance can be summarised as follows:

- The compensation coils effectively eliminate the coil magnetic field saturation, thus reducing the eddy current losses

- The compensation coils effectively reduce the equivalent coil inductance, thus increasing the rate of rise of the excitation current

- The passive compensation coil actuator has a similar operation to the original MCA, but lower equivalent inductance. It can separate the two contacts of the vacuum interrupter in 3.7 ms at a capacitor voltage of 80 V

- The series connection actuator can withstand higher capacitor voltage, which allows higher energy stored in the pre-charged capacitor. It, therefore, can operate multiple times after each charge

- The parallel connection actuator performs at the fastest operating speed with the lowest capacitor voltage but has the highest energy consumption for one operation

- The hybrid connection actuator balances the performance between the series and parallel connection actuators, and achieves reasonable coil excitation current and operating speed

Overall the experimental results indicate the great potential of the designed actuator proposed in this Thesis for MVDC circuit breaker applications.

In summary, this Thesis provides valuable guidance for the magnetic decoupled windings design for dual wound generators and provides a novel idea for compensation coils for moving coil actuators, which provides the potential technologies for MVDC systems.

7.2. Future works

It is recommended that further research can be carried out in the following areas:

7.2.1. Magnetically decoupled design for a dual wound generator

- End-winding experimental analysis

The next research step for the dual wound generator could be the analysis of the end-windings. For machine designs, the end-windings effects are always a concern, as they contribute to unexpected harmonics. The 2D finite element modelling investigated in this Thesis only considered the in-slot windings. The experimental test results for the prototype dual wound generator in this Thesis included both the in-slot windings and also the end-windings effects. The author's previous research in [112] proposed a simplified 2D and 3D end-windings model to analyse the end-windings effects using the Biot-Savart law. It would therefore be beneficial to separately test and measure the end-windings magnetic field distributions, to verify the results from the finite element end-windings model.

- Dual wound motor applications

Generally, a dual wound machine can either operate as a generator or an electric motor. Dual wound three-phase motors have been proven to have the potential to improve the torque density and torque quality, with even higher efficiency. The dual wound generator designed in this research project is a synchronous machine with windings in both the rotor and stator frame, which can also operate as a synchronous motor. Benefiting from the decoupled winding design, it provides the possibility to design two independent control systems for this dual wound machine when operating as a dual wound motor.

- Permanent magnet dual wound machine applications

Permanent magnet machines have been proven to have better power density and promise higher efficiency compared to induction machines, which is a result of the development of NdFeB magnets. Future works may consider replacing the wound rotor of the dual wound machine with a permanent magnet rotor. This can be either an interior permanent magnet machine or a surface permanent magnet machine, which would depend on specific application requirements. It is noted that a permanent magnet arrangement may be carefully considered and designed to generate magnetic fields to only couple with the corresponding stator windings.

7.2.2. Novel design of moving coil actuator topology with compensation coils

- Cryogenic environment test

The moving coil actuator proposed in this Thesis from its initial design was considered for cryogenic electric aircraft applications. The materials used for the prototype MCA can withstand a cryogenic environment. Future experiments on the operation of the prototype

MCA could include a cryogenic environment, which may challenge the reliability of the movable parts. However, the lower operating temperature would result in the copper wires of the coils having lower resistance, thus supporting a higher excitation current.

- Test the actuator with a resonance circuit or in a hybrid DC circuit breaker

The actuator developed in this Thesis can separate the two contacts of a vacuum interrupter but is not able to break a fault current. This actuator topology is designed for hybrid DC circuit breakers, thus no resonance circuit is designed. To test it as a DC fault protection device, it must either operate with a passive or active resonance circuit (Section 2.2.1.4 and 2.2.1.5) or work as the mechanical switch in a hybrid DC circuit breaker. Future works on testing the performance of the actuator may contain the operation in a hybrid DC circuit breaker as a mechanical switch to block the full system voltage.